Probing the SU(N) Fermi-Hubbard model with ytterbium atoms in an optical lattice
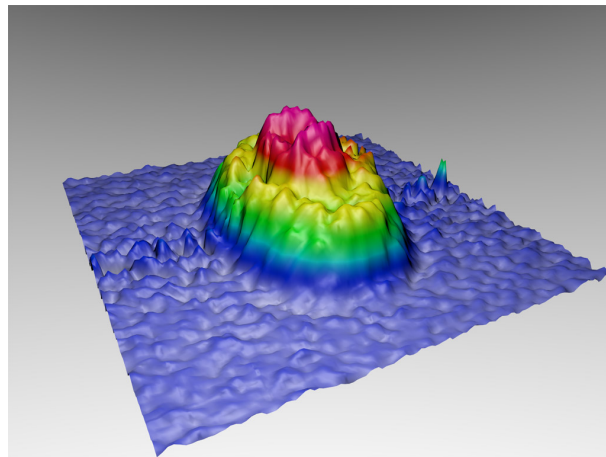
Christian Hofrichter

München, 2016

Probing the SU(N) Fermi-Hubbard model with ytterbium atoms in an optical lattice

Christian Hofrichter

Dissertation an der Fakultät für Physik
der Ludwig–Maximilians–Universität München

vorgelegt von
Christian Hofrichter
geboren in Dresden

München, 10. Mai 2016

Erstgutachter: Prof. Dr. Immanuel Bloch
Zweitgutachter: Prof. Dr. Ulrich Schollwöck
Tag der mündlichen Prüfung: 17. Juni 2016

Zusammenfassung

Diese Doktorarbeit beschreibt die experimentelle Umsetzung des 3D $SU(N)$ Fermi-Hubbard Modells und die direkte Messung der Zustandsgleichung mit Hilfe eines ultrakalten Quantengases von fermionischen Ytterbium-Atomen in einem optischen Gitter. Ultrakalte, neutrale Atome in optischen Gittern stellen ein gut kontrollierbares und hochflexibles System dar um Modelle aus der Festkörperphysik, wie z.B. das Hubbard Modell, zu untersuchen. Insbesondere erlauben Ytterbium-Atome, diese Modelle mit $SU(N)$ Symmetrie zu realisieren, da bei ihnen der Kernspin nahezu vollständig von der elektronischen Konfiguration der Atome entkoppelt ist. Als Folge dieser erweiterten Symmetrie hängen die thermodynamischen Größen von N – der Anzahl der Spinkomponenten im Quantengas – ab, und man erwartet neuartige Phasenzustände dieser Systeme bei niedrigen Temperaturen.

Durch Messen der lokalen Eigenschaften eines ^{173}Yb Quantengases, erhalten wir die Zustandsgleichung des $SU(6)$ und $SU(3)$ Fermi-Hubbard Modells. Die Zustandsgleichung erlaubt es uns, direkten, modellunabhängigen Zugang zu den thermodynamischen Größen des Gases im Gitter zu erlangen. Hiermit ist es möglich, durch Ändern der Wechselwirkungsstärke den Übergang von einer Fermi-Flüssigkeit zu einem $SU(N)$ Mott-Isolator zu beobachten, sowie die Kompressibilität des Gases für unterschiedlich starke Wechselwirkungen zu ermitteln. In dem Experiment beobachten wir eine niedrige spezifische Entropie des $SU(6)$ Gases, niedriger als die von unkorrelierten Spins, was auf partielle Spinkorrelationen im Quantengas hinweist. Die Möglichkeit, die Zustandsgleichung solcher Systeme mit hohem Spin direkt zu bestimmen, sowie die niedrige Entropie die erzielt wurde, stellen einen wichtigen Schritt für die Realisierung von $SU(N)$ Spin-Hamiltonoperatoren dar, sowie für die Charakterisierung von neuartigen $SU(N)$ Phasenzuständen.

Abstract

This thesis reports on the experimental realization of the 3D SU(N) Fermi-Hubbard model and the direct probing of the equation of state with an ultracold quantum gas of fermionic ytterbium in an optical lattice. Ultracold atoms in optical lattices constitute a flexible and highly tunable system to investigate Hamiltonians of condensed matter physics such as the Hubbard model. In particular, ytterbium atoms are ideal candidates for the realization of the Fermi-Hubbard model with SU(N)-symmetry due to a high decoupling of the nuclear spin from the electronic configuration. As a consequence of this enlarged symmetry, thermodynamic properties of the atomic sample depend on N, the number of spin components in the quantum gas, and novel, exotic phases are predicted to emerge at low temperatures.

By locally probing a quantum gas of ^{173}Yb in a 3D optical lattice, we determine the equation of state of the SU(6) and SU(3) Fermi-Hubbard model. The measurement of the equation of state allows us to obtain direct, model-independent access to the thermodynamic quantities of the lattice gas. In this way, we can characterize the crossover from a Fermi liquid to an SU(N) Mott insulator when tuning the interaction strength, and can probe the compressibility of the quantum gas in different interaction regimes. Moreover, we find a low specific entropy of the SU(6) gas below that of uncorrelated spins, indicating the presence of partial spin correlations in the atomic sample. The ability to access the equation of state of such high spin systems, as well as the low obtained entropy, represent an important step towards the realization of SU(N) spin Hamiltonians and the characterization of novel SU(N) phases.

Contents

Contents

Chapter 1

Introduction

With the advent of quantum mechanics at the beginning of the 20th century, applications of quantum-mechanical models in different fields of physics rapidly developed. Initially used for the description of single particles like atoms or electrons, quantum mechanics soon became indispensable to explain many-body phenomena in condensed matter physics on a microscopic level, like superfluidity or superconductivity [1–3]. To predict experimental observations in such systems, simplified models are used that try to explain the behavior within a minimal framework. Conventional superconductivity for example could be modeled by Baarden-Cooper-Schrieffer (BCS) theory by explaining the behavior with a pairing mechanism for electrons [2]. Other effects such as a vanishing conductivity of certain materials for strong Coulomb repulsion and for partially filled bands – the group of Mott insulators – could be described with the highly celebrated Hubbard model [4]. Due to the complexity of solids however, these simple models are often not able to explain all experimentally observed effects. Moreover, the many-body aspect in condensed matter systems makes it in general impossible to solve such models exactly. Because of these difficulties, it is for example still an ongoing debate if high-temperature superconductivity, which cannot be described by BCS theory, is captured within the Hubbard model [5–7]. This is even more remarkable considering the fact that high-temperature superconductors are studied for more than 30 years [8–11], which illustrates the need for new tools to study such strongly correlated systems.

Ultracold quantum gases

Ultracold quantum gases are a versatile tool to investigate quantum many-body phenomena. With the progress in laser cooling and trapping over the past decades, it became possible to cool atomic gases to quantum degeneracy. A milestone for reaching the quantum regime was the first creation of a Bose-Einstein condensate

(BEC) with ultracold gases, a phase of matter that was predicted by S. N. Bose and A. Einstein in 1924, but could not be observed before 1995 [12–14].

Shortly after the first condensation of a BEC, degenerate Fermi gases comprising several thousand atoms, which possess the same quantum statistics as electrons, were obtained as well in such experiments [15]. These achievements sparked a series of new developments in the field of atomic physics. The discovery of magnetic Feshbach resonances allowed for controlling interactions between the atoms, making cold atom experiments a flexible toolbox to study attractive as well as repulsive interactions of various strengths [16, 17]. In this way, the BEC-BCS crossover could be realized with ultracold quantum gases [18–20]. Another breakthrough concerning many-body physics with quantum gases was the realization of the Hubbard model with optical lattice potentials, as proposed by Jaksch et al. in 1998 [21]. Such lattices resemble the periodic structure of crystals and make it possible to enter the strongly correlated regime with ultracold atomic gases. The metal to Mott transition for fermionic quantum gases could be experimentally observed for the first time in 2008 [22, 23].

It turns out that the Hubbard model is in general a much more faithful description of ultracold atoms in optical lattices than it is for electrons in real solids. The Hubbard model assumes interactions only within a single orbital, an assumption that is perfectly fulfilled for cold atom experiments. In contrast to this, a large class of Mott insulators in solids possess electrons in d-orbitals with orbital degeneracy [24]. Moreover, defects in the crystal structure, as they happen in solids, do not exist in optical lattice potentials. In this respect, ultracold atom experiments can be considered quantum simulators, as originally envisioned by R. Feynman [25], for systems like the Hubbard model. Feynman's idea was to use a simulator that can be easily controlled in order to imitate and simulate the physics of another system, instead of trying to compute the problem mathematically. For this to work, the experiment should approximate the system as well as possible and allow for tuning the relevant parameters contained within the simulated model.

Apart from the tunability of such quantum simulators, another important aspect is the capability to probe these systems easily. Over the past years, the detection methods of quantum gases improved substantially. Many diagnostic techniques to study many-body systems were developed such as band-mapping [26], noise correlations [27, 28] or the ability to detect doublons in an optical lattice [23]. Recent progress in the detection and cooling techniques now even permits studying many-body systems directly with microscopes [29, 30]. Such quantum microscopes are able to resolve single atoms in optical lattices. This flexibility offers the possibility to probe density-density correlations or magnetic correlations directly in the trap and allows investigating quantum gases in more detail than ever before. In addition, more sophisticated lattice geometries were implemented such as super lattices [31], artificial gauge fields [32] or honeycomb and triangular lattices [33–35], which allow extending the range of physical systems that can be realized experimentally.

While the first cold atom experiments were realized mostly with alkali elements,

new systems that possess additional properties are employed in experiments these days. Ultracold, deeply bound polar molecules [36–40], elements with strong magnetic dipole moments such as erbium and dysprosium [41, 42], as well as Rydberg atoms [43, 44] which provide long-range interactions, have been accomplished. Moreover, degenerate quantum gases of alkaline earth-like elements such as ytterbium have been cooled and offer unique features.

Alkaline earth-like atoms

In contrast to alkali elements, which possess a single valence electron, alkaline earth-like elements exhibit a more complex level structure with two valence electrons, and possess several meta-stable states that can serve as an additional degree of freedom. These elements offer a variety of bosonic and fermionic isotopes, which possess different interaction properties. Moreover, some fermionic isotopes feature a large nuclear spin. The first BEC of ytterbium was created in 2003 by the group of Y. Takahashi [45]. In the last years, several other alkaline earth-like elements have been cooled to degeneracy [46–48] and a fermionic Mott insulator was realized with these elements [49].

The large nuclear spin and the presence of meta-stable states make such ultracold gases ideal for quantum simulation and for the realization of optical clocks. The weakly allowed ultra-narrow optical transition from the ground state to the meta-stable state permits implementing atomic lattice clocks with high precision. In 2015, such clocks achieved a precision with a relative uncertainty of about 10^{-18} [50, 51]. This is better than the current primary frequency standard with caesium, which is used for the definition of the second in the metric system. Therefore, optical lattice clocks have the potential to replace this standard in the future. The obtained precision of these clocks allows measuring for example extremely small frequency deviations in order to detect new physical effects. A change of fundamental physical constants over time, leading to frequency shifts of the optical transition, could be detected if the resolution of the clock is high enough to spot these changes [52–54]. Other applications of the long lifetime of the meta-stable states, in combination with an ultra-narrow laser linewidth, involve using alkaline earth-like elements for a highly sensitive detection of gravitational waves [55], which were predicted by Einstein's general relativity theory and which could only be detected very recently [56].

Quantum simulations

Besides for applications as optical clocks, alkaline earth-like atoms can be employed to realize certain condensed matter systems as they feature an almost perfect decoupling of the nuclear spin from the electronic structure in the ground state and in the lowest meta-stable state. This unique property has a variety of applications in the fields of

quantum simulation and quantum information and motivated a number of proposals over the past years [57–61].

The decoupling of the nuclear spin from the electronic configuration has direct consequences for the interaction between the atoms. Contact interactions are independent of the nuclear spin and become SU(N)-symmetric, where N is determined by the number of nuclear spin components of the isotope. The effects of this enlarged spin-symmetry are manifold. The SU(N)-symmetric Hubbard model for example features exotic phases that have not been observed before in solid-state systems. Alkaline earth-like atoms allow extending these models beyond the conventional spin-1/2 case in condensed matter physics, and could permit observing new phases like chiral spin liquids or phases with topological order [62–64]. In the context of solid-state physics, the SU(4)-symmetric version of the Fermi-Hubbard model has been theoretically studied for transition-metal oxides where the orbital degeneracy leads to an effective higher spin system [65]. Simulating such systems is not only interesting from the theoretical point of view but also has applications in other fields like quantum chromodynamics (QCD) [66]. There, the SU(3) symmetry is realized by the flavor of the quarks. Moreover, spin-1 exchange bosons in QCD, which mediate the forces in this field theory, also belong to the SU(3) symmetry group. The connection of this field with ultracold atom physics has been realized and proposals have even been made to simulate lattice gauge theories used for QCD with alkaline earth-like atoms in optical lattices [67].

In addition to the unique ground state properties, the meta-stable state in alkaline earth-like atoms can be considered as a second orbital for quantum simulation due to its long lifetime. This offers additional intriguing possibilities such as the realization of orbital-dependent optical potentials and allows investigating the Kondo lattice model or the Kugel-Khomskii model with enlarged spin symmetry [58, 68]. These systems have been studied in condensed matter physics over the past decades and describe materials of interacting electrons in different orbitals such as heavy fermion materials [69, 70] or Mott insulators in transition metal oxides [71]. The generalized SU(N)-symmetric version of such systems is expected to show an even richer phase diagram due to its enlarged spin symmetry. In this way ultra-cold atom experiments with alkaline earth-like atoms can constitute a valuable tool for answering some interesting open questions about the properties and types of phases for a variety of single and two-orbital systems, which are studied in condensed matter physics or even go beyond existing realizations of spin-1/2 systems which are used for describing interacting electrons.

This thesis

In this thesis we study an ultracold quantum gas of ytterbium in state-dependent and state-independent optical lattices. In particular, the thermodynamic properties

of the SU(N) Fermi-Hubbard model (FHM) in a 3D optical lattice are investigated. The experimental apparatus that was constructed offers the possibility to measure local quantities of the in-trap density distribution of the gas. With our preparation and detection methods, we are able vary and detect the spin mixture of the gas as well as to control the interaction parameters in the optical lattice. This provides full control over the relevant parameters to probe the metal to Mott crossover for an SU(N) Fermi gas. Our main results comprise the measurement of the equation of state and the compressibility of the FHM for an SU(3) and SU(6) Fermi gas and for various interaction strengths.

The main part of this thesis deals with the production, detection and manipulation of ultracold quantum gases of ytterbium. A state-dependent lattice setup was implemented for the simulation of two-orbital Kondo type physics and might become relevant for extending the single-orbital Hubbard model investigated in this work to two-orbital systems. Throughout this thesis, the fermionic isotope ^{173}Yb is considered mostly and we will focus mainly on the ground state of ytterbium. A detailed description of the interaction measurements, involving the meta-stable $^3P_0$-state that were done with this apparatus, as well as a detailed description of the clock laser used to couple the meta-stable state can be found in [72–74].

Outline

The thesis is organized as follows. Chapter 2 gives a summary about the relevant properties of ytterbium concerning laser cooling and trapping. The available isotopes and the different scattering lengths are presented. In the context of ultracold quantum gases in optical lattices, we motivate the SU(N)-symmetric interactions and the emergence of the orbital-dependent polarizability for the ground- and meta-stable state.

In chapter 3, the SU(N) Fermi-Hubbard model (FHM) and the two-orbital Kondo lattice model is introduced. In particular, the equation of state of the FHM in the Mott regime is given and its dependence on experimentally relevant parameters such as the temperature is investigated. We illustrate the rich phase diagram of the SU(N) FHM for higher spin systems that is expected to differ strongly from its spin-1/2 version. At the end of this chapter, we extend the FHM to a two orbital version and introduce the Kondo lattice Hamiltonian.

In chapter 4, the experimental apparatus and the laser systems that were constructed for producing, manipulating and detecting ultracold ytterbium atoms are presented. We show the vacuum chamber of the setup, where the quantum gas is trapped and give a short overview of the relevant parameters of the laser systems involved for cooling ytterbium to quantum degeneracy.

The preparation, detection and characterization of SU(N)-symmetric Fermi gases is described in chapter 5. In this chapter, we characterize the imaging system used

for the in-situ detection of the atomic sample. Moreover, the experimentally relevant parameters of the atomic sample, such as the temperature of the SU(N) Fermi gas after evaporation, are presented and the and detection of the nuclear spin of the Fermi gas is explained.

Chapter 6 introduces the experimental realization of the state-independent and state-dependent lattices that are employed in the experiment. This chapter describes the optical lattice that is used for precision spectroscopy and for studying Hubbard physics. Moreover, the measurement of the relative polarizability in a state-dependent lattice is presented. At the end of this chapter, we will give some brief results of ytterbium ground-state atoms that are loaded in a state-dependent lattice and which are optically dressed with the clock transition.

In chapter 7, we present the measurements of the equation of state of the SU(N) Fermi-Hubbard model. After motivating the experimental sequence used for this experiment, we explain and characterize the reconstruction of the in-trap cloud density. After that, the equation of state of the SU(3) and SU(6) Fermi gas, as well as the measured compressibility for different interaction regimes, are presented. Moreover, we estimate the three-body loss coefficient for ^{173}Yb ground-state atoms.

At the end of this thesis, in chapter 8, we conclude and give an outlook about further prospects regarding two-orbital system with tunable interactions, the orbital Feshbach resonance and the realization and detection of magnetically ordered phases in high spin systems.

Publications

The main results, obtained throughout this PhD thesis, have been published in the following journals:

C. Hofrichter, L. Riegger, F. Scazza, M. Höfer, D. R. Fernandes, I. Bloch, and S. Fölling, "Direct Probing of the Mott Crossover in the SU(N) Fermi-Hubbard Model", Physical Review X **6**, 021030 (2016)

M. Höfer, L. Riegger, F. Scazza, C. Hofrichter, D. R. Fernandes, M. M. Parish, J. Levinsen, I. Bloch, and S. Fölling, "Observation of an Orbital Interaction-Induced Feshbach Resonance in ^{173}Yb", Physical Review Letters **115**, 265302 (2015)

F. Scazza, C. Hofrichter, M. Höfer, P. C. De Groot, I. Bloch, and S. Fölling, "Observation of two-orbital spin-exchange interactions with ultracold SU(N)-symmetric fermions", Nature Physics **10**, 779–784 (2014)

Chapter 2

Ytterbium - an alkaline earth-like element

In this chapter, we give an overview about the general properties of ytterbium that are relevant for producing degenerate quantum gases. Ytterbium, as a rare earth element, possesses similar electronic properties as elements of the alkaline earth group. We first introduce the physical and chemical properties of ytterbium like the abundance of its isotopes. After that, we show the electronic level structure with the relevant optical transitions that are used in the experiment. We explain the features of these transitions and the associated states that give ytterbium its unique properties. After that, we discuss the $\mathrm{SU}(N)$-symmetric interactions that arise for such elements in the ground state, a feature that will become particularly relevant in chapter 3 and chapter 7. At the end of this chapter, we show the polarizability of the ground- and meta-stable state of ytterbium, which is relevant for the implementation of a state-dependent potential that was realized recently with a second lattice setup.

Alkaline earth elements belong to group-II of the periodic table. This group comprises the following elements: beryllium (Be), magnesium (Mg), calcium (Ca), strontium (Sr), barium (Ba), and radium (Ra). Common for these elements is a noble gas configuration for the inner shells with two outer valence electrons in a filled s-shell. Because of the filled inner shells, the chemical and electronic properties are mainly given by the two valence electrons.

In contrast to these elements, ytterbium (Yb) belongs to the group of rare earth elements with an electronic configuration $[\mathrm{Xe}]4\mathrm{f}^{14}6\mathrm{s}^2$. Its name arises from the place of its discovery close to Ytterby in Sweden by the Swiss chemist Jean Charles Galissard de Marignac in 1878. Due to the filled f-shell and two electrons in the s-shell, ytterbium behaves electronically similar to alkaline earth elements. Therefore, the group of elements with two electrons in the s-shell like ytterbium, mercury or cadmium and the group of alkaline earth elements are commonly referred to as alkaline earth-like elements.

Isotope	Mass (u)	Abundance (%)	Nuclear spin	Statistics
^{168}Yb	167.934	0.12	0	bosonic
^{170}Yb	169.935	2.98	0	bosonic
^{171}Yb	170.936	14.09	1/2	fermionic
^{172}Yb	171.936	21.69	0	bosonic
^{173}Yb	172.938	16.10	5/2	fermionic
^{174}Yb	173.939	32.03	0	bosonic
^{176}Yb	175.943	13.00	0	bosonic

Table 2.1: Natural abundance of the seven stable ytterbium isotopes. Data for the isotope abundance is taken from [78]. The atomic mass of the different isotopes is taken from [79].

2.1 Physical and chemical properties

Ytterbium is a soft, shiny metal with a density of $6.90\,g/cm^3$, which oxidizes slowly in air and dissolves in water. It is a rather heavy element with a proton number of $Z = 70$. Ytterbium has a melting point of 894 °C and boils above 1196 °C [77]. Because of the high melting point, it requires elevated oven temperatures of several hundred degrees Celsius compared to alkali elements in order to obtain sufficiently high fluxes of ytterbium atoms for quantum gas experiments. The required temperatures to achieve a substantial vapor pressure for trapping atoms are however still within reach experimentally.

Ytterbium possesses seven stable isotopes as shown in table 2.1. As opposed to strontium, it offers a relatively high abundance of several bosonic and fermionic isotopes that can be used in the experiment. Two fermionic isotopes, ^{171}Yb and ^{173}Yb, are present in ytterbium and possess a nuclear spin. In contrast to that, the bosonic isotopes have no nuclear spin ($I = 0$). The high abundance of several isotopes together with favorable scattering lengths for several isotopes (see section 2.4) allows cooling various combinations of Bose and Fermi mixtures sympathetically as well as single isotope cooling.

2.2 Electronic structure

Ytterbium, as well as alkaline earth elements, features a helium-like level structure with a spin-singlet and spin-triplet manifold. Because of the filled s-shell the two valence electrons can align in parallel and form a spin triplet ($S = 1$) or align anti-parallel forming a spin singlet ($S = 0$). The level structure of ytterbium is well described by LS-coupling where the total spin of the electrons **S** and the total orbital angular momentum **L** couple together to form the total electronic angular
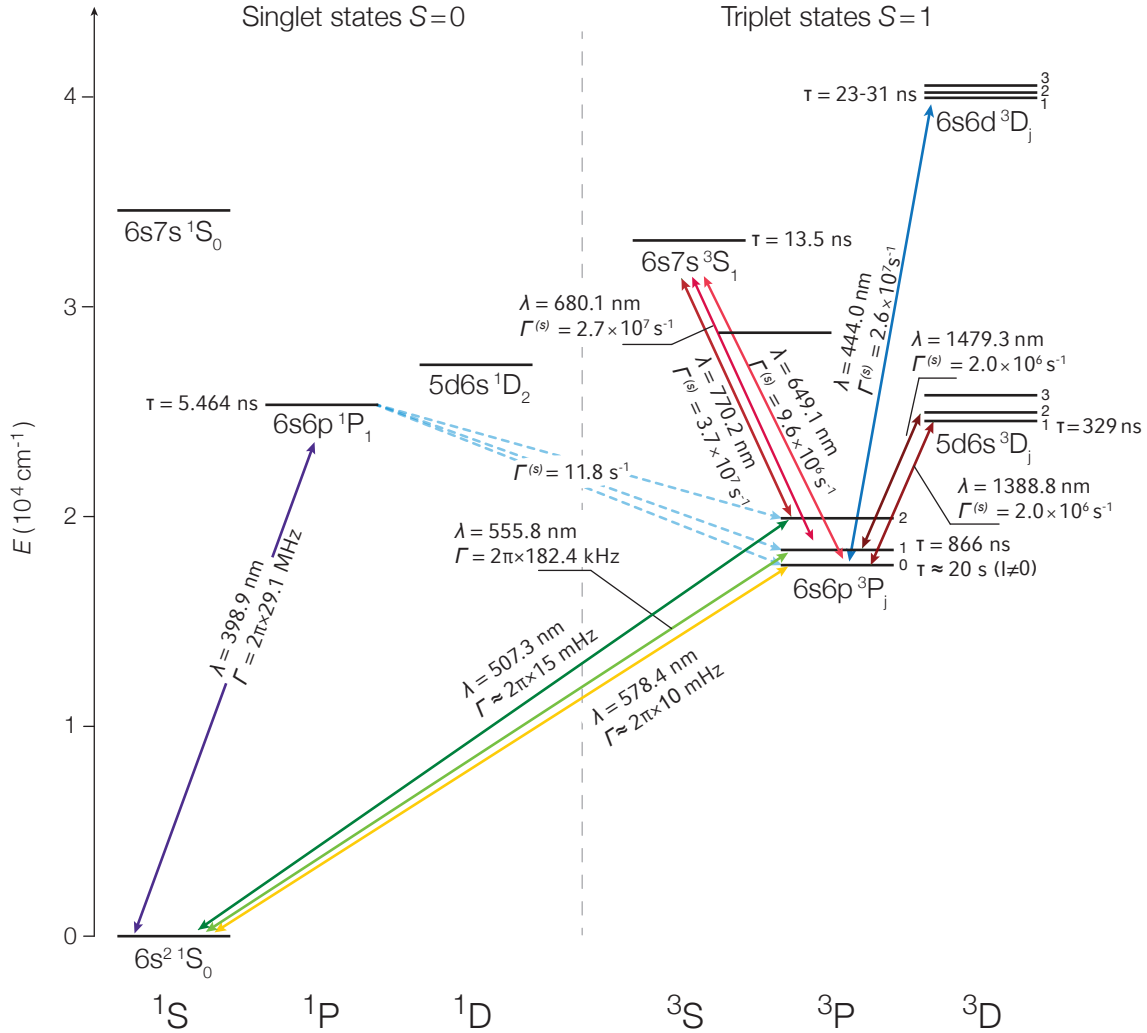
Figure 2.1: Illustration of the electronic level structure of ytterbium. The solid arrows indicate the most relevant optical transitions to excited states (horizontal lines) with the linewidth Γ. The excited-state lifetimes τ are taken from [80–84]. Dashed lines denote decay channels of the $^1P_1$ state with the decay rate taken from [85]. Otherwise, decay rates are calculated with the dipole matrix elements from [83]. Figure adapted from [73].

momentum $\mathbf{J} = \mathbf{L} + \mathbf{S}$. A detailed scheme of the level structure for ytterbium with the most relevant optical transitions is shown in Fig. 2.1.

2.2.1 The ground state

The ground state $^1S_0$ of ytterbium is a spin singlet with no total electronic angular momentum ($J = 0$). The nuclear spin I is the only spin present, and the total spin of the atom is given by $F = I$. The absence of a total electronic angular momentum has direct implications on the properties of the ground state. One consequence is a decoupling of the nuclear spin degree of freedom from the electron shell which gives rise to $\mathrm{SU}(N)$-symmetric interactions for the fermionic isotopes as we will see in section 2.3. Another consequence is the lack of any hyperfine structure in the ground state and an almost complete insensitivity to magnetic fields because of the weak or zero nuclear magnetic moment for fermionic and bosonic isotopes respectively. The only magnetic moment of the ground state stems from the nuclear spin. As the nuclear magneton is about a factor of 1800 lower than the Bohr magneton of the electron, due to large proton to electron mass ratio, the weak magnetic moment arising from the nuclear spin is usually negligible experimentally.

Consequently, magnetic trapping as well as Stern-Gerlach separation of spin states with magnetic field gradients are impractical because of the high magnetic fields that would be required, or even impossible for isotopes without a nuclear spin. We will see in chapter 5 how an optical method can be used to separate the nuclear spin states. At the same time, the magnetic field insensitivity makes it impossible to use magnetic Feshbach resonances, which are commonly used for alkali elements to change the interaction strength between the atoms. Nevertheless, this insensitivity to magnetic fields is also an advantage for high precision spectroscopy, as residual fields will not cause a frequency shift or broadening of optical transitions.

2.2.2 Optical cooling transitions

Two transitions are usually used to cool ytterbium atoms, a broad optical transition in the singlet manifold and a narrow optical transition in the triplet manifold. Both optical transition frequencies have an isotope dependence, which is summarized in table 2.2.

The broad optical transition with a wavelength of $\lambda = 399\,\mathrm{nm}$ connects the ground state $^1S_0$ with the $^1P_1$-state. This transition is dipole allowed, in the blue visible spectrum of the light and has a high scattering rate $\Gamma = 2\pi \times 29.1\,\mathrm{MHz}$. Due to the small branching ratio in ytterbium, the $^1S_0 \rightarrow {}^1P_1$ transition can be regarded as almost closed as the excited $^1P_1$-state decays mostly to the ground state. A very weak decay of the $^1P_1$-state to the $5d6s\,{}^3D_{1,2}$ states and from there to the $^3P_{0,1,2}$ states has been measured which is however not significant for our applications of Zeeman slowing and imaging [82, 90]. The branching ratio for the decay to the $5d6s\,{}^3D_{1,2}$

Isotope	$^1S_0 \to {}^1P_1$ (MHz)	$^1S_0 \to {}^3P_1$ (MHz)	$^1S_0 \to {}^3P_0$ (MHz)
^{168}Yb	1887.40	3655.13	n/a
^{170}Yb	1192.39	2286.35	n/a
^{171}Yb (centroid)	939.52	1825.72	1811.28164
^{172}Yb	533.31	1000.02	n/a
^{173}Yb (centroid)	291.52	555.78	551.53839
^{174}Yb	0	0	0
^{176}Yb	-509.31	-954.83	n/a

Table 2.2: Relative isotope shifts with respect to ^{174}Yb for the two cooling transitions used in the experiment and the clock transition $^1S_0 \to {}^3P_0$. The isotope shifts for the cooling transition have been obtained from [86] and [87]. The isotope shifts for the clock transition are taken from [88, 89].

states is about $1 : 10^7$ and approximately two orders lower than in strontium [91, 92]. To close this loss channel, i.e. when trapping atoms in a magneto-optical trap using this transition, repumper lasers can be employed. Light that is resonant with the $6s6p\,^3P_0 \to 6s7s\,^3S_1$ and the $6s6p\,^3P_2 \to 6s7s\,^3S_1$ transition allows bringing atoms back to the cooling cycle that decayed to the meta-stable $^3P_{0,2}$ states [93]. By using repumper lasers on these transitions in a magneto-optical trap for ^{174}Yb, a 30 % increase in total atom number and increased lifetime by a factor of two could be measured [85].

The second optical transition used for cooling in this experiment is the $^1S_0 \to {}^3P_1$ transition with a wavelength $\lambda = 555.8\,$nm in the green visible spectrum of the light. This transition connects the singlet manifold with the triplet manifold of the level structure. As this transition involves an electron spin flip from a state with $S = 0$ to a state with $S = 1$, it is in principle dipole forbidden. However, spin-orbit interaction admixes this state with the $^1P_1$-state [94]. Therefore, it can decay via a weakly electric dipole transition and a lifetime of $\tau = 866\,$ns. The linewidth of this transition is relatively narrow with $\gamma = 182\,$kHz, which makes the transition particular useful for optical cooling in the magneto-optical trap (MOT). The Doppler temperature associated with this linewidth is only $T_D = 4.4\,\mu$K and allows producing very cold gases in a MOT [95]. The $^1S_0 \to {}^3P_1$ transition can be considered almost closed as the $^3P_1$ state decays mainly to the ground state. Only a very weak and completely negligible magnetic dipole decay to the $^3P_0$ state is possible [96].

Hyperfine splittings

In contrast to the ground state and the $^3P_0$ state, which do not possess hyperfine structure due to the absence of a total electronic angular momentum, the excited $^1P_1$

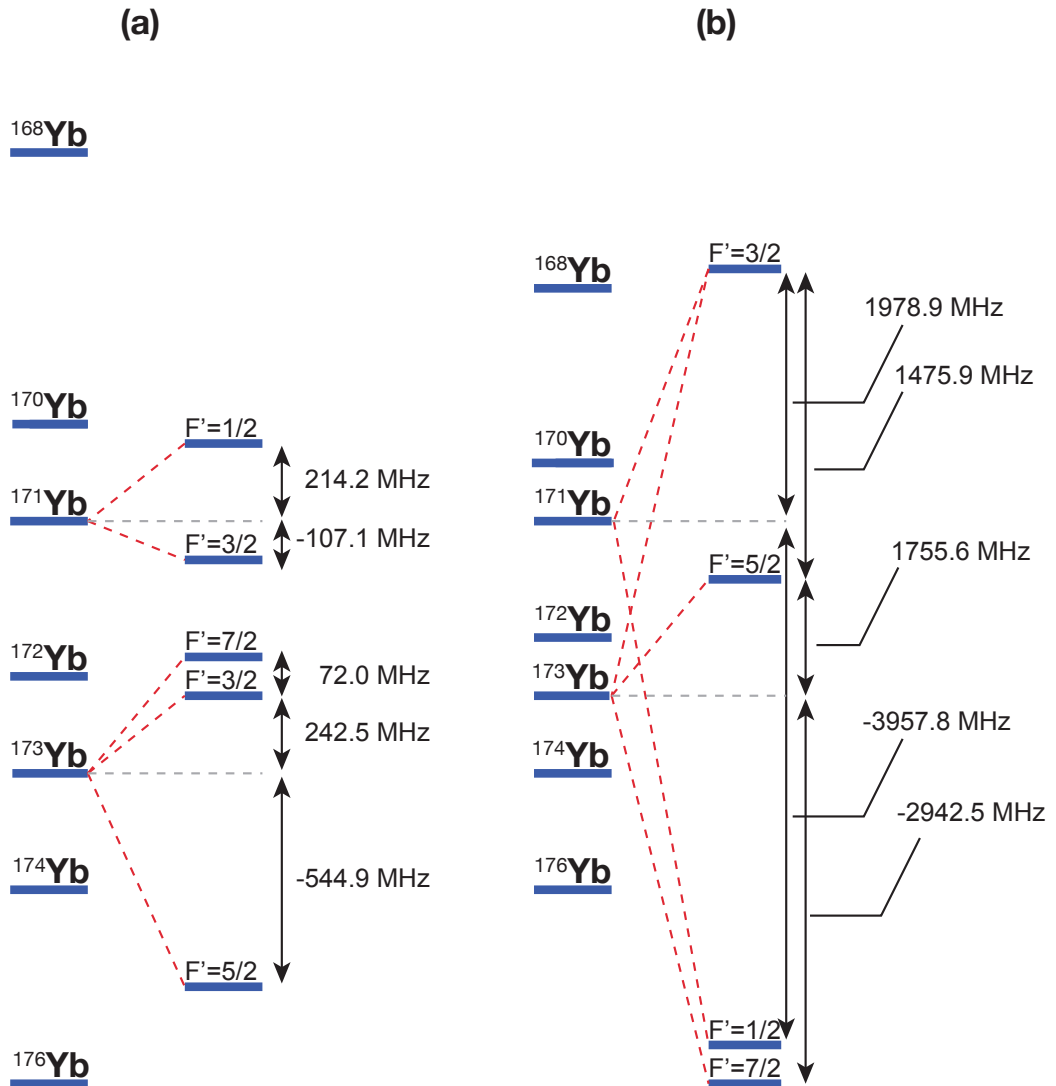**(a)**   **(b)**

Figure 2.2: Illustration of the isotope shifts of ytterbium including the hyperfine splitting of the fermionic isotopes. **(a)** Level structure of the $^1S_0 \to {}^1P_1$ transition. **(b)** Level structure of the $^1S_0 \to {}^3P_1$ transition. The isotope shifts of the right figure are scaled down by a factor of three as compared to the left one.

and $^3P_1$-state possess a hyperfine splitting for the fermionic isotopes. The bosonic isotopes lack a nuclear spin ($F = I = 0$) and only a single transition without hyperfine splitting $F = 0 \to F' = 1$ is possible for these isotopes.

For the fermionic isotopes ^{171}Yb and ^{173}Yb , the hyperfine splitting of the $^1P_1$ state is on the order of a few hundred megahertz as shown in Fig. 2.2. This makes them conveniently accessible for intra-cavity laser diodes, which have only a limited tuning range. Opposed to that, the hyperfine splitting of $^3P_1$-state is in the order of a few gigahertz due to parallel aligned spins of the valence electrons. In the latter case, the hyperfine splitting is as large as the maximum isotope shift of the transition.

2.2.3 Metastable states

A common feature of ytterbium as well as other alkaline earth elements is the existence of two meta-stable states, the $^3P_0$ state and the $^3P_2$ state.

The $^3P_0$ state in ytterbium has a lifetime of about 20 s, which makes this state ideal to study multi-orbital physics with ultracold atom experiments. Moreover, this state has no angular momentum ($J = 0$) like the ground state, which leads to a very good decoupling of the nuclear spin from the electronic structure and results in $SU(N)$-symmetric interactions.

The clock transition

The $^1S_0 \to {}^3P_0$ transition connects the ground state with the lowest meta-stable state. This transition is dipole forbidden and therefore extremely narrow. In addition to that, the $^3P_0$-state is insensitive to magnetic fields due to the absence of an electronic angular momentum. The ultra-narrow linewidth and the magnetic field insensitivity make this transition ideal for precise measurements of interaction shifts as well as for optical clocks. Therefore, the $^1S_0 \to {}^3P_0$ transition is often referred to as the clock transition. However, the narrow linewidth also imposes high demands to the laser linewidth and the stabilization of the laser in order to achieve sufficiently high Rabi couplings and a high frequency resolution [97–99].

The clock transition has a wavelength of $\lambda = 578.4$ nm, which is in the yellow visible light spectrum. The absolute transition frequency for ^{174}Yb is $\nu = 518\,294\,025\,309\,217.8(0.9)$ Hz [88]. An isotope shift of a few gigahertz exists and has been measured for at least three isotopes as summarized in table 2.2. The clock transition is actually doubly forbidden due to the selection rule $J = 0 \to J = 0$ and due to an electron spin flip which is required for the excitation ($S = 1 \to S = 3$). Only an admixing due to hyperfine coupling with the $^1P_1$ and $^3P_1$ state makes this transition weakly allowed for fermionic isotopes. This admixing has been calculated for ytterbium and the associated lifetimes are about 20 s for ^{171}Yb and about 23 s for ^{173}Yb and correspond to natural linewidths of $\Gamma \approx 2\pi \times 7$ mHz and and $\Gamma \approx 2\pi \times 8$ mHz respectively [100].

Because of the absence of hyperfine structure for the bosonic isotopes, the $^3P_0$ state can only decay for bosonic isotopes via a two-photon process with negligible probability and the transition is essentially forbidden [81]. In order to make this transition dipole allowed, a magnetic field has to be applied that can admix the $^3P_1$ state with the $^3P_0$ state [101, 102]. The coupling strength of the clock transition due to this admixing then becomes directly proportional to the applied magnetic field strength.

The $^3P_2$ state

The $^3P_2$ state is the second meta-stable state in alkaline earth-like atoms with a lifetime of about $10\,\mathrm{s}$ [81]. This state can decay over different channels. The main contribution is a decay process to the $^3P_1$ state, which decays to the ground state. Due to the long lifetime of the $^3P_2$ state, the associated $^1S_0 \rightarrow {}^3P_2$ transition has a very narrow natural linewidth of $\gamma \approx 10\,\mathrm{mHz}$ at a wavelength of $\lambda = 507.3nm$. As opposed to the $^3P_0$ state, this state possesses hyperfine structure and strong magnetic field sensitivity due to its total electronic angular momentum ($J = 2$). The $^3P_2$ state of ytterbium was used to implement a magnetically tunable Feshbach resonance between the ground state and the meta-stable state [103]. In addition, the narrow optical transition was employed for spatially resolved imaging of a BEC [104] as well as for the preparation of a single layer BEC in an optical lattice in combination with a quantum gas microscope [105]. In the latter case, a magnetic field gradient together with the magnetic field sensitivity of the $^3P_2$ state and the very narrow linewidth was employed to remove atoms from individual layers, thereby preparing a single layer atomic sample.

2.3 SU(N) symmetric interactions

An important property of alkaline earth-like atoms is the presence of SU(N)-symmetric interactions in the ground state as well as in the $^3P_0$ state. Here N denotes the number of nuclear spin components (e.g $N = 6$ for ^{173}Yb with $I = 5/2$). For both states the vanishing angular momentum ($J = 0$) leads to a decoupling of the nuclear spin with the electronic state configuration. As the scattering length is only determined by the electronic configuration of the atoms, the nuclear spin decoupling leads to SU(N)-symmetric interactions between the atoms. This results in a number of interesting applications for simulating many-body physics as explained in chapter 1.

The independence of the scattering length with respect to the nuclear spin-state m_F can be understood by considering the interaction potential of two colliding atoms in the limit of low temperatures. Let us first study the spin-1/2 case. For the typical densities reached in the experiments, the gas is so dilute that only binary collisions
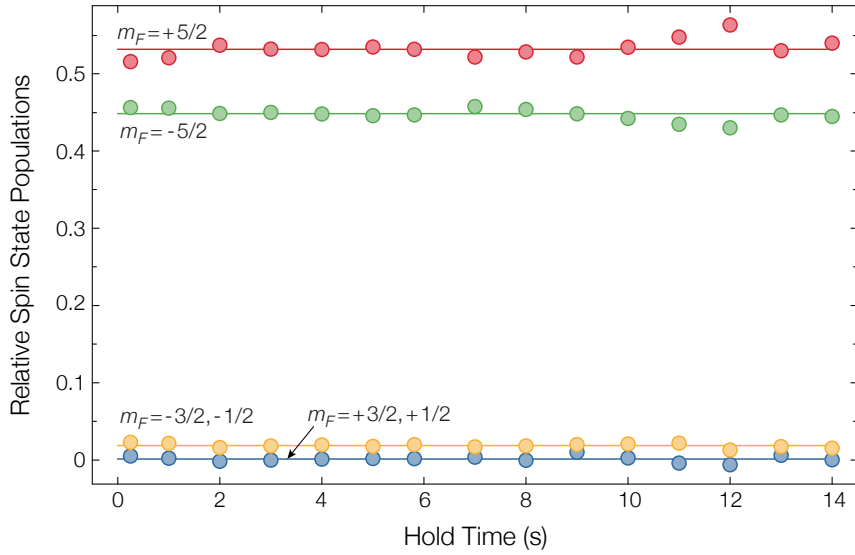
Figure 2.3: Measurement of the spin population in an SU(*N*) Fermi gas as a function of hold time (figure adapted from [72]). A Fermi gas of ^{173}Yb (N=6) was prepared in an optical dipole trap with only two populated spin components. The absence of spin changing collisions leads to a conservation of the particle number per sin state.

have to be considered. In addition, at low temperatures, the de Broglie wavelength is much larger than the interaction range and the scattering becomes isotropic and energy-independent. At sufficiently low temperature, the inter-atomic potential for spin-1/2 fermions and bosons can be approximated with a pseudo-potential that reproduces the scattering length of the real potential. The real interaction potential can then be replaced by an effective contract potential that contains a delta-function [106]

$$V(\mathbf{r}) = \frac{4\pi a_{\alpha,\alpha'}\hbar^2}{m}\delta(\mathbf{r}). \tag{2.1}$$

Here m denotes the mass of the colliding atoms and $\delta(\mathrm{r})$ defines the delta-function contact potential. The only free parameter in this equation is $a_{\alpha,\alpha'}$ which denotes the scattering length between the ground state ($\alpha \in |g\rangle$) or the $^3P_0$ excited-state atoms ($\alpha \in |e\rangle$). The scattering length is given by the phase shift which the two colliding atoms acquire during the traversal of the interaction potential and is mostly determined by the last bound state in that potential. A positive scattering length corresponds to repulsive interactions while a negative scattering length corresponds to attractive interactions.

The formula given above can be generalized to fermions with N spin-components as shown by Yip et al. [107]

$$V(\mathbf{r}) = \sum_{\substack{F_t=0 \\ F_t=even}}^{N-2} \frac{4\pi a_{\alpha,\alpha}^{F_t}\hbar^2}{m}\delta(\mathbf{r})P_{F_t}. \tag{2.2}$$

Here P_{F_t} denotes the projector on states with even total spin $F_t = 0, 2, 4..N-2$ of the atom pair. At low temperatures, only s-wave collisions are possible energetically, and collisions with higher angular momentum are suppressed due to the centrifugal barrier of the inter-atomic potential. In this limit, only states with even values of F can contribute to scattering, as their associated total wave function is anti-symmetric in this case. In order to describe a Fermi system with N spin components, $N/2$ scattering lengths are in general necessary because of the different electronic configurations of the atom pair.

When two atoms with spin $\mathbf{F_1} = |F, m_{F_1}\rangle$, $\mathbf{F_2} = |F, m_{F_2}\rangle$ and a total spin of the pair $|F_t, m_{F_t} = m_{F_1} + m_{F_2}\rangle = \mathbf{F_1} + \mathbf{F_2}$ collide, the interaction Hamiltonian of Eq. 2.2 will in general lead to a coupling of the initial m_F states to other states [108, 109]. Due to momentum conservation, the modulus of the spin of the pair F_t, and m_{F_t}, its spin projection is conserved, but not the spin projection of the individual atoms.

In general, for arbitrary scattering lengths, the symmetry of Eq. 2.2 is given by the special unitary group $SU(2)$. In the special case of $F = 3/2$, a higher SO(5) symmetry is realized without any tuning of the scattering lengths [110]. However, for alkaline earth-like atoms, the nuclear spin is decoupled from the electronic structure. Therefore, the contract potential and the scattering lengths are the same for all spin components and Eq. 2.2 acquires a higher SU(N) symmetry. Only collision channels for which the spin projection m_{F_1}, m_{F_2} for the ingoing particles and m_{F_3}, m_{F_4} for the outgoing particles are the same, have a non-vanishing matrix element

$$\langle F, m_{F_4}|\langle F, m_{F_3}|V|F, m_{F_1}\rangle|F, m_{F_2}\rangle. \tag{2.3}$$

Consequently, in contrast to the general case with $SU(2)$ symmetry as given above, not only the total spin and its spin projection are a conserved quantity, but also the spin projection m_F of each atom is preserved for SU(N)-symmetric interactions. Spin relaxations to other m_F states are therefore forbidden.

The emergent SU(N) symmetry has direct consequences for the properties of the quantum gas. The absence of spin relaxation allows preparing interacting systems with a varying number of populated spin components without repopulation of other m_F-states due to collisions. To illustrate this, Fig. 2.3 shows the spin population for a gas of ^{173}Yb with $F = 5/2$ ($N = 6$) as a function of the hold time. The system was prepared with only two populated m_F-states. Even after several seconds no noticeable repopulation of initially non-populated m_F-states takes place. This shows the absence of significant spin changing collisions on typical timescales that are relevant in our experiments. Theoretical estimates for the SU(N) symmetry breaking of alkaline earth-like atoms have been given by Gorshkov et al.[58]. For the ground

Isotope	^{168}Yb	^{170}Yb	^{171}Yb	^{172}Yb	^{173}Yb	^{174}Yb	^{176}Yb
^{168}Yb	**252.0(34)**	117.0(15)	89.2(17)	65.0(19)	38.6(25)	2.5(34)	−359.0(30)
^{170}Yb		**63.9(21)**	36.5(25)	−2.1(36)	−81.3(68)	518.0(51)	−209.5(23)
^{171}Yb			**−2.8(36)**	−84.3(68)	−578(60)	429(13)	141.6(15)
^{172}Yb				**−599(64)**	418(13)	200.6(23)	106.2(15)
^{173}Yb					**199.4(21)**	138.8(15)	79.8(19)
^{174}Yb						**104.9(15)**	54.4(23)
^{176}Yb							**−24.2(43)**

Table 2.3: S-wave scattering length of the atoms in the ground state in units of a_0 between the different ytterbium isotopes. Data taken from [113].

state the variation of the scattering length for different nuclear spins is estimated to be below 10^{-9}. In the excited state, the nuclear spin decoupling is somewhat lower due to the admixing with other states that possess electronic angular momentum. However, it is predicted to be still below 10^{-3}. Both values are so small that they are negligible for most of the experiments.

The implications of the SU(N) symmetry on thermodynamic properties of a quantum gas are manifold and can for example be observed in a Fermi gas in the bulk. As a result of SU(N)-symmetric interactions, the compressibility and density of an interacting Fermi gas will change with the enlarged symmetry [111]. Moreover, properties like the momentum distribution, the excitation spectrum or collective modes of the interacting gas will vary with the number of spin components, which has been experimentally confirmed in one dimension [112]. SU(N)-symmetric interactions also allow studying many-body physics in periodic potentials with enlarged symmetry like the SU(N) Fermi-Hubbard model, which we will investigate in chapter 7.

2.4 Scattering properties

In the previous section we introduced the scattering length and motivated the emergent SU(N)-symmetry in the ground state. Although the scattering length of the ground state is the same for all spin-components within an isotope, it is however different between the individual ytterbium isotopes. The isotope-dependent scattering lengths for the ground state, as shown in table 2.3, have been determined to high precision in [113] and are relevant to decide for the optimal cooling strategy, e.g. intra-isotope or sympathetic cooling in a mixture. The diagonal entries in this table represent the intra-isotope scattering length. ^{173}Yb is the only fermionic isotope with a favorable intra-isotope scattering length of around $200a_0$ for which efficient evaporative colling can be performed without sympathetic cooling. In contrast to that, ^{171}Yb has almost vanishing attractive interactions ($a_{g,g} < 0$) and can only

Isotope	^{171}Yb	^{173}Yb
a_{gg}	$-2.8(36)$[113]	$199.4(21)$[113]
a_{eg}^+	n/a	$1878(37)$[76]
a_{eg}^-	$-25(25)$[116]	$219.5(29)$[72]
a_{ee}	n/a	$306.2(106)$[72]

Table 2.4: S-wave scattering lengths in units of a_0 between the ground state and the $^3P_0$ meta-stable state for both fermionic ytterbium isotopes.

be cooled sympathetically with a second isotope for example ^{174}Yb. The bosonic isotopes ^{168}Yb,^{170}Yb and ^{174}Yb also have favorable scattering lengths and have each been cooled to degeneracy independently [45, 114, 115].

2.4.1 Scattering properties of the meta-stable state

Due to its long lifetime and its applications for quantum-simulation proposals, the scattering properties of the meta-stable ($^3P_0$) state of the fermionic ytterbium isotopes are of particular interest. Until recently, the scattering length between the ground state ($|g\rangle$) and meta-stable state ($|e\rangle$) was not known for ^{173}Yb but has been determined in [72]. For SU(N)-symmetric interactions the scattering properties between two atoms will depend only on the orbital configuration which can be a singlet or triplet. Therefore, interactions between the two electronic orbitals, with the nuclear spin states denoted as $|\downarrow\rangle$ and $|\uparrow\rangle$, are described by four elastic scattering lengths, which are listed for ^{173}Yb and ^{171}Yb in table 2.4. Here $a_{e,e}$ denotes the scattering length between excited-state atoms, a_{eg}^+ denotes the scattering length of the spin-singlet (orbital-triplet) state

$$|eg^+\rangle = \frac{1}{2}(|eg\rangle + |ge\rangle) \otimes (|\uparrow\downarrow\rangle - |\downarrow\uparrow\rangle) \tag{2.4}$$

and a_{eg}^- denotes the scattering length of the spin-triplet (orbital-singlet) state

$$|eg^-\rangle = \frac{1}{2}(|eg\rangle - |ge\rangle) \otimes (|\uparrow\downarrow\rangle + |\downarrow\uparrow\rangle). \tag{2.5}$$

Surprisingly, a very big difference of the scattering lengths a_{eg}^+ and a_{eg}^- has been found for ^{173}Yb, which gives rise to a big exchange coupling between the two corresponding states. As a result of this strong coupling in ^{173}Yb, inter-orbital exchange interactions could be observed recently in the bulk and also in the lattice [72, 117]. The reason for the big exchange coupling is a bound state in one of the collision channels close to the continuum of the entrance channel as explained in the next section.
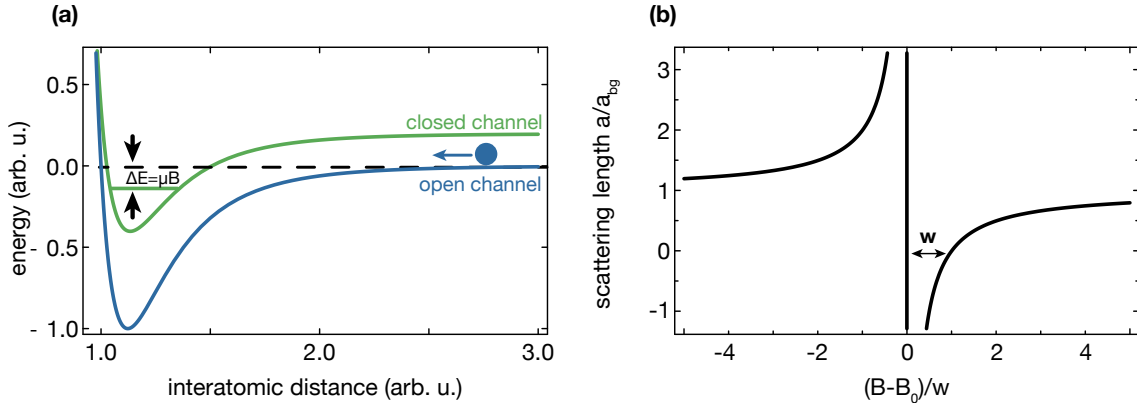
Figure 2.4: Illustration of the two-channel model of a magnetic Feshbach resonance. **(a)** A differential Zeeman shift μB between the two channels can be used to bring the bound state of the closed channel into resonance with the open channel. **(b)** Bringing the bound state into resonance with a magnetic field B_0 causes the scattering length to diverge. The scattering length is negative (positive) when the bound state is above (below) the threshold of the open channel (dashed line).

2.4.2 Feshbach resonances

Feshbach resonances are a convenient tool in cold atom physics to change the scattering properties between alkali atoms in the vicinity of such a resonance with a magnetic field [118]. This allows tuning the scattering length a over a wide range $-\infty < a < \infty$, therefore changing even the sign of the interaction between the atoms.

Magnetic Feshbach resonances

When considering binary collision between two atoms with spin $|F, m_{F_1}\rangle$ and $|F, m_{F_2}\rangle$ in a magnetic field, different interaction potentials exist. These potentials depend on the spin configuration $\mathbf{F}_{tot} = \mathbf{F}_1 + \mathbf{F}_2$ of the atom pair with fixed spin projection $M = m_{F_1} + m_{F_2}$. Typically, the atoms collide in the energetically lowest interaction potential, which is called the open channel. In contrast to that, interaction potentials with a bigger Zeeman energy are called closed channels, as the atoms do not possess enough kinetic energy to access these potentials. Each of these channels possesses several bound states that can be shifted relative to each other with a magnetic field due to a differential Zeeman shift between the different spin configurations. In general, the scattering length is determined by the position of the last bound state within the interaction potential of the open channel. When a bound state of the closed channel is now shifted with the magnetic field into resonance of the open channel, a Feshbach resonance appears, as illustrated in Fig. 2.4(a). As shown in Fig 2.4(b), the scattering length is strongly modified in the vicinity of this resonance

[119, 120] due to the resonant coupling to the bound state and is given by

$$a_s(B) = a_{bg} \left(1 - \frac{w}{B - B_0} \right).$$ (2.6)

Here a_{bg} denotes the background scattering length in the absence of a resonance, B_0 is the position of the resonance and w denotes the width of the resonance.

The absence of hyperfine structure of the ground state of alkaline earth-like elements does not allow using magnetic Feshbach resonances as described above. Other schemes have therefore been proposed to circumvent the absence of a magnetic Feshbach resonance for these elements. These schemes rely on a similar coupling of the interaction channels as explained above, e.g. by off-resonant light, to change the scattering length.

Optical Feshbach resonance

Instead of using a magnetic field to couple the open channel and the closed channel, off-resonant light with respect to a photoassociation resonance can be used instead to couple two potentials. This scheme has been proposed by Fedichev et al. and is called optical Feshbach resonance (OFR) [121]. OFRs were implemented for alkali elements but they suffer from photon scattering because of the close detuning to the bound state, which causes heating of the quantum gas [122]. The detuning from a photoassociation resonance is limited by the nearby presence of other photoassociation resonances. Alkaline earth-like atoms provide a narrow inter-combination line that somewhat mitigates this problem and OFRs has been already demonstrated successfully with strontium and ytterbium [123–125]. However, OFRs will in general break $SU(N)$-symmetric interactions when the ground state is coupled with an excited state that possesses a total electronic angular momentum $j > 0$. In addition, many applications of Feshbach resonances like for evaporative cooling require timescales in the order of seconds and it remains questionable if the problem of finite photon scattering and heating can be circumvented completely.

Orbital Feshbach resonance

The presence of a molecular bound state in the $|eg^+\rangle$ channel of ^{173}Yb with a small binding energy make this isotope particularity suited to employ an orbital Feshbach resonance to tune the scattering length between the ground- and excited-state atoms. Such a scheme has been proposed by Zhang et al. [126] and has recently been demonstrated independently by Höfer et al. and Pagano et al. using ^{173}Yb [76, 127].

The term orbital resonance stems from the fact that for this resonance the orbital degree of freedom plays the role of the electronic spin in a magnetic Feshbach resonance. In the Zeeman basis, the eigenstates are given by $|c\rangle = (|g\uparrow, e\downarrow\rangle - |e\downarrow, g\uparrow\rangle)/\sqrt{2}$ and $|o\rangle = (|g\downarrow, e\uparrow\rangle - |e\uparrow, g\downarrow\rangle)/\sqrt{2}$ and play the role of the open ($|o\rangle$)
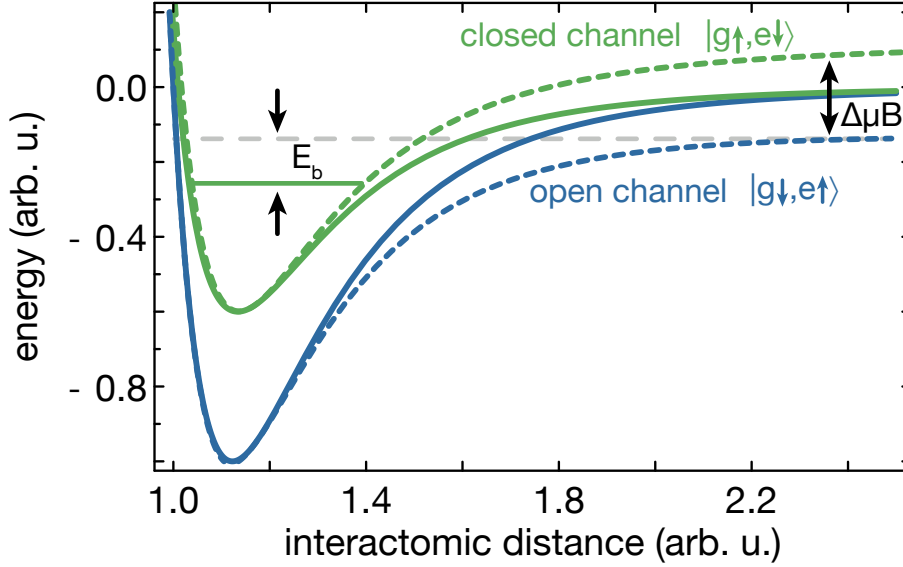
Figure 2.5: Illustration of the orbital Feshbach scheme. The solid (dashed) curves denote the interaction potential of the two orbital configurations at zero (finite) magnetic field. The magnetic field couples the electronic singlet and triplet state and causes a deformation of the potential at large interatomic distances. A shallow bound state with binding energy E_b in the closed channel can be brought into resonance with the open channel by a differential Zeeman shift $\Delta\mu B$ to create a Feshbach resonance.

and closed ($|c\rangle$) channel. In contrast to that, the interaction potential is diagonal in the $|eg\rangle^{\pm} = (|c\rangle \mp |o\rangle)/\sqrt{2}$ basis, which was introduced in section 2.4.1. The magnetic field will therefore mix the nuclear spin singlet and triplet states, creating a coupling between the open and the closed channel. A small differential Zeeman shift between the $|eg\rangle^{\pm}$ states allows bringing the open channel into resonance with a bound state of the closed channel, as illustrated in Fig. 2.5. In ^{173}Yb, a molecular bound state which is close detuned to the entrance channel with a binding energy of only $E_b/h \simeq 32\,\mathrm{kHz}$ at zero magnetic field exists. This bound state, which gives also rise to the large exchange energy, makes this isotope particularity suited to be used for the orbital resonance, as the required magnetic fields are still moderate to bring the state into resonance with the open channel.

When using a regularized pseudo-potential, the scattering length of the open channel can be described by [126]

$$a_{eg} = \frac{-(a_{eg}^+ + a_{eg}^-)/2 + a_{eg}^+ a_{eg}^- \sqrt{m\delta/\hbar^2}}{(a_{eg}^+ + a_{eg}^-)/2\sqrt{m\delta/\hbar^2} - 1}, \tag{2.7}$$

where δ denotes the differential Zeeman shift between the two states, m denotes the

atom mass and $a_{eg}^{\pm}$ is the corresponding scattering length of the $|eg\rangle^{\pm}$ state.

The Feshbach resonance appears when the differential Zeeman shift δ becomes comparable to the binding energy E_b of the bound state in the $|eg^+\rangle$ channel. At resonance the Zeeman shift is then given by

$$\delta = \frac{\hbar^2}{m/4(a_{eg}^+ + a_{eg}^-)^2}. \tag{2.8}$$

The coupling between the two states of the orbital Feshbach resonance is actually universal with respect to the two involved m_F states – a feature of the SU(N)-symmetric interactions in ytterbium. The achieved lifetime for this resonance is about $400\,\mathrm{ms}$ at the resonance position $B_0 = 55(8)G$ with typical densities of $n \simeq 5 \times 10^{13}\,\mathrm{cm}^{-3}$. Therefore, the lifetime in the vicinity of the Feshbach resonance is comparable to other alkali elements [128]. Moreover, the width of the Feshbach resonance is about $277_{62}^{87}\,\mathrm{G}$ wide. The effective range r_0, which is inversely proportional to the width of the resonance, can be compared to the typical length scale of the system such as the van der Waals radius r_{vdw}. Resonances are classified as narrow if $r_0 \gg r_{vdw}$ or wide otherwise [118]. By using such a classification, the orbital Feshbach resonance can be considered as a narrow resonance. Due to the narrow character of this resonance, the superfluid transition temperature of a Fermi gas with attractive interactions is expected to be higher than for wide Feshbach resonances which are usually studied with alkali elements [129].

2.5 Polarizability of electronic states

Optical potentials are an essential tool to study ultracold quantum gases. The availability of meta-stable states in ytterbium allows implementing for example state-dependent and independent optical potentials for the ground state and the lowest meta-stable state, as we will show in chapter 6. In this case, state-dependent refers to a potential that has different depths for the two electronic orbitals. To realize such a potential, it is essential to know the polarizability α for the two states, which depends on the wavelength of the light being used. The polarizability of an atom can be understood by the interaction of its electronic shell with the oscillating electric field of the light. The rapidly varying electric field $\mathbf{E}$ will induce an oscillating dipole moment $\mathbf{d}$ on the atom. The polarizability relates the induced dipole moment with respect to the electric field and is defined as

$$\mathbf{d} = \alpha(\omega)\mathbf{E} \tag{2.9}$$

with ω denoting the light frequency. The induced dipole moment will interact with the electric field and produces a time varying energy shift $\delta V = -\mathbf{d} \cdot \mathbf{E}$. The time averaged quantity of this energy shift, as denoted by the brackets, $\frac{1}{2}\langle \delta V \rangle$ is called the
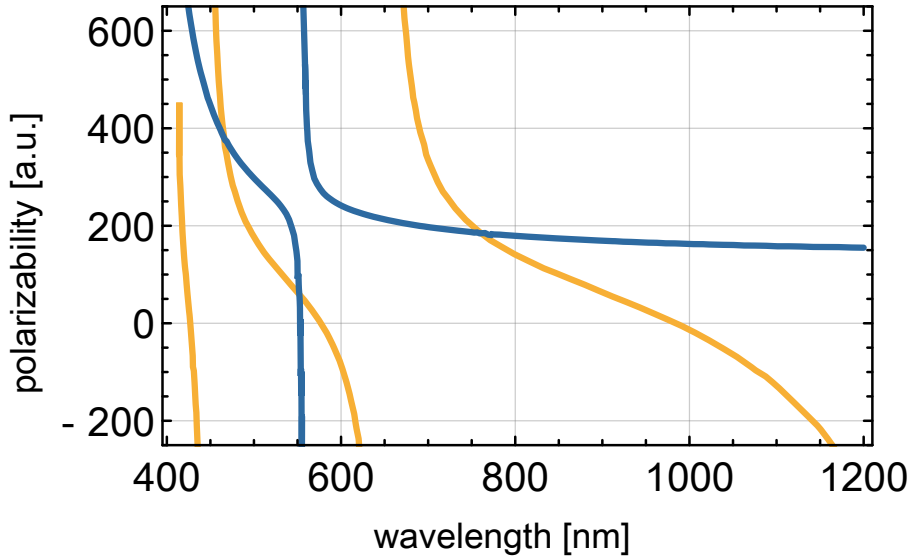
Figure 2.6: Polarizability of ytterbium displayed in atomic units as a function of the wavelength. The blue (yellow) curve shows the polarizability of ytterbium in the ground state (meta-stable $^3P_0$ state). Data taken from [131].

AC Stark shift and defines a conservative potential [130]. We will see in chapter 4, that the AC Stark shift is directly proportional to light intensity and the real part of the polarizability, which permits implementing optical traps by the spatially varying intensity of a laser beam.

In the presence of a resonant optical transition, e.g. the $^1S_0 \rightarrow {}^1P_1$ transition, the polarizability of the atom will be enhanced for light frequencies close to such a resonance. In general, the polarizability of the electronic states will be different for a given wavelength of the light as the resonance position of such optical transitions depends on the electronic state. Those wavelengths for which the polarizabilities for two electronic states are exactly the same are called magic wavelengths and are highly relevant for precision spectroscopy and optical clocks. For magic wavelengths the differential light shift between the two states will vanish, which makes for example optical transitions between the two states independent of the used trap depth and spatial inhomogeneities. As opposed to that, wavelengths were the polarizability is opposite in sign for the two states are called anti-magic wavelengths. Another relevant case for the simulation of two-orbital many-body physics e.g. the Kondo lattice model is a wavelength were the polarizability for only one of the two states vanishes.

The exact polarizability of the different states can be calculated by including the full level structure of the atoms. Such calculations include relativistic many-body calculations and have to account for all the optical transitions in the electronic shell of the atom. Such a calculation has been done by Dzuba et al. for ytterbium [131].

Fig. 2.6 shows the obtained polarizability for the ground state and the $^3P_0$ state of ytterbium using the data of Dzuba et al. The blue curve denotes the polarizability of the ground state. In this curve the broad $^1S_0 \rightarrow {}^1P_1$ transition at $\lambda = 400\,\text{nm}$ and the $^1S_0 \rightarrow {}^3P_1$ at $\lambda = 556\,\text{nm}$ can be clearly identified due to the divergence of the polarizability. The yellow curve shows the polarizability of the meta-stable $^3P_0$ state. The polarizability for this curve is mainly determined by the presence of the $^3P_0 \rightarrow {}^3S_1$ transition at $\lambda = 649\,\text{nm}$ and the $^3P_0 \rightarrow 6s6d^3D$ transition at $\lambda \approx 444\,\text{nm}$ [82].

Outside the optical resonances, three magic wavelengths with equal polarizability for the two states can be identified at $\lambda_m^1 = 465.4\,\text{nm}$, $\lambda_m^2 = 551.5\,\text{nm}$ and $\lambda_m^3 = 759.4\,\text{nm}$. Anti-magic wavelengths with opposite polarizability can be found at $\lambda_{am}^1 = 436\,\text{nm}$, $\lambda_{am}^2 = 619.0\,\text{nm}$ and $\lambda_{am}^3 = 1117\,\text{nm}$. A vanishing polarizability, outside the optical resonances, for either of the two states appears at $\lambda_z^1 = 410.8\,\text{nm}$, $\lambda_z^2 = 550\,\text{nm}$, $\lambda_z^3 = 576.8\,\text{nm}$ and $\lambda_z^4 = 984.7\,\text{nm}$.

It should be noted that there will be in general a weak isotope dependence of the magic and anti-magic wavelength. This frequency shift for the magic wavelength has been measured between ^{171}Yb and ^{174}Yb and is typically in the order of $\delta\nu \approx 1\,\text{GHz}$ for the different isotopes [132].

The optimal choice of wavelength for the optical lattice should be sufficiently far detuned from any optical transition to avoid excessive photon scattering and heating, but might be limited by technical restrictions. In the current implementation of the state-dependent lattice in our experiment, we chose a wavelength $\lambda = 670\,\text{nm}$, which is sufficiently far detuned from the resonance at $\lambda_{res} = 649\,\text{nm}$. Moreover, commercial laser systems for that wavelength like laser diodes or solid-state lasers are available.

Chapter 3

Single and two-orbital physics in periodic potentials

This chapter starts with a short introduction on single particle physics that emerges in periodic potentials. We highlight common concepts known from solid-state physics, like the band structure, Bloch waves and Wannier states, which become relevant for the interacting many-body systems later on. In chapter 2, we motivated the SU(N)-symmetric interactions between ultracold ytterbium atoms in the ground state that allow us to implement the SU(N) Fermi-Hubbard Hamiltonian (FHM) in optical lattice potentials. Here, we investigate this Hamiltonian and point out the impact of the SU(N) symmetry on the thermodynamic properties of this system. In particular, implications of SU(N)-symmetric interactions for typical observable parameters in the strongly interacting regime will be demonstrated. After that, we will give an overview of the different phases of the SU(N) FHM, which are predicted by theory in the low-temperature regime. At the end of this chapter, we extend the single-orbital model to a two-orbital version. As a prominent example, the Kondo lattice model (KLM), which can be realized using the ground state and meta-stable state in a state-dependent lattice, emerges in a certain limit of the general two-orbital FHM.

3.1 Quantum mechanics in periodic potentials

We start by describing the physics of non-interacting particles in a periodic potential such as an optical lattice potential. The presences of a periodic potential will drastically modify the dispersion relation of the particle compared to the free particle case. It deviates from the quadratic behavior of a free particle and a band structure with energy gaps develops. The solution of the Schrödinger equation with a periodic potential is extensively studied in solid-state textbooks and only a brief summary is
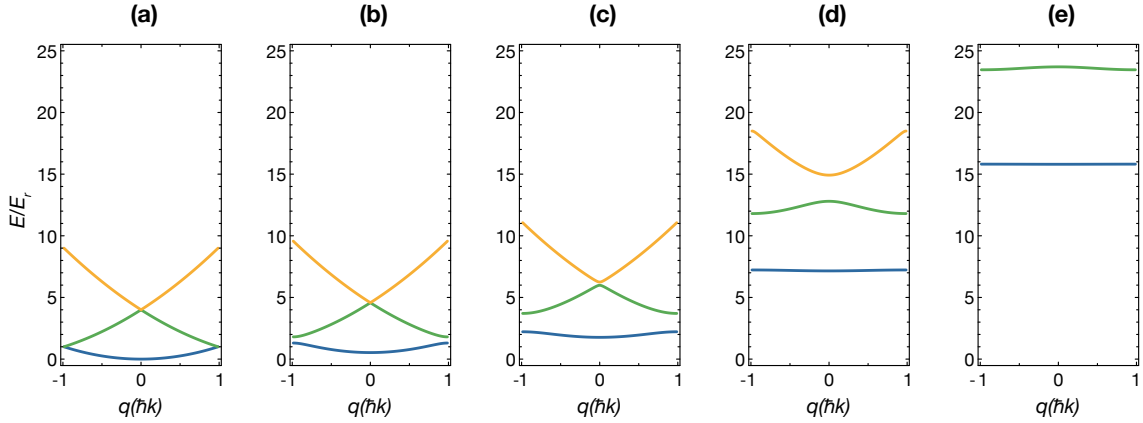
Figure 3.1: Band structure of the lowest three energy bands, denoted by blue, green and yellow lines. An energy gap opens, which increases with lattice depth (a) $V = 0E_r$, (b) $V = 1E_r$, (c) $V = 3E_r$, (d) $V = 10E_r$, (e) $V = 20E_r$.

given here.

3.1.1 Bloch waves

Let us start by considering the Hamiltonian describing a single particle in a periodic potential, which reads

$$H = -\frac{\hbar^2}{2m}\frac{\partial^2}{\partial x^2} + V_{lat}(x).$$ (3.1)

The periodic potential $V_{lat}(x)$ has translational symmetry such that $V_{lat}(x + d) = V_{lat}(x)$. For simplicity, we can restrict ourselves to the one-dimensional case along a single direction of the lattice, as the motion of a particle in a three-dimensional sinusoidal simple cubic lattice can be separated along each axis. Due to the translational symmetry of the Hamiltonian, the Bloch theorem applies. It states that the solution to the Schrödinger equation is given by Bloch waves that can be written as a product of a plane wave and a function that has the same periodicity as the potential

$$\phi_{n,q}(x) = \mathrm{e}^{iqx/\hbar}u_{n,q}(x).$$ (3.2)

In this equation, n denotes the band index, q defines the quasi-momentum with $|q| < \hbar\pi/d$ and $d = \lambda/2$ is the lattice periodicity. For a given quasi-momentum q, infinitely many solutions with different band indices n exist.

Using the Bloch waves of Eq. 3.2 for the stationary Schrödinger equation, the eigenvalue problem can be written as

$$Hu_{n,q}(x) = \left(-\frac{\hbar^2}{2m}\left(-i\frac{\partial}{\partial x} + \frac{q}{\hbar}\right)^2 + V_{lat}(x)\right)u_{n,q}(x) = E_q^n u_{n,q}(x).$$ (3.3)

It is possible to expand the potential $V_{lat}(x)$ and the function $u_{n,q}(x)$ in a discrete Fourier series due to the periodicity

$$V_{lat}(x) = \sum_r V_r e^{2irkx} \qquad \text{and} \qquad u_{n,q}(x) = \sum_l c_l^{n,q} e^{2ilkx} \qquad r,l \in \mathbb{Z} \qquad (3.4)$$

with $k = \frac{\pi}{d}$. We can substitute Eq. 3.4 into Eq. 3.3. The kinetic energy term then becomes

$$\frac{\hbar^2}{2m} \left(-i\frac{\partial}{\partial x} + \frac{q}{\hbar} \right)^2 u_{n,q}(x) = \sum_l \frac{\hbar^2(q/\hbar + 2kl)^2}{2m} c_l^{n,q} e^{2ilkx}. \qquad (3.5)$$

Correspondingly, the potential energy term after substitution reads

$$V_{lat}(x)u_{n,q}(x) = \sum_{r,l} V_r e^{2ik(r+l)x} u_{n,q}(x). \qquad (3.6)$$

For a sinusoidal potential, such as in the experiment, only three Fourier components are non-zero

$$V_{lat}(x) = -V_x \cos^2(kx) = -\frac{V_x}{4}(e^{2ikx} + e^{-2ikx} + 2). \qquad (3.7)$$

and Eq. 3.3 can be written in matrix form

$$\sum_l H_{l,l'} \cdot c_l^{n,q} = E_q^n c_{l'}^{n,q} \qquad (3.8)$$

with E_q^n being the eigenenergies of the nth band for the quasi-momentum q of the Hamiltonian

$$H_{l,l'} = \begin{cases} \left(\frac{q}{\hbar k} + 2l \right)^2 E_r - V_x/2 & \text{for } |l - l'| = 0 \\ -V_x/4 & \text{for } |l - l'| = 1 \\ 0 & \text{for } |l - l'| > 1 \end{cases} . \qquad (3.9)$$

Here, we introduced the recoil energy $E_r = \hbar^2 k^2/(2m)$, which is a convenient energy scale for the atoms in the optical lattice and used throughout this thesis. The eigenvalues and eigenvectors for the Hamiltonian in Eq. 3.9 can be easily calculated numerically, if the Hamiltonian is truncated for large positive and negative Fourier components l.

Because of the periodicity of the potential, two quasi-momenta q and q' that differ by a reciprocal lattice vector $q' = q + 2\hbar k$ are the same. It is therefore sufficient to consider only quasi-momenta of the first Brillouin zone $q \in [-\hbar\pi/d, \hbar\pi/d]$ for the description of the band structure.

Fig. 3.1 illustrates the result of a band structure calculation of the first three bands for various lattice depths. In the case of a vanishing lattice potential, the dispersion relation is that of a free particle with the momentum folded back to the first Brillouin zone. In contrast, for increasing lattice potentials, the dispersion relation differs from the free particle case for higher momenta. A gap opens and a band structure of the energy spectrum emerges. For deeper lattice potentials, the bands become narrower and the energy gaps between the bands increase.
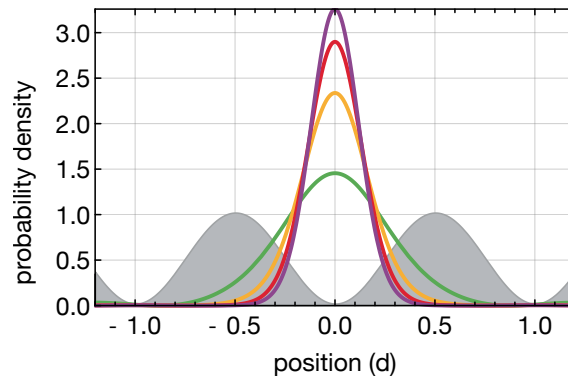
Figure 3.2: Illustration of the probability density of the Wannier function in the lowest band of a sinusoidal lattice potential (grey curve) for various lattice depths as function of position: $V = 1E_r$ (green line), $V = 5E_r$ (yellow line), $V = 10E_r$ (red line) and $V = 15E_r$ (purple line).

3.1.2 Wannier basis

Even though the completely delocalized Bloch waves are the correct solution to the Schrödinger equation of a particle in a periodic potential, it is sometimes more convenient to describe the physics of the system in a localized basis. This is useful for the description of localized particles, for example due to interactions. Using a Fourier transform and considering only the lowest band ($n = 1$), it is possible to transform the Bloch waves of Eq. 3.2 and obtain the Wannier states

$$w(x - x_i) = \frac{1}{\sqrt{\mathcal{N}_{lat}}} \sum_q e^{iqx_i/\hbar} \phi_q(x). \tag{3.10}$$

The sum in Eq. 3.10 runs over all possible quasi-momenta q and $\mathcal{N}_{lat}$ denotes the number of lattice sites. Wannier states describe maximally localized particles on a lattice site x_i. However, the construction of the Wannier function as given above is not unique but the individual phases of the Bloch waves have to be chosen correctly in order to construct a maximally localized state [133].

The probability distribution of the lowest-band Wannier function for different lattice depths is illustrated in Fig. 3.2. For low lattice depths, the Wannier function extends significantly into the potential barrier and becomes narrower and more localized to a single site for increasing lattice depths.

Using the Wannier basis, the Hamiltonian of equation 3.1 can be written in second quantization as

$$H = -\sum_{i,j} \left(t_{i,j} c_i^\dagger c_j + h.c \right) \tag{3.11}$$

where $c_i^\dagger$, c_j are the creation, annihilation operators for a particle on site i and

$$t_{i,j} = \int w^*(x - x_i) \left(-\frac{\hbar^2}{2m} \nabla^2 + V_{lat}(x) \right) w(x - x_j) dx \tag{3.12}$$

denotes the hopping matrix element between two lattice sites i and j.

As the Wannier functions become more and more localized for increasing lattice depth, only the tunneling matrix element in Eq. 3.12 between neighboring sites, denoted by $\langle i, j \rangle$, has a significant contribution. By contrast, the overlap integral between sites that are further away is exponentially suppressed. This limit, called the tight-binding limit, is usually a good approximation for lattice depths $V_x \geq 3E_r$. In the tight-binding (t.b.) limit, the Hamiltonian of Eq. 3.11 simplifies to

$$H = -t \sum_{\langle i,j \rangle} \left(c_i^\dagger c_j + h.c \right) \tag{3.13}$$

and the dispersion relation of the lowest band becomes cosinusoidal with $\mathcal{E}(q) = -2t \cos(qd)$. In this limit, the bandwidth W in a one-dimensional lattice can be expressed as $W = 4t$.

For deep lattice potentials, the particles become more and more localized and the mobility of the particle as well as the bandwidth decreases. The reduced mobility of the particle can be explained by an increased effective mass

$$\frac{1}{m^*} = \frac{1}{\hbar^2} \frac{\partial^2 \mathcal{E}(q)}{\partial q^2} \stackrel{t.b.}{=} \frac{2td^2}{\hbar^2} \tag{3.14}$$

which is inversely proportional to the band curvature.

The concepts, given above, were derived for the one-dimensional case and can be easily generalized to three dimensions. A three-dimensional Wannier function can be readily constructed

$$w(\mathbf{x} - \mathbf{x_i}) = w(x - x_i)w(y - y_i)w(z - z_i) \tag{3.15}$$

with $\mathbf{x_i} = (x_i, y_i, z_i)$. Accordingly, the bandwidth in the tight-binding limit is given by $W = 12t$ in the three-dimensional case. As shown in the next section, the bandwidth is one of the two relevant energy scales in the Fermi-Hubbard Hamiltonian and determines the kinetic energy of the particle.

3.2 The SU(N) Fermi-Hubbard model

We have motivated in chapter 1, that ultracold atoms allow the implementation of quantum many-body systems as realized in condensed-matter physics. A common property of the models, used to describe interacting electrons in solids, is the emergence of strong correlations between fermions at low temperatures due to interactions.

As a consequence, such models are in general not exactly solvable. To study the physics contained therein, one has to rely on approximative numerical methods like Quantum Monte Carlo or density matrix renormalization group (DMRG) in one dimension [134–136]. On the other hand, this makes ultracold atom experiments, which realize such physics, a valuable tool for benchmarking measurements against such numerical calculations.

The FHM contains only two energy scales, a hopping or tunneling parameter and an on-site interaction energy term. It extends the simple, non-interacting band theory description of a solid, by including interaction effects. Despite the fact that it is a minimal description with only two parameters, it is able to describe non-trivial physical properties such as the metal to Mott insulator transition [24], band magnetism [137–139] and is also believed to incorporate high-T_C superconductivity [5, 24].

Because of its importance in solid-state physics, the FHM has been extensively studied over the past decades from both the experimental and the theory side [24, 140, 141]. Despite its simplicity, the FHM can only be solved analytically in one dimension using the Bethe ansatz [142, 143]. However, most of the studies so far have been done for the SU(2) FHM, which is relevant for the description of electrons but much less is known for the generalized SU(N)-symmetric case [62, 64, 144].

In transition-metal oxides, the SU(4)-symmetric version of the FHM is used to study two-orbital systems [65] but it has also attracted general interest in theoretical physics in the context of large-N expansion [6, 145].

The Hamiltonian for the extended SU(N) FHM reads

$$\hat{H} = -t \sum_{\langle i,j \rangle, \sigma} (\hat{c}^{\dagger}_{i,\sigma} \hat{c}_{j,\sigma} + \text{H.c.}) + \frac{U}{2} \sum_{i, \sigma \neq \sigma'} \hat{n}_{i,\sigma} \hat{n}_{i,\sigma'} + \sum_{i, \sigma} V_i \hat{n}_{i\sigma}. \qquad (3.16)$$

Here, $\langle i, j \rangle$ denote neighboring sites, t is the tunneling matrix element between nearest neighbors, as given in Eq. 3.12 and V_i accounts for a (harmonic) confining potential. The energy term U describes the interaction energy between two fermions on the same site and is given by the overlap of the Wannier functions

$$U = \frac{4\pi \hbar^2 a_s}{m} \int_{-\infty}^{\infty} |w(\mathbf{x})|^4 \, d^3x \qquad (3.17)$$

where a_s is the scattering length and $w(\mathbf{x})$ denotes the Wannier function as defined in Eq. 3.10. The operator $\hat{c}^{\dagger}_{i,\sigma}$ ($\hat{c}_{i\sigma}$) in Eq. 3.16 creates (annihilates) a fermion on site i with spin index $\sigma = 1..N$ and $\hat{n}_{i\sigma} = \hat{c}^{\dagger}_{i\sigma} \hat{c}_{i\sigma}$ are the respective number operators. For $N = 2$, this Hamiltonian reduces to the conventional spin-1/2 SU(2) FHM. The SU(N) symmetry in the Hamiltonian above arises because the tunneling matrix element and the interaction energy U are independent of the spin index σ because of the m_F-independent scattering lengths as explained in chapter 2.

Spin symmetry of the Hamiltonian

The spin permutation operator is defined as

$$S_n^m = \sum_i S_n^m(i) = \sum_i \hat{c}_{i,m}^\dagger \hat{c}_{i,n}. \tag{3.18}$$

It satisfies the SU(N) spin algebra $[S_n^m, S_q^p] = \delta_{mq} S_n^p - \delta_{np} S_q^m$ which can be shown by using the fermionic anti-commutation relations $\{\hat{c}_{i,m}, \hat{c}_{j,n}^\dagger\} = \delta_{i,j}\delta_{m,n}$. The symmetries and conserved quantities of Eq. 3.16 can be proven by showing that the spin permutation operator commutes with the Hamiltonian

$$[S_n^m, H] = 0 \quad \forall m, n = 1..N. \tag{3.19}$$

As the Hamiltonian of Eq. 3.16 commutes with every generator S_n^m of the Lie group that defines the SU(N) spin algebra, is therefore SU(N)-symmetric. Moreover, with

$$S_m^m = \sum_i \hat{c}_{i,m}^\dagger \hat{c}_{i,m} = n_m \tag{3.20}$$

being the total particle number with spin index m, the particle number per spin state is a conserved quantity. Due to this conservation, it is possible to prepare empty m_F-states ($S_m^m = 0$) and realize the Fermi-Hubbard Hamiltonian of a lower spin system. To give an example, let us consider ^{173}Yb. This isotope possesses a nuclear spin $I = 5/2$ with six spin components. Using optical pumping techniques, a system with only two spin components ($N = 2$) can be prepared, which realizes the SU(2) FHM in an optical lattice.

3.2.1 Metal to Mott crossover

Depending on the temperature of the system and the interaction strength, the FHM features different phases as illustrated for repulsive interactions in Fig. 3.3. The phases of the FHM with attractive interaction are similarly feature-rich. The attractive side of the FHM features a crossover from a superfluid BCS phase to a BEC for increasing interaction strength [64, 66, 146, 147]. Interestingly, it can be shown with the Lieb-Mattis transformation that a mapping between the attractive and the repulsive side of the SU(2) FHM in a bipartite lattice exists [148, 149].

In the following, we will consider temperatures above magnetic ordering and only repulsive interactions ($U > 0$), which is the parameter regime relevant in the experiment with ^{173}Yb.

The interaction-driven transition from a conducting metal to an insulating Mott phase for an integer filling fraction can be understood intuitively by the competition of the two energy terms t and U. It is energetically favorable for non-interacting fermions to be delocalized over several lattice sites as this reduces the kinetic energy,
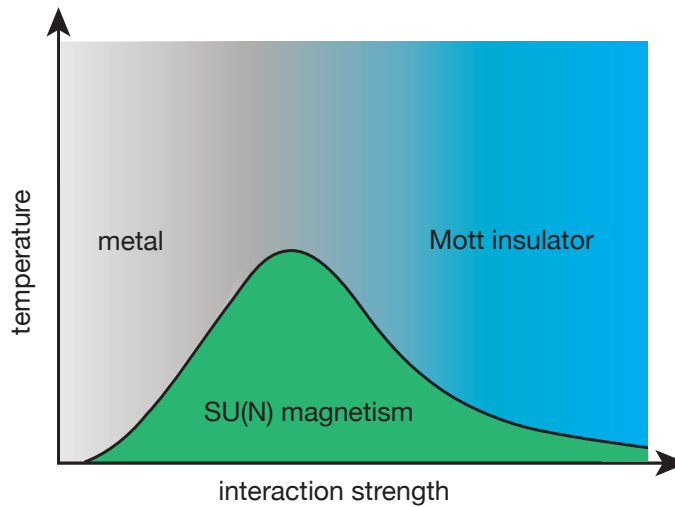
Figure 3.3: Sketch of the phase diagram of the repulsive ($U > 0$) SU(N) FHM for half-filling as a function of the interaction strength U/t. For temperatures above magnetic order, a crossover from a metal phase to a SU(N) Mott insulating regime exists. At sufficiently low temperatures, SU(N) magnetism appears with exotic phases – beyond Néel order – depending on N.

given by the first term of Eq. 3.16. However, because of the interaction energy U of several fermions occupying the same site, it becomes energetically favorable to have localized fermions with an integer filling of particles per site for sufficiently strong interactions. This regime is called the Mott regime and is characterized by an energy gap U and a vanishing compressibility

$$\tilde{\kappa} = \frac{\partial n}{\partial \mu}. \tag{3.21}$$

In the equation above, n denotes the density and μ defines the chemical potential.

Due to the competition of the two energy scales, the interaction energy U has to be compared to the kinetic energy $t^* = 2tz$ with z being the coordination number in the lattice. Therefore, we use the ratio $U/12t = U/t^*$ to describe the interaction strength of the 3D FHM for different regimes.

Weakly interacting regime

In the weakly interacting case ($U \ll t^*$), the kinetic energy dominates over the interaction energy. In this regime, the Fermi gas is described by a conducting metal for a partially filled band or by a non-conducting band insulator in the case of filling one. The band insulator is incompressible, as it would require energy of the amount of the band gap to place another particle. As opposed to that, the metal is compressible since there are free states available at the Fermi surface. Hence,

increasing the chemical potential will change the density in the metal phase and the system will show a finite compressibility.

In the absence of interaction, it is convenient to transform the creation operators to momentum space. For simplicity we consider the kinetic energy part of a 1D Fermi-Hubbard Hamiltonian without interaction ($U = 0$) and L spatial sites

$$H_0 = -t \sum_{j=1}^{L} \sum_{\sigma} (\hat{c}_{j,\sigma}^{\dagger} \hat{c}_{j+1,\sigma} + \hat{c}_{j+1,\sigma}^{\dagger} \hat{c}_{j,\sigma}). \tag{3.22}$$

The creation operators can be transformed to momentum space by a discrete Fourier transform

$$\hat{c}_{q,\sigma}^{\dagger} = \frac{1}{\sqrt{L}} \sum_{j=1}^{L} e^{iqj\Phi} \hat{c}_{j,\sigma}^{\dagger} \quad q = 0, ..., L-1 \tag{3.23}$$

with $\Phi = 2\pi/L$. Using the Fourier inversion

$$\hat{c}_{j,\sigma}^{\dagger} = \frac{1}{\sqrt{L}} \sum_{q=0}^{L-1} e^{-iqj\Phi} \hat{c}_{q,\sigma}^{\dagger} \tag{3.24}$$

the Hamiltonian can be recast in the following form

$$H_0 = -2t \sum_{q} \sum_{\sigma} \cos(\Phi q) \hat{n}_{q,\sigma} \tag{3.25}$$

with $\hat{n}_{q,\sigma} = \hat{c}_{q,\sigma}^{\dagger} \hat{c}_{q,\sigma}$ being the number operator in momentum space. Eq. 3.25 denotes the dispersion relation in the tight binding limit of a particle with quasi-momentum q, multiplied by the occupation number of the mode $|q, \sigma\rangle$ that can go up to the spin multiplicity N.

Mott regime

In the strongly interacting case ($U \gg t^*$) and for an integer filling fraction, the fermions are localized and a Mott insulator forms. Adding another particle costs interaction energy U and therefore the state shows a vanishing compressibility. Calculations show that the transition between the weakly interacting metal phase to the strongly interacting Mott regime is actually not a phase transition but a smooth crossover in the SU(2) FHM [150, 151]. The required temperature for a first or second order phase transition is below the Néel temperature and therefore only a crossover exists. This behavior of the SU(2) FHM is in stark contrast to the superfluid to Mott phase transition in the bosonic case. Calculations however predict that for higher spin symmetries, e.g. in the case of half-filling for the SU(4) and SU(6) FHM, a phase transition appears as the required temperature for magnetic order decreases but the critical transition temperature increases [152]. Depending on the interaction strength, this phase transition can be of first or second order.

For sufficiently strong interactions, deep in the Mott regime, tunneling is suppressed and only virtual tunneling between the sites has to be considered. In this limit, the Hamiltonian in Eq. 3.16 reduces to a spin model [153, 154]. By using second order perturbation theory, the FHM can then be transformed to an $\mathrm{SU}(N)$ Heisenberg model, which reads

$$H_{Heis} = \frac{2t^2}{U} \sum_{m,n,\langle i,j \rangle} S_n^m(i) S_m^n(j) \tag{3.26}$$

where S_n^m denotes the spin operator, that was defined in Eq. 3.18. As shown in section 3.2.4, the ground state of the $\mathrm{SU}(N)$ Heisenberg model features different exotic phases that will depend on N and the filling fraction per lattice site.

For temperatures above magnetic order, deep in the Mott regime, the kinetic energy can often be neglected compared to the interaction energy for the description of the system. By dropping the kinetic energy term in Eq. 3.16, the Hamiltonian can be diagonalized in the Wannier basis

$$H_{al} = \frac{U}{2} \sum_{i,\sigma \neq \sigma'} \hat{n}_{i,\sigma} \hat{n}_{i,\sigma'} + \sum_{i,\sigma} V_i \hat{n}_{i,\sigma}. \tag{3.27}$$

This limit is referred to as the atomic limit. In the regime where the atomic limit holds, tunneling is small enough to be negligible for the thermodynamic properties of the system, but of course still needed to thermalize the system. In the atomic limit, we can give analytic expressions of thermodynamic properties such as temperature or entropy of the FHM, because the Hamiltonian can be analytically diagonalized. By using a second order perturbative tunnel coupling of adjacent lattice sites, these calculations can be extended towards the regime of small but finite tunneling rates at temperatures $T \gg t/k_{\mathrm{B}}$, which is explained in the following section.

3.2.2 Thermodynamic properties in the Mott regime

In the following, we will discuss the thermodynamic properties of the $\mathrm{SU}(N)$ FHM by using the atomic limit and by using a low-tunneling model.

We can describe the system in the grand canonical ensemble, which represents an ensemble of particles that can exchange particles and energy with a reservoir. In the grand canonical ensemble, the partition function for a Hamiltonian H with fixed particle number N_p then reads [155]

$$Z_{\mathrm{G}}(\mu, T) = \mathrm{Tr} \, e^{-\beta H - \mu N_p} = \sum_{n=0}^{N_p} \sum_{j} \langle n, j | \, e^{-\beta H - \mu n} \, | n, j \rangle \tag{3.28}$$

where the index j denotes all the possible states for a fixed number of particles of the Hamiltonian, μ is the chemical potential of the grand canonical ensemble and T denotes the temperature of the system.

In the atomic limit, the partition function factorizes into individual partition functions for each lattice site and can be written for a single lattice site i as

$$z_0(\mu, T, i) = \sum_{n=0}^{N} \binom{N}{n} e^{-\beta\left(\frac{U}{2}n(n-1)-(\mu-V_i)n\right)},$$ (3.29)

where the summation over j, denoting the possible spin combinations on a lattice site for a given particle number, has been carried out already. In the above equation, N denotes the number of spin components and the binominal coefficient accounts for the number of different spin combinations on the lattice site.

From Eq. 3.29 it becomes evident that the spatially varying potential V_i can be regarded as a local change of the effective chemical potential μ. If V_i is varying slowly compared to the typical length scales of the system, it is justified to introduce a local chemical potential $\mu_l(i) = \mu - V_i$ to describe the physics. This approximation is called local density approximation (LDA) and will be explained in section 5.3.1.

In LDA, the grand potential becomes

$$\Omega_0(\mu_l, T) = -k_{\mathrm{B}}T \ln z_0(\mu_l, T).$$ (3.30)

Using the grand potential, all the macroscopic thermodynamic quantities can be derived. We immediately obtain the average density

$$\langle n_0(\mu_l, T) \rangle = -\frac{1}{d^3}\frac{\partial \Omega_0(\mu_l, T)}{\partial \mu_l} = \frac{1}{d^3 z_0(\mu_l, T)} \sum_{n=0}^{N} n \binom{N}{n} e^{-\beta\left(\frac{U}{2}n(n-1)-\mu_l n\right)},$$ (3.31)

where $d^3 = (\lambda/2)^3$ refers to the lattice unit cell. Accordingly, the entropy per site in the atomic limit can be calculated

$$s_0(\mu_l, T) = -\frac{\partial \Omega(\mu_l, T)}{\partial T} = k_{\mathrm{B}} \ln(z_0(\mu_l, T)) + \frac{1}{T}\langle \epsilon_0(\mu_l, T) \rangle$$ (3.32)

with $\langle \epsilon_0(\mu_l, T) \rangle$ given by

$$\langle \epsilon_0(\mu_l, T) \rangle = \frac{1}{z_0(\mu_l, T)} \sum_{n=0}^{N} \left(\frac{U}{2}n(n-1) - \mu_l n\right) \binom{N}{n} e^{-\beta\left(\frac{U}{2}n(n-1)-\mu_l n\right)}.$$ (3.33)

To gain an understanding of the arising Mott shell structure with an integer number of particles per site, it is illustrative to consider the limit of $T \ll U$, where one term is dominating in Eq. 3.29. In this limit, the partition function reduces to

$$z_0 \approx \binom{N}{n_0} e^{-\beta\left(\frac{U}{2}n_0(n_0-1)-\mu_l n_0\right)}.$$ (3.34)

In the equation above n_0 denotes the particle number per site that will maximize (minimize) the partition function (the grand potential) for a fixed chemical potential

μ_l. An integer filling will maximize the partition function for any chemical potential and a Mott shell structure emerges. Accordingly, the entropy per site for low temperatures in the atomic limit reduces to

$$s_0(\mu_l, T) \approx k_{\mathrm{B}} \ln\left[\binom{N}{n_0(\mu_l)}\right], \tag{3.35}$$

which defines the entropy per lattice site of the Mott shell with n_0 particles, attributable to the remaining spin degree of freedom.

High temperature series expansion

We have seen in the previous section that the atomic limit, despite being a very rough approximation of the FHM in the strongly interacting regime, allows obtaining analytical expressions for thermodynamic quantities. The atomic limit is however not able to capture spin correlations between neighboring sites due to the absence of tunneling, which is required to build up correlations. These correlations will depend on the spin statistics and modify the thermodynamic quantities of the system.

Starting from the atomic limit, it is however possible to include a weak tunnel coupling by a perturbative series expansion in $t/(k_{\mathrm{B}}T)$. This so called high-temperature series expansion (HTSE) will converge for temperatures $T > t/k_{\mathrm{B}}$ [156, 157]. In the Mott regime, where tunneling is usually low, this is a good approximation at experimentally realizable temperatures. Series of up to 12th order have been obtained but are usually very cumbersome to calculate [158]. As these expansions include a weak tunnel coupling term, they are also able to catch nearest neighbor spin correlations to some extent. The high-temperature series expansion will eventually fail for temperatures approaching the critical temperature for magnetic ordering, where long-range correlations over many sites will arise [159].

By using a second order series expansion in t/T, the grand potential in Eq. 3.30 can be extended to include finite hopping

$$\Omega(\mu_l, T) = \Omega_0(\mu_l, T) + \Delta\Omega \tag{3.36}$$

$$\Delta\Omega = \beta\left(\frac{t}{z_0}\right)^2 zN\left[\frac{1}{2}\sum_{n_1=1}^{N}\binom{N-1}{n_1-1}^2 x^{2n_1-1}y^{(n_1-1)^2}\right. \tag{3.37}$$

$$\left. - \frac{1}{\beta U}\sum_{n_1 \neq n_2}^{N}\binom{N-1}{n_1-1}\binom{N-1}{n_2-1}\frac{x^{n_1+n_2-1}y^{\frac{1}{2}n_1(n_1-1)+\frac{1}{2}(n_2-1)(n_2-2)}}{n_1 - n_2}\right]$$

with $x = \mathrm{e}^{\beta\mu}$, $y = \mathrm{e}^{-\beta U}$ and z being the number of next neighbors in the lattice [160]. This series expansion is valid as long as $t < k_B T$ and used in chapter 7 to fit the density profile of the experimental data.
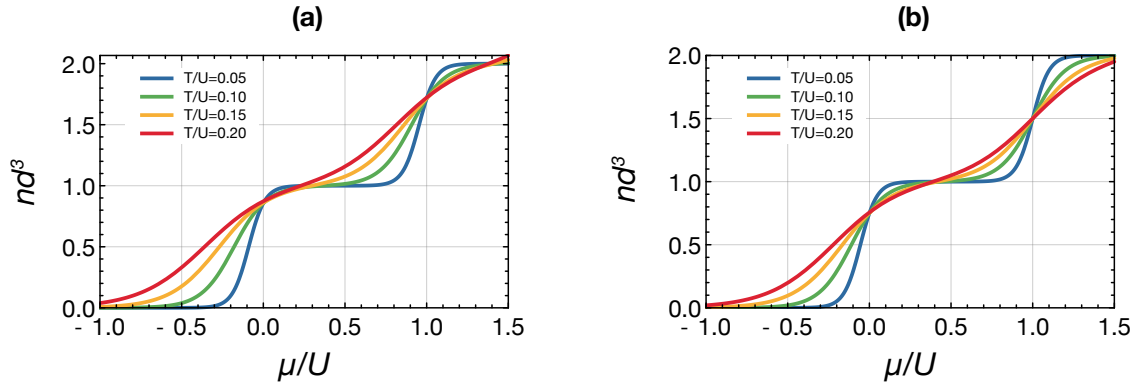
Figure 3.4: Density profiles in the Mott regime for different temperatures of (a) an SU(6) Fermi gas and (b) an SU(3) Fermi gas calculated in the atomic limit. Blue curve: $T/U = 0.05$; green curve: $T/U = 0.1$; yellow curve: $T/U = 0.15$; red curve: $T/U = 0.2$

3.2.3 SU(N)-dependence of thermodynamic properties

Let us now examine the dependence of typical thermodynamic properties on the number of spin components N in the Mott regime. In Fig. 3.5, the density and the compressibility are shown as a function of the chemical potential for $N = \{2, 3, 6\}$ in the atomic limit and with the second order HTSE model. In addition, the density dependence of a bosonic quantum gas is given as well, to illustrate the influence of quantum statistics. Both models show a different non-trivial functional dependence of the density on the number of spin components. Compared to the case of two spin components, the curves for the density as a function of the chemical potential will shift towards lower chemical potential for the SU(3) and SU(6) case as illustrated in Fig. 3.5(a) and Fig. 3.5(b).

This becomes also apparent when studying the compressibility as a function of chemical potential, as illustrated in Fig. 3.5(c) and Fig. 3.5(d). In the case of the $n = 1$ Mott shell, the SU(3) and SU(6) gas show a compressibility minimum for lower chemical potential compared to the SU(2) gas.

In the case of half filling ($n = N/2$), because of the particle-hole symmetry, a general relation between the chemical potential and N, the number of spin components, can be given via $\mu = U/2(N - 1)$. For the chemical potential that corresponds to half filling, the minimum in the compressibility is found exactly at $\mu = U/2(N - 1)$. For the SU(3) gas, there is no half filling that corresponds to an integer particle number per site. In this case, a shift of the minimum of the compressibility is observed from $\mu = 0.5\,U$ (and $\mu = 1.5\,U$) towards lower (higher) chemical potentials as illustrated in Fig. 3.5(c).

When comparing the second-order HTSE model to the atomic limit, the major differences between the two models are in the metal part between the Mott shells.
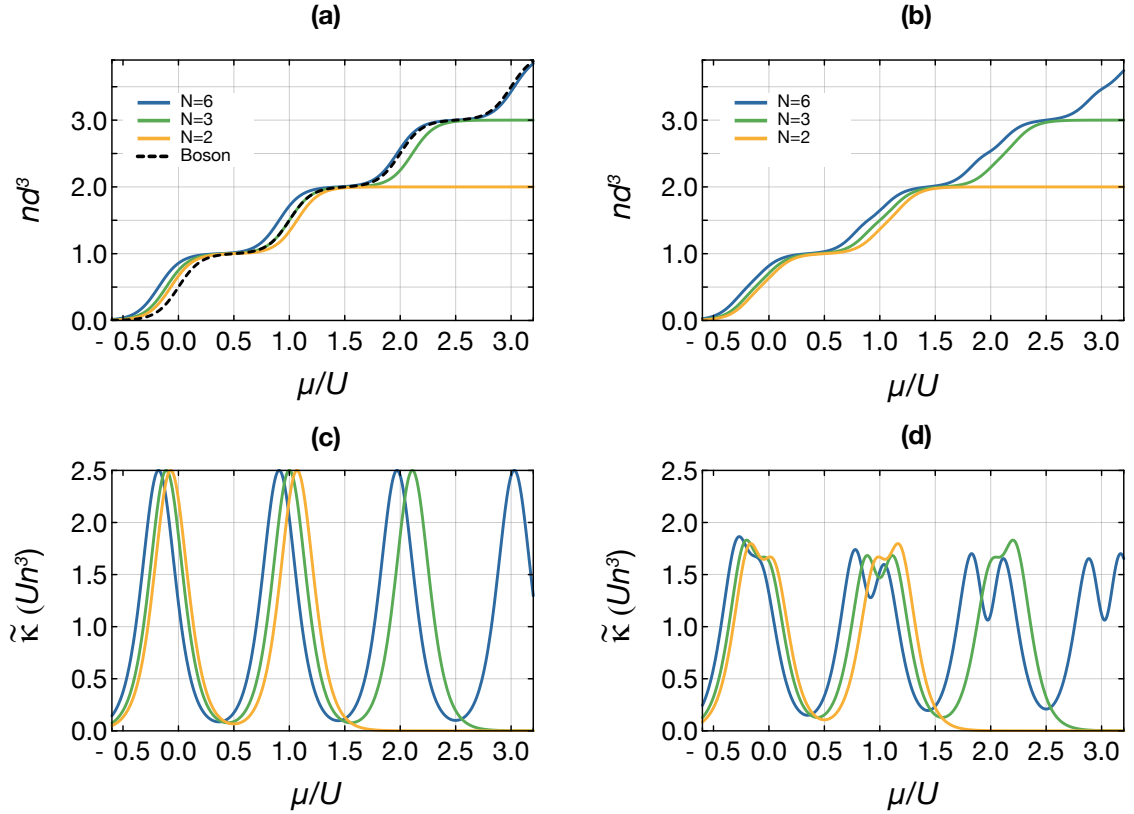
Figure 3.5: SU(N)-dependence of density and compressibility as a function of chemical potential in the Mott regime ($T/U = 0.1$) for a spin-balanced SU(6) (blue), SU(3) (green) and SU(2) (yellow) Fermi gas. (a) Density in the atomic limit. The black dashed line shows the density profile for a bosonic Mott insulator to illustrate the role of spin statistics. (b) Density obtained with the HTSE model including a finite tunnel coupling ($U/t^* = 1.7$). (c) Compressibility in the atomic limit (d) Compressibility with finite tunneling ($U/t^* = 1.7$) obtained with the HTSE model.
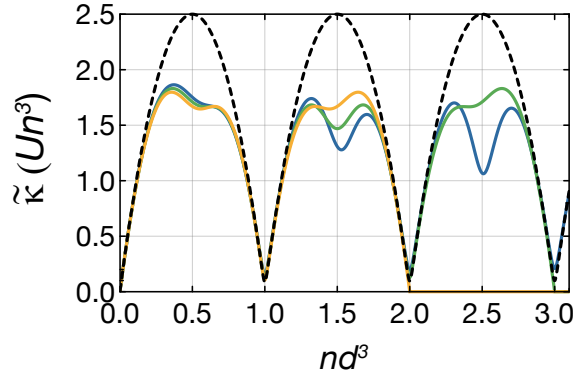
Figure 3.6: Compressibility of an SU(N) Fermi gas plotted as a function of density for $T/U = 0.1$. The black dashed line shows the compressibility in the atomic limit, which is independent of the number of spin components, for an SU(N) Fermi gas. Blue, green and yellow curves show the calculated compressibility using the HTSE model for an SU(6), SU(3) and SU(2) Fermi gas respectively with $U/t^* = 1.7$.

Introducing a finite tunnel coupling reduces the size of the Mott plateaus and increases the size of the metal part, as illustrated in Fig. 3.5c and Fig. 3.5d. The compressibility in the HTSE model is lower in the metal part with finite tunneling, while it is only slightly higher in the Mott regime compared to the atomic limit. Interestingly, when plotting the compressibility as a function of density, the curves for different N will collapse on each other in the atomic limit, whereas the HTSE model predicts differences for N mainly in the metallic region of the system (see Fig. 3.6).

Regarding the entropy, we also observe differences between the two models in the different regions. The entropy is slightly higher in the Mott region with finite tunneling, as it reduces the excitation gap. In the metallic part, the entropy however is significantly reduced by tunneling compared to the atomic limit. This can be understood by an increased bandwidth due to tunneling, which reduces the density of states in the low energy spectrum.

Pomeranchuk cooling

A consequence of the enlarged spin symmetry is the N-dependence of the Pomeranchuk cooling effect, which can already be observed at experimentally achievable temperatures. This effect was originally proposed for ^{3}He in 1950. ^{3}He has the property that the entropy below a temperature of 0.3K is higher in the solid than in the liquid phase. The idea by Pomeranchuk was to solidify Helium under pressure at temperatures below 0.3K and therefore cool the gas when it is compressed without heat input [3].

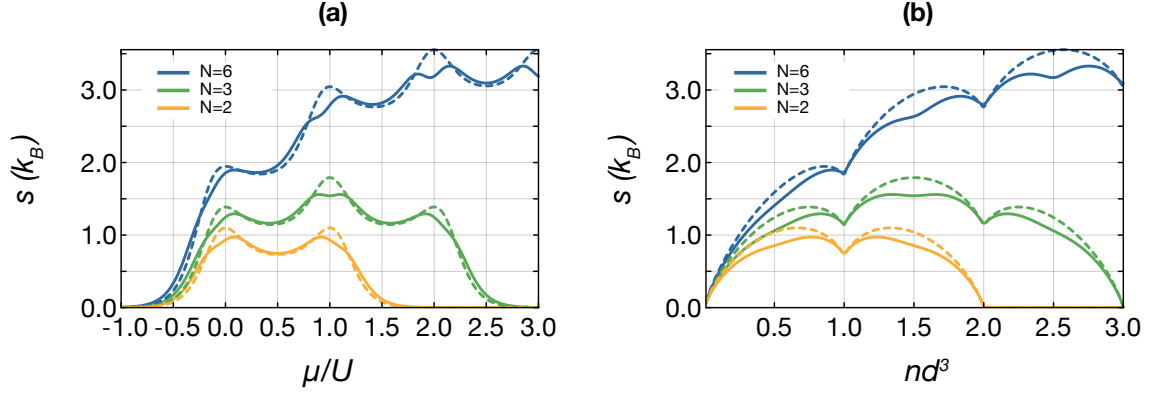A similar effect arises during the transition of a Fermi gas from a conducting metal

Figure 3.7: Entropy per site for an SU(6) (blue), SU(3) (green) and SU(2) (yellow) Fermi gas in the Mott regime at $T/U = 0.1$. The dashed lines show the atomic limit, while the solid lines depict the result obtained with the HTSE model (a) Entropy per site as a function of chemical potential (b) Entropy per site as of function of the filling.
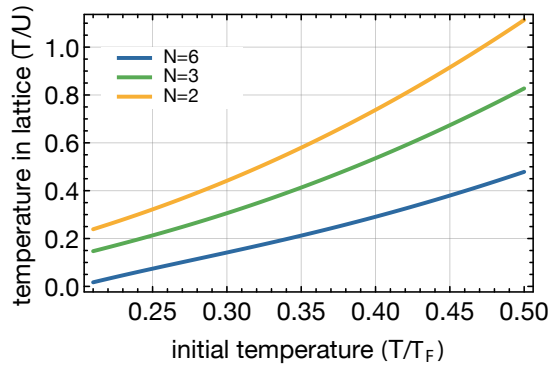

Figure 3.8: Illustration of the Pomeranchuk cooling effect in the strongly interacting regime for an SU(6) (blue), SU(3) (green) and SU(2) (yellow) Fermi gas. The figure shows the resulting temperature in the lattice as a function of the initial temperature of a non-interacting SU(N) Fermi gas. The calculation was done in the atomic limit for adiabatic loading (constant entropy), with a total particle number $N_p = 22000$ and a mean harmonic confinement of the dipole trap $\bar{\omega} = 213\,\text{Hz}$.

with weak interactions to a non-conducting Mott insulator [49]. When the Fermi gas enters the Mott regime, the system becomes incompressible and local density fluctuations are suppressed. Deep in the Mott regime, we can therefore describe the Mott insulator with the atomic limit model by considering single isolated sites if we can neglect spin correlations. A large amount of entropy can get absorbed by the isolated spins, leading to a reduction in temperature similar to the Pomeranchuk cooling in ^{3}He. In this regime, the entropy per particle of the FHM with n particles per site is given by Eq. 3.35 for temperatures above magnetic order. As a consequence, an SU(6) gas can store more entropy per particle than an SU(2) gas for a fixed temperature. By fixing the total entropy and particle number of the system, the SU(6) gas will be colder that its SU(2) counterpart, which explains the stronger Pomeranchuk cooling effect for large N.

The hand-waving argument given above can be reproduced in the atomic limit model. Fig. 3.8 shows the temperature for various N as a function of the initial reduced temperature T/T_{F} in an optical dipole trap. The calculation assumes adiabatic loading (constant entropy) for obtaining the final temperature in the lattice. As we will see in chapter 5, the reduced temperature T/T_{F} of the Fermi gas is a measure for the entropy per particle. For a fixed initial temperature, the Pomeranchuk cooling effect in the lattice as a function of the spin dimension of the quantum gas becomes apparent as illustrated in Fig. 3.8. Fixing T/T_{F} for different numbers of spin components N is actually a realistic scenario when cooling the quantum gas to degeneracy via evaporative cooling in the experiment. At very low temperatures, more and more states below the Fermi energy are already populated and scattering into free states below the Fermi energy becomes suppressed. Therefore, efficient evaporative cooling will stop at similar reduced temperatures for the different SU(N)-symmetric Fermi gases.

3.2.4 SU(N) magnetism

In the last two paragraphs, we showed that the density and the thermodynamic observables in the Mott regime depend on the number of spin components in the system. Moreover, due to Pomeranchuk cooling, the Mott insulator will show different temperatures for fixed entropy depending on the number of spin components. These SU(N)-dependent effects already happen at experimentally realizable temperatures. However, the most striking difference to the SU(2) FHM appears in the low temperature regime at temperatures below magnetic ordering. These temperatures so far cannot be reached experimentally. Very little is known yet about the properties below the critical temperature T_c for magnetic ordering. As the singlet state will consist of N particles, magnetic order will be in general more complex than antiferromagnetic ordering for the SU(2) case. The observed phase of the system will depend on various parameters such as the filling, the spin-balance, the number of spin components, the dimension of the system and the coupling strength. Some predictions have been given for 1D and 2D systems.
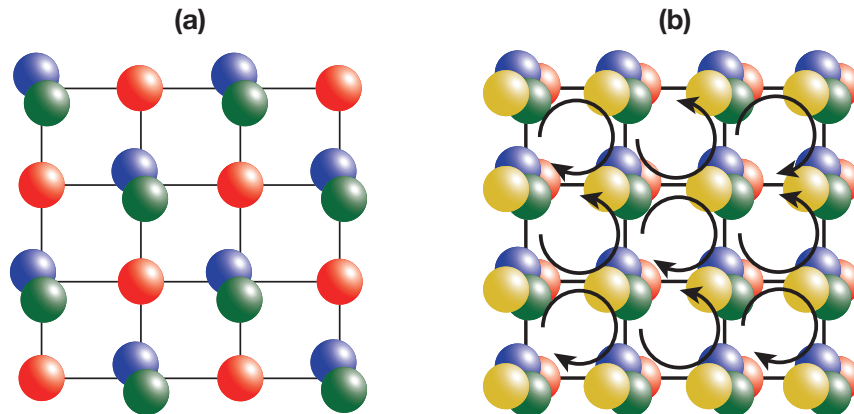
Figure 3.9: Predicted phases for an SU(3) and SU($N > 6$) Fermi gas at half-filling on a square lattice for weak to intermediate coupling strength of the 2D FHM [64]. (a) SU(3) flavor density wave (denoted by colored spheres) with two flavors occupying the same lattice site, while the third flavor occupies a different sub-lattice (b) For $N > 6$, a staggered flux phase containing an alternating spin current (arrows) on a 2×2-plaquette is predicted.

Magnetism in the weak coupling regime

In the weak to intermediate coupling limit, the 2D SU(N) Hubbard model can show different ordered phases. A flavor density wave is predicted for $N < 6$ that will break translational invariance of the lattice and SU(N) symmetry as illustrated in Fig. 3.9(a) [64, 161]. This flavor density wave can be seen as a generalized type of Néel-ordered state for systems possessing a spin greater than one-half. The enhanced lattice period of each flavor can be detected experimentally by Bragg scattering that addresses the individual flavors separately and which can reveal the structure factor. For $N > 6$, the ground state is believed to be a staggered flux phase as depicted in Fig. 3.9(b) and may possess a spin current that is alternating between the different plaquettes. This phase does not break SU(N) symmetry but it breaks translational invariance and time-reversal symmetry of the FHM.

Magnetism in the strong coupling regime

In the strong coupling limit the system is well described by an SU(N) Heisenberg model for integer fillings. Similar to the case of weak to intermediate coupling strength, the Heisenberg model predicts a feature rich phase diagram. In one dimension, the SU(N) Heisenberg model describes SU(N) spin chains [154, 165, 166].

Considering 2D square lattices, different N-dependent phases are theoretically predicted, as shown in Fig. 3.10. In this figure, the vertical axis shows the filling on a single site denoted by m, while the number of sites to form a singlet is plotted on the horizontal axis and given by k. The total number of spins can then be expressed
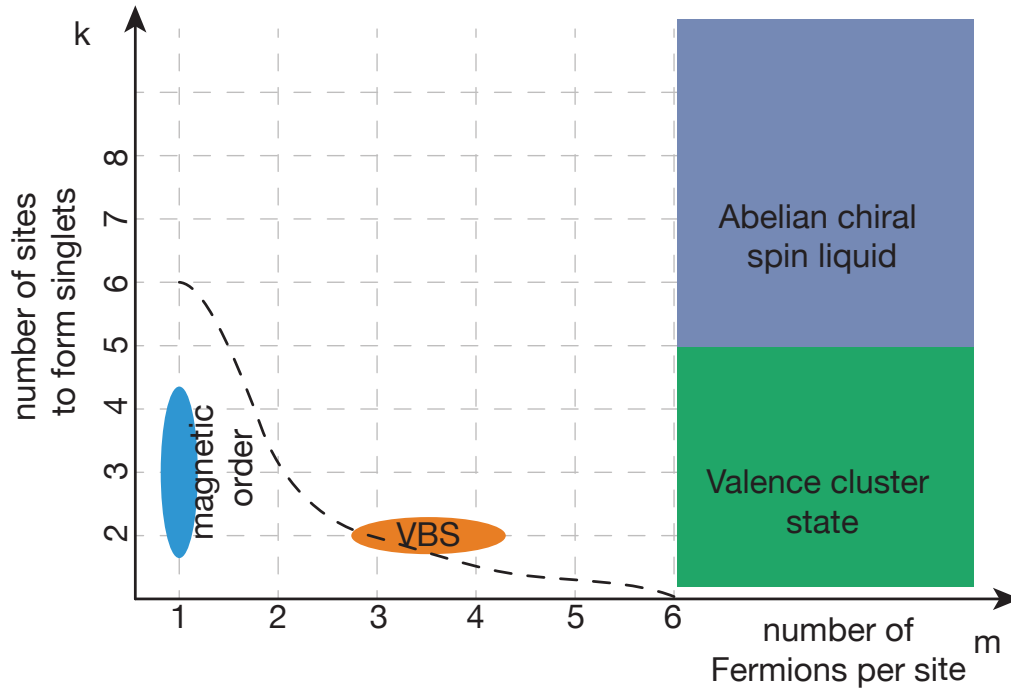
Figure 3.10: Illustration of the phase diagram of the SU(N) Heisenberg model on a square lattice. To form a singlet in an SU(N) system, N particles are needed. The vertical axis states the number of particles per site, while the horizontal axis states the number of sites needed to form a singlet. Filled regions indicate fillings for which predictions of a ground state have been given. The dashed line indicates the border that separates the region of the Heisenberg model that can be experimentally accessed with ^{173}Yb (left side) from higher SU(N) Heisenberg models (right side). For $k = 3, 4$ and $m = 2$ a valence bond solid is predicted [162]. Magnetically ordered states were found for $m = 3, 4$ and $k = 1$ [163, 164]. Using the large N-expansion, the valence cluster states and the chiral spin liquid were derived [63].

as $N = m \cdot k$. The region to the left of the dashed line in Fig. 3.10 marks the experimentally accessible regime for ^{173}Yb with $N = 6$. In the case of one atom per site ($m = 1$), magnetically ordered states are predicted up to $N = 4$ [163, 164], with the antiferromagnetically ordered Néel state for SU(2) being the most established ground state. For a higher fillings ($k = 3, 4$) a nonmagnetic valence bond solid (VBS), breaking lattice symmetry, is predicted for SU(6) and SU(8) systems [162]. Calculations using the large-N expansion indicate that the ground state for higher fillings ($k > 5$) is an Abelian chiral spin liquid (ACSL) [63]. This state breaks time reversal and parity symmetry and supports excitations with fractional quantum number and statistics. The ACSL phase is actually the spin-system analog to a fractional quantum Hall state for $k \geq 5$. At lower fillings ($k < 5$), the large N-expansion predicts a valence cluster state (VCS) that is nonmagnetic and breaks lattice symmetry in addition [63]. It is however unclear down to which filling the ACSL and VCS will extend in the illustrated phase diagram. Some calculations predict that it might even hold down to the experimentally very relevant case of $m = 1$ ($k = N$) in a honeycomb lattice configuration [167]. However, the type of magnetic order in SU($N>2$) systems still remains to be verified.

3.3 Two-orbital physics

The single-orbital Fermi-Hubbard Hamiltonian of the previous section, describing interacting ground state fermions in an optical lattice, can be expanded by a second electronic orbital. When omitting the trapping potential, the Hamiltonian of the two-orbital FHM in the Wannier basis, and for the lowest energy band of the lattice, reads [58]

$$\hat{H} = - \sum_{\langle i,j \rangle, \alpha, \sigma} t_\alpha (\hat{c}^\dagger_{i,\alpha,\sigma} \hat{c}_{j,\alpha,\sigma} + \text{H.c.}) + \sum_{i,\alpha,\sigma \neq \sigma'} \frac{U_{\alpha,\alpha}}{2} \hat{n}_{i,\alpha,\sigma} \hat{n}_{i,\alpha,\sigma'} \tag{3.38}$$

$$+ V_{ex} \sum_{i,\sigma,\sigma'} \hat{c}^\dagger_{j,g,\sigma'} \hat{c}^\dagger_{j,e,\sigma} \hat{c}_{j,g,\sigma} \hat{c}_{j,e,\sigma'} + V \sum_{i,\sigma,\sigma'} \hat{n}_{j,g,\sigma} \hat{n}_{j,e,\sigma'}. \tag{3.39}$$

The parameter t_α describes a state-dependent tunneling matrix element, $c^\dagger_{i,\alpha,m}$ ($c_{i,\alpha,m}$) denote the fermionic creation (annihilation) operator on site i for the electronic state $\alpha \in \{|g\rangle, |e\rangle\}$ with spin σ. The on-site interaction energies are given by

$$U_{\alpha,\alpha} = \frac{4\pi\hbar^2 a_{\alpha,\alpha}}{m} \int_{-\infty}^{\infty} |w_\alpha(\mathbf{x})|^4 \, d^3x$$

$$U^\pm_{e,g} = \frac{4\pi\hbar^2 a^\pm_{e,g}}{m} \int_{-\infty}^{\infty} |w_g(\mathbf{x})|^2 |w_e(\mathbf{x})|^2 \, d^3x$$

$$V = (U^+_{e,g} + U^-_{e,g})/2$$

$$V_{ex} = (U^+_{e,g} - U^-_{e,g})/2,$$

where $a_{\alpha,\alpha}$ ($a_{e,g}^{\pm}$) denotes the scattering length within (between) the orbitals. For doubly occupied lattice sites with two different electronic states, the two-particle wave function can be either symmetric or antisymmetric in the electronic orbital. The symmetric orbital configuration has a spin-singlet configuration $|s\rangle$

$$|eg\rangle^{+} = (|eg\rangle + |ge\rangle) \otimes |s\rangle \tag{3.40}$$

with an on-site interaction energy denoted by $U_{e,g}^{+}$. The anti-symmetric orbital configuration possesses a spin-triplet configuration $|t\rangle$

$$|eg\rangle^{-} = (|eg\rangle - |ge\rangle) \otimes |t\rangle \tag{3.41}$$

with an interaction energy $U_{e,g}^{-}$. It should be noted that, because of the different interaction potentials for the two orbital configurations that determine the scattering lengths $a_{e,g}^{\pm}$, the energies V and V_{ex} in the two-orbital Fermi-Hubbard Hamiltonian will in general be different.

The Hamiltonian presented above has a symmetry of $U(1) \times SU(N)$, where the additional symmetry of the unitary group $U(1)$ arises because of the elasticity of collisions between the two electronic orbitals. Because of the second orbital and the various interaction energies in the Hamiltonian, the phases for this model are even more feature rich than the phase diagram of the single-orbital $SU(N)$ FHM. Limiting cases of vanishing tunnel matrix element for one or both of the two electronic states are often studied to gain insight into the physics of such systems. In the strongly interacting limit $U_{\alpha,\alpha'} \gg t_g$ and $U_{\alpha,\alpha'} \gg t_e$ this Hamiltonian reduces to a spin Hamiltonian. In the case of one atom per site, the generalized $SU(N)$-symmetric version of the Kugel-Khomskii model is realized. Another often-studied model that can be implemented in an ultracold ytterbium experiment with a state-dependent potential is the Kondo lattice model.

3.3.1 Kondo physics

The Kondo lattice model (KLM) originated as an extension from the Kondo impurity model, which describes the interaction of conducting electrons with a single impurity. The Kondo impurity model was historically studied to understand the resistivity minimum as a function of temperature for certain metals with magnetic impurities [168]. In contrast to the resistivity dropping with decreasing temperature for normal non-superconducting metals, it was found by Kondo that the resistivity would increase again by $\propto -V_{ex} \log(T)$ at low temperatures due to the magnetic impurity interacting with the conducting electrons.

In 1977, Doniach extended this idea and proposed the KLM [169] to explain the behavior of heavy fermion (HF) materials. These materials show a huge linear heat capacity at low temperatures and usually a quadratic dependence of the resistivity as a function of temperature in the low temperature limit [170, 171]. Some HF
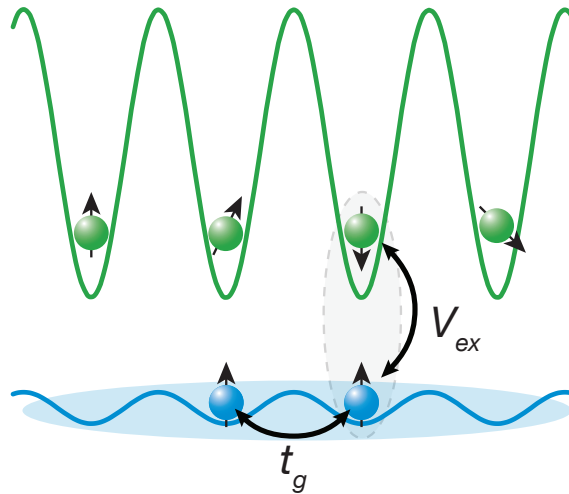
Figure 3.11: Scheme of the lattice potential and the interaction between two species in the Kondo lattice model. A mobile species (blue) can tunnel in a shallow lattice between neighboring sites, while the localized magnetic impurities (green) are frozen out in a deep lattice. The mobile species interacts with the immobile species via the spin-exchange interaction V_{ex}.

materials are unconventional superconductors at low temperatures [172, 173], e.g. possess a pairing mechanism of the electrons that leads to superconductivity which is not described by BCS theory [174].

The KLM arises from the two-orbital FHM described by Eq. 3.39 in the limiting case for $t_e = 0$ with a filling $n_e = 1$ of one atom per site in one orbital. In addition, this model assumes a vanishing on-site interaction $U_{g,g}$ of the atoms in the other orbital. Under these assumptions the two-orbital Fermi-Hubbard Hamiltonian reduces to the Kondo lattice Hamiltonian

$$H_{Kl} = -t_g \sum_{\langle i,j \rangle, \sigma} \hat{c}^\dagger_{i,g,\sigma} \hat{c}_{j,g,\sigma} - 2V_{ex} \sum_{j,\sigma,\sigma'} \hat{c}^\dagger_{j,g,\sigma} \hat{c}^\dagger_{j,e,\sigma'} \hat{c}_{j,g,\sigma'} \hat{c}_{j,e,\sigma}. \tag{3.42}$$

The KLM describes the interaction between a mobile species, e.g. electrons in a conducting band, with an immobile species in a second flat band as illustrated in Fig. 3.11. The immobile species acts as localized spins that interact with the mobile species in the conducting band via the Heisenberg exchange interaction. Similar to the single orbital FHM, the particle-particle correlations that arise due to tunneling make this model equally hard to solve as the FHM. Depending on the interaction parameter $v = -2V_{ex}/t_g$, the Kondo lattice model exhibits different phases.

In the strong coupling limit ($|v| \gg 1$) the mobile species will bind to the localized spins and both species will form a singlet or triplet depending on the sign of V_{ex}. This effect is called Kondo screening and leads to heavy fermion properties in the case of anti-ferromagnetic coupling ($V_{ex} < 0$). The energy scale for Kondo screening is the
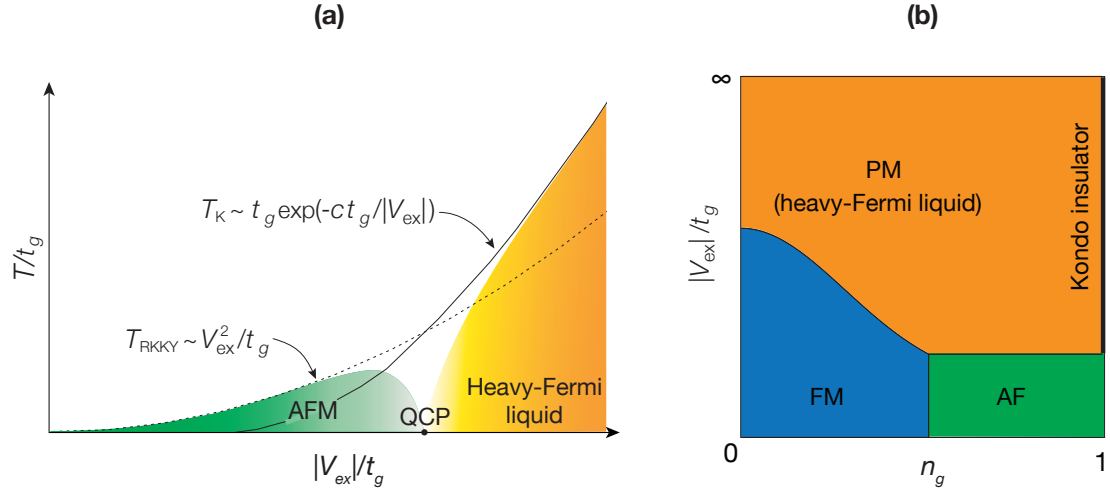
(a)

$T_\text{K} \sim t_g \exp(-c\,t_g/|V_\text{ex}|)$

$T_\text{RKKY} \sim V_\text{ex}^2/t_g$

AFM

QCP

Heavy-Fermi
liquid

T/t_g

$|V_{ex}|/t_g$

(b)

PM
(heavy-Fermi liquid)

Kondo insulator

FM

AF

$|V_\text{ex}|/t_g$

n_g

Figure 3.12: **(a)** 1D Doniach phase diagram of the Kondo lattice model with anti-ferromagnetic coupling as a function of the interaction parameter V_{ex}/t_g [58]. For strong interactions, below the Kondo temperature T_K (solid black line) with $T_K > T_{RKKY}$, a Fermi liquid with heavy fermion properties is expected. For weak interactions, RKKY-interaction dominates at temperatures $T_{RKKY} > T_K$ (dashed black line) and mediates magnetic order between the isolated, localized spins. A quantum critical point (QCP) connects both regimes at zero temperature. **(b)** Ground state of the 2D Kondo lattice model with anti-ferromagnetic coupling as a function of the filling n_g [175]. For low interaction strengths, ferromagnetic or anti-ferromagnetic magnetic order arises, depending on the filling n_g. For high interaction strengths and fillings below one, the system is in a paramagnetic phase possessing heavy fermion properties. At filling one, the system is isolating at strong couplings and forms a Kondo insulator.

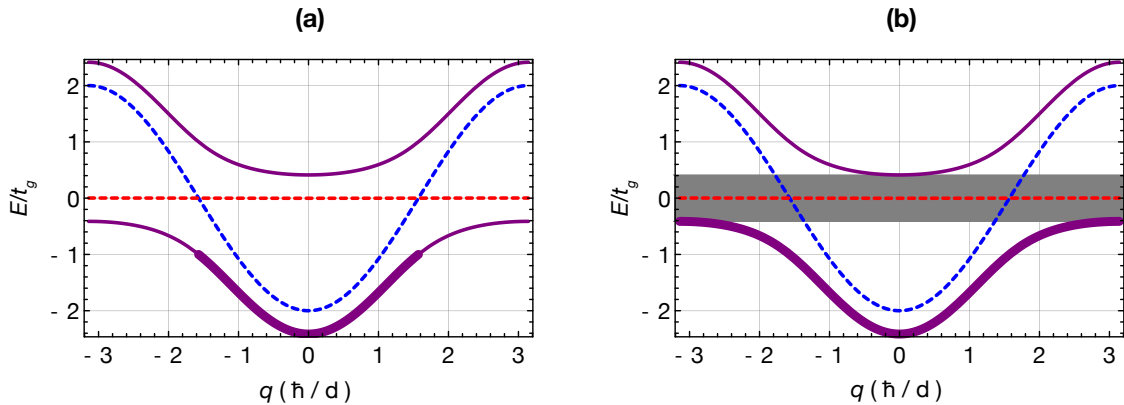**(a)**　　　　　　　　　　　　　　　**(b)**

Figure 3.13: Schematic of the band hybridization and the Kondo insulator that emerges for strong couplings. (a) The dashed lines denote the non-hybridized bands of the immobile spins (red) and the mobile species (blue). Due to the strong coupling between the two species the band structure hybridizes (purple line), giving rise to a higher effective mass for the mobile species. The thick purple line indicates the filling of the band up to the Fermi energy. (b) Emergence of the Kondo insulator. The hybridized band is filled completely and separated by an energy gap Δ (grey shaded region) from the upper band causing the system to be isolating at filling $n_g = 1$.

same as for the single Kondo impurity model and is given by the Kondo temperature which scales as $T_K \propto t_g \mathrm{e}^{-t_g/|V_{ex}|}$ [176]. In this regime, the heavy fermion properties can be understood in a mean field picture by the hybridization of both bands. For strong anti-ferromagnetic couplings, a Kondo singlet forms and the immobile spins have to be included into the Fermi sea of the mobile species. This hybridization will lead effectively to a reduced bandwidth of the hybridized band compared to the conduction band without coupling, as illustrated in Fig. 3.13(a). The associated effective mass of the hybridized band will therefore increase and the system behaves like heavy fermions. For strong couplings, an avoided crossing between the two bands exists with a band gap $\Delta \simeq t_g v$. Moreover, because of the hybridization, the lowest band will be filled completely for $n_g = 1$ (one ground-state particle per site) and form the Kondo insulator as shown in Fig. 3.13(b).

In the weak coupling limit ($v \ll 1$), the mobile species mediates spin order between the localized particles, which is known as Ruderman-Kittel-Kasuya-Yosida (RKKY) interaction [177–179]. The critical temperature given for this type of magnetic ordering is $T_{RKKY} \propto V_{ex}^2/t_g$ and scales as V_{ex}^2 due to scattering of the mobile species in second order via the exchange interaction with the immobile spins. The Doniach phase diagram of the KLM with the scaling of the Kondo temperature T_K and the RKKY temperature T_{RKKY} for different couplings is illustrated in Fig. 3.12(a).

The type of magnetic order that the KLM will exhibit can be either ferromagnetic or anti-ferromagnetic. The RKKY interaction that mediates magnetic order competes

with the formation of a paramagnetic phase with heavy fermion properties, which gives rise to a rich phase diagram. In 2D, the phases of the KLM are expected to range from ferromagnetic ordering to anti-ferromagnetic ordering for weak couplings and the KLM is expected to possess a paramagnetic, heavy Fermi liquid phase at strong couplings as illustrated in Fig. 3.12(b). The types of phases will depend on the sign of the coupling v, the dimension of the system and the filling n_g.

Kondo-type physics with ytterbium in a state-dependent lattice

Ytterbium is particularly suited for the study of the KLM. The meta-stable states with typical lifetimes of several seconds are ideal for the realization of the second orbital in the KLM. Moreover, by choosing an appropriate wavelength for the state-dependent optical lattice, the two states can have very different lattice depths to realize the condition of an immobile species and a conducting species. In addition, the SU(N) symmetric interactions of the quantum gases are essential to study Kondo physics with enhanced symmetry but are also necessary to avoid spin-changing collisions when studying the SU(2) KLM. For ^{173}Yb a large, ferromagnetic exchange interaction $V_{ex} = h \cdot (22 \pm 1)\,\text{kHz}$ was found for a lattice depth $V = 43\,E_r$ [72], which should allow to access the strong coupling regime of the KLM. Proposals exist to use a confinement-induced resonance in one or two dimensions, which allows changing the sign of the coupling as well as the coupling strength in order to study antiferromagnetic and ferromagnetic exchange interactions [180].

The hybridization of both bands in the strong coupling limit of the KLM is similar to the band hybridization that emerges between the ^{1}S$_0$ and the ^{3}P$_0$ state for strong Rabi couplings ($\Omega \gg 4t_g$) when the ground state is optically dressed in a state-dependent lattice (see section 6.2.2). In the case of optical dressing, the strong Rabi coupling leads to a complete mixing of both bands and increases the effective mass of the ground-state atoms. Similar to the heavy Fermi properties in the KLM, this enhanced mass can be probed by measuring the center of mass oscillation of the atomic sample (see Eq. 6.8).

Chapter 4

Experimental setup

In this chapter, we present the experimental apparatus and the laser setup used for the production and the investigation of ultracold degenerate ytterbium quantum gases. The ultracold quantum gas is created by all-optical cooling in the main chamber of the apparatus. The employed cooling techniques are similar to the ones used for alkali elements and became standard techniques for reaching quantum degeneracy over the past years. A detailed description e.g. of evaporative cooling or magneto-optical trapping can be found for example in [181].

The cooling of ytterbium atoms is performed in three stages. The atoms are first evaporated in an oven in order to generate an atomic beam, which is directed into a Zeeman slower. Afterwards, the slowed atoms are captured by a magneto-optical trap (MOT) in the main chamber of the experiment. The magneto-optical trap is loaded for several seconds before we transfer the atomic sample in an optical dipole trap. Evaporative cooling is then used to reach quantum degeneracy.

In the following paragraphs, we first describe the different sections of the experimental apparatus that are responsible for the different stages of cooling. A more detailed description of the apparatus can be found in the following reference [73]. Moreover, we depict the beam configuration in the main chamber and present the in-situ imaging system and the high power coils, which were installed as a recent upgrade to the setup. In addition, we give a brief overview of the laser setups that are used for the cooling and the imaging of ytterbium atoms.

4.1 Vacuum chamber

Figure. 4.1 illustrates the experimental apparatus with the different cooling sections. This setup can be divided into three different sections, an oven section, a Zeeman slower section and the main chamber where we perform all the experiments. The apparatus is placed on an optical table and is surrounded by three optical breadboards, which host the optics.
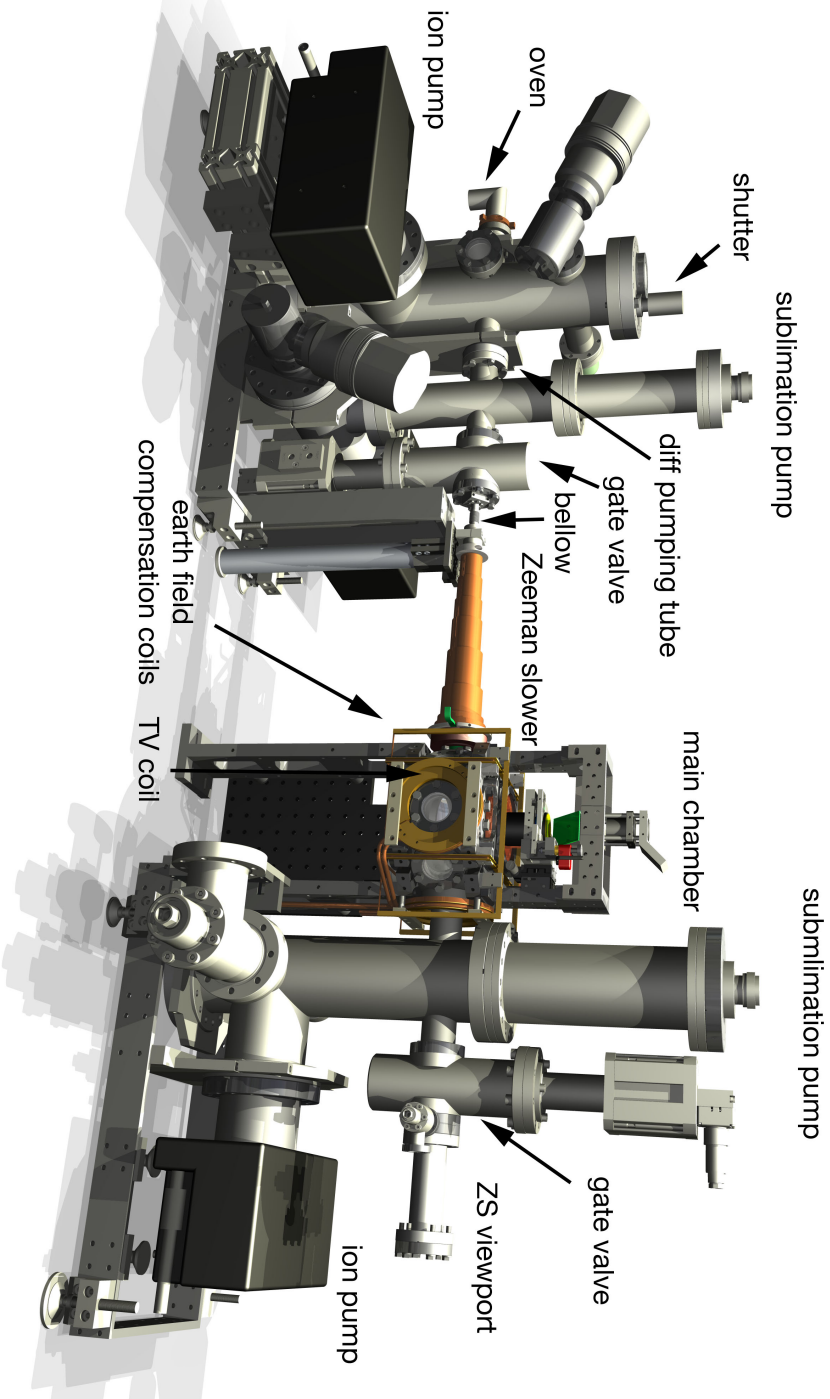
Figure 4.1: CAD model of the experimental apparatus used to produce and cool ytterbium atoms to quantum degeneracy. The apparatus consists of several sections. Ytterbium atoms are sublimated in the oven section. Cooling to quantum degeneracy is performed in the main chamber after the Zeeman slower section. Several pairs of magnetic coils allow canceling the earth magnetic field as well as the magnetic field of the Zeeman slower in the main chamber. The vacuum of the apparatus is maintained by several pumping stages that consist of ion- and sublimation pumps. The optical assembly and the optical tables are omitted in this illustration.

Oven section

In the first stage of the experiment, a beam of ytterbium atoms is produced by sublimation in an oven. This oven consists of three segments, which are separately heated to generate a temperature gradient between the different segments. The first segment of the oven contains the ytterbium reservoir, which consists of about 50 g ytterbium metal pieces. In the last segment of the oven, small nozzles with 200 μm diameter and a length of 1 cm are installed in order to produce a collimated atomic beam. An uncollimated atomic beam would reduce the operation time of the oven and would lead to unnecessary deposition of ytterbium material in the experiment chamber. The nozzles produce a small acceptance angle and therefore only atoms witch a motion directed towards the Zeeman slower section can leave the oven. The oven segment containing the nozzles is operated at the highest temperature of the three segments. The temperature gradient between the sections ensures that atoms that are deposited next to the nozzles or walls, and are not able to leave the oven, are recycled by creating a net flux back to the colder section which contains the ytterbium reservoir.

To achieve a sufficiently high flux of about 2×10^{14} atoms/s during operation, the three oven sections are heated by power supplies with resistive heaters to 400 °C, 420 °C and 440 °C respectively. Several thermocouples monitor the temperature of the oven sections and three PID controllers regulate the different sections to the set temperature. In order to enhance the lifetime of the oven, the standby temperature of the three segments is set 100 °C lower.

A mechanical shutter, which can be operated through a vacuum feedthrough with a stepper motor, ensures that the atom beam is blocked after the loading sequence of the magneto-optical trap. We obtain a long vacuum lifetime of the atoms of about 90 s when the atomic shutter is closed. This lifetime is reduced to about 30 s when the shutter is permanently open due to the flux of the atomic beam.

Zeeman slower section

A differential pumping tube connects the oven section of the vacuum chamber with the Zeeman slower section. The vacuum pressure in the oven section is about $P = 5 \times 10^{-9}$ mbar due to the high temperature of the oven segment and the atom flux. The differential pumping, which has an inner diameter of $D = 8$ mm and length of $L = 116$ mm, acts as an aperture for the particles and produces a pressure gradient between the oven section and the main vacuum chamber where we conduct the experiments. In this way, we achieve a vacuum pressure $P \simeq 1 \times 10^{-11}$ mbar in the main chamber which is sufficiently low to conduct cold atom experiments.

Because of the high temperatures of about 400 °C to produce a sufficiently high atom flux, the atoms will leave the oven section with a velocity $v \approx 290$ m/s. This velocity is too high in order to capture the atoms directly with the magneto-optical
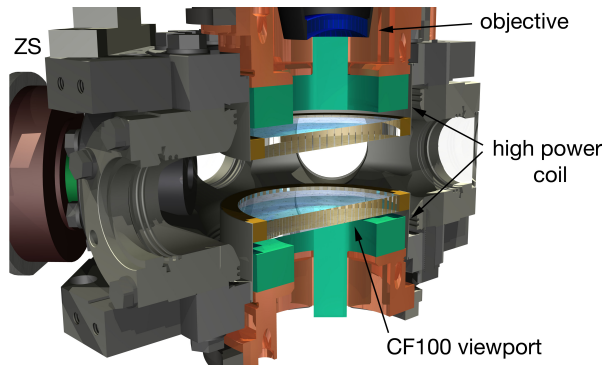
Figure 4.2: Half-section view of the main chamber where the experiments are performed. A pair of coils at the top and bottom of the chamber allows producing magnetic fields in Helmholtz and anti-Helmholtz configuration e.g. for optical pumping or magneto-optical trapping. The high-resolution objective is mounted above the top CF100 viewport of the chamber for in-situ imaging of the atomic sample.

trap. Therefore, a Zeeman slower stage, starting directly behind the oven section, is used to slow down the atomic beam. A detailed description about the Zeeman slower design can be found in the following thesis [73].

The basic operation principle of a Zeeman slower is the velocity dependent Doppler effect in combination with the Zeeman shift in a magnetic field that will bring atoms within a certain velocity class into resonance with counter propagating light [182]. While the atoms propagate through the slower, the absorbed light will exert a net force opposite to the direction of movement and will slow down the atoms. In addition a spatially varying magnetic field throughout the slower compensates the reduced Doppler shift when the atoms are slowed down to keep the light resonant. The slower in our experiment is 30 cm long and operates on the stretched state $(F, m_F = \pm F \to F' = F + 1, m_{F'} = m_F \pm 1)$ of the broad $^1S_0 \to {}^1P_1$ transition. Typical optical powers for the slower vary between $40 - 50$ mW. The slower consists of several magnetic solenoid coil sections, which produce an increasing magnetic field towards the main chamber. The maximum magnetic field at the exit of the slower is 450 G for ^{173}Yb, which corresponds to a detuning of -650 MHz from the $F = 5/2 \to F' = 7/2$ hyperfine transition. For this detuning, the maximum capture velocity is about $v_c \simeq 260$ m/s and the exit velocity at the end of the slower is $v_f \simeq 8$ m/s, which is well within the capture range of our green magneto-optical trap.

Main chamber

The main chamber of the experimental apparatus, where all the experiments are performed with ytterbium quantum gases, is situated after the Zeeman slower section.
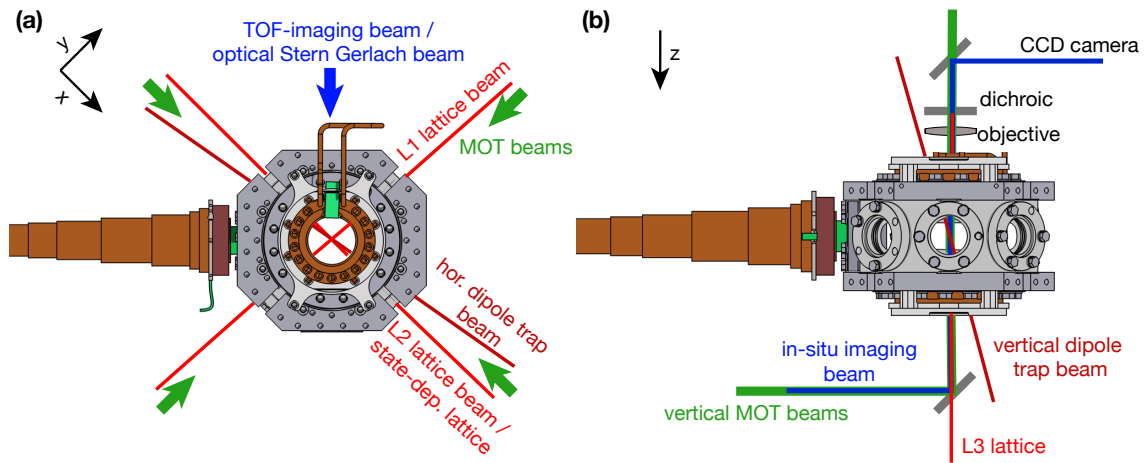
Figure 4.3: Illustration of the optical beam configuration used for cooling, trapping and manipulating ytterbium atoms in the main chamber. The blue beams illustrate the imaging paths, the red beams depict the beam path for the various lattice arms and the crossed dipole trap and the green beams illustrate the beam configuration of the magneto-optical trap, **(a)** top view of the main chamber **(b)** view from the side of the chamber.

All the relevant beams used for cooling, trapping and imaging are intersecting in this chamber. Figure 4.3 illustrates the optical beam configuration used in the experiment.

The main chamber has an octagon shape with six CF40 viewports at the side and two CF100 viewports at the top and bottom of the chamber. For better optical access to the atoms, the top and bottom windows are recessed in the viewports as illustrated in figure 4.2. Moreover, the bottom window has a small tilt with respect to the top one in order to avoid possible and unwanted reflections of optical beams from the two windows. An ion-pump as well as a titanium sublimation pump are installed in the tower next to the main chamber in order to achieve sufficient pumping for reaching a low pressure. The obtained vacuum pressure in the main chamber of $P \simeq 1 \times 10^{-11}$ mbar is low enough to avoid excessive vacuum losses and we obtain vacuum lifetimes of about 90 s.

4.1.1 Imaging objective

As an upgrade to the experiment, we installed a high-resolution imaging objective.[1] The objective consists of a quadruplet lens system, as illustrated in Fig. 4.4(a), and has an effective focal length of 67 mm. The first lens of the quadruplet has a diameter of $D = 37.1$ mm, which yields a numerical aperture of $NA = 0.27$ and we obtain a
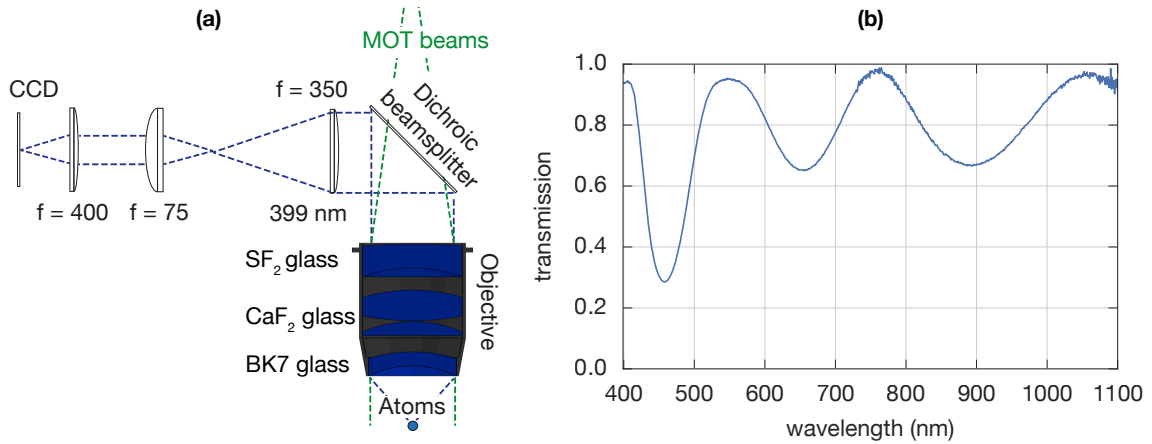
---

[1]designed by Lens Optics

Figure 4.4: **(a)** Illustration of the imaging beam path including the beam path for the imaging light and the MOT beams. The objective consists of four lenses and realizes with the lens behind a telescope. The image is further magnified before the camera by a second telescope system. **(b)** Optical transmission of the quadruplet lens system of the objective, measured by the manufacturer, as a function of the wavelength.

resolution of this imaging system of about $1.2\,\mu$m (see section 5.1.1). The quadruplet lens system is designed to transmit the laser light used for imaging, magneto-optical cooling and the lattices. Therefore, the lenses were manufactured with an anti-reflection coating for four different wavelengths $\lambda_1 = 399$ nm, $\lambda_1 = 556$ nm, $\lambda_1 = 799$ nm and $\lambda_1 = 1112$ nm to achieve a high transmission (see Fig. 4.4(b)).

The imaging objective is placed above the main chamber of the apparatus as illustrated in figure 4.2. A pair of translation stages allows positioning the objective precisely to focus on the atoms. A second lens[2] behind the objective and an additional $16:3$ telescope yield a total magnification $M = 28$ for the imaging system. The pictures of the atomic sample obtained with this objective are recorded by a water cooled, low noise CCD camera, which is optimized for the blue light of our imaging wavelength.[3]

4.1.2 High-power coil

Our main magnetic coils are placed over the top viewport and below the bottom viewport of the main chamber at a distance of 63 mm between each other. These coils are glued with a $50\,\mu$m heat conducting but electrically insulating glue layer[4] to a copper mount, which is water-cooled, as illustrated in picture 4.5. The coils

---

[2]$f = 350$ mm
[3]Andor iXon
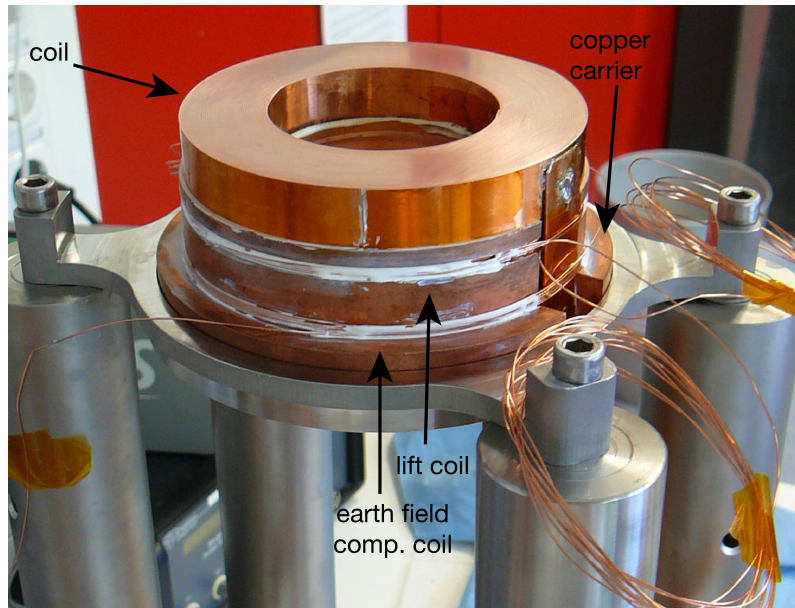[4]Atom adhesives AA-Supertherm 195

Figure 4.5: High power coil assembly before integration into the setup. The coil is mounted on a copper carrier that is water-cooled. The mount additionally includes a coil for compensation of the vertical component of the magnetic earth field and in addition a lift coil to create an independent magnetic bias field.

consist of $N = 43$ windings of flat copper wire ($W \times H = 15 \times 0.47\,\mathrm{mm}$) and are capable of carrying a current of about 200 A over a few seconds. The maximum achievable magnetic field with our power supplies is $B_{max} \simeq 1200\,\mathrm{G}$. Moreover, a set of earth field compensation coils and lift coil is installed on the same mount that carries the high power coils. These coils can be used to cancel the vertical magnetic field component of the earth field and allow shifting the vertical position of the compressed MOT when loading atoms to the optical dipole trap.

The main coils are connected to a set of MOSFET switches, which make it possible to operate the coil pair in Helmholtz or anti-Helmholtz configuration. This allows us to use the coils for the creation of a magnetic field for the MOT as well as for state preparation and spectroscopy where a homogeneous magnetic field is required. The coils can be operated with two power supplies. One power supply is optimized for stable operation at low currents, as needed for the magneto-optical trap or for the creation bias fields. The second power supply can produce currents up to 220 A in order to create strong magnetic fields as used for spectroscopy. In order to avoid excessive heating of the coils and the nearby main chamber, a safety circuit limits the duration of the current from the big power supply to about 2 s. In addition a pair of thermocouples monitor the temperature of the copper mounts and will engage our main safety circuit if the temperature is exceeding a certain temperature threshold.

4.2 Laser systems

This section gives a brief overview of the laser systems that are used for slowing, magneto-optical trapping and imaging of ytterbium atoms. Since the employed optical transitions are in the visible spectrum of the light, the light is created by frequency doubling of infrared light with nonlinear optical crystals.

4.2.1 Blue laser setup

The blue light for the $^1S_0 \to {}^1P_1$ transition is produced by intra-cavity frequency doubling. An external cavity diode laser (ECDL) running at a wavelength of $\lambda = 798$ nm generates an optical output power of about 60 mW. In a second stage, the light from the ECDL is amplified by a tapered amplifier and we obtain a typical optical power of 1 W. After amplification, the light is frequency doubled by a BiBO crystal in a bow-tie cavity which is angle phase matched [183]. To achieve optimal phase matching the crystal is heated with a PID controlled electric heater to 44.5°C. The bow-tie cavity is stabilized to the ECDL, which in turn is stabilized with a beat-lock to a second, lower-power ECDL that emits light directly at the wavelength $\lambda = 399$ nm. This second ECDL is locked via FM spectroscopy in an ytterbium vapor cell to the $^1S_0 \to {}^1P_1$ transition frequency of ytterbium [184] and serves as the frequency reference for the main laser system.

After frequency doubling we achieve an optical power of about 250 mW which is used for the different imaging arms and the Zeeman slower in the experimental setup. Two acousto-optic modulators shift the frequency in the imaging arm by about +480 MHz and compensate partially the detuning of the Zeeman slower. Due to the flexible beat-lock mechanism, the frequency detuning of the main ECDL can additionally be varied within the experiment sequence to bring the laser into resonance with the $^1S_0 \to {}^1P_1$ transition for imaging the atomic sample.

4.2.2 Green laser setup

The green laser setup is used to produce light for driving the $^1S_0 \to {}^3P_1$ transition. We use this light for our magneto-optical trap, for optical pumping, the optical Stern-Gerlach beam and for photoassociation.

A commercial fiber laser[5] running at a wavelength $\lambda = 1112$ nm produces the infrared light for this setup. The fiber laser has a linewidth of 65 kHz, possesses a piezo with a tuning-range of 13 GHz and produces an optical power of about 2 W. The infrared light is frequency doubled with a periodically poled crystal, which is stabilized to 26.3 °C in a bow-tie cavity. By using such a configuration, we obtain an optical output power of 1 W at the wavelength $\lambda = 555.8$ nm, corresponding to a

---

[5] Menlo laser systems Orange One-2

conversion efficiency of about 50 %. The frequency doubled, green light is split to six fiber-coupled ports for each beam of the magneto-optical trap. An additional path splits of a part of the total power of about 100 mW for the light of the optical Stern-Gerlach beam. This light is frequency shifted by +850 MHz with an AOM in double passage configuration.

The laser is stabilized by the Pound–Drever–Hall technique to a high finesse cavity, with a finesse of about 1×10^4 at the wavelength $\lambda = 1112$ nm [185]. The same cavity is also used to stabilize the yellow clock laser and possesses a finesse of about 1×10^5 at a wavelength of $\lambda = 578.4$ nm. To isolate the cavity maximally from acoustic noise and temperature fluctuations, it is placed in a vacuum cell. The high reflective mirrors of the cavity are optically contacted to an ultra-low expansion (ULE) glass substrate, which ensures minimal thermal expansion upon temperature changes. Further details about the cavity design, the stabilization of the clock laser and the mounting can be found in references [73, 186].

4.3 Optical traps

4.3.1 Magneto-optical trap

We use a magneto-optical trap to capture the atoms after the Zeeman slower stage. A MOT uses the dissipative forces of close detuned light with respect to an optical transition in combination with a quadrupole magnetic field to capture and cool atoms [187, 188]. In this way, temperatures close to or even below the Doppler temperature can be reached. The temperature of the atoms in the MOT depends on the light intensity I and the detuning Δ of the light. According to Doppler cooling theory, this temperature is given by

$$T = \frac{\hbar \Gamma^2}{8 k_B \Delta} \left(1 + \frac{I}{I_{sat}} + 4 \frac{\Delta^2}{\Gamma^2} \right), \tag{4.1}$$

where $I_{sat} = \pi h c \Gamma / (3 \lambda^3)$ denotes the saturation intensity for the wavelength λ of the cooling transition and Γ denotes the scattering rate. It should be noted however that deviations to the formula given above have been observed for higher intensities with alkaline earth-like atoms [189, 190]. Using Eq. 4.1, the lowest temperature of the atomic sample is obtained for $\Delta = \Gamma/2$ and $I \to 0$. For these parameters the Doppler temperature $T_D = \frac{\hbar \Gamma}{2 k_B}$ is reached, which is only $4.4 \, \mu$K for the intercombination line $^1S_0 \to {}^3P_1$ in ytterbium. The narrow intercombination line for alkaline earth-like atoms with the associated low Doppler temperature is therefore ideal to be used for magneto-optical trapping to achieve cold atomic gases before evaporative cooling.

For the fermionic isotopes in ytterbium, which possess a nuclear spin, sub-Doppler cooling has also been reported [189]. Such sub-Doppler cooling schemes rely on a substructure of the atomic state, like the presence of a nuclear spin in the case of
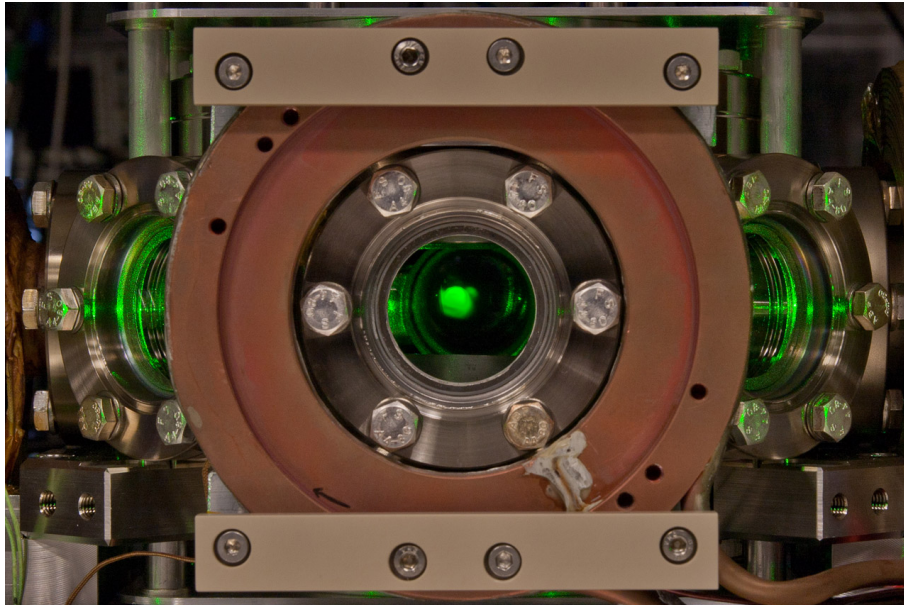
Figure 4.6: Side view of the main chamber with one transverse coil visible in front of the chamber. The picture shows the green fluorescence of the ytterbium atoms that are trapped in the MOT during the loading sequence.

fermionic isotopes, and a pumping mechanism between these sublevels to overcome the limit of the Doppler temperature [191–193].

In our experiment, six optical beams with a waist of about $7\,\mathrm{mm}$ are used to create a 3D MOT. The capture velocity of the MOT can be estimated by realizing that the maximum radiation force is given by $F_{max} = \hbar k \Gamma / 2$, where $k = 2\pi/\lambda$ denotes the wavevector of the cooling transition. For a beam diameter $D \approx 14 mm$ of the MOT beams this leads to a capture velocity of

$$v_c = \sqrt{\frac{D\hbar k\Gamma}{m}} \approx 8\,\mathrm{m/s},\tag{4.2}$$

which is comparable to the exit velocity of the atoms after the Zeeman slower.

If the linewidth of the cooling transition is very narrow, such as in strontium where $\Gamma = 2\pi \times 7.4\,\mathrm{kHz}$, the dissipative light forces of the MOT are so weak that gravitation becomes relevant. In this case a gravitational sagging of the atoms in the MOT is observed, which leads to an overall higher absorption of photons from the bottom MOT beam. In such a scenario, it has to be considered that the atoms in the MOT will get partially polarized [194, 195]. This effect is however less relevant for ytterbium due to the larger linewidth as opposed to strontium. Moreover, when loading the atoms from the MOT to the dipole trap, the magnetic field is rapidly turned off leading to a fast depolarization of the atomic sample in the dipole trap.

sequence	detuning (Γ)	peak int. (I_0/I_{sat})	mag. gradient (G/cm)
MOT loading	-5	≈ 560	2
MOT compression	-1	$\approx .1$	20

Table 4.1: Detuning, peak intensity and magnetic field gradient used for the loading MOT and the compressed MOT in the experiment.

MOT loading sequence

Our experiment sequence starts by slowing the atoms with the Zeeman slower while loading the MOT for about 8 s. During loading, the peak intensity of the MOT beams is about $I_0 \approx 560 I_{sat}$. The typical detuning of the MOT during the loading sequence is -5Γ with a magnetic field gradient of 2 G/cm, as shown in table 4.1. The magnetic field gradient in this configuration of the MOT is mainly given by the Zeeman slower compensation coils. The low magnetic field gradient maximizes the capture volume of the MOT and accounts for the diverging atomic beam after the Zeeman slower.

After loading, the MOT is compressed by decreasing the detuning to -1Γ and by simultaneously changing the magnetic field gradient to 20 G/cm. This increases the atomic density and is ideal for transferring the atoms into the dipole trap, which covers only a fraction of the MOT volume. In parallel with changing the magnetic field gradient, the intensity of the MOT beams is ramped down to $0.1\,I/I_{sat}$. This reduces the temperature of the atoms to about $10-20\,\mu$K. Fig. 4.7**(a)** depicts the ramp sequence of the magnetic field, the intensity and the detuning of the MOT when loading the dipole trap. For the compression, the intensity and detuning of the MOT are chosen as a compromise between lowest temperature and highest density in order to maximize the atom number loaded into the optical dipole trap before evaporation. After compression of the MOT, we achieve typical atom numbers of $N \simeq 5 \times 10^7$ for ^{173}Yb. The density profile of the compressed MOT during the transfer of the atoms to the optical dipole trap is shown in Fig. 4.7**(b)**. The core of the compressed MOT in this picture is optically dense. The horizontal deformation of the density profile is caused by the horizontal dipole trap beam, which is intersecting the compressed MOT at the upper half of the cloud. To match the cloud position of the compressed MOT in the vertical direction to our optical dipole trap beam position, we use the lift coil that is installed on the carrier of the high power coils in order to create a vertical bias field to change the equilibrium position of the MOT.

4.3.2 Optical dipole trap

We perform all-optical evaporation of the ytterbium atoms in a far detuned optical dipole trap to reach quantum degeneracy of the atomic gas. The spatially varying
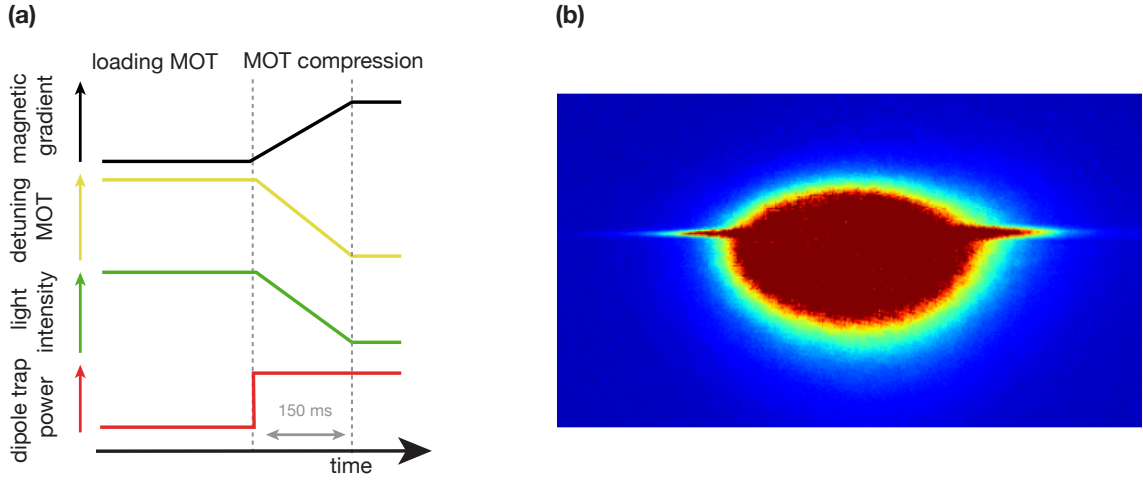
(a)

(b)

Figure 4.7: Ramping sequence during dipole trap loading of the magnetic field gradient, the light intensity and the detuning of the MOT. After switching on the dipole trap potential, the magnetic field gradient is increased and the light intensity of the MOT is reduced in order to cool and compress the MOT for optimal dipole trap loading. The ramping sequence was optimized for maximum transfer of atoms.

intensity of off-resonant optical beams can be used to create conservative trapping potentials for neutral atoms. In general, the resulting optical potential created by a laser beam is given by the light intensity dependent AC-Stark shift

$$U_{dip} = -\frac{1}{2\epsilon_0 c} Re[\alpha(\omega)]I(\mathbf{r}). \tag{4.3}$$

Here U denotes the trapping potential, corresponding to the AC-Stark shift, $I(\mathbf{r})$ refers to the spatially varying light intensity of the optical beam, c denotes the speed of light and ϵ_0 defines the electric constant. The polarizability of the atom, which was introduced in section 2.5, is denoted in this formula by α.

The polarizability can be calculated by a semiclassical, approximate model. In this approximation, the atom is treated quantum mechanically as a two-level system interacting with the classical electric field. The dipole trap potential can then be expressed as

$$U_{dip} = -\frac{3\pi c^2}{2\omega_0^3} \left(\frac{\Gamma}{\omega_0 - \omega} + \frac{\Gamma}{\omega_0 + \omega} \right) I(\mathbf{r}) \tag{4.4}$$

where ω_0 denotes the light frequency of the resonant transition in the two-level approximation, Γ denotes the radiative decay rate of the transition and ω refers to the frequency of the dipole trap light [130]. For our experimental dipole trap parameters, in the case of far detuned trapping light in the infrared, the detuning $\Delta = \omega_0 - \omega$ is essentially given by the detuning of the dipole trap light to the strong $^1S_0 \rightarrow {}^1P_1$ transition at $\lambda_0 = 399$ nm.

By using the same approximation, a compact form of the photon scattering rate can be given in the case of a semi-classical approximation of the polarizability

$$\Gamma_{sc} = -\frac{3\pi c^2}{2\hbar\omega_0^3}\left(\frac{\omega}{\omega_0}\right)^3\left(\frac{\Gamma}{\omega_0-\omega}+\frac{\Gamma}{\omega_0+\omega}\right)^2 I(\mathbf{r}). \qquad (4.5)$$

The scattering of photons causes heating of the atoms and scales with $1/\Delta^2$. In contrast to that, the trapping potentials U_{dip} is proportional to $1/\Delta$. Due to this different scaling behavior, it is therefore favorable to choose the detuning of the trap as large as technically possible in order to reduce heating effects while still obtaining sufficiently deep traps for the available light power in the experiment.

Crossed optical dipole trap

In our experiment, the dipole trap potential is realized by two crossed laser beams at a wavelength of $\lambda = 1064\,\text{nm}$. For this wavelength, high power lasers are commercially available and the detuning is sufficiently large to the $^1S_0 \rightarrow\ ^1P_1$ transition at $\lambda = 399\,\text{nm}$. In the experiment we are using a 25 W Nd:YAG laser[6] to produce the optical power of the dipole trap beams. The laser power is split for the two arms of the dipole trap and coupled to a high power fiber with a large mode field diameter[7].

At the experiment table, the light of each fiber is outcoupled and shaped by telescopes to the corresponding beam size that will produce the wanted waists at the atom position. The elliptic, horizontal beam has a waist of $w_h = 153\mu\text{m}$ in the horizontal, and $w_v = 20\mu\text{m}$ in the vertical direction. The maximum power in the horizontal beam path, limited by Brillouin scattering in the fiber, is about $P \simeq 11W$. The vertical dipole trap beam has a spherical beam shape with a waist of $w = 86\mu\text{m}$ and a maximum power of about $P \simeq 10W$. The two dipole trap beams are focused into the main chamber and do intersect at the position of the compressed MOT. Both beams are power stabilized by acusto-optic modulators (AOM) with a frequency difference of 160 MHz in order to avoid interference effects. At the same time, the power can be controlled with the AOM in order to perform the evaporation.

The crossed setup offers the advantage that the atoms can be evaporated in the vertical direction, along the direction of gravitation, by lowering the horizontal dipole trap. At the same time, the vertical dipole trap beam can confine the atoms strongly in the other two directions. This results in a high collision rate and fast and efficient evaporation. Table 4.8 summarizes the dipole trap confinement and trap depth for the case after MOT loading and the case after evaporation when the horizontal beam power was reduced.

Initially, when trapping the atoms of the compressed MOT, most of the optical power (P=11W) is in the horizontal dipole trap arm while the vertical dipole trap arm

---

[6]Innolight Mephisto
[7]NKT Photonics LMA-PM-15

Dipole trap	power hor. DT / vert. DT (W)	trap depth (μK)	conf. freq. $\nu_x/\nu_y/\nu_z$ (Hz)
loading	11/1.3	82	20/103/1432
after evaporation	0.4/6	0.31	22/27/215

Table 4.2: Confinement frequencies, optical power and trap depth of the crossed optical dipole trap before evaporation and after evaporation.

has a power of $P \simeq 1W$. As the trapping against the gravitational force is realized by the horizontal dipole trap this ensures the deepest trap depth and therefore the highest number of trapped atoms from the compressed MOT. Moreover, the power between the two dipole trap arms can be varied with a motorized rotating waveplate in order to rebalance light power from the horizontal dipole trap arm to the vertical one. This allows increasing the confinement of the atomic sample with the vertical dipole trap beam during evaporative cooling.

After loading atoms from the compressed MOT to the optical dipole trap, the evaporation sequence starts. The sequence consists of a 1 s hold time in the trap, in order to damp out a possible sloshing after MOT loading and to let the gas thermalize, followed by a ramp down of the horizontal dipole potential. During the ramp down for about 14 s, the horizontal dipole trap power is exponentially reduced in order to decrease the trapping potential. A cut of the dipole trap potential before and after evaporation is shown in Fig. 4.8. Predominantly, atoms with a kinetic energy higher than the average energy of the atomic sample will leave the trap along the direction of gravity where the potential barrier is lowest. At the same time, elastic collisions thermalize the sample. This process is called evaporative cooling and results in a reduction of the initial temperature of the atomic gas. In this way, evaporative cooling increases the phase space density and allows entering the degenerate regime of quantum gases where the de Broglie wavelength becomes comparable to the inter-particle distance [196].
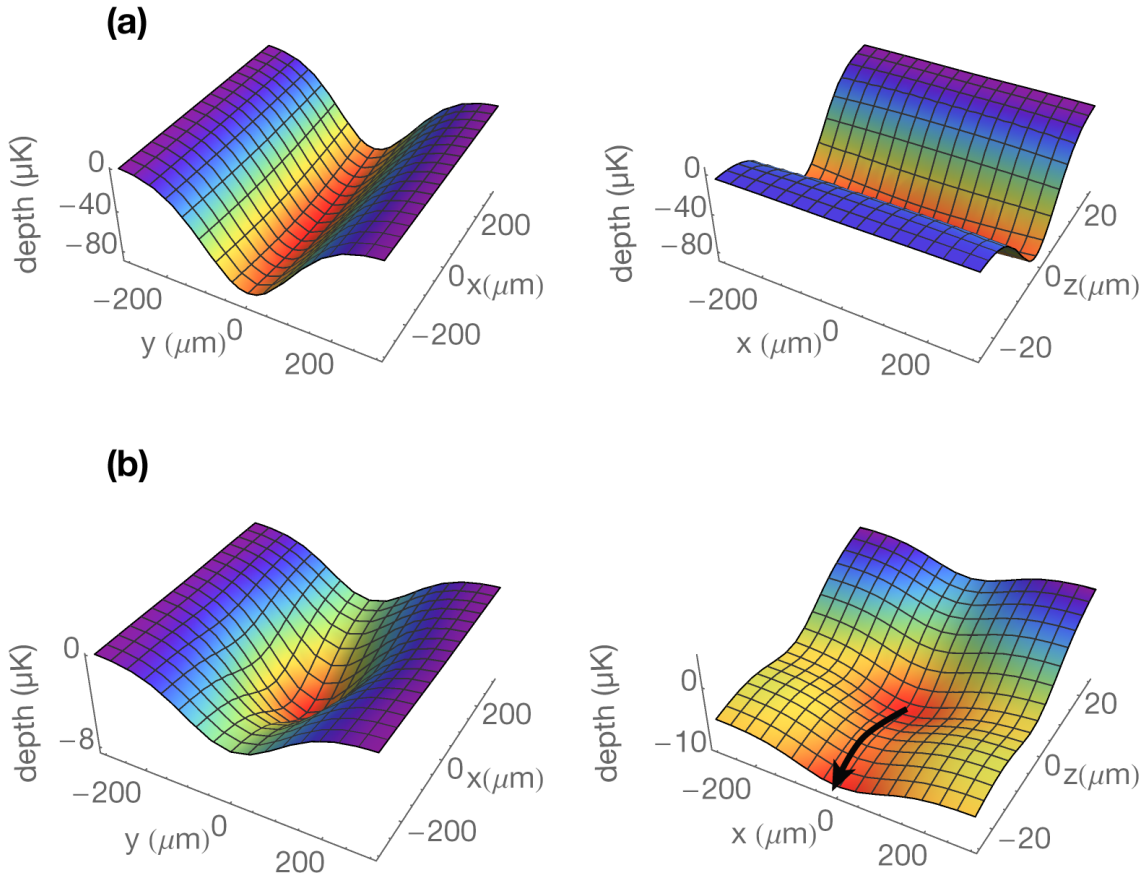
Figure 4.8: Cut through the crossed dipole trap potential along the z-direction (left column) and the y-direction (right column). **(a)** Dipole trap potential at the beginning of the evaporation with $P = 11\,\text{W}$ in the horizontal dipole trap arm and $P = 1\,\text{W}$ in the vertical dipole trap arm **(b)** Dipole trap potential at the end of evaporation with $P = 0.4\,\text{W}$ in the horizontal dipole trap arm and $P = 6\,\text{W}$ in the vertical dipole trap arm. The black error indicates the evaporation channel along the direction of gravity.

Chapter 5

Preparation and characterization of SU(N) Fermi gases

The enlarged spin symmetry in ^{173}Yb requires the ability to detect and manipulate the number of nuclear spin states of the atoms. This is achieved with optical techniques and permits preparing various kinds of spin mixtures. For the isotope ^{173}Yb this allows us to prepare Fermi gases with a varying number of spin states from a single spin component up to six spin components and their individual populations.

In this chapter we will give a brief overview of the preparation, detection and characterization of the SU(N) Fermi gas. Our experimental apparatus allows probing the in-situ density distribution with high resolution and the measurement of the momentum distribution of the atomic sample in time-of-flight. For the in-situ measurements, we use a strongly saturated absorption beam to probe the sample. The resolution of the objective is high enough to access local quantities of the gas, a feature that will become important in chapter 7. Moreover, we will show in this chapter how we detect and count the different nuclear spin states. At the end of this chapter we will present the equation of state of a non-interacting Fermi gas which is used for the characterization of the temperature and the entropy of the SU(3) and SU(6) Fermi gas in the trap.

5.1 Measuring the momentum and density distributions

We use resonant imaging light on the $^1S_0 \rightarrow {}^1P_1$ ($F = 5/2 \rightarrow F' = 7/2$) transition to image the atoms using the absorption imaging technique. The absorption of the atomic sample can be either measured in-situ to probe the density distribution in the trapping potential or after time-of-flight expansion of the atoms from the trap.

5.1.1 In-situ imaging

In-situ imaging allows studying local quantities of trapped quantum gases. With high enough resolution, different phases can be detected. The imaging system described here is based on a high-resolution objective with an optical resolution of about $1.2\,\mu$m that is able to measure locally resolved quantities of the atomic sample as demonstrated in chapter 7. The resolution of the objective does not allow to image individual atoms in the lattice but is high enough to probe spatially varying phases of the atomic sample that extend over a much larger scale of several micrometers.

Recently quantum microscopes were realized with an even higher resolution [29, 30, 197]. These microscopes are able to resolve single atoms in an optical lattice. The imaging in this case is usually done in fluorescence for several hundred milliseconds to about a second. At the same time, the atoms must be cooled for example by Raman sideband cooling during the imaging sequence in order to confine them locally to a single lattice site. This procedure of cooling and imaging is technically very demanding and the requirements on the objective to achieve the required resolution are a lot higher than in our case. Only very recently single site resolved fermions with alkali elements were achieved by using such a technique [198–200].

Due to the high optical density, we decided to image the atoms with a strongly saturated absorption beam that is able to penetrate the dense atomic sample. Moreover, as the interatomic distance of the atoms in the lattice is comparable to the optical wavelength, collective effects during the excitation of the atoms with the imaging light can arise that will lead to a detuning of the imaging transition due to dipolar interactions [201]. This effect can be mitigated by choosing the imaging intensity high enough that the optical transition is power broadened and the detuning effects become negligible.

Saturated absorption imaging

Absorption imaging is a standard technique to image the atoms. The atoms are illuminated by a laser beam that is resonant with a closed optical transition and partially absorb the light. The resulting shadow in the beam is then detected with a CCD camera. The CCD array measures the number of photoelectrons for each pixel, which is directly related to the impinging light intensity $I(x,y)$ on the CCD camera.

The attenuation of the imaging light intensity I can be described by

$$\frac{dI(x,y,z)}{dz} = -\sigma n(x,y,z)I \tag{5.1}$$

$$\sigma = \frac{\sigma_0}{1 + I(x,y,z)/I_{sat}}, \tag{5.2}$$

where $I_{sat} = \hbar\omega^3\Gamma/12\pi c^2$ denotes the saturation intensity of the imaging light, ω denotes the light frequency and Γ the natural linewidth of the imaging transition.
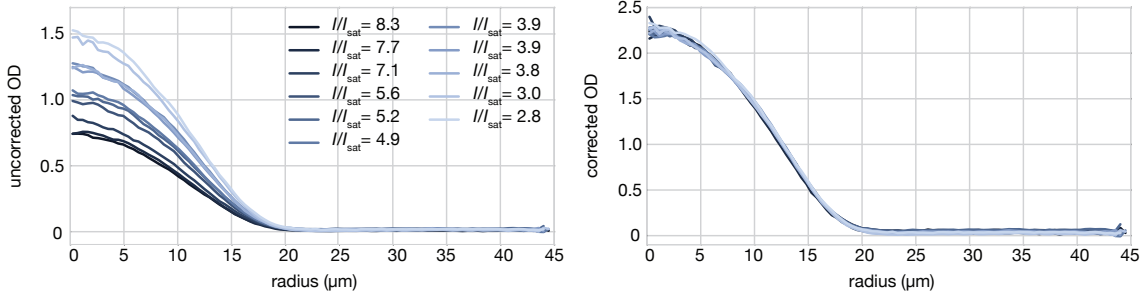
Figure 5.1: Strongly saturated absorption imaging of an atom cloud. (Left) Uncorrected optical density of the cloud, using Eq. 5.3 for different light intensities. (Right) Corrected optical density, using Eq. 5.5, taking the strong saturation of the imaging transition into account. A value of $\alpha \simeq 3.05$ and $\beta \simeq 0.0028$ was found for a $5\,\mu$s pulse duration, which kept the optical density independent of the impinging light intensity.

The optical cross section σ is light intensity dependent and proportional to the resonant optical cross section $\sigma_0 = 3\lambda^2/(2\pi)$ of a two-level system.

In the case of unsaturated absorption imaging, $I \ll I_{sat}$, the optical cross section in Eq. 5.2 is constant and integrating Eq. 5.1 immediately yields the Lambert-Beer law

$$\tilde{n}(x,y) = \int_{-\infty}^{\infty} n(x,y,z)dz = -\frac{1}{\sigma_0}\ln\left(\frac{I_f(x,y)}{I_i(x,y)}\right) = -\frac{1}{\sigma_0}OD, \qquad (5.3)$$

where $I_i(x,y)$,$I_f(x,y)$ denotes the light intensity before and after absorption of the atomic sample and $OD = \ln\left(\frac{I_f(x,y)}{I_i(x,y)}\right)$ defines the optical density of the cloud. It should be noted that the above definitions of I_{sat} and σ are strictly valid only in a two-level system. In our case, the approximation of a two-level system does not hold because different m_F-states in the ground state are populated and we decided to do nuclear spin-insensitive imaging.

Due to the typical high densities when imaging the cloud in-situ, we rely on a strongly saturated imaging beam with $I \gg I_{sat}$. An advantage of this method compared to unsaturated absorption imaging is the fact that the atomic sample does not become optically dense for the limited dynamic range of the CCD camera because enough photons are penetrating the cloud. Other techniques, like phase contrast imaging that do not rely on direct absorption of photons, also exist for imaging optically dense systems but require a phase plate to create a homodyne-like interference pattern on the camera [202, 203]. Phase contrast imaging is actually a standard technique in optical-microscopy to image living cells that are almost transparent to imaging light [204–206].

In the case of strongly saturated absorption imaging, the absorption described by Eq. 5.1 will yield a modified Lambert-Beer law due to the light-intensity-dependent

cross section [207]

$$\tilde{n}(x,y) = -\frac{1}{\sigma^*} \ln \left(\frac{I_f(x,y)}{I_i(x,y)} \right) + \frac{I_i(x,y) - I_f(x,y)}{\sigma^* I_{sat}^*} \tag{5.4}$$

$$= -\alpha \ln \left(\frac{c_f(x,y)}{c_i(x,y)} \right) + \beta(c_i(x,y) - c_f(x,y)). \tag{5.5}$$

where $c_i(x,y)$ $(c_f(x,y))$ denotes the accumulated counts per pixel on the CCD sensor of the camera without (with) absorption of the light from the atomic sample for a given imaging pulse duration. The first term describes the normal unsaturated absorption, while the second term accounts for the intensity dependent optical cross section. Similar to the unsaturated case, we define the optical density of the atomic sample as

$$OD = \ln \left(\frac{c_f(x,y)}{c_i(x,y)} \right) + \frac{\beta}{\alpha}(c_i(x,y) - c_f(x,y)). \tag{5.6}$$

The density is measured by taking two images, one without atoms and one picture with the light impinging on the atoms, which allows us to measure the intensity $I_i(x,y)$ and $I_f(x,y)$. In the equation above, I_{sat}^* and σ^* describe the effective saturation intensity and cross section. Effects like imperfections in the beam polarization, optical pumping effects during imaging together with different Clebsch-Gordan coefficients of the m_F-states and residual magnetic fields will modify the saturation intensity and the optical cross section of an ideal two-level system. Therefore, in the case of saturated absorption imaging the correct values α and β have to be determined. This is done by varying the light intensity and finding the correct ratio α/β that will keep the shape of the atomic cloud and the measured density of the atomic sample independent of the light intensity used, as shown in Fig. 5.1. For the calibration of the absolute optical cross section, we then rely on the method described in section 7.2.

In order to achieve a sufficiently high imaging resolution two effects should be considered. The pulse duration of the imaging pulse should not be too long in order to avoid blurring of the image due to the motion of the atoms. The atomic motion is diffusive in the image plane during the pulse duration due to the random direction of scattered photons. As opposed to that, we expect a ballistic expansion perpendicular to the image plane, along the image beam direction. The diffusive motion allows us to image the atomic sample long enough to obtain a strong absorption signal and retain the imaging resolution of the objective. In the experiment we decided to use a maximum image pulse duration of 5μs with an intensity of about $I = 10 - 15 I_{sat}$. For this pulse duration, the atomic sample will move about $6\,\mu$m along the imaging beam direction. This distance can be compared to the depth of field (DOF) of the imaging system, which determines the maximum distance that an object can be displaced from the object plane while still being imaged sharply. For a microscope,

the DOF can be expressed as

$$d_{DOF} = d_{wave} + d_{geom} = n \left(\frac{\lambda}{NA^2} + \frac{c}{M \cdot NA} \right) \qquad (5.7)$$

where λ denotes the imaging wavelength, n is the refractive index, NA is the numerical aperture of the imaging system, M is the magnification of the imaging and c denotes the pixel size of the CCD camera. The first term accounts for the axial imaging resolution, which is determined by wave optics, and describes the limited resolution due to the diffraction limit of the imaging system. The second term accounts for the blurring of the image when the object is displaced from the focus plane using geometrical optics [208]. For the parameters of our imaging system with $NA = 0.27$, $c = 13\,\mu m$ and $M = 28$ (see section about calibrating the imaging system), we obtain $d_{DOF} = 7.2\,\mu m$ which is comparable to the distance that the atomic sample will move along the beam direction during the imaging pulse. Therefore, a blurring of the image due to atoms moving through the focus should not be a major problem.

When considering the movement of the atoms within the image plane, which is diffusive, we expect a movement of only $400\,nm$ during the pulse duration, which is small compared to our optical resolution.

While the motion of the atoms during the imaging pulse is one aspect, it should also be noted that the acceleration of the atoms due to the absorption of photons will create a Doppler shift that might bring the atomic sample out of resonance from the imaging transition. This would lead effectively to an underestimation of the measured density. Care has to be taken therefore that the number of absorbed photons is still low enough to avoid a strong Doppler shift with respect to the linewidth of the imaging transition. The maximum number of scatted photons before the Doppler velocity is reached can be estimated by $n_{dop} = \Gamma m/(\hbar k^2)$, where Γ is the linewidth, m the atom mass and k the wavevector of the imaging light. For the chosen imaging pulse time of $5\,\mu s$ we expect a scattering of 500 photons for the imaging linewidth $\Gamma = 2\pi \times 29.1\,MHz$, which is small compared to $n_{dop} = 2000$ photons that can be scattered before Doppler velocity is reached.

Calibrating the imaging system

In order to determine the image magnification of the imaging system we use an in-situ density modulation pattern with known periodicity. For this, we load a degenerate quantum gas into a bichromatic lattice, where one lattice is running at wavelength $\lambda \simeq 759$ nm and the other lattice at a wavelength $\lambda \simeq 670\,nm$. The resulting modulation of the combined potential of the two lattices has a periodicity of $2.84\,\mu m$. By fitting the expected modulation pattern of the bichromatic lattice to the measured density modulation, as shown in Fig. 5.2, we can determine the corresponding size of a camera pixel in the object plane and the overall image magnification.
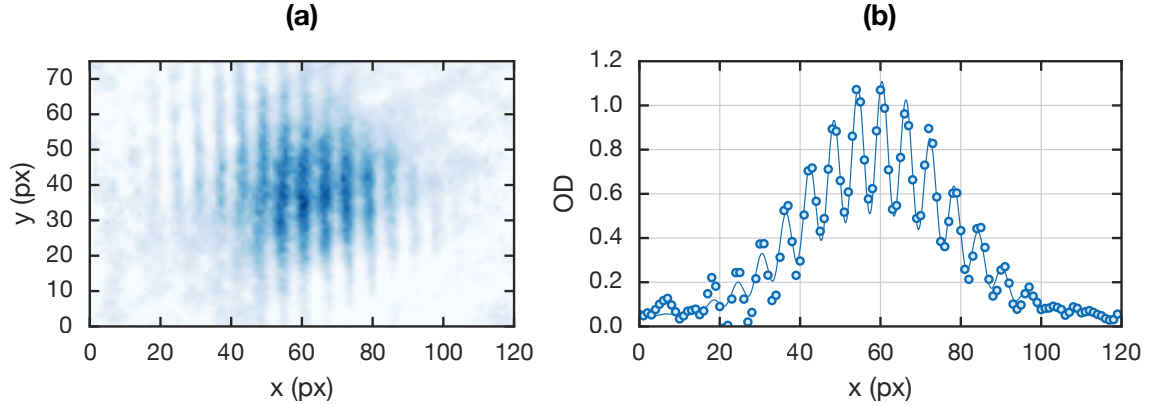
Figure 5.2: Density modulation pattern used for calibrating our imaging system. **(a)** In-situ density modulation created by loading the atoms into a bichromatic lattice running at $\lambda_1 = 670\,\text{nm}$ and $\lambda_1 = 759\,\text{nm}$. **(b)** Optical density, averaged over the y-direction of the atomic sample and fitted modulation pattern (solid line). The fit yields a distance of 6 pixel for the modulation, corresponding to an image magnification of $0.47\mu\text{m/px}$.

Determining the imaging resolution

To determine the actual resolution of the imaging system we use a method described in [209] to measure the image response function with a thermal atomic gas. The image response function $\mathcal{M}^2(\mathbf{k})$ in 2D gas is related to the density fluctuation $\delta\tilde{n}(\mathbf{k}) \equiv \tilde{n}(\mathbf{k}) - \langle\tilde{n}(\mathbf{k})\rangle$, where $\langle\tilde{n}(\mathbf{k})\rangle$ denotes the mean column density in momentum space with $\mathbf{k} = \frac{2\pi}{L}(l_x, l_y)$, L is the linear image size and l_x, l_y are integers. The density fluctuations can be expressed as

$$\langle|\delta\tilde{n}(\mathbf{k})|^2\rangle = N_p S(\mathbf{k})\mathcal{M}^2(\mathbf{k}). \tag{5.8}$$

Here N_p denotes the total atom number and $S(\mathbf{k})$ is the static structure factor of the gas. The structure factor describes the correlations between the atoms and contains the statistical information of the quantum gas [210, 211].

For a thermal gas, there are no correlations between the atoms and the structure factor becomes momentum-independent and one. If the vertical extension of the cloud is smaller than the focus depth, we can use Eq. 5.8 to characterize the imaging system. The image response function including spherical aberration and astigmatism can be modeled in order to quantify aberrations and the resolution.

When the imaging light passes through the objective, the phase as well as the amplitude are distorted by imperfections of the optics. This can be described by an
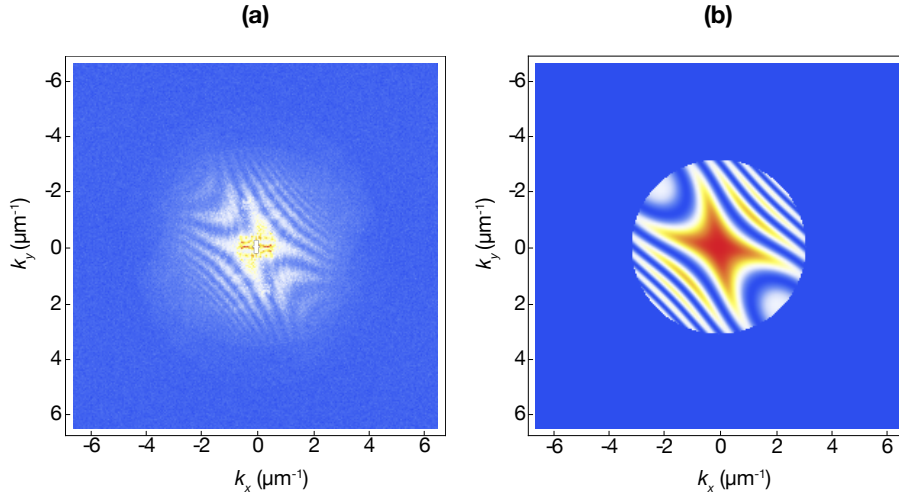
Figure 5.3: **(a)** Measured image response function of a thermal gas obtained by taking 350 images and taking the average of the squared modulus of the density fluctuations of each image from the average density of all images. **(b)** Simulated image response function used to characterize the imaging system with modeled spherical aberrations and astigmatism.

exit pupil function $p(r, \theta)$ with

$$p(r, \theta) = U(r/a, \theta) \exp^{i\Theta(r/a, \theta)} \tag{5.9}$$

$$U(\rho, \theta) = H(1 - \rho)e^{-\rho^2/\tau^2} \tag{5.10}$$

$$\Theta(\rho, \theta) = S_0\rho^4 + \alpha\rho^2 \cos(2\theta - 2\phi) + \beta\rho^2, \tag{5.11}$$

where r, θ are cylindrical coordinates. $U(\rho = r/a, \theta)$ determines the transmittance through the objective with an aperture a, τ determines the finite incidence angle of the transmitted light and Θ models the wavefront aberration. For the wavefront aberrations of the objective, only a few parameters are important. Spherical aberrations are modeled with the parameter S_0, ϕ accounts for astigmatism caused for example by the optical axis being misaligned and β accounts for defocusing when the atoms move through the focus during the imaging pulse.

Fig. 5.3(a) shows the measured image response function obtained by averaging 350 images of a thermal gas of ^{173}Yb in the dipole trap. The vertical extension of the gas is calculated to be about $3\,\mu$m for the used trap configuration in this measurement. To match the measured image response function we use Eq. 5.9 to model a pupil function with aberrations. The parameters for the aberrations of this model were determined manually. Fig. 5.3(b) shows the modeled image response function and the corresponding point spread function (PSF) is shown in Fig. 5.4(a). The point spread function can be compared to the one of a diffraction-limited imaging system to estimate the imaging resolution. For a diffraction-limited system, the PSF is given by
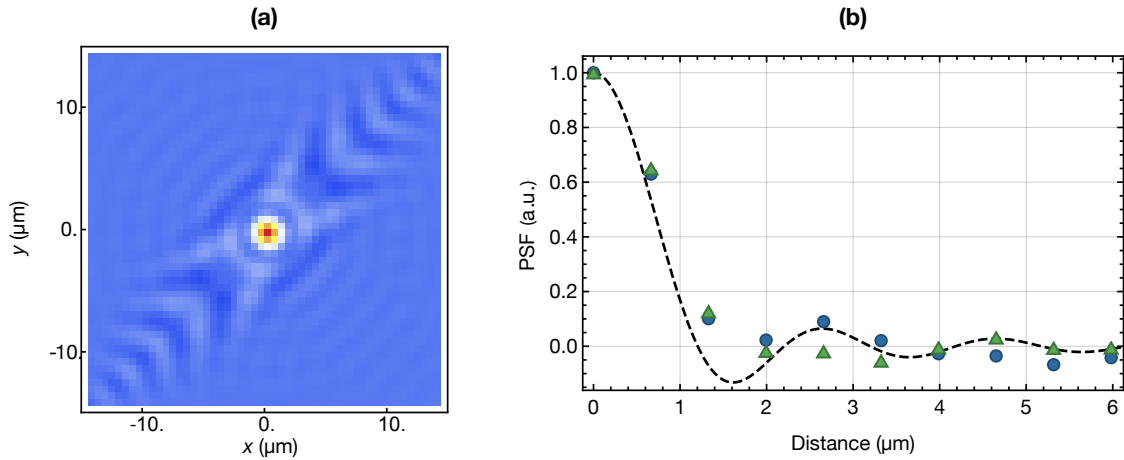
Figure 5.4: **(a)** Point spread function (PSF) of the image response function shown in 5.3(b) **(b)** Cut along the x-axis (blue points) and y-axis (green points) of the point spread function. The dashed line denotes the PSF of a diffraction-limited system with an imaging resolution of $1.2\,\mu$m.

$PSF(\rho) = J_1(\rho)/\rho$ with J_1 being the Bessel function of first kind, $\rho = 3.8317r/r_0$ and r_0 denoting the imaging resolution. A common definition for the optical resolution r_0 is to define the first zero of the Bessel function as the imaging resolution, which is the Rayleigh criterion. The dashed line in Fig. 5.4(b) illustrates the PSF of a diffraction-limited imaging system with an optical resolution of $r_0 = 1.2\,\mu$m, which is approximating the PSF of the imaging system with aberrations quite well.

5.1.2 Time-of-flight imaging

As opposed to in-situ imaging, time-of-flight (TOF) imaging allows measuring the momentum distribution of the atomic sample. When all the trapping potentials are switched off instantaneously, the cloud will expand and fall under the influence of gravity. After a sufficiently long expansion time, when the width of the cloud is large compared to its initial size, the cloud width will directly reflect the initial in-trap momentum distribution of the atoms, if interactions between the atoms can be neglected. For shorter expansion times however, the initial could width has to be taken into account. When using TOF imaging, the density of the atomic sample after expansion is usually sufficiently low for long expansion times and a high optical density of the atomic sample is therefore not a major concern as opposed to in-situ imaging.

We use time-of flight imaging in our experiment for counting the spin population of the Fermi gas after applying the optical Stern-Gerlach method to separate the spin states as well as for measuring the momentum distribution of the atomic sample.
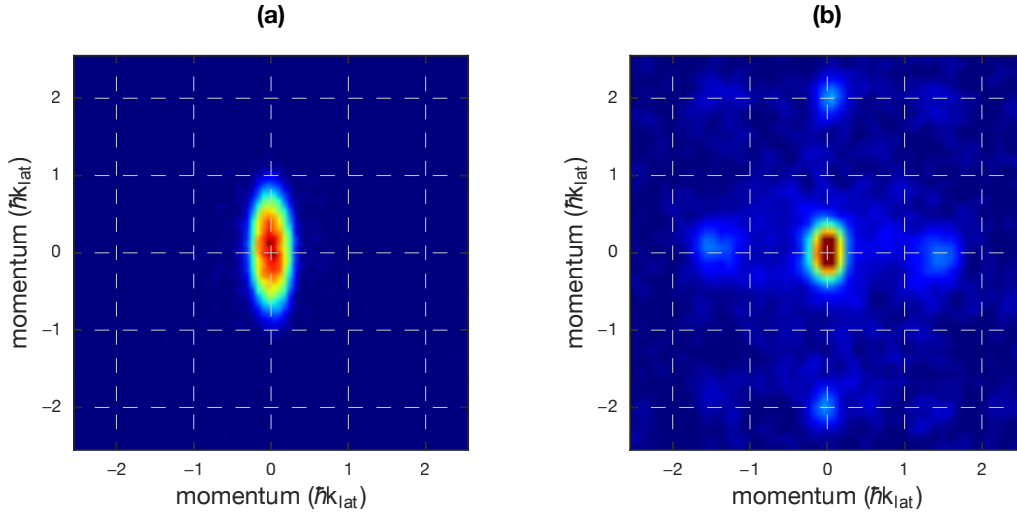
Figure 5.5: Momentum distribution of an expanding BEC with time-of-flight imaging (a) Momentum distribution of a BEC of ^{174}Yb in the optical dipole trap. The aspect ratio of the cloud corresponds to the momentum distribution given by the inverse Thomas-Fermi radii in the trap. (b) Momentum distribution of a superfluid in a 3D optical lattice. The interference peaks have a spacing of $2\hbar k_{lat}$ but the horizontal lattice is imaged under an angle of $45°$.

Prominent examples for time-of-flight imaging include the study of the momentum distribution of a Bose Einstein condensate, which expands anisotropically from an anisotropic trap as shown in Fig. 5.5(b). Moreover, in lattice experiments with bosonic quantum gases, this method reveals the characteristic superfluid to Mott transition, which is accompanied by the disappearance of characteristic interference peaks. In the superfluid state the atoms are delocalized and occupy mainly the quasi-momentum state $q = 0$. In this regime, the momentum distribution will show interference peaks with a spacing of $2\hbar k_{lat}$ as illustrated in Fig. 5.5(b). As opposed to that, in the Mott insulating state, the atoms are effectively localized and occupy several momentum states. The Mott insulator for Bose gases is therefore accompanied by a loss of the phase coherence between the atoms at different lattice sites and the momentum distribution after TOF expansion will not show any sharp feature but a broad peak [212–214].

5.2 Nuclear spin detection and manipulation

5.2.1 Spin-selective detection

In order to image different spin state populations of the atoms, e.g. after optical pumping, a method to separate the spin components is needed. For alkali elements,

this is usually realized by a Stern-Gerlach experiment, which splits the different spin components in a magnetic gradient field. The idea is to use the m_F-selective force to separate the atoms spatially during time-of-flight in a magnetic gradient field and count the different spin-state populations when imaging.

Optical Stern-Gerlach method

Due to the absence of a total electronic angular momentum in the ground state of ytterbium, the magnetic Stern-Gerlach scheme is not applicable, as the required magnetic field gradient for separating the nuclear spin states is impractical. Therefore, we use an optical Stern-Gerlach (OSG) scheme in our experiment to achieve the required splitting of the nuclear spin components. To implement the OSG method, a circularly polarized beam is used that is close detuned to an optical transition [215, 216]. The intensity gradient of the beam will cause a dipole force that is m_F-dependent due to the different line strengths of the optical transition [130].

Fig. 5.6(b) shows the relative strengths of the nuclear spin-dependent forces. This calculation was done for a 800MHz blue detuned OSG beam relative to the $^1S_0 \rightarrow {}^3P_1(F = 5/2 \rightarrow F = 7/2)$ hyperfine transition. Due to the varying Clebsch-Gordon coefficients, the circular polarized light causes a m_F-dependent force, which depends on the intensity gradient and detuning of the beam. For the m_F-dependent OSG force not only the $F = 5/2 \rightarrow F = 7/2$ transition but also contributions from other hyperfine transitions have to be considered for the individual m_F-states. As the detuning of the OSG beam is small compared to the hyperfine splitting, the nuclear spin states will be red-detuned for some hyperfine transitions. This results for example in a small negative net force for the $m_F = -5/2$ state as opposed to the other states because the contributions of the red-detuned hyperfine transitions will dominate in this case.

In the experiment, the OSG force is realized by a beam with a waist of 75 μm and an 800 MHz blue detuning from the $^1S_0 \rightarrow {}^3P_1(F = 5/2 \rightarrow F = 7/2)$ transition. The optical power of this beam is about 40 mW. As shown in Fig. 5.6(a), the center of the OSG beam is slightly displaced from the position of the atoms in the trap to the top along the vertical direction. This is necessary to push the atoms down, along the gravitation direction, during time-of-flight. In order to separate the atoms, the beam is activated during the release of the atoms from the trap. The OSG beam will create a m_F-dependent force that will additionally accelerate the atoms during the expansion. The longest pulse duration is about 4 ms after which the atoms will not experience a OSG force anymore as they have left the beam by that time. The additional momentum, caused by the nuclear spin dependent force, will lead to a spatial separation of the different spin components after an expansion time of about 15 ms. Fig. 5.6(c) shows an SU(6) Fermi gas after time-of-flight expansion with the optical Stern-Gerlach method. All the six spin components of the Fermi gas can be resolved spatially. The actual curvature of the cloud arises due to the
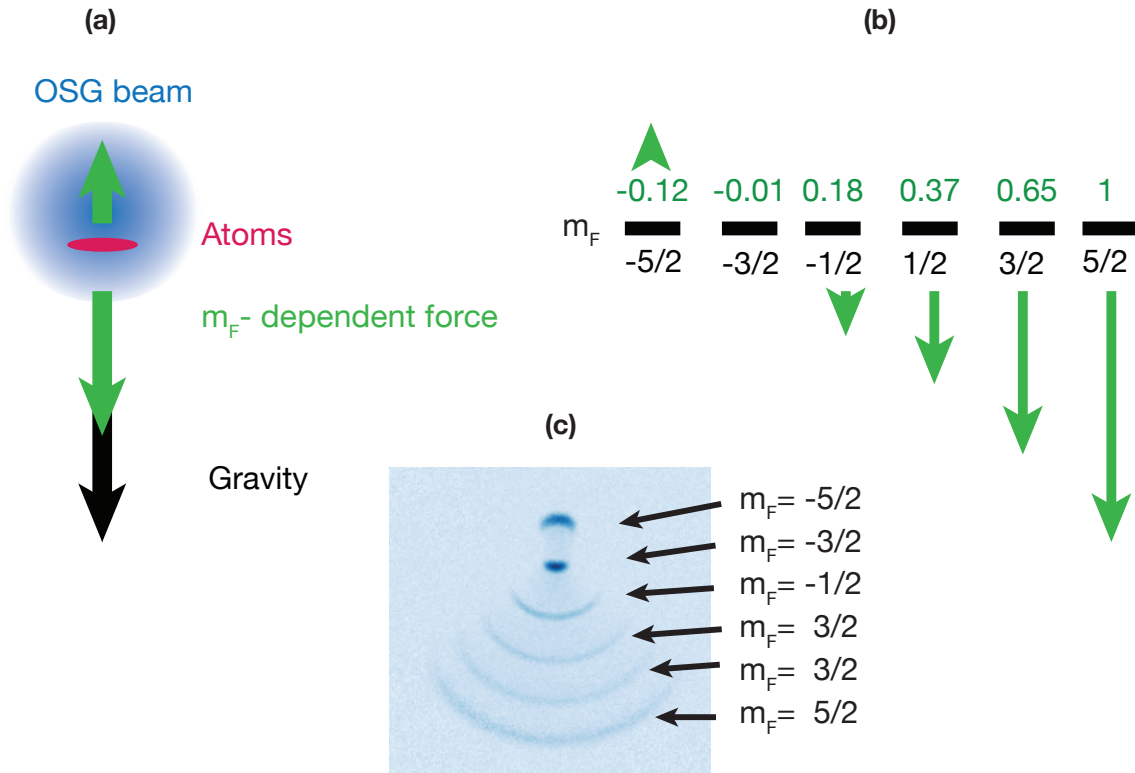
Figure 5.6: Optical Stern-Gerlach (OSG) method to separate the nuclear spin components. **(a)** Illustration of the OSG beam configuration that is used in the experiment to split the m_F-states. A blue detuned beam is employed for the OSG pulse, which is aligned slightly on the top of the atoms to create a nuclear spin dependent force along the vertical direction. **(b)** Relative ratios of the m_F-selective forces with respect to the $m_F = 5/2$ state for the specific detuning used in the experiment. **(c)** Absorption image of the atomic sample after free expansion. The picture shows the optical density of the cloud after an OSG pulse of 3 ms and 12 ms time-of-flight expansion. The separation of the six different m_F-states in ^{173}Yb becomes visible. The curvature of the different rings is caused by the finite OSG beam size that creates a radial force.

finite beam size as the OSG beam is pushing the atoms radially away from the center of the beam. We decided for a blue detuned OSG beam with respect to the $^1S_0 \rightarrow\ ^3P_1(F = 5/2 \rightarrow F = 7/2)$ transition as this configuration offers an advantage over a red detuned beam. The finite size of the atom cloud is compressed with a blue detuned OSG beam compared to the free expansion of the atoms, as atoms that are closer to the OSG beam center are accelerated more than those atoms that are further away. This leads to a compression of the cloud width of the atoms in the same m_F-state after time-of-flight expansion.

5.2.2 State preparation

To produce various kinds of spin mixtures of ^{173}Yb we use optical pumping techniques. The atoms can either be pumped between neighboring m_F- states or individual m_F-states can be depleted selectively by spilling those atoms out of the trap. The idea of the latter method is to remove certain nuclear spin components in a shallow optical trap by scattering a few photons and allow the Fermi gas to thermalize afterwards. This method offers the advantage that the spin balancing can be better controlled than with optical pumping under the assumption that the initial SU(6) Fermi gas which is loaded from the magneto-optical trap is sufficiently spin-balanced.

Optical pumping

Our optical pumping scheme relies on the possibility to split the m_F-states of the $^3P_1$ excited state. The splitting of the $^1S_0 \rightarrow\ ^3P_1$ transition in a magnetic field is only determined by the splitting of the $^3P_1$ state and amounts to 596.6 kHz/(G m$_F$) for ^{173}Yb on the stretched hyperfine transition $F = 5/2 \rightarrow F' = 7/2$. We use the magnetic coils and the light beams of the magneto-optical trap (MOT) to perform the pumping. By switching the coils into Helmholtz configuration we create a homogeneous magnetic field of about $B \simeq 18$ G which splits the m_F-states by several MHz. The narrow natural linewidth $\gamma = 182$ kHz of the $^1S_0 \rightarrow\ ^3P_1$ transition makes it possible to selectively address the optical transitions of the different m_F-states with polarized light. The optical pumping with this scheme is performed after loading the atoms from the magneto-optical trap to the dipole trap, right at the beginning of the evaporation process.

Fig. 5.7 shows the m_F-selective addressing and pumping with the $^1S_0 \rightarrow\ ^3P_1$ intercombination line. Depending on the laser detuning, individual m_F-states can be pumped to neighboring states by using circular polarized light. A variable sequence of pumping pulses, in addition to the m_F-dependent selectivity, gives full control for preparing any kind of spin mixture. As an example, Fig. 5.8 illustrates three different pumping schemes used in the experiment to achieve spin-balanced two and three-component Fermi gases.
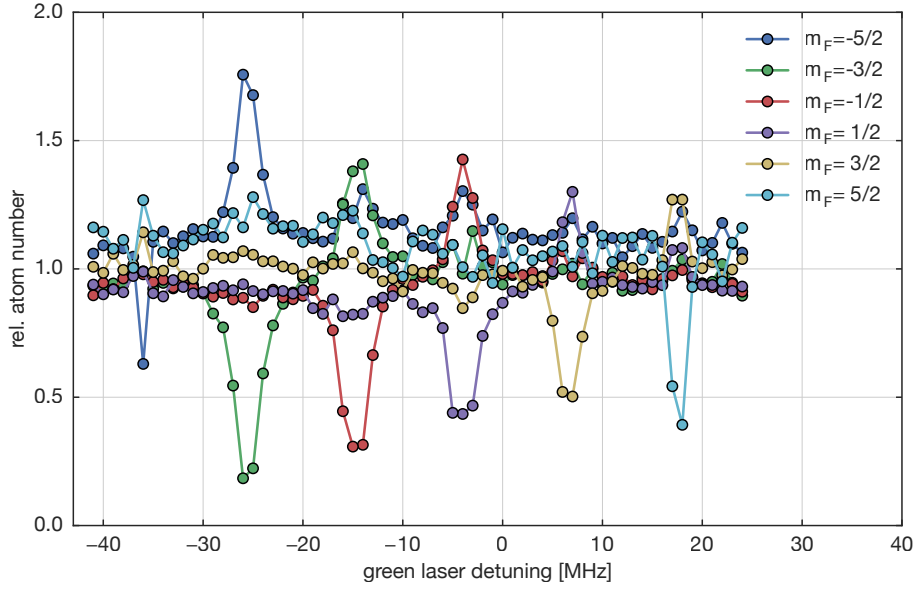
Figure 5.7: Optical pumping on the $^1S_0(F = 5/2) \rightarrow {}^3P_1(F = 7/2)$ transition with σ^- light. A magnetic field of $B = 18\,\text{G}$ is used to split the different m_F-states to pump selectively. The figure shows the relative decrease/increase in the atom number for each m_F-state as a function of the laser detuning when pumping individual m_F-states to neighboring states.
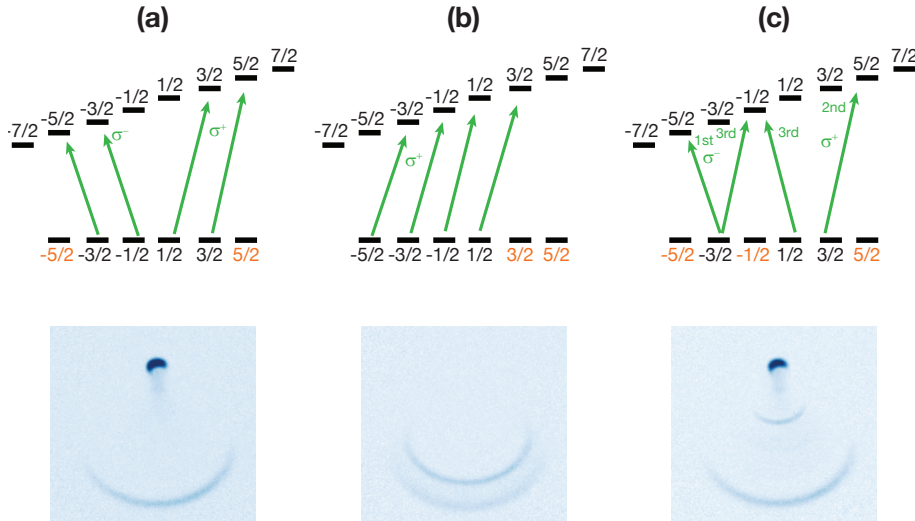

Figure 5.8: Upper row: Illustration of different optical pumping sequences on the $^1S_0 \rightarrow {}^3P_1$ transition. The schemes show different ways for producing balanced spin-mixtures with two and three nuclear spin components for ^{173}Yb. (a) SU(2) gas with $m_F = \pm 5/2$ (b) SU(2) gas with $m_F = 5/2\,\&\,3/2$ (c) SU(3) gas with $m_F = \pm 5/2, -1/2$ Bottom row: Separation of the spin mixtures with the optical Stern-Gerlach method for the different pumping sequences.
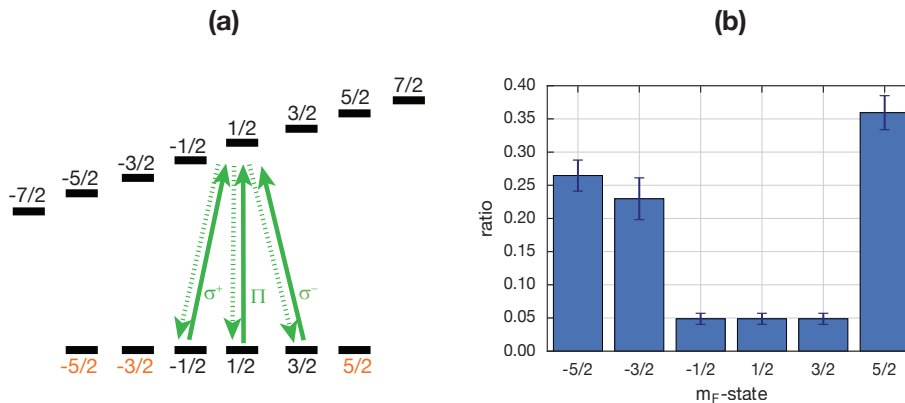
Figure 5.9: Illustration of an optical scheme for the preparation of a three-component Fermi mixture. **(a)** A combination of $\sigma^\pm$ and π-light is used to remove the three central m_F-states for the creation of an SU(3) Fermi gas. A magnetic field is applied for m_F-selective addressing. By driving the corresponding optical transitions for the individual m_F states a few scattered photons are enough to push out the atoms from a shallow trap **(b)** Scan of the residual population after creating a three-component Fermi gas. The error bars denote the standard deviation of the plotted fraction. The plotted residual fraction is only an upper estimate due to possible off-resonant addressing of other m_F-states during the spectroscopy.

The preparation schemes for producing the different spin mixtures assume a spin balanced SU(6) gas. The initial spin balancing of the Fermi gas is ensured by the diabatic magnetic field switching of the magneto-optical trap when transferring the atoms to the optical dipole trap. This switching of the coils will project each nuclear spin state into a superposition of spin states that will eventually dephase due to inhomogeneities for example in the magnetic field. In this way, a possible spin imbalance of the atoms in the magneto-optical trap will get scrambled during evaporation in the optical dipole trap.

Push beam

Spin balanced mixtures, especially three-component ones, can be created by removing atoms in certain nuclear spin states from the trap after evaporation. In this scheme, the splitting of the m_F states is also realized by a magnetic field. With this method a three-component spin mixture can be produced by using a combination of $\sigma^\pm$ and π-light which will deplete three adjacent m_F-states (e.g $m_F = \pm 5/2$ and $m_F = -3/2$). If the trapping potential is sufficiently shallow, only a few scattered photons are enough to spill out the atoms from the trap in an m_F-selective way, as depicted in Fig. 5.9. The preparation of the spin mixture is performed after evaporation, when the optical dipole trap has a depth of about $k_B \times 300\,\mathrm{nK}$ corresponding to a trap

depth of $V = 2E_r$ at a wavelength $\lambda = 556\,\text{nm}$. Therefore, two scattered photons are on average enough to spill out an atom from the trap. The Fermi gas is then allowed to thermalize and cool for about 10 seconds. This method is used for the state preparation of the SU(3) gas in the measurement, which is studied in chapter 7.

5.3 Thermometry of Fermi gases

To quantify temperature and entropy of the SU(N) Fermi gas after preparing the spin mixture and after all optical cooling, we measure the in-trap density profile of the atomic sample. The density profile of the atomic sample allows us to perform thermometry. Therefore, we will derive the particle number and entropy of harmonically trapped and homogeneous Fermi gases as a function of temperature and chemical potential. The results derived for the homogeneous Fermi gas will become relevant in chapter 7 to fit the equations of state of the Fermi-Hubbard model in the weakly interacting regime.

In the case of negligible interactions, the atomic sample is well described by an ideal Fermi gas. For an ideal Fermi gas, the average occupation of the eigenstates with energy ϵ_i of the Hamiltonian is given by the Fermi-Dirac distribution

$$F(\epsilon_i) = \frac{1}{e^{(\epsilon_i - \mu)/k_B T} + 1}, \tag{5.12}$$

where T determines the temperature of the Fermi gas and μ denotes the chemical potential, which controls the atom number. This formula holds for a single-component Fermi gas but can be generalized to N spin components by a factor N in front of $F(\epsilon)$. At zero temperature, the lowest energy eigenstates are all occupied up to the Fermi energy E_F and the Fermi-Dirac distribution becomes a step function with

$$F(\epsilon_i) = \begin{cases} 1 & \text{for} \quad \epsilon_i \leq E_F \\ 0 & \text{for} \quad \epsilon_i > E_F. \end{cases} \tag{5.13}$$

The Fermi temperature is given by $T_F = (E_F - \epsilon_0)/k_B$ with ϵ_0 being the lowest energy of the eigenstates. Often, the fugacity $z = e^{\mu/(k_B T)}$ is introduced to characterize the degeneracy of the quantum gas.

Harmonically trapped Fermi gas

When the kinetic energy of the atoms is bigger than the distance of the energy levels ϵ_i, it is convenient to consider a continuous energy spectrum with a density of states to calculate thermodynamic quantities. For a Fermi gas trapped in a 3D harmonic potential

$$V(x, y, z) = \frac{1}{2}m(\omega_x^2 x^2 + \omega_y^2 y^2 + \omega_z^2 z^2) \tag{5.14}$$
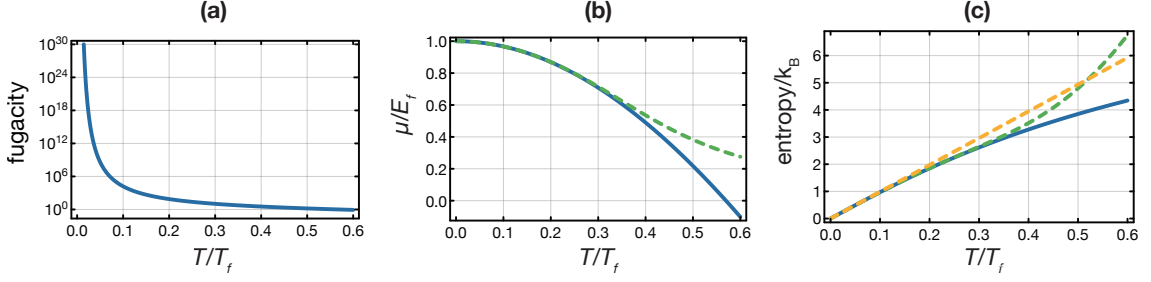
Figure 5.10: Thermodynamic quantities as a function of temperature of a spin-polarized Fermi gas for $N_p = 30000$ atoms and $\bar{\omega} = 2\pi \times 49.5$Hz. **(a)** fugacity **(b)** chemical potential (blue curve) and the approximate solution using Eq. 5.19 (green dashed curve) **(c)** entropy per particle (blue curve). The yellow dashed curve shows the Sommerfeld expansion $S/(N_p k_B) = \pi^2 T/T_F$ and the green dashed curve shows the series expansion by using Eq. 5.21.

the density of states with energy ϵ is given by

$$g_{3D} = \frac{\epsilon^2}{2\hbar^3 \bar{\omega}^3} = A\epsilon^2 \tag{5.15}$$

with $\bar{\omega} = (\omega_x \omega_y \omega_z)^{1/3}$ being the mean trap frequency.

We can use the density of states in order to give the grand potential for an ideal Fermi gas [155]

$$\Omega = k_B T \int_0^\infty d\epsilon \, g_{3D} \ln(1 - F(\epsilon)). \tag{5.16}$$

The integral can then be simplified by partial integration to

$$\Omega = -\frac{A}{3} \int_0^\infty d\epsilon \, \epsilon^3 F(\epsilon) = 2A(k_B T)^4 \mathrm{Li}_4\left(-e^{\frac{\mu}{k_B T}}\right), \tag{5.17}$$

where Li denotes the polylogarithmic function. By using the grand potential, a relation between the atom number N_p and the chemical potential of the gas is obtained

$$N_p = -\frac{\partial \Omega}{\partial \mu} = \int_0^\infty d\epsilon \, g_{3D}(\epsilon) F(\epsilon) = -2A(k_B T)^3 \mathrm{Li}_3\left(-e^{\frac{\mu}{k_B T}}\right) \tag{5.18}$$

$$\approx \frac{A}{3}\left(\pi^2 (k_B T)^2 \mu + \mu^3\right). \tag{5.19}$$

With Eq. 5.17, it is possible to calculate the entropy of the Fermi gas

$$S = -\frac{\partial \Omega}{\partial T} = 2A(k_B T)^3 \left[\mu \mathrm{Li}_3\left(-e^{\frac{\mu}{k_B T}}\right) - 4k_B T \mathrm{Li}_4\left(-e^{\frac{\mu}{k_B T}}\right)\right] \tag{5.20}$$

$$\approx \frac{7}{45} A k_B^4 \pi^4 T^3 + \frac{1}{3} A k_B^2 \pi^2 T \mu^2. \tag{5.21}$$

82

In Eq. 5.19 and Eq. 5.21 the polylogarithm $\mathrm{Li}_s(-z)$ was expanded in a series, which is a good approximation for fugacities $z \gg 1$ [217]. We can use this series expansion with $\mu \approx (3N/A)^{1/3}$ to lowest order and $T_F = \mu(T=0)/k_B = 1/k_B(3N/A)^{1/3}$ to give an approximation for the entropy S

$$S \approx k_B N_p \pi^2 \frac{T}{T_F} + \mathcal{O}(T^3),\tag{5.22}$$

which is the Sommerfeld expansion. To lowest order, the entropy of an ideal Fermi gas is directly proportional to the reduced temperature T/T_F. By substituting the expression for T_F into Eq. 5.18 we also obtain a relation of the fugacity with the reduced temperature that describes the degeneracy of the gas

$$Li_3(-z) = -\frac{1}{6(T/T_F)^3}.\tag{5.23}$$

Homogeneous Fermi gas

Although the Fermi gas is evaporated in a harmonic trap, it is sometimes useful to study the case of a homogeneous Fermi gas in a box potential. This is for example relevant when using local density approximation, where the spatially varying potential is divided into several boxes, each of constant atomic density, that possess different chemical potentials. The density of states in a three-dimensional box potential with volume V is given by

$$g_{box} = \frac{2\pi(2m)^{3/2}V}{h^3}\sqrt{\epsilon}\tag{5.24}$$

where m denotes the mass of the particle. By following the same ansatz as in Eq. 5.16, we obtain for the density of a homogeneous (single component) Fermi gas

$$N_p = -\left(\frac{mk_{\mathrm{B}}T}{2\pi\hbar^2}\right)^{3/2} V \,\mathrm{Li}_{3/2}\left(-e^{\mu/k_{\mathrm{B}}T}\right)\tag{5.25}$$

and for the entropy

$$S = \sqrt{2(\pi k_B m)^3 T}\left[2\mu\mathrm{Li}_{3/2}\left(-e^{\mu/k_{\mathrm{B}}T}\right) - 5k_B T\mathrm{Li}_{5/2}\left(-e^{\mu/k_{\mathrm{B}}T}\right)\right]/h^3.\tag{5.26}$$

We will use Eq. 5.25 in section 7.3 for the fit of the equation of state in the weakly interacting regime of the Fermi-Hubbard model.

5.3.1 Local probing of trapped Fermi gases

With the thermodynamic relations derived in the previous section, we can perform thermometry of the trapped Fermi gas. The reduced temperature T/T_F is an important observable for the characterization of the gas, as it characterizes its

degeneracy. As shown in Eq. 5.22, thermodynamic quantities like the specific entropy directly scale with the reduced temperature to first order. The temperature of the gas is obtained by a Fermi fit to the density distribution. Due to special scaling relations in the case of a harmonically trapped gas, we will see that it is not important whether the fit is performed after expansion from the trap or in-situ.

The density profile of the Fermi gas can be obtained by using local density approximation (LDA), which is a good description for the typical large systems of several thousand atoms as realized in experiments [218]. In LDA, the heterogeneous system is described by a locally homogeneous system. This is realized by replacing the chemical potential μ with $\mu = \mu_0 - V(x, y, z)$ where $V(x, y, z)$ defines the trapping potential and μ_0 is the chemical potential at the center of the trap. LDA is justified when the relevant energy scale is much larger than the single-particle oscillator energy, e.g. $\mu_0 \gg \hbar\omega_{x,y,z}$. When treating the trapped Fermi gas in LDA, we can use Eq. 5.25 to obtain

$$n(x, y, z, T) = -\left(\frac{mk_{\mathrm{B}}T}{2\pi\hbar^2}\right)^{3/2} \mathrm{Li}_{3/2}\left(-e^{\frac{1}{k_{\mathrm{B}}T}(\mu_0 - \frac{1}{2}m(\omega_x^2 x^2 + \omega_y^2 y^2 + \omega_z^2 z^2))}\right) \tag{5.27}$$

where we substituted μ with $\mu = \mu_0 - V(x, y, z)$.

In the case of a harmonically trapped Fermi gas, a scaling relation of the density with time t after expansion exists [219]

$$n(x, y, z, t) = \frac{1}{\gamma_x(t)\gamma_y(t)\gamma_z(t)} n(x/\gamma_x(t), y/\gamma_y(t), z/\gamma_z(t)) \tag{5.28}$$

with $\gamma_i(t) = \sqrt{1 + \omega_i^2 t^2}$. This scaling relation, together with Eq. 5.27, yields for the measured column density $\tilde{n}(x, y)$ [1]

$$\tilde{n}(x, y) = \int_{-\infty}^{\infty} dz\, n(x, y, z, t) = K_1 \mathrm{Li}_2\left(-e^{\frac{1}{k_{\mathrm{B}}T}(\mu_0 - (\frac{x^2}{2\sigma_x^2} + \frac{y^2}{2\sigma_y^2}))}\right) \tag{5.30}$$

$$= A\mathrm{Li}_2\left(-ze^{-\frac{(x-x_0)^2}{2\sigma_x'^2} - \frac{(y-y_0)^2}{2\sigma_y'^2}}\right) / \mathrm{Li}_2(-z) \tag{5.31}$$

$$K_1 = \frac{-N}{2\pi/(2\pi k_B T)^3 \omega_x \omega_y \omega_z \sigma_x \sigma_y} \tag{5.32}$$

$$\sigma_i = \frac{\gamma_i(t)}{\omega_i}\sqrt{\frac{k_B T}{m}} \tag{5.33}$$

---

[1]which can be proven by using the following relation:

$$\int_{-\infty}^{\infty} dz\, Li_n(-e^{\mu/(k_B T)}e^{-z^2}) = \sqrt{\pi} Li_{n+1/2}(-e^{\mu/(k_B T)}) \tag{5.29}$$
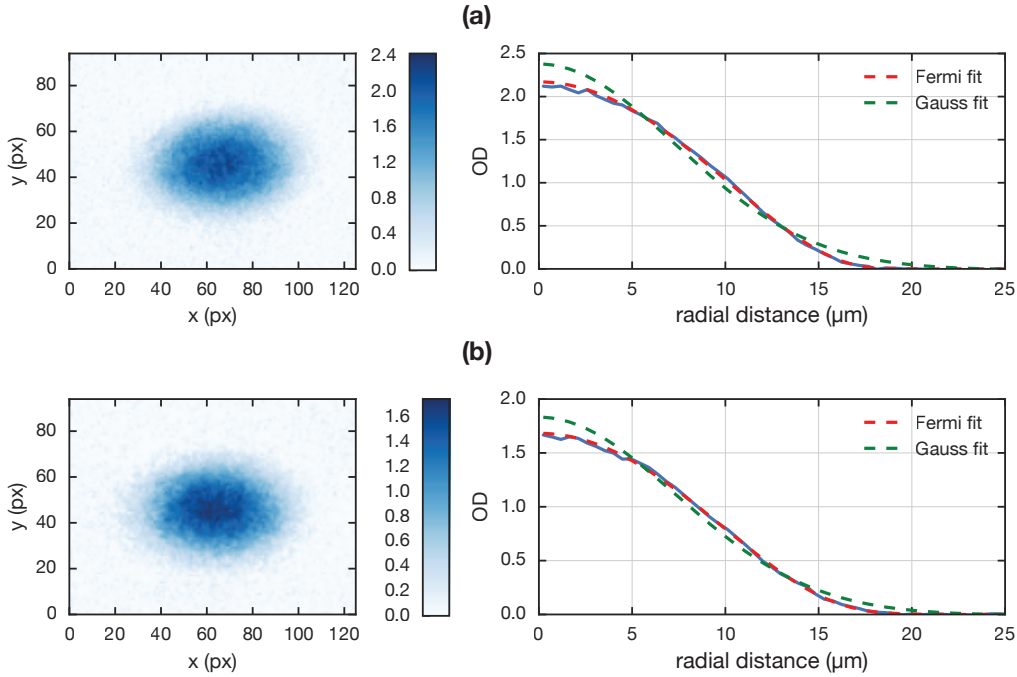
Figure 5.11: Left side: Optical density of a degenerate Fermi gas of ^{173}Yb imaged in-situ in the trap. Right side: Azimuthally averaged density profile (blue curve). The green curves show a cut of the Fermi fit to the density profile of the SU(6) and SU(3) gas respectively, while the red curves show a cut of the best fit of a Gaussian. For both Fermi gases, the discrepancy to the non-degenerate Gaussian density distribution is visible. **(a)** SU(6) Fermi gas with $N_p \approx 26000$ and $T/T_F = 0.07$. **(b)** SU(3) Fermi gas with $N_p \approx 24000$ and $T/T_F = 0.12$.

where we additionally introduced the number of spin-components N for a non-interacting Fermi gas. We can use Eq. 5.31 to fit the fugacity and therefore measure the reduced temperature using Eq. 5.23. In the classical, non-degenerate case ($z \ll 1$) Eq. 5.31 will approach a Gaussian distribution.

Fig. 5.11 shows a Fermi fit to the in-situ density distribution of the SU(6) and SU(3) Fermi gas. The SU(6) gas was evaporated in the optical dipole trap for 25 seconds. We prepared the three-component spin mixture at the end of evaporation by the method described in section 5.2.2. In both cases, the gas has reached quantum degeneracy and deviations from a Gaussian density distribution, which would describe a thermal gas, are visible. For the SU(6) gas the achieved temperature at the end of evaporation is so low that the measured temperature might already be limited by the precision of the Fermi fit. The Fermi fits allow quantifying the degree of quantum degeneracy of the Fermi gas and allow obtaining the entropy per particle. This becomes for example useful when studying the lattice loading dynamics in a round-trip experiment as shown in section 7.3. Sufficiently low temperatures

together with adiabatic loading of the atoms into the lattice are necessary to enter the insulating Mott regime in the optical lattice.

Interactions

Interactions of a two-component Fermi gas can be described by Landau Fermi-liquid theory [220, 221]. This theory accounts for interactions by describing the Fermi liquid by quasi-particle excitations that have a one-to-one correspondence to the excited states of a non-interacting Fermi gas. This theory can be extended to N spin components to describe an SU(N) Fermi liquid beyond a mean-field approach [111]. The corrections of the thermodynamic quantities such as the compressibility, the spin susceptibility or the mass of the particles with respect to a non-interacting Fermi gas, scale with $k_F a$, where $k_F = \sqrt{2mE_F}/\hbar$ denotes the Fermi wavevector, m the atom mass, E_F the Fermi energy and a the scattering length. The compressibility $\kappa = \partial n/\partial \mu$ of an SU(N) Fermi liquid with respect to a non-interacting SU(N) Fermi gas is given by

$$\frac{\kappa_0 - \kappa}{\kappa} = (N-1)\frac{2k_F a}{\pi}\left(1 + \frac{2k_F a}{15\pi}(22 - 4\ln 2)\right) \tag{5.34}$$

where κ_0 denotes the compressibility of the non-interacting gas. This correction scales with the number of spin components as $N-1$ and reduces the compressibility for repulsive interaction with respect to the non-interacting case. The scaling behavior with the number of spin components can be understood by the number of possible interactions channels of an SU(N) Fermi gas.

We can consider a trapped and interacting Fermi gas in LDA with a locally varying chemical potential that corresponds to a local Fermi wavevector $k_F(\mathrm{r})$. The Fermi wavevector will increase towards the center of the trap due to a larger chemical potential and the corrections due to interactions become stronger in the trap center. For repulsive interactions, the reduced compressibility as given by Eq.5.34 with respect to a non-interacting Fermi gas will therefore lead to a lower density in the trap center compared to a non-interacting Fermi gas. Moreover, these corrections are more pronounced for an SU(6) Fermi gas than for example for an SU(3) gas.

The correction of the compressibility and density can be estimated by realizing that the Fermi energy for N_p particles is given by $E_F = \frac{\bar{\omega}}{2\pi}(6N_p/N)^{1/3}$. For typical atom numbers $N_p \approx 35000$ we expect only weak corrections of the compressibility and the density in the dipole trap as $k_F a \leq 0.08$. This is confirmed by the good match of the non-interacting Fermi fit to the in-trap density distribution of the gas. However, in a shallow lattice where the on-site interaction can be described in mean-field approximation by an effective scattering length a that can be much larger than the bare scattering length, the effects of interactions become relevant. Deviations of the density distribution from the non-interacting case can indeed be observed in a shallow lattice for higher fillings, as demonstrated in section 7.3.

Chapter 6

Ultracold ytterbium atoms in optical lattices

In this chapter, we will discuss the implementation of periodic potentials with optical lattices. Such lattice potentials allow us to implement condensed matter systems with ultracold atoms. A degenerate Fermi gas of ytterbium in an optical lattice will, for example, faithfully realize the $SU(N)$ Fermi-Hubbard model. We show in this chapter how optical lattices are experimentally realized in our setup by superimposing three pairs of mutually orthogonal waves with linear polarization. We also discuss the calibration of the lattice as well as the detection of single and double occupancy by probing the density distribution in-situ.

The presence of meta-stable states in ytterbium makes this element especially suited to implement state-dependent optical potentials. We will review the magic lattice setup used in this experiment and discuss a state-dependent lattice configuration that can be employed to implement Kondo physics with two electronic orbitals. The polarizability and the lifetime of the meta-stable state in the state-dependent lattice will be characterized. At the end of this chapter, we will briefly present some results in a state-dependent lattice by using the clock transition to dress the electronic ground state and the lowest meta-stable state.

6.1 Optical lattice potentials

The optical lattices potentials that are used in our experiment are produced by retro-reflecting a laser beam with linear polarization. By superimposing an ingoing circular beam with the retro-reflected beam, a standing wave with intensity

$$I(x, y, z) = I_0 e^{-2\frac{y^2+z^2}{w_x^2}} \cos^2(kx) \tag{6.1}$$
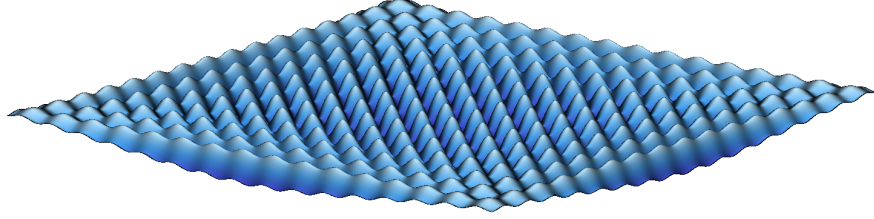
Figure 6.1: Illustration of an optical lattice potential in the x-y plane resulting from the superposition of three retro-reflected Gaussian beams. The harmonic confinement in this illustration is exaggerated with respect to the lattice depth for better visibility.

forms. This intensity modulation, according to Eq. 4.3, produces a light-intensity dependent AC Stark shift that creates a periodic potential, which confines the atoms. The lattice in our experiment consists of three mutually orthogonal, retro-reflected beams with linear polarization that are focused on the atoms. This produces a 3D lattice with simple cubic symmetry. The lattice potential, created by the beams, can be expressed as

$$V(x,y,z) = V_x e^{-2\frac{y^2+z^2}{w_x^2}} \cos^2(kx) + V_y e^{-2\frac{x^2+z^2}{w_y^2}} \cos^2(ky) + V_z e^{-2\frac{x^2+y^2}{w_z^2}} \cos^2(kz)$$

$$\simeq V_x \cos^2(kx) + V_y \cos^2(ky) + V_z \cos^2(kz) + \frac{1}{2}m(\omega_x^2 x^2 + \omega_y^2 y^2 + \omega_z^2 z^2),$$

$$(6.2)$$

with $k = \frac{2\pi}{\lambda}$ denoting the wavevector of the lattice light and $w_{x,y,z}$ defines the waist of the Gaussian beam. In the second line of Eq. 6.2, the Gaussian potential was approximated by a harmonic potential with

$$\omega_x = \sqrt{\omega_{x,lat}^2 - \omega_{x,ac}^2} \qquad , \qquad (6.3)$$

where

$$\omega_{x,lat} = \sqrt{\frac{1}{m}\left(\frac{4V_y}{w_y^2} + \frac{4V_z}{w_z^2}\right)} \qquad (6.4)$$

denotes the harmonic confinement produced by the lattice beam. The harmonic approximation of the Gaussian beams is usually justified as the beam waists are much bigger than the extension of the atom cloud in the lattice and hence only the harmonic part of the potential has to be considered.

As the intensity of the optical beam and therefore the AC Stark shift decreases away from the beam center, there is a second contribution to the harmonic potential, which produces a small anti-confinement given by

$$\omega_{x,ac} = \frac{h}{m\lambda}\sqrt{\frac{1}{w_y^2}\left(\frac{V_y}{E_r}\right)^{1/2} + \frac{1}{w_z^2}\left(\frac{V_z}{E_r}\right)^{1/2}} \qquad (6.5)$$
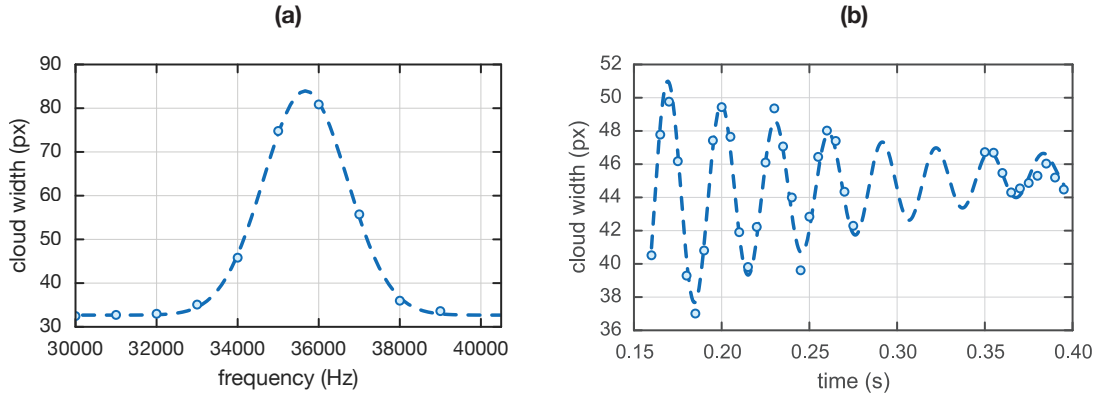
Figure 6.2: Lattice calibration to determine the harmonic confinement and lattice depth. **(a)** Atom cloud width (in-situ) as a function of the parametric heating frequency of the lattice arm. The resonance frequency at 35.7kHz corresponds to a lattice depth of $30E_r$. **(b)** Oscillation of the atom cloud width after a fast quench of the trap potential. The measured breathing frequency equals two times the harmonic confinement of the trapping potential. Due to interactions in the SU(6) Fermi gas, a damping of the oscillation in the lattice can be observed. The damping is modeled by an exponential $e^{-t/\tau}$ with $\tau = 190\,\text{ms}$.

with $E_r = (\hbar k)^2/(2m)$ denoting the recoil energy and m denoting the atom mass. By permuting the respective indices in Eq. 6.5, the other two harmonic confinements frequencies $\omega_{x,y}$ are obtained correspondingly.

6.1.1 Lattice calibration

For most of the experiments that are performed in an optical lattice, precise knowledge about the depth of the lattice and the overall harmonic confinement is essential. This becomes especially relevant in chapter 7, where the spatially varying harmonic potential allows us to use the local density approximation in order to give the equations of state of the gas.

One technique to determine the lattice depth is parametric heating. The intensity of the lattice light and hence the lattice depth can be modulated sinusoidally with an acousto-optic modulator. When the modulation frequency is resonant with a transition between two bands of the same parity, for example $\nu_{mod} = (\mathcal{E}_3(q) - \mathcal{E}_1(q))/h$, the atoms are resonantly excited [222]. This excitation produces heating and therefore a measurable increase in the width of the atomic sample. By comparing the excitation frequency with the band structure calculation (see Fig. 3.1), the lattice depth can be inferred. This calibration method works best for deep lattices, as in this case, the energy bands are sufficiently flat for all quasi-momenta q and the excitation becomes quasi-momentum independent.

Fig. 6.2(a) shows the parametric heating of the atomic sample by modulating one lattice arm. In this measurement, the width of the cloud was measured in-situ and the modulation frequency of the lattice light was swept. The obtained resonance between the lowest band and the second excited band at $\nu_{mod} = 35.7\,\text{kHz}$ corresponds in this configuration to a lattice depth of about $V = 30\,E_r$. The main uncertainty for the lattice depth calibration using this method stems from the width of the obtained resonance.

In addition to the measurement of the lattice depth, the harmonic confinement of the overall trapping potential can be probed. To characterize the harmonic confinement, created for example by the lattice beams and the optical dipole trap, it is possible to excite a breathing mode of the atomic sample by suddenly changing the trapping potential. After a quench of the potential, the atom cloud will start oscillating in width along the direction of the harmonic confinement that was changed abruptly. Fig. 6.2(b) shows the oscillation of the cloud width after a potential quench with a fitted breathing frequency $\omega_{br} = 2\pi \times 33\,\text{Hz}$. This breathing frequency is directly proportional to the harmonic confinement $\omega_{br} = 2\omega$. The observed damping in the oscillations of the SU(6) Fermi gas, as shown in Fig. 6.2(b), is caused by interactions. Collisions between the atoms will lead to a momentum change and produce a dephasing of the common mode oscillation of the atomic sample.

6.1.2 Probing double occupancies

Occupancies of several atoms per lattice site can be detected using photoassociation (PA). Two free atoms can form a bound pair by absorbing a photon when the light is resonant with a bound state of the electronically excited molecule. Due to the short lifetime of the excited molecule, the molecule will eventually decay and the released energy will cause a loss of the atom pair from the trap [223, 224]. This allows us to detect higher occupancies of lattice sites via the measured atom loss.

For ^{173}Yb we use a photoassociation resonance on the $^1S_0 \rightarrow {}^3P_1$ intercombination line, which is $329\,\text{MHz}$ red detuned to the single particle excitation. Fig. 6.3 shows the photoassociation spectroscopy of a two-component Fermi gas in a $35E_r$ deep lattice which was carried out with a $10\,\text{ms}$ PA pulse at an intensity $I = 0.2\,\text{mW/cm}^2$. The high intensity of the PA pulse and the presence of various other resonances that are close detuned to this transition will eventually associate atom pairs possessing any combination of m_F-states after several milliseconds pulse duration.

Photoassociation provides a useful tool to quantify and adjust the filling in the lattice. The photoassociation pulse will lead to a parity projection of the occupation number on a lattice site to either zero or one. An even number of atoms per site is projected to zero while an odd occupation number is projected to one remaining particle. To freeze out the density of the atomic sample during the PA pulse, the lattice is ramped up to $35E_r$ ($t = h \times 0.5\,\text{Hz}$) before applying the pulse.

Neglecting fillings of more than two atoms per lattice site, the atomic density after
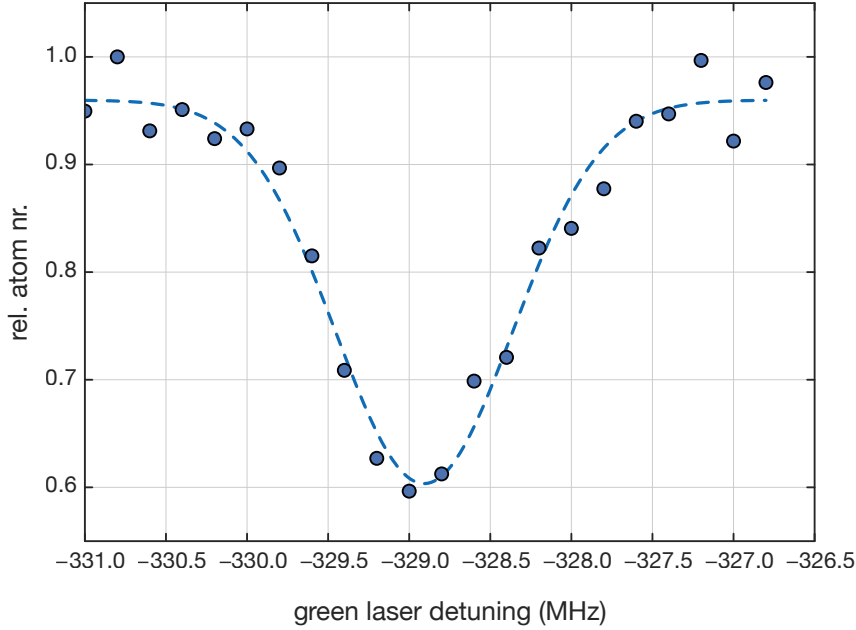
Figure 6.3: Photoassociation spectroscopy with the narrow intercombination line for ^{173}Yb in a 3D optical lattice. When the light is resonant with a bound-state of the electronically excited molecules, two free atoms can form a short-lived bound pair. The decay of these molecules is observed as a measurable atom loss on resonance.

the PA pulse directly reflects the density distribution of singlets, while the density distribution of doubles is given by the difference signal with and without PA pulse.

Fig. 6.4 shows the optical density of the atomic sample in the lattice before and after PA for various fillings at an interaction strength $U/(12t) = 11$. Characteristic for the strongly interacting regime is a suppression of higher occupancies for low fillings due to the high on-site interaction energy. When the filling in the lattice becomes high enough the number of double occupancies eventually increases as shown in Fig. 6.4(b). This will happen in the trap center first, where the filling is highest. Upon increasing the atom number, the region of the trap that contains double occupancies will grow. As shown in Fig. 6.4(c), this leads to a characteristic hole in the density distribution of the atomic sample after photoassociation.

6.2 State-dependent and independent lattices

A special property of ytterbium is the presence of a long-lived, meta-stable state that can be addressed with the clock transition. The associated narrow linewidth of this transition can be used for the realization of optical lattice clocks with alkaline earth-like atoms [50, 51, 132, 225], for precision spectroscopy to study for example interaction properties between the two electronic orbitals [72, 226], but also for state
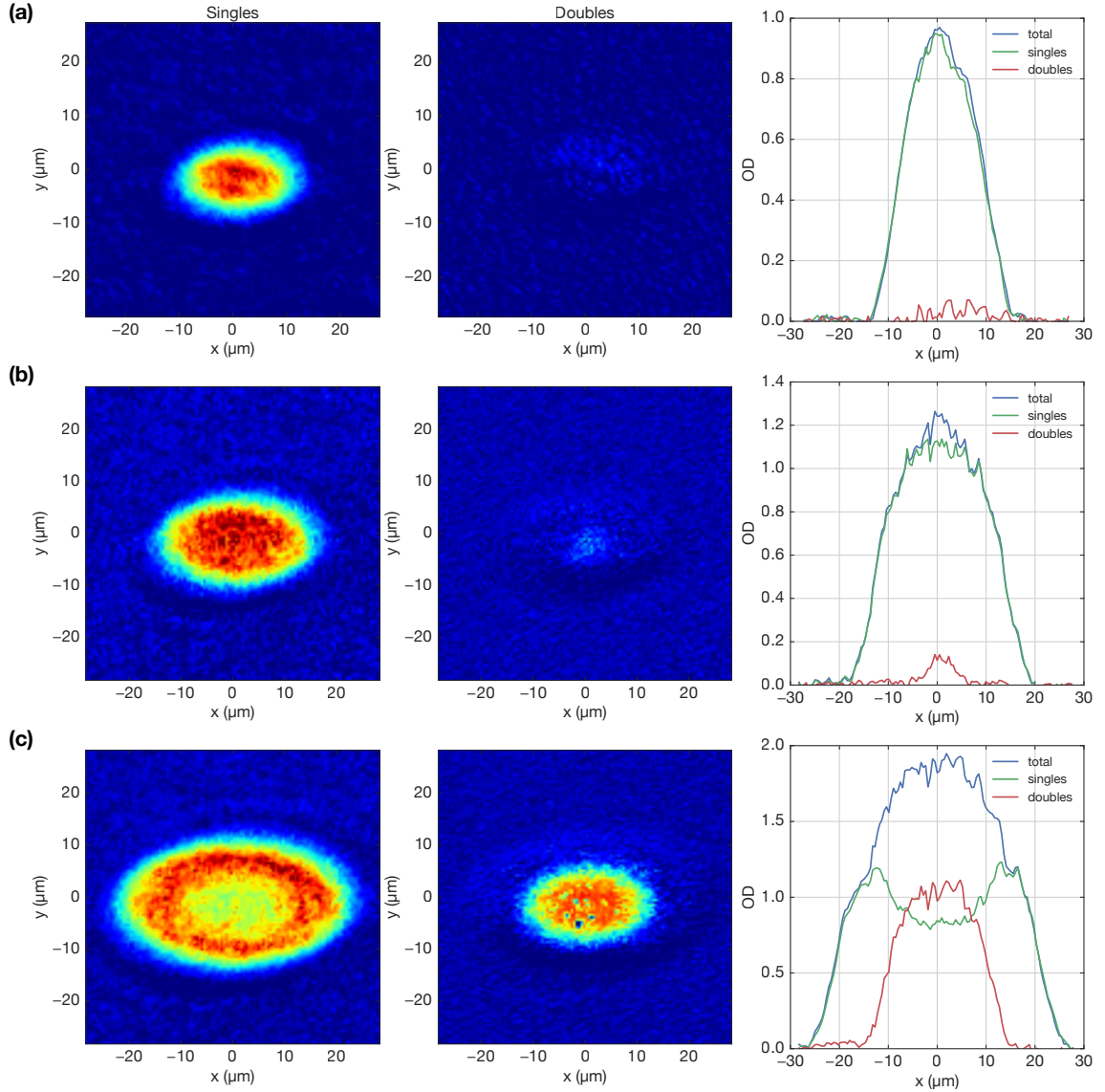
Figure 6.4: Single and double occupancy in a 3D optical lattice at an interaction strength $U/(12t) = 11$ for various atom numbers N_p. The single occupancy is measured with PA. The double occupancy is determined by the difference of the PA measurement with respect to a reference measurement that yields the total density. Each image is averaged over 10 repetitions of the experiment (a) $N_p \approx 5500$ (b) $N_p \approx 12000$ (c) $N_p \approx 35000$. The right column shows the corresponding cut of the optical density along the x-direction averaged in a window of $7.5\,\mu$m. For low and intermediate atom numbers a suppression of double occupancies is detectable, while for high atom numbers double occupancy emerges predominantly in the center of the trap.

preparation e.g. for the implementation of two-orbital many-body systems. In order to not reduce the resolution of the narrow optical transition for precision spectroscopy, the optical lattice must run at a specific wavelength – the magic wavelength λ_m – as only there the AC Stark shifts of the ground state $|g\rangle$ and the excited state $|e\rangle$ are identical [227, 228]. Therefore, at magic wavelength, any shift or broadening due to inhomogeneities of the lattice potential, like the spatially varying confinement, will be canceled between the two states.

While is necessary to run the optical lattice close to the magic wavelength when doing precision spectroscopy, the realization of two-orbital models like the Kondo lattice model requires a state-dependent lattice witch different polarizabilities for the ground- and meta-stable state. This will result in different lattice depths for the atoms in either of the two states and makes it possible to localize one species as needed for implementing the Kondo lattice Hamiltonian. To realize such a state-dependent lattice a laser system running at a wavelength of $\lambda \simeq 670$ nm was installed and the relative polarizability between the two orbitals is characterized in section 6.2.2.

In the experiment, we are currently using two different laser setups for the horizontal lattice arms. A Ti:Saph laser that is optimized to run at wavelengths close to the magic wavelength of the clock transition [229]. This setup is used to perform most of the spectroscopic measurements including the results presented in chapter 7. The state-dependent lattice is produced by another Ti:Saph laser that is optimized for $\lambda \simeq 670$ nm.

6.2.1 The magic wavelength lattice and the clock transition

The frequency tunability of the Ti:Saph laser, used for the generation of the state-independent lattice, allows us to run this laser precisely at magic wavelength $\lambda_m \simeq 759.4$nm. As the lattice light is red detuned, with respect to the strong $^1P_1$ transition in ytterbium, the atoms are trapped in the intensity maxima of the resulting standing wave. The lattice beam configuration is illustrated in Fig. 4.3. The vertical lattice (L3) is produced by a Gaussian beam with a waist $w_{L3} = 127\mu$m. The two horizontal lattice arms (L1 and L2) are created by retro-reflected elliptic beams with waists $w_z = 40\,\mu$m and $w_{x,y} = 160\,\mu$m. The elliptic beams were chosen to adapt to the oblate geometry of the optical dipole trap and to maximize the light intensity and hence the lattice depth for experimentally available laser powers. Moreover, the elliptic shape of the dipole trap and lattice beams might simplify the loading of a single vertical plane of the lattice when using a bichromatic lattice setup for the vertical lattice arm. Details about the bichromatic vertical lattice setup can be found in [230].

The Ti:Saph laser that is used for the generation of the magic lattice light is capable of producing an output power of about $P \simeq 6$W, which is distributed among the three lattice arms. The experimentally achievable output power together with the lattice beam waists permits lattice depths up to $V_{x,y,z} = 40E_r$. This is enough
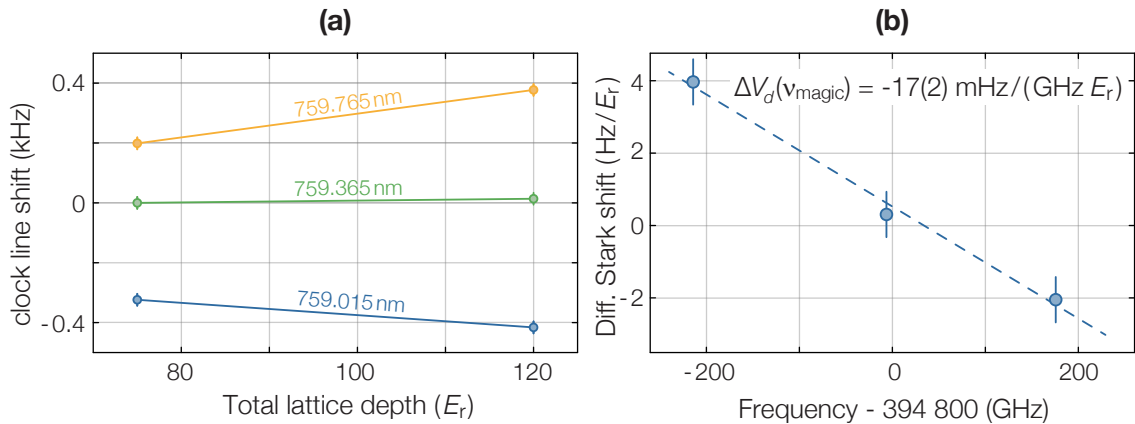
Figure 6.5: Frequency shift of the clock transition around the magic wavelength of the lattice. (a) Measured frequency shift of the clock transition by incoherent spectroscopy for three different lattice wavelengths. (b) Differential frequency shift per lattice depth as a function of the lattice light frequency.

for entering the Mott insulating regime of an ytterbium Fermi gas but also sufficient to perform spectroscopy with the clock transition in the Lamb-Dicke regime.[1]

Determining the magic wavelength

Running the lattice at magic wavelength is relevant for the study of the interaction properties between atoms in the two orbitals. The scattering properties between the states can be inferred by measuring for example the frequency shift of the clock transition [72]. Precise knowledge of the scattering lengths between the orbitals is important for optical lattice clocks where interactions between the atoms will lead to a so-called cold collisional shift that will limit the resolution of the clock [231–233]. Moreover, knowledge of the interaction properties is a prerequisite for the realization of two-orbital models. A detailed description of the clock laser used in our experiment and, specifically, the measurements of the interaction shifts of ^{173}Yb in the magic lattice, can be found in [73].

Precisely at the magic wavelength of the lattice light, the differential AC Stark shift between the ground state and the $^3P_0$ state will vanish. At this wavelength, the excitation with the clock laser becomes independent of the spatially varying lattice intensity. The magic wavelength can therefore be found by measuring light intensity dependent AC Stark shift as a function of the lattice depth as shown in Fig. 6.5. The measured shift $\Delta\nu_d$ allows us to determine the slope $\Delta\nu_d(\nu)$. By linear regression, we determine the zero crossing $\nu = \nu_{magic}$, which corresponds to a magic wavelength $\lambda_m \approx 759.30(4)$ nm of the lattice light as shown in Fig. 6.5b.

---

[1]In the Lamb-Dicke regime the coupling to the state becomes quasi-momentum independent. This is equivalent to saying that there will be no Doppler broadening for the transition due to the recoil energy of the absorbed photon.
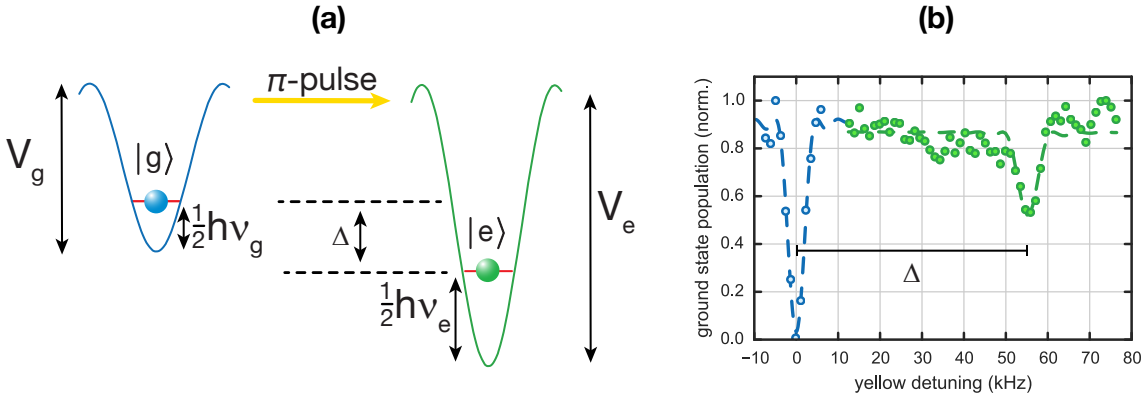
Figure 6.6: Orbital excitation in a state-dependent lattice with different polariz-abilities for the two states. **(a)** Excitation scheme with a π-pulse on the $^1S_0 \rightarrow$ $^3P_0$ transition. Due to the deeper lattice potential for the excited state, the clock transition will be shifted by Δ with respect to the ground state. **(b)** Measured frequency shift Δ of the clock transition in a $V_g = 10E_r$ state-dependent lattice running at wavelength $\lambda = 670$ nm. The plot shows the ground-state fraction of a spin-polarized atomic sample after an excitation with a coherent pulse for different detunings of the yellow clock laser. The blue (green) curve shows the transition frequency in a magic (state-dependent) lattice. The pulse duration of the clock laser was chosen to be a π-pulse for the magic lattice configuration.

6.2.2 A state-dependent lattice for two-orbital physics

As shown in chapter 2, the different polarizabilities between the ground state and the $^3P_0$ state make ytterbium an ideal element for the realization of far detuned state-dependent lattices. State-dependent optical potentials for different spin components have been realized for alkali elements, like rubidium, with laser light close detuned to the D1- and D2-transition of the $F = 1$ and $F = 2$ ground states [234–237]. However, the close detuning of the lattice light to one of the optical transitions causes significant heating due to photon scattering and limits the lifetime of the atoms in the lattice. A recent implementation is circumventing this problem by using a modulated magnetic field gradient to change the amplitude and sign of the tunneling matrix element of a two-component Fermi gas in order to create a state-dependent potential which breaks SU(2) symmetry of the system [238]. In contrast to such implementations, state-dependent potentials, preserving SU(N) symmetry, can easily be implemented for the lowest electronic orbitals with alkaline earth-like atoms. As the meta-stable states in ytterbium possess optical transitions very much different from those of the ground state, it is possible to choose a lattice wavelength, still far detuned to any optical transition, with different polarizabilities for the two orbitals, as shown in Fig. 2.6. This avoids the problem of excessive heating due to photon scattering of the lattice light.

Here we are characterizing the relative polarizability between the ground state and the meta-stable state in a state-dependent lattice running at wavelength $\lambda = 670\,\text{nm}$. This wavelength offers a higher polarizability for the $|e\rangle$ atoms than for the $|g\rangle$ atoms. Consequently, it becomes possible to localize the species in the meta-stable state, while the species in the ground state is allowed to tunnel. As an additional benefit, the localization of the $|e\rangle$ atoms avoids inelastic collisions between them.

Relative polarizability between the two orbitals

The relative polarizability between the two orbitals determines the individual lattice depths of the two species. A deep lattice, which localizes one species, is necessary for implementing the Kondo lattice model with ultracold ytterbium atoms. Fig. 6.6(b) shows the excitation scheme used for the measurement of the relative polarizability between the two orbitals. When the atoms are excited to the meta-stable state, we measure a frequency shift of the clock transition, caused by the differential AC Stark shift between the states.

For deep lattices, the lattice potential for the individual lattice sites can be well approximated by a harmonic potential for the energetically lowest states. In addition to the AC Stark shift of the lattice potential, we have to account for an additional shift, which goes into the opposite direction due the different ground-state energies $\frac{1}{2}h\nu_{e,g}$ of the harmonic oscillator. Moreover, under realistic conditions, the retro-reflected lattice beam will not create a full modulation of the lattice potential. As a consequence, there will be an additional AC Stark shift caused by a part of the laser light which is not contributing to the modulated lattice potential. When accounting for all these effects, the total frequency shift of the clock transition can be expressed as

$$\Delta_f = \frac{V_e - V_g}{h} + (b_e - b_g) - \frac{1}{2}(\nu_e - \nu_g) = (\gamma - 1)\left(\frac{V_g}{h} + b_g\right) - \frac{1}{2}\nu_g(\sqrt{\gamma} - 1) \quad (6.6)$$

here Δ_f denotes the measured frequency shift in Hertz with respect to the clock transition in the magic lattice, $V_{g,e}$ are the respective lattice depths in the state-dependent potential for the ground and meta-stable state and $\nu_{g,e}$ denote the respective harmonic oscillator frequencies. The frequency shift due to the AC Stark shift that is caused by imperfect alignment of the retro-reflected beam is denoted as $b_{g,e}$. This shift was measured separately without the lattice beam being retro-reflected. The factor $\gamma = \frac{\alpha_e}{\alpha_e}$ in Eq. 6.6 states the relative polarizability of the excited state with respect to the ground state and therefore determines the relative lattice depth V_e/V_g (see Eq. 4.3).

In Fig. 6.6 we present the measured AC Stark shift for a $10\,E_r$ deep lattice, where the lattice depth is given for the species in the ground state. First, the clock transition in the magic lattice is probed with a π-pulse to measure the transition frequency without AC Stark shift. As explained in the previous section, this frequency is independent of the lattice depth.
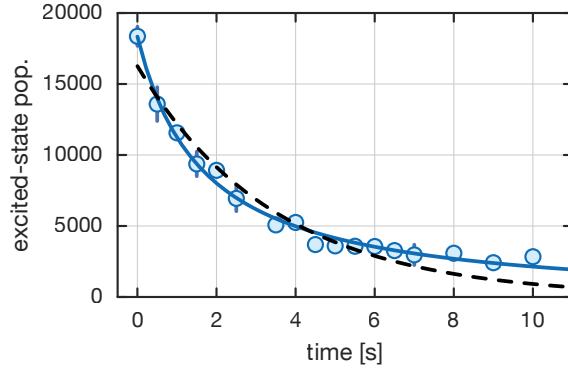
Figure 6.7: Lifetime measurement of a spin-polarized Fermi gas of $|e\rangle$ atoms in the state-dependent lattice. The figure shows the decay of the atoms in the excited state due to photon scattering, finite vacuum lifetime and inelastic (p-wave) collisions. The black dashed line denotes the fit of an exponential decay describing single particle losses with a lifetime $\tau_{1/e} \simeq 3.5\,\mathrm{s}$. The blue line shows a fit that also includes two particle losses, which scale with the density squared, in addition to single particles losses. For this fit, the lifetime of the exponential describing single particle losses is $\tau_{1/e} \simeq 25\,\mathrm{s}$, which is compatible with our vacuum lifetime.

The atoms are then excited with the same pulse length in a state-dependent lattice to the $^3P_0$-state and the frequency shift Δ_f is probed. The finite size of the lattice beam causes a broadening of the clock transition due to the spatially varying AC Stark shift. As a consequence, the detuning of the optical transition is varying spatially and the pulse excitation is not 100% efficient anymore, in contrast to the π-pulse excitation in the magic lattice.

To determine the relative polarizability between the two orbitals, we calibrate the lattice depth for the ground state via parametric heating in order to determine V_g and ν_g (see section 6.1.1). Eq. 6.6 then yields a polarizability ratio $\gamma = 3.41^{+0.21}_{-0.19}$ for the measurement shown in Fig.6.6. The main error for the value γ stems from the uncertainty of the lattice depth. The value of the relative polarizability between the orbitals is in good agreement with the theoretically predicted value $\gamma_{theo} = 3.43$ from the calculated polarizabilities in [131].

Lifetime in the state-dependent lattice

The lifetime of the excited-state atoms in the state-dependent lattice is an important parameter for the realization of multi-orbital models. For example, photon scattering due to a resonant background of the lattice light with the optical transition at $\lambda = 650\,\mathrm{nm}$ could cause heating of the atoms in the $^3P_0$-state and would limit the lifetime of the excited state in the lattice.

Fig. 6.7 shows the lifetime measurement of a spin-polarized Fermi gas in a state-

dependent lattice. For the measurement, a π-pulse was used to excite the atoms in a $10E_r$ deep lattice. A possible remaining ground-state population was removed by a cleaning pulse on the $^1P_1$ imaging transition. A second π-pulse, with a variable delay, was then applied to bring the remaining atoms in the $^3P_0$-state back to the ground state for imaging. The fit shown in Fig. 6.7 corresponds to a lifetime $\tau_{1/e} \simeq 3.5s$. The scattering rate of the lattice light is expected to be $\Gamma_{sc} \simeq 0.01$Hz and and the vacuum lifetime is in the order of $\tau_{vac} \simeq 30$s. Both time scales are much longer than the observed lifetime. An explanation for the discrepancy could be inelastic p-wave collisions between excited-state atoms due to the high density in the optical lattice, similar to the effect observed for ^{171}Yb [232]. Such inelastic collisions would scale with the squared density of the atomic sample. Indeed, the decay is modeled very well by a fit function that includes inelastic two-body decays in addition to an exponential, which describes single particle loss, as illustrated in Fig. 6.7. Nevertheless, the achieved lifetime of several seconds should be enough for typical lattice experiments with sequences not longer than a few hundred milliseconds at maximum lattice depth.

Enhanced atom mass in a state-dependent lattice

The state-dependent 670 nm lattice can be used together with the meta-stable state to realize heavy particle physics. By choosing the detuning of the clock transition in a way that it is resonant between the Bloch bands of the ground-state ($|g\rangle$) and the excited-state ($|e\rangle$) atoms, for the same quasi-momentum q, we coherently couple the two electronic states and mix the two energy bands for a given quasi-momentum depending on the detuning of the laser and the coupling strength. Due to the different polarizability of the two states, the lattice depths are very different. The coherent coupling of the clock transition mixes the lowest Bloch bands for $|g\rangle$ and $|e\rangle$ and changes the curvature of each band at the quasi-momentum q. This causes an enhanced effective mass for the $|g\rangle$ atoms (see Eq. 3.14).

This effect is very similar to the hybridization of the two energy bands in the Kondo lattice model (KLM) which arises due to the exchange coupling and causes the heavy fermion properties for an anti-ferromagnetic coupling [70, 169, 175]. In this case, the exchange energy of the KLM is replaced by the Rabi frequency due to the optical coupling. The Rabi coupling described here is therefore independent of the Fermi or Bose statistics. For a small momentum spread in the lattice, we therefore decided to use bosonic ^{174}Yb for this measurement.

When dressing the two Bloch bands, the Hamiltonian for the corresponding atom-light interaction in the lattice, given in the basis of $|g\rangle$, $|e\rangle$, reads

$$H_D = \begin{pmatrix} \mathcal{E}_g(q) & \Omega/2 \\ \Omega/2 & \mathcal{E}_e(q) - \delta \end{pmatrix}. \tag{6.7}$$

Here, we set $\hbar = 1$, Ω is the Rabi frequency of the clock transition, and $\mathcal{E}_g(q)$, $\mathcal{E}_e(q)$ denote the dispersion relations of the band structure for $|g\rangle$ and $|e\rangle$ respectively,
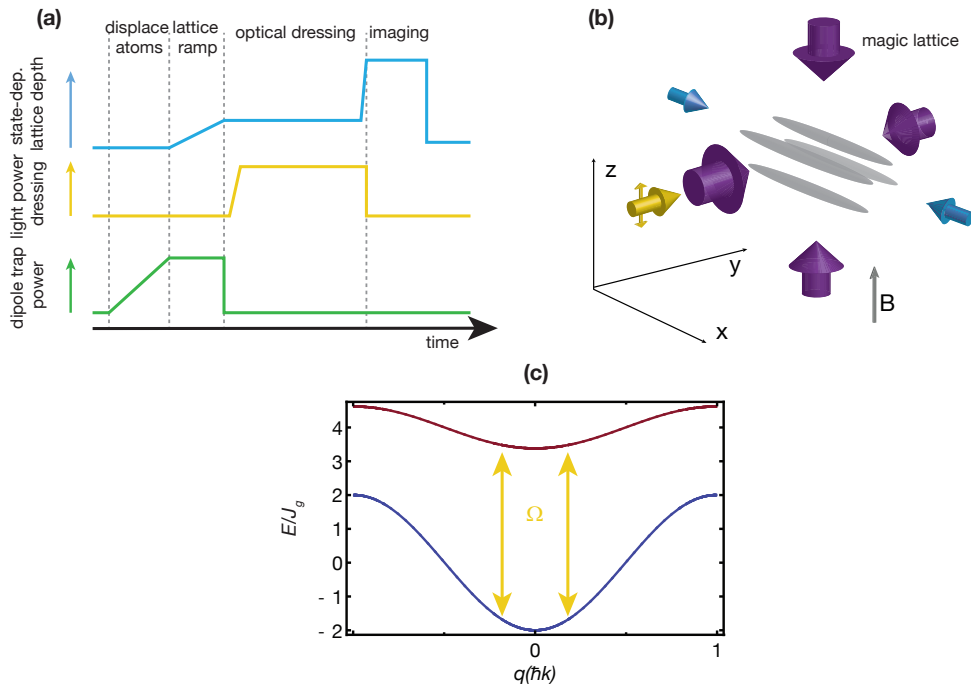
Figure 6.8: Optical dressing in a state-dependent lattice **(a)** Scheme for optical dressing and sloshing to probe the effective mass. The sloshing in the state-dependent lattice (blue) is initiated by displacing the atoms with an optical dipole trap beam (green). The clock transition (yellow) is then driven to couple both electronic states. **(b)** Lattice configuration used for this experiment. The laser light driving the clock transition is directed along the deep magic lattice (purple) to be in the Lamb-Dicke regime for the electronic excitation. **(c)** By coupling the Bloch bands for the ground (blue) and excited state (red) with the clock transition (yellow) for a fixed quasi-momentum, the Bloch bands mix locally and increase the effective mass of the atoms.

which are shown for different Rabi couplings in Fig. 6.9. Depending on the detuning δ, we can mix the two bands for different quasi-momenta and create an avoided crossing accompanied by an effective mass change close to that point. The energy range of the band mixing and the enhancement of the effective mass will depend on the Rabi coupling (see Fig. 6.10). If the Rabi coupling is sufficiently high ($\Omega \gg J_g$), the two energy bands are mixed for all quasi-momenta and the bandwidth for $|g\rangle$ and $|e\rangle$ becomes the average of the two energy bands without optical coupling.

The effect of the enhanced mass can be measured in a sloshing experiment as illustrated in Fig. 6.8 because the sloshing frequency scales with the mass like

$$\omega_{sl} = \omega_h \sqrt{\frac{m}{m_\Omega}} \tag{6.8}$$

where ω_h is the harmonic confinement of the trap, m_Ω denotes the effective mass and m is the bare mass of the atom. Fig. 6.11 shows the sloshing in a state-dependent lattice with and without optical coupling for bosonic ^{174}Yb. In contrast to the fermionic isotopes, a strong magnetic field needs to be applied to drive the clock transition with sufficiently high Rabi frequencies. Due to the absence of hyperfine interaction for the bosonic isotopes of ytterbium which possess no nuclear spin, the magnetic field is required to admix dipole-allowed states such as the $^3P_1$-state to the $^3P_0$-state in order to create a finite coupling of the clock transition [101]. For the measurements presented here, we used a magnetic field of $1000\,\text{G}$, which is produced by our main coils.

The sloshing is performed in a 3D lattice. One lattice arm in this lattice configuration consists of the state-dependent lattice running at a wavelength $\lambda = 670\,\text{nm}$ with a lattice depth $V = 2E_r$ for the ground-state atoms. The other two lattice arms are running close to the magic wavelength with a depth $V_z = 25E_r$ and $V_y = 20E_r$. The laser light, driving the clock transition, is directed along the direction of the deep magic lattice, which provides the Lamb-Dicke regime for the electronic excitation.

The displacement from the equilibrium position is performed along the direction of the state-dependent lattice by displacing the atoms in the trap with the gradient of the vertical optical dipole trap beam. After a sudden switch-off of the optical dipole trap, the sloshing of the atoms is initialized. We then switch on the optical coupling adiabatically in order to mix the two energy bands of the electronic states. The Rabi coupling for this run was chosen to be $\Omega = 500\text{Hz} = 1.33 J_g/\hbar$ for a detuning which addresses the quasi-momenta around $q = 0$. Upon coupling the two electronic states, we observe a lower sloshing frequency due the enhanced mass, as shown in Fig. 6.11, in contrast to the uncoupled scenario. We measure a sloshing frequency $\omega_{sl}^{dres.} = 2\pi \times (28.8 \pm 1.8)\text{Hz}$ for the dressed case and $\omega_{sl}^{no\,dres.} = 2\pi \times (35.7 \pm 0.5)\text{Hz}$ for the case without coupling. The decrease of the sloshing frequency is consistent with the increase of the effective mass $m_\Omega = 1.42\,m_{\Omega=0}$ which is expected for the Rabi coupling used in this experiment and for the polarizability of the excited state that was determined in the previous section.
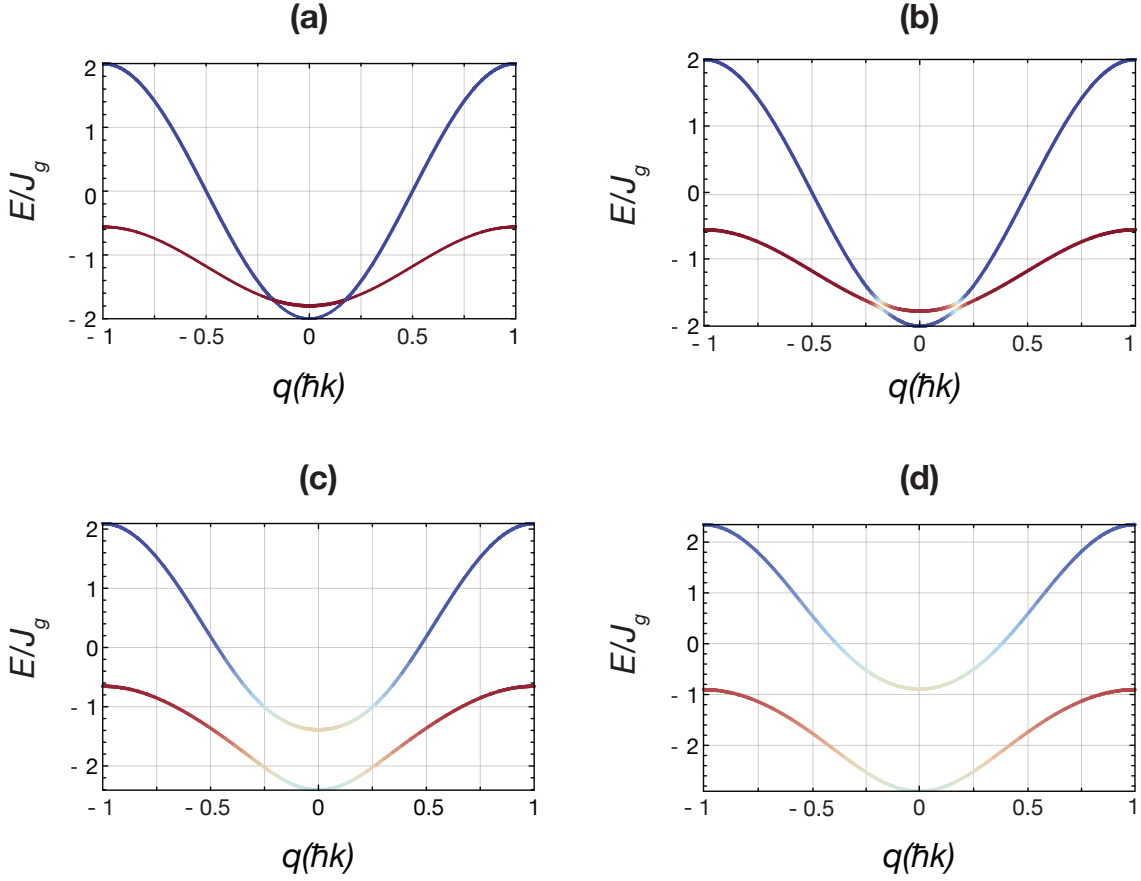
Figure 6.9: Band structure for the ground state (blue) and the excited state (red) in a state-dependent lattice for different Rabi couplings Ω. Here, the detuning of the laser is already subtracted by shifting the Bloch bands with respect to each other. The detuning of the Rabi coupling was chosen to be in resonance with the excited state close to the quasi-momentum $q = 0$ (crossing of the red and blue line in Fig.(a)). Depending on the detuning, the light coupling causes a local, quasi-momentum-dependent mixing of the two bands (indicated by the line color) where the resonance condition is fulfilled. In the limit of $\Omega \gg J_g$ both bands are fully mixed for all quasi-momenta with the bandwidth being the average of the uncoupled ground and excited-state bandwidth. **(a)** $\Omega = 0J_g$ **(b)** $\Omega = 0.1J_g$ **(c)** $\Omega = 1J_g$ **(d)** $\Omega = 2J_g$.
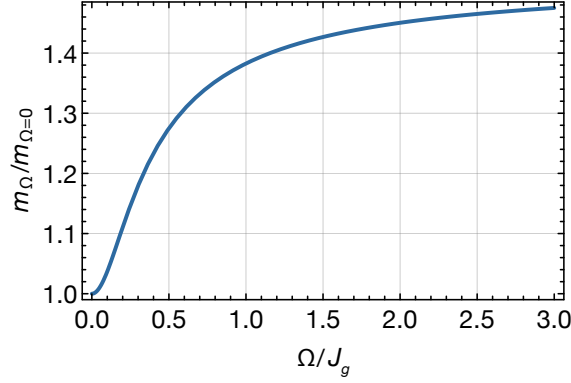
Figure 6.10: Effective mass m_Ω normalized to the bare mass $m_{\Omega=0}$ at quasi-momentum $q = 0$. The plot shows the mass ratio as a function of the coupling strength Ω for the detuning of the Rabi coupling that is shown in Fig. 6.9.
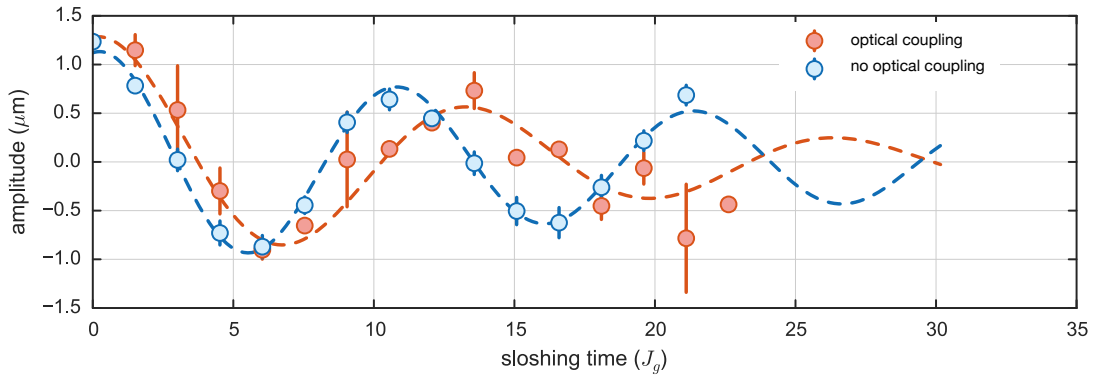
Figure 6.11: Sloshing in a state-dependent lattice. The two bands are coupled by the clock transition with a Rabi coupling $\Omega = 1.33 J_g$ and zero detuning ($|g, q = 0\rangle \rightarrow |e, q = 0\rangle$). A sloshing motion is produced by exciting the atoms from the equilibrium position with a small trap displacement and observing the frequency of the center-of-mass oscillation which is related to the effective mass (see Eq. 6.8).

Chapter 7

Equation of state of the SU(N) Fermi-Hubbard model

In the last part of this thesis, we take advantage of our imaging system to locally probe an ytterbium Fermi gas in an optical lattice with simple cubic symmetry. Optical lattices provide a faithful realization of the Fermi-Hubbard model (FHM) and allow changing the interaction parameter of this model in a controlled way. Due to an almost perfect decoupling of the nuclear spin from the electronic configuration in ytterbium, as explained in chapter 2, the interactions between the atoms become $SU(N)$-symmetric. This allows us to investigate the $SU(N)$ Fermi-Hubbard model with ultracold ytterbium atoms. The enlarged spin symmetry for ytterbium leads to different thermodynamic properties of the atomic sample compared to the FHM describing spin-1/2 particles, as we explained in section 3.2. Especially in the low temperature regime, novel phases with magnetic order are predicted that reach beyond the Néel order observed for spin-1/2 particles. Although fermionic quantum gases in optical lattices have been studied with ultracold atoms for the two spin component case [22, 23, 239], the presented results constitute the first in-situ measurement of the $SU(N)$ FHM.

In this chapter, we first present the experimental sequence used for our measurements – specifically the ramping sequence of the lattice – and we calculate the overall harmonic confinements of the trapping potential, which play a central role for obtaining the equation of state (EoS) with local density approximation (LDA). Afterwards, we introduce the reconstruction procedure of the density that is used to measure the EoS for the quantum gas in the lattice. By using LDA and probing the density of the gas in a spatially varying trapping potential – given by the harmonic confinement of this potential – we probe the EoS of the $SU(N)$ FHM for various interaction regimes and for different numbers of spin components $N = \{3, 6\}$. In this way, we can give model-free access to the thermodynamic properties of the FHM with enlarged spin symmetry. Moreover, we characterize in this chapter the crossover
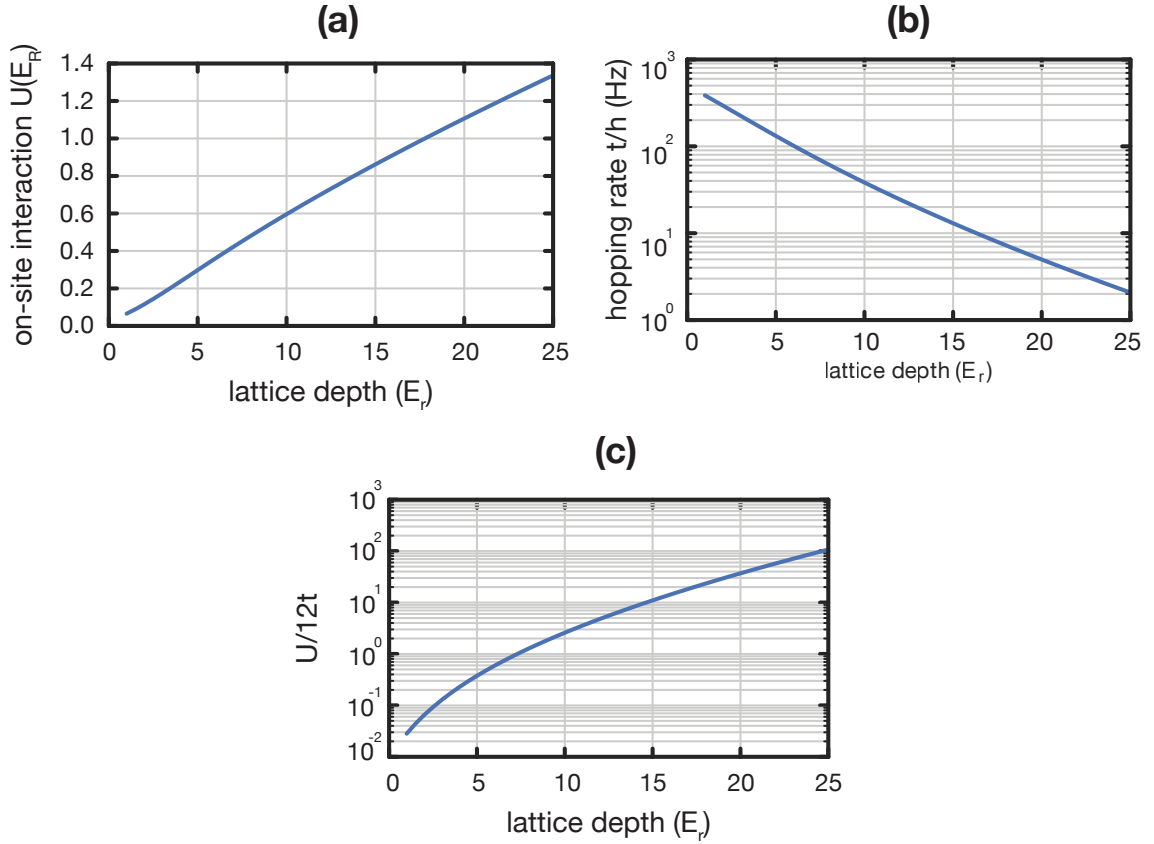
(a)

(b)

(c)

Figure 7.1: Scaling of the interaction energy U and the tunnel matrix element t of the Fermi-Hubbard model in a 3D lattice for different lattice depths. **(a)** On-site interaction energy U. **(b)** Hopping rate t/h . **(c)** Ratio of interaction energy to kinetic energy $U/12t$ in the 3D lattice configuration.

for both quantum gases from a weakly interacting metal to the insulating Mott phase as a function of the interaction by using the local compressibility of the system. At the end of this chapter, we discuss the specific entropy reached in this experiment for both gases and give an estimate for the three-body loss coefficient for ^{173}Yb that we observed at very high densities. The specific entropy reached for the SU(6) gas is below that of uncorrelated spins but above long-range Néel order, which makes this system a promising starting point for observing exotic, highly spin-symmetric magnetically ordered quantum phases, as introduced in chapter 3.

The main part of the experimental data in this chapter has been published in Ref. [75].
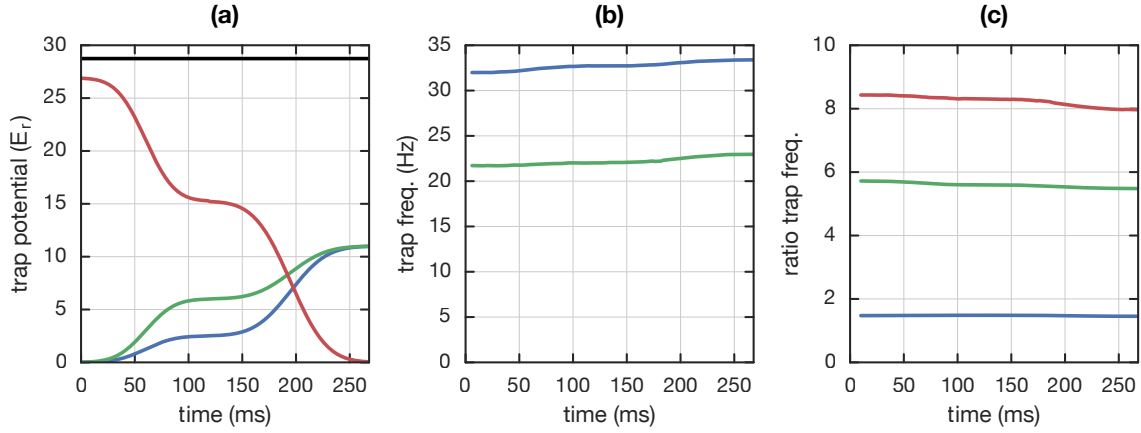
Figure 7.2: Lattice loading sequence as a function of time for a final lattice depth of $11E_r$. **(a)** Trapping potentials in units of E_r as a function of time for the horizontal lattice arms (blue), vertical lattice arm (green), vertical dipole trap beam (red) and horizontal dipole trap beam (black) **(b)** Absolute harmonic confinement frequencies as a function of time for f_x, along the x-direction (green curve) and f_y along the y-direction (blue curve). **(c)** Ratio of trapping frequencies, corresponding to the aspect ratio of the atomic sample, as a function of time for f_y/f_x (blue curve), f_y/f_z (green curve) and f_x/f_z (red curve).
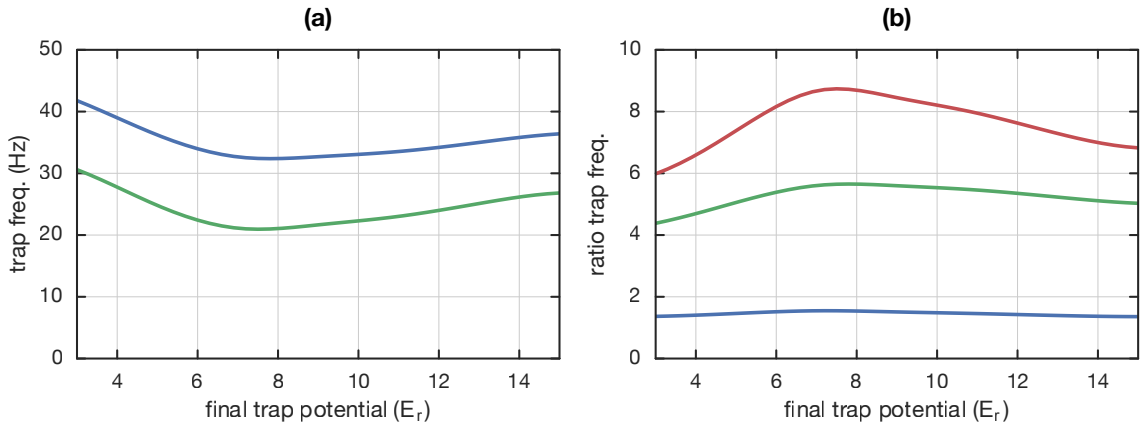
Figure 7.3: Confinement frequencies for different final lattice depths used in the measurements. **(a)** Absolute confinement frequencies f_x (green curve) and f_y (blue curve) for the final lattice geometry at the end of the ramp. **(b)** Ratio of confinement frequencies f_y/f_x (blue curve), f_y/f_z (green curve) and f_x/f_z (red curve) in the final lattice geometry.

7.1 Experimental sequence

We will first give a short explanation of the lattice loading sequence, which will become relevant later on for the measurement of the equation of state. After forced evaporation in the optical dipole trap for about 20 seconds, we obtain a six-component degenerate Fermi gas of ^{173}Yb with $T/T_F \leq 0.1$. The SU(3) gas is prepared by removing three out of six spin components with an optically resonant push beam from the optical dipole trap at the end of evaporation, as described in chapter 5. We then proceed by loading the Fermi gas into a three dimensional cubic lattice running at a wavelength $\lambda = 759.3$ nm. The lattice potential is formed by three pairs of counter-propagating waves. The actual beam configuration of the 3D lattice and the crossed optical dipole trap corresponds to the one that is illustrated in Fig. 4.3.

During the whole experiment sequence, the horizontal dipole trap is kept on to hold the atoms against the gravitational force. In order to compensate the increasing harmonic confinement when ramping up the lattice, the vertical dipole trap is ramped down simultaneously. Fig. 7.2 shows the lattice loading sequence used for this measurement. In a first step, the lattice is ramped up to $3E_r$ ($1E_r = h \cdot 2$ kHz) in 120 ms, which avoids band excitations, in order to transfer the atoms into the lowest band of the optical lattice. In a second ramp, the final lattice depth is varied between $3-15E_r$ in 150 ms. The ramp times were optimized for best adiabatic lattice loading with a round-trip experiment as explained in section 7.3.2 and represent an optimum between most adiabatic loading and other technical heating effects that will increase for slower ramps. For the lattice depth calibration, we followed the procedure described in section 6.1.1.

Due to the absence of a magnetic Feshbach resonance in alkaline earth-like atoms that can be used to vary the interaction energy U between the atoms in the ground state, we change the lattice depth in order to tune the interaction. Increasing the lattice depth will exponentially suppress the hopping rate t/h while the on-site interaction U will moderately increase as shown in Fig. 7.1(a) and Fig. 7.1(b). This allows us to tune the interaction strength by almost two orders of magnitude for the experimentally relevant lattice depths in our measurements (see Fig. 7.1(c)). It should be noted that, due to the exponential suppression of the tunneling, adiabaticity will finally break down for the chosen ramp times for lattice depths deeper than $V = 15E_r$ as the tunneling time approaches the lattice ramp duration.

The vertical dipole trap beam is used to vary the harmonic confinement in the lattice. We chose the ramp of the vertical dipole trap in a way that the ratios of the trap frequencies stay approximately constant during the loading sequence as illustrated in Fig. 7.2(c). This ratio corresponds directly to the aspect ratio of the cloud. A constant trap frequency ratio will reduce mass redistribution in the atomic sample during the ramp, which becomes particularly relevant when the interaction strength is high enough to enter the Mott regime. In this regime, the overall mass transport of the atoms is reduced due to the onset of an incompressible Mott phase

and a high mass redistribution during the ramp can lead to non-adiabatic lattice loading and heating of the Fermi gas. Moreover, the confinement of the vertical dipole trap is varied depending on the final lattice depth to preserve the $x - y$ aspect ratio of the atomic sample in the lattice for the different interaction regimes, which we measure in individual runs. Fig. 7.3 depicts the change of the trap frequencies and their ratios for different interaction strengths. The trap frequencies were measured individually for each beam with a sloshing experiment for three different trap depths. These results were then used for the calculation of the harmonic confinement of the overall trapping potential that includes the 3D optical lattice and the crossed optical dipole trap. It should be noted that the vertical trap frequency ($\omega_z = 2\pi \times 183\,\text{Hz}$) is only determined by the horizontal dipole trap beam. Therefore, the ratio of the horizontal trap frequencies with respect to the vertical trap frequency is changing for the different interaction regimes.

7.2 Obtaining the equation of state

The equation of state of a system is a relation that describes the thermodynamic properties of the system for a given set of state variables like temperature, chemical potential and number of spin components. Due to this property, obtaining the EoS of a system is useful to characterize different phases and to benchmark numerical simulations against measurements. This is particularly interesting for the FHM, which cannot be solved analytically in dimensions higher than one and therefore access to the EoS can only be obtained via approximate numerical simulations. In this respect, ultracold atoms in optical lattices can serve as a quantum simulator as the EoS of such systems can be measured.

By local probing of a trapped Fermi gas, the thermodynamic properties of interacting fermions in the bulk in the unitary limit[1] have been measured [240]. Moreover, bosonic Mott insulators have been probed via local measurements of the density [29, 30, 241] and recently the compressibility of the SU(2) FHM was studied [239]. All the results were obtained for fermionic systems with two spin components but so far a measurement of the EoS of the FHM with higher spin symmetry was not achieved.

In this section, we describe how the EoS of the system can be measured in a 3D system and characterize the precision of the reconstruction procedure. Moreover, we show how the imaging cross section is calibrated.

---

[1]in the unitary regime, $\frac{1}{k_F a}$ approaches zero with k_F denoting the Fermi wavevector and a is the scattering length between the atoms. In this limit the thermodynamic properties of the gas becomes universal, meaning independent of the details of the interaction potential.

7.2.1 Inverse Abel transformation

In our experiment, we can only measure the heterogeneous, optically integrated column density $\tilde{n}(x, y)$ directly. Due to the high optical densities in the 3D lattice, strongly saturated absorption imaging, as described in chapter 5, is used to image the cloud.

Determining local thermodynamic quantities directly from the integrated column density is not trivial for a 3D density distribution as the imaging process yields only the integrated signal over several lattice planes and therefore signatures of the different phases are washed out. The EoS describing the system is however obtained by determining the 3D density $n(\mu, T, V, N)$ of the gas as we showed already in section 3.2.2. Consequently, a reconstruction of the 3D density from the integrated column density is necessary. For an atomic sample with cylindrical symmetry, it is possible to reconstruct the density via the inverse Abel transform

$$n(r, y) = -\frac{\omega_z}{\pi \omega_x} \int_r^\infty \frac{\partial \tilde{n}(x', y)/\partial x'}{\sqrt{x'^2 - r^2}} dx'. \tag{7.1}$$

Here, $r = \sqrt{x^2 + \frac{\omega_z^2}{\omega_x^2} z^2}$ denotes the distance to the symmetry axis and $\tilde{n}(x, y)$ is the measured column density. The factor ω_z/ω_x accounts for the correct aspect ratio of the gas in the trapping potential and maps the ellipsoidal density distribution to a cylindrically symmetric problem where the symmetry assumption of the inverse Abel transformation holds.

After the density is reconstructed, we map the trapped, heterogeneous gas to a locally homogeneous gas by using local density approximation (LDA) as explained in section 5.3.1. In the grand canonical ensemble the chemical potential μ is therefore replaced with $\mu = \mu_0 - V(\mathbf{x})$. In this formula, μ_0 denotes the chemical potential in the center of the trap and $V(\mathbf{x}) = \frac{1}{2}m(\omega_x^2 x^2 + \omega_y^2 y^2 + \omega_z^2 z^2)$ is a position-dependent energy offset due to the harmonic trapping potential. In LDA, the chemical potential will change with the spatially varying trapping potential and allows us to measure the EoS $n[\mu = \mu_0 - V(\mathbf{x})]$ for different chemical potentials with a single realization of the experiment.

In order to rule out artifacts of the Abel inversion we simulated the exact trapping geometry of the system. Fig. 7.4(a) shows a cut through the central plane of a simulated density profile for an SU(6) Fermi gas in the atomic limit. The simulated trap geometry accounts for our Gaussian beam profiles. The temperature of the Fermi gas in the simulation was chosen to be $T/U = 0.1$, which is similar to the experimentally obtained temperatures in the SU(6) gas. By integrating the density, we obtain the column density used for testing the Abel inversion. The inverse Abel transformation of the data is performed with the Gaussian basis set expansion method (BASEX) [242]. Apart from the singularity at the symmetry axis, the density profile of the input data is perfectly reconstructed when accounting for the
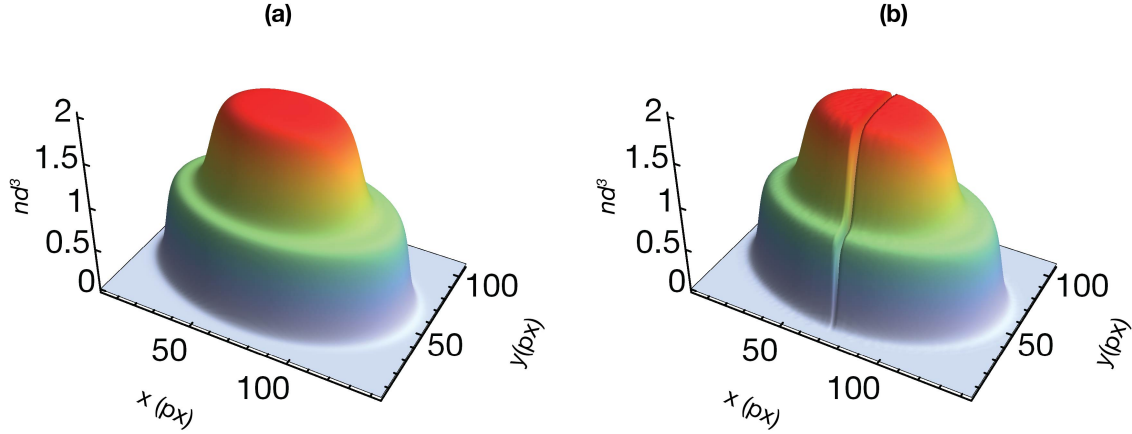
Figure 7.4: Reconstruction of the density profile with the inverse Abel transformation. **(a)** Simulated central plane density of an SU(6) Fermi gas in the atomic limit with a temperature $T = 0.1U$ and for a lattice depth $V = 11E_r$. The simulated trap geometry corresponds to the one in the experiment and accounts for the Gaussian beam profiles of the trapping potentials. **(b)** Density profile obtained from the simulated column density via the inverse Abel transformation.
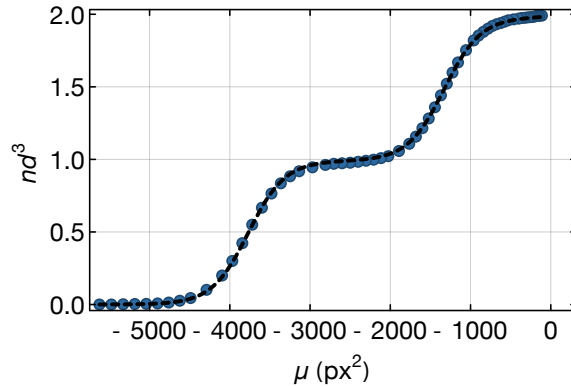

Figure 7.5: Fitted temperature to the reconstructed density shown in Fig. 7.4**(b)**. The fit of HTSE model yields a temperature of $T/U = 0.102 \pm 0.001$ in good agreement to the simulated temperature of the input data ($T/U = 0.1$).

correct trap aspect ratio as illustrated in Fig. 7.4(b). By azimuthally averaging the obtained density profile, we can compare quantitatively to the original profile and find a very good match of the fitted temperature of the low tunneling model to the simulated data. The fit yields a temperature $T = 0.102 \pm 0.001U$, as illustrated in Fig. 7.5, which is in good agreement with the simulated temperature of $T = 0.1U$. This demonstrates that the reconstruction process with the Abel inversion for the experimentally relevant parameter regime does not produce a loss of information and the assumption of a harmonic trapping potential of our Gaussian beams is justified for the particular trap geometry that is used in the experiment.

7.2.2 Local pressure method

While Abel inversion is one method to reconstruct the density of the atomic sample in order to obtain the EoS, another method exists which allows determining the pressure of the system [243]. This method was for example employed to study the equation of state of an interacting Fermi gas of ^{6}Li in the unitary limit [240].

The pressure P of the gas is obtained by integrating the measured column density $\tilde{n}(x, y)$ along one direction $P \propto \int \tilde{n}(x, y) dy$. This can be proven, starting with the Gibbs-Duhem identity

$$dP = SdT + nd\mu. \tag{7.2}$$

Setting $dT = 0$, $\mu = \mu_0 - 1/2m \sum_i \omega_{i=x,y,z}^2 x_i^2$ and realizing that $d\mu = -\frac{m\omega_y\omega_z}{2\pi}dydz$ when the coordinate x is fixed, one obtains

$$
\begin{aligned}
P(x, 0, 0) &= \int n(\mu)d\mu = -\frac{m\omega_y\omega_z}{2\pi} \int n(x, y, z)dydz \\
&= \frac{m\omega_y\omega_z}{2\pi} \int \tilde{n}(x, y)dy.
\end{aligned} \tag{7.3}
$$

The density can then be expressed as

$$n(x, 0, 0) = \left(\frac{\partial P}{\partial \mu(x)}\right)_T = -\frac{1}{2\pi}\frac{\omega_y\omega_z}{\omega_x^2 x}\frac{d}{dx}\int_{-\infty}^{\infty} \tilde{n}(x, y)dy. \tag{7.4}$$

This formula of the density is equivalent to the one obtained by the inverse Abel transformation as demonstrated in Appendix A. Fig. 7.6 shows the pressure obtained by integrating the data set that is illustrated in Fig. 7.4 and correspondingly the obtained density profile. One advantage of this method compared to Abel inversion is that the pressure can be obtained directly by integration. However, another derivation of the noisy experimental data is required to obtain the density of the system. In certain cases, e.g. to study the metal to Mott insulator crossover of the Fermi-Hubbard model, the density and its derivative, the compressibility of the system, are important observables and it can be more useful to retrieve the density directly with Abel inversion.
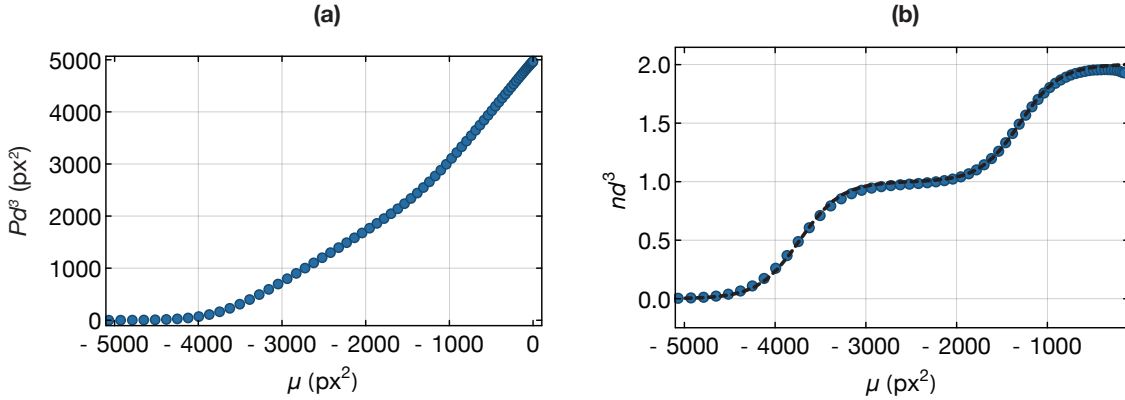
Figure 7.6: **(a)** Pressure of the SU(6) Fermi gas obtained by integrating the 2D density along the y-direction. **(b)** Density of the Fermi gas as a function of the chemical potential obtained by building the first derivative of the pressure. The black line denotes the original input data.

7.2.3 Calibration of the imaging cross section

In order to reconstruct the 3D density with the Abel inversion correctly, we have to determine precisely the imagining cross section σ, which enters in the measured column density as we showed in section 5.1.1. When imaging the atomic sample in a nuclear spin insensitive way at a weak magnetic field, the effective imaging cross section in ytterbium with several m_F states can be very different to the one of an ideal two-level system. This can be understood by the different transition strengths of the imaging transition for the m_F states, which are given by the Clebsch-Gordan coefficients. In the case of imaging with with σ^+-light for example, the line strength of the $|F = 5/2, m_F = 5/2\rangle \rightarrow |F' = 7/2, m'_F = 7/2\rangle$ transition is 21 times stronger than the $|F = 5/2, m_F = -5/2\rangle \rightarrow |F' = 7/2, m_{F'} = 3/2\rangle$ transition. The absorption and emission of photons during the short imaging pulse will optically pump the atoms between the different m_F states. Consequently, different m_F states can have distinct contributions to the overall number of absorbed photons in the imaging beam. Such an effect, as well as residual magnetic fields which will scramble the polarization of the imaging light, can influence the measured optical cross section of the atomic sample.

To determine the cross section, we can compare the atom number that is expected from the measured optical density, to the expected atom number of the Fermi gas fit with known trapping potential and measured temperature. This approach yields $\sigma = (0.222 \pm 0.034)\sigma_0$, where $\sigma_0 = \frac{3}{2\pi}\lambda^2$ denotes the optical cross section for an ideal two-level system. The main error in this method stems from the uncertainties of the harmonic confinements that enter into the Fermi gas fit to determine the atom number. A second approach involves using the fitted amplitude of the Mott plateau with the HTSE model to obtain the optical cross section. This method is quite
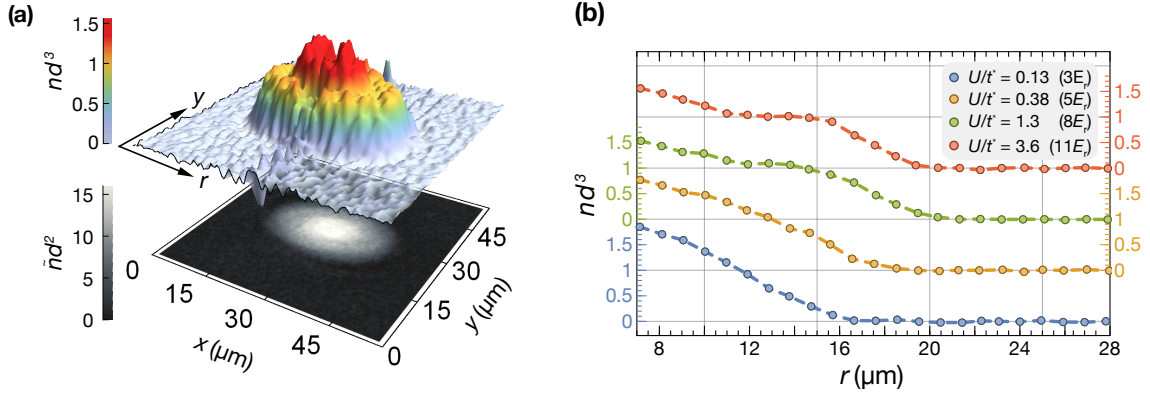
Figure 7.7: Density profile of an SU(6) Fermi gas in the lattice. Three experimental realizations were averaged for the depicted profiles. **(a)** Integrated column density of the atomic sample (bottom) and 3D density after Abel inversion (top) for an interaction strength $U/t^* = 6.4$ ($V = 13E_r$). **(b)** Averaged density profiles of an SU(6) gas in an optical lattice with harmonic confinement. The different curves show the 3D density as a function of the radial distance for various interaction regimes U/t^*. Figure taken from [75].

precise and yields $\sigma = (0.257 \pm 0.013)\sigma_0$ for the SU(6) gas. The error of this method stems only from the fit uncertainty of the amplitude. Therefore, the fit from the HTSE model to the Mott plateau of the SU(6) gas is used for the calibration of the optical cross section. The obtained densities are then expressed in units of the unit cell $1/d^3$, where $d = \lambda_{lat}/2$ denotes the spacing of the optical lattice, which fixes the Mott plateau of the SU(6) gas to $nd^3 = 1$. An independent fit of the HTSE model to the Mott plateau of the SU(3) gas yields $nd^3 = 0.94 \pm 0.02$ and therefore a somewhat lower value than the calibration with the SU(6) data. A possible explanation for the observed discrepancy might be different contributions of populated m_F-states to the overall imaging cross section due to the strongly varying Clebsch-Gordan coefficients between the m_F-states.

7.3 Thermodynamics of the SU(N) Fermi-Hubbard model

To analyze the data, we use the BASEX method to perform Abel inversion and reconstruct the density distribution in the optical lattice. The inverse Abel transformation is commonly used where a reconstruction of a projected image is required, like in the field of photoion and photoelectron imaging to study molecular dynamics [244, 245]. However, the derivative in Eq. 7.1 will lead to noise amplification on the experimental data due to the singularity towards the symmetry axis. It is therefore impractical to

use Eq. 7.1 directly on real data with significant amounts of noise. Consequently, sophisticated algorithms like the Fourier Hankel method or the BASEX method have been developed to perform a high fidelity Abel inversion of the projection while still being robust to noise and preserving as much information as possible [242, 246]. Especially in the cloud center of the absorption image, where the column density is highest, the number of transmitted photons can be low and the signal to noise ratio is reduced. This noise is actually amplified by the inverse Abel transformation and leads to an unstable behavior of the transformation close the symmetry axis of the cloud ($r = 0$) [242]. For the analysis of experimental data, we therefore consider only azimuthally integrated data with a radius $r > 7\,\mu$m in the analysis. These points have typically a standard error of the mean below $2\,\%$. The obtained data is then azimuthally averaged in a window of $\pm 4.8\,\mu$m around the y-axis of the cloud (see Fig. 7.7(a) for the coordinate system).

The averaged, reconstructed density profile of an SU(6) gas is shown in Fig. 7.7(b) for different interaction regimes. As the measurements are carried out in a 3D optical lattice, we denote the kinetic energy of the particles as $t^* = 12t$, with t being the tunnel matrix element in the FHM. For the plotted profiles with interactions above $U/t^* = 0.4$, the presence of a plateau with constant density becomes visible. With the known harmonic confinement of the trapping potential, we can use LDA to give the EoS $n(\mu)$ of the density for the various interaction regimes.

Let us first consider the case of weak interaction in the FHM for which $U < t^*$. In this regime, the kinetic energy dominates over the interaction energy and we expect a normal metal with delocalized atoms. When probing the EoS $n(\mu)$ for that interaction strength, we observe a smooth decrease of the density from the center towards the edge of trap indicating a compressible metallic state for all chemical potentials (see Fig. 7.8(a)). In the presence of a weak lattice, the system can be modeled by Fermi liquid theory. In particular, in the wing of the cloud, the density is low enough that interactions between fermions will become negligible. Therefore, we fit in the weakly interacting regime the EoS

$$n(\mu, T) = -N \left(\frac{m k_{\mathrm{B}} T}{2\pi \hbar^2} \right)^{3/2} \mathrm{Li}_{3/2} \left(-e^{\mu / k_{\mathrm{B}} T} \right) \tag{7.5}$$

of a non-interacting Fermi gas to the wing of the cloud in order to obtain μ_0 and $k_B T$ for this regime. In this formula, N denotes the number of spin components in the gas. In the limit of negligible interactions, the role of N to the EoS is trivial as it appears in Eq. 7.5 as a prefactor. The fit to the data includes only points with low density for which $nd^3 < 0.5$. At low densities, we observe a good agreement of the data to the fit but see deviations from the Fermi fit towards higher densities. Theses deviations can be explained by interactions. In order to correctly describe the measured EoS even in this regime, a more sophisticated model, which incorporates interactions in a weak lattice, would be needed. However, the behavior can be understood qualitatively
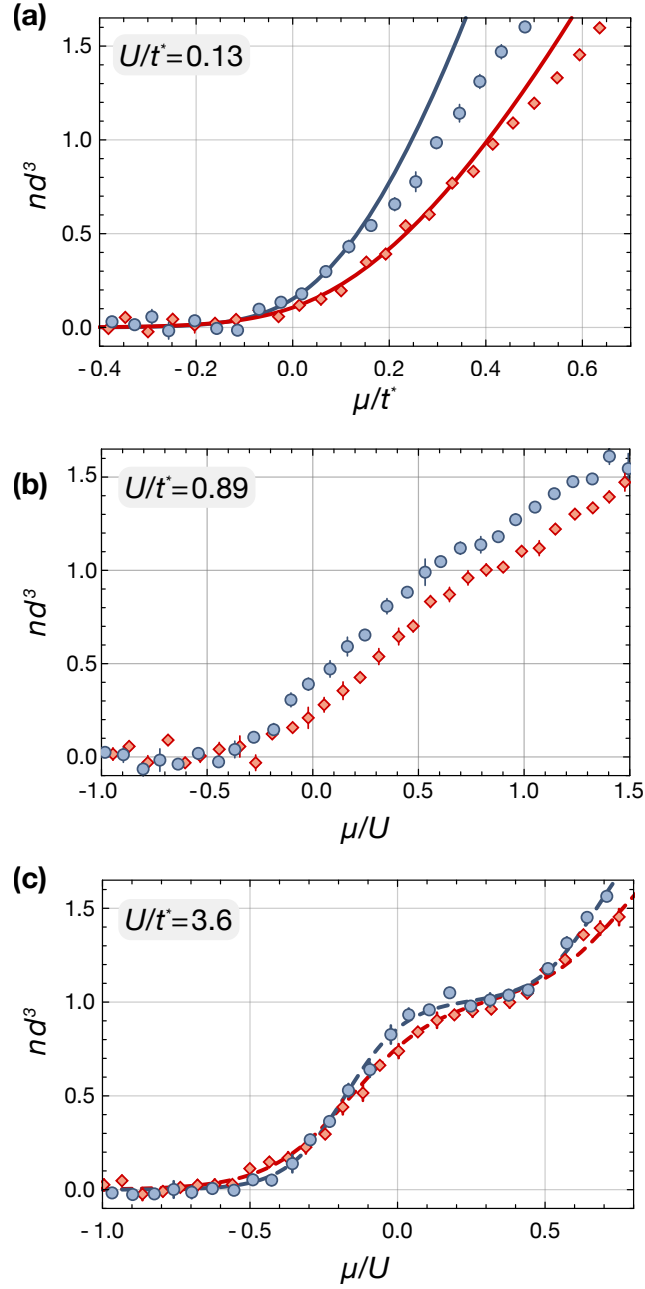
Figure 7.8: EoS of the SU(6)- (blue circles) and the SU(3)- (red diamonds) Fermi gas in a lattice. The density is plotted as a function of the chemical potential for different interaction strengths: (a) $U/t^* = 0.128$ (b) $U/t^* = 0.89$ and (c) $U/t^* = 3.6$. The solid curves show the fits to the EoS of the non-interacting Fermi gas. For this fit only data points $nd^3 < 0.5$ are included. The dashed lines are the fits of the second order, low-tunneling model (HTSE model) for the SU(6) (blue) and SU(3)(red) gas. Error bars denote the s.e.m. of the binned data.

with SU(N) Fermi liquid theory. When comparing the fits to the measured EoS, one notices a bigger deviation of the fit to SU(6) data at high densities compared to the SU(3) case. This can be understood by the fact that the number of possible interaction channels in the quantum gas scales with $N - 1$ due to Pauli blocking as explained in section 5.3.1. For the same chemical potential, the SU(6) gas is therefore expected to show stronger deviations from the non-interacting Fermi gas fit than the SU(3) gas.

In the strongly interacting regime, where $U > t^*$, the interaction energy dominates over the kinetic energy term in the FHM. In this regime, we distinguish a metallic outer layer $0 < nd^3 < 1$ and a metallic core $nd^3 > 1$, separated by a Mott shell with a density of $nd^3 = 1$ as shown in Fig. 7.8(c). Both the SU(6) gas and the SU(3) gas show a plateau in the density distribution, a clear signature for an incompressible Mott insulator that has formed in the strongly interacting regime. For this interaction strength, the low tunneling model, introduced in section 3.2.2, is used to fit the EoS, which accounts for a weak tunnel coupling in the lattice (see Eq. 3.37). The model is used to fit the chemical potential μ_0 and the temperature to the EoS.[2] For an interaction strength $U/t^* = 3.6$, we determine a temperature of $T/U = 0.13$ for the SU(6) gas and $T/U = 0.18$ for the SU(3) gas. The difference in temperature between the SU(6) and the SU(3) gas arises mainly due to the Pomeranchuk cooling effect. The Pomeranchuk cooling effect scales with the number of spin components and is therefore expected to be stronger for the SU(6) gas, which explains the lower temperatures in the Mott regime (see sec. 3.2.3).

We demonstrated in section 3.2.2 that the EoS in the strongly interacting regime is dependent on the number of spin components N in a non-trivial way. The N-dependence in the EoS arises due to the different quantum statistics, e.g. the number of spin components, which enter in the partition function, as already explained. To emphasize the influence of the number of spin components, we fit the low-tunneling HTSE model that describes a two-component Fermi gas to the SU(6) data with temperature T and μ_0 as free fit parameters. Fig. 7.9 illustrates the best fit of the two models to the experimental data. A stronger discrepancy of the SU(2) model to the data compared to the SU(6) model can be observed, which cannot be explained by a temperature or chemical potential μ_0 of the model. This comparison indeed highlights the importance of the number of spin components to the EoS already at temperatures above magnetic order.

We now consider intermediate interaction strengths. In the intermediate interaction regime, with $U \approx t^*$, both the kinetic energy and the interaction energy are equally strong. Therefore, no negligible parameter in the Fermi-Hubbard model exists that allows for an approximate solution of the EoS. The HTSE model in this regime will

---

[2]The HTSE model has a high sensitivity to the trap confinement compared to the precision of the independent trap calibrations. We therefore allow a variation of the confinement parameter in the model within the bounds given by our calibration
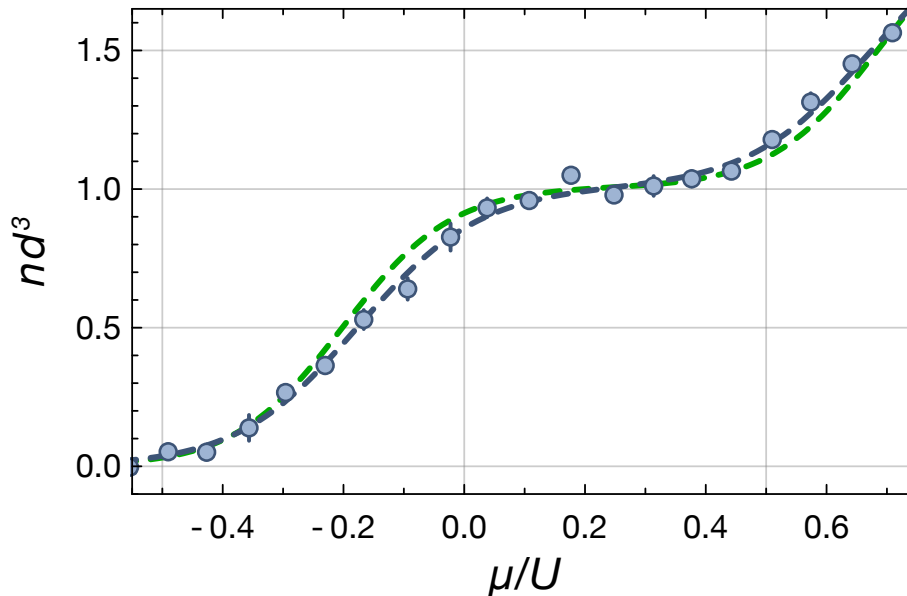
Figure 7.9: Dependence of the EoS on the number of spin components N. The dashed lines are the fits of the low-tunneling model (HTSE model) for $N = 6$ (blue dashed line) and $N = 2$ (green dashed line) to the measured SU(6) Fermi gas in the lattice (blue circles). The temperature and the central chemical potential μ_0 are free fit parameters in both models. Error bars denote the s.e.m. of the binned data.

not apply anymore as the tunneling energy can be higher or equal to $k_B T$. For these interaction strengths, the system is in a strongly correlated many-body state and no exact prediction of the EoS is available yet. As shown in Fig.7.8(b), the EoS differs clearly from the two previous cases that we discussed so far and the density levels off for higher chemical potentials in contrast to the weakly interacting case. However, a model-free access to the EoS of the system allows us to determine thermodynamic properties such as the compressibility even in this regime.

7.3.1 Local compressibility

The possibility to probe local quantities with our imaging system allows extracting the local compressibility of the Fermi gas for different interaction strengths. As a vanishing compressibility is a characteristic property of the Mott insulator in the FHM, the local compressibility is useful for quantifying different phases in the system. We determine the compressibility $\tilde{\kappa} = \frac{\partial n}{\partial \mu}$ by linear regression of the density $n(\mu)$.

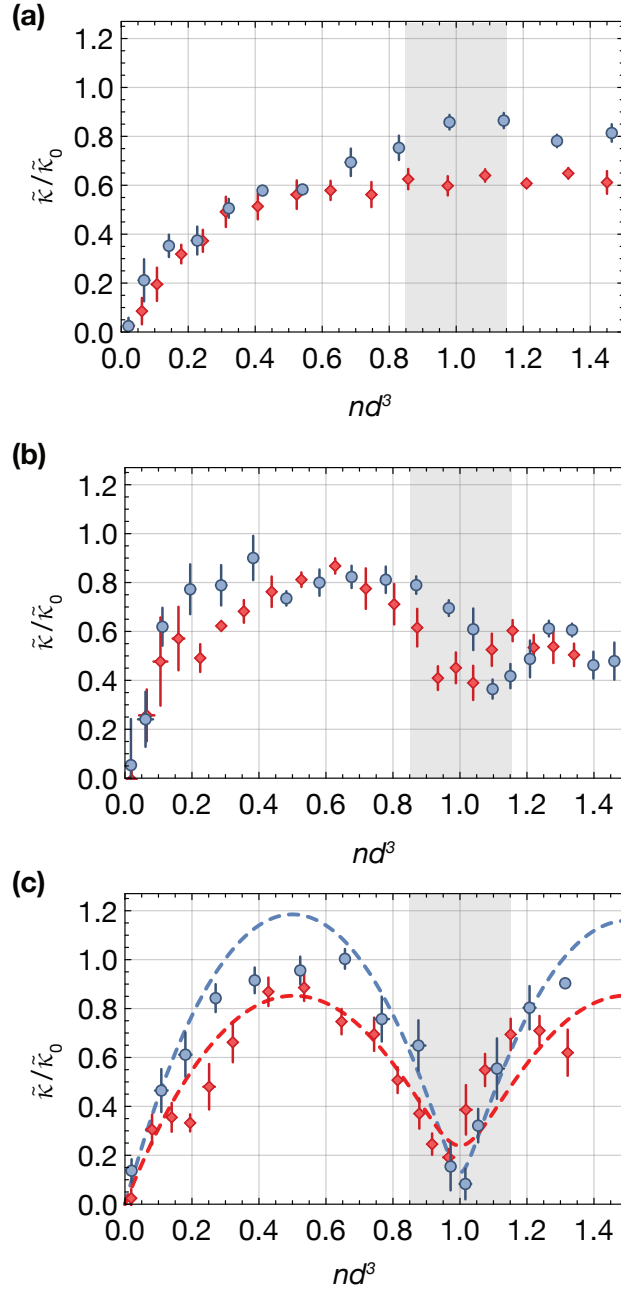The compressibilities for the three different interaction regimes are illustrated in

Figure 7.10: Compressibility as a function of density of the SU(6) (blue) and SU(3) (red diamonds) Fermi gas in a lattice. **(a)** Compressibility in the weakly interacting regime $U/t^* = 0.128$ **(b)** intermediate regime $U/t^* = 0.89$ **(c)** Mott regime $U/t^* = 3.6$. The dashed lines are obtained by deriving the fitted low-tunneling model plotted in Fig. 7.8. For determining the minimum compressibility $\tilde{\kappa}_{min}$ of the system, an interval around unit filling is used (gray shaded area). Error bars denote the confidence interval of the linear regression.
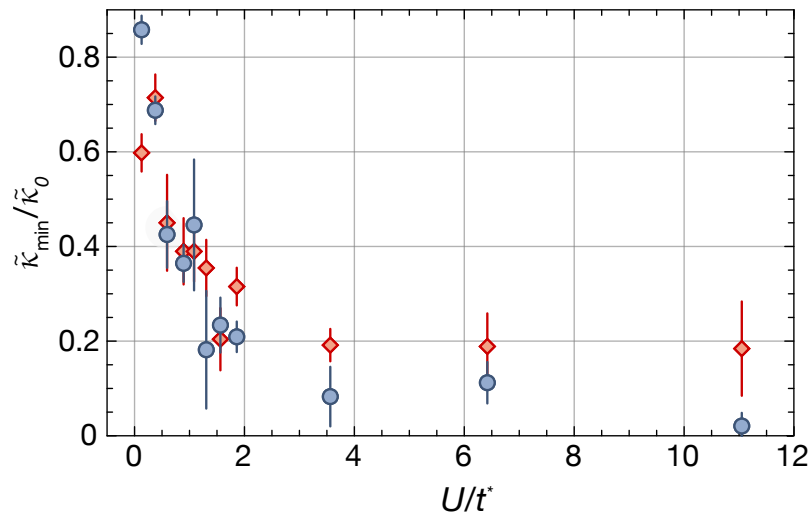
Figure 7.11: Minimum compressibility $\tilde{\kappa}_{\min}/\tilde{\kappa}_0$ as a function of interaction strength of an SU(6)- (blue circles) and SU(3)- (red diamonds) spin-symmetric Fermi gases in a lattice. The minimum of the compressibility is determined for the shaded region depicted in Fig. 7.10. Error bars denote the confidence intervals of the linear regression used to obtain $\tilde{\kappa}$.

Fig. 7.10 as a function of density. In these plots, the compressibility is rescaled by

$$\tilde{\kappa}_0 = \frac{3m}{4\pi\hbar^2 d}\left(\frac{6}{\Gamma(5/2)}\right)^{3/2}, \tag{7.6}$$

where Γ denotes the Gamma function and d is the lattice spacing. The parameter κ_0 defines the compressibility of a non-interacting SU(6) Fermi gas at zero temperature and density $n = 1/d^3$. By plotting the compressibility as function of the density for the different interaction regimes, the compressibility is obtained in a model independent way that does not rely on fitting the central chemical potential μ_0.

In the weakly interacting regime, we measure a compressible metal as shown in Fig. 7.10(a). For low densities, the gas is so dilute that it can be described by an ideal classical gas. In this limit, the compressibility is directly proportional to the density and independent to the number of spin components N. However, at higher densities we observe an N-dependence of the compressibility for the same reason that was given when describing the EoS.

For intermediate interaction strength, with $U/t^* \simeq 0.13$, we measure the onset of a Mott shell which builds up at a filling around $nd^3 = 1$ as illustrated in Fig 7.10(b). Interactions become more dominant than in the weakly interacting regime and reduce the compressibility. At the same time, the compressibility at a density of $nd^3 = 0.5$ is increasing with respect to the weakly interacting case.

Let us now consider the strongly interacting case, which is shown in Fig. 7.10(c).

In this limit, the Mott shell has fully developed and we observe a Mott phase with an almost vanishing compressibility at $nd^3 = 1$. The small but nonvanishing compressibility of the Mott insulator can be attributed to the finite temperature in the system. At a density of $nd^3 = 0.5$, the compressibility is highest and we measure a compressible metallic region for this density.

The distinct feature of an almost vanishing compressibility for a filling of one particle per site can be used to probe the emergence of the Mott shell as function of interaction strength. For this we extract the minimum compressibility in a range $nd^3 \in [0.85, 1, 15]$ for various interaction regimes. We observe a gradual reduction of the compressibility when increasing the interaction strength up to $U/t^* \approx 2$ as shown in Fig. 7.11. For higher values, the minimum compressibility is not changing anymore, as the Mott insulator has already formed completely. The appearance of the SU(3) Mott insulator with respect to the interaction strength is compatible with a dynamic mean field calculation for an SU(3) gas. This calculation predicts the emergence of the Mott plateau between $U/t^* = 1.22$ and $U/t^* = 1.43$ [247]. However, it should be noted that these calculations were performed for temperatures $T = 0.05t$, whereas the temperature in the experiment are around $T \approx 4t$ in the Mott regime. Due to the higher temperature, a smoothing of the crossover between a compressible metal and the incompressible Mott phase is expected. For the appearance of the SU(6) Mott insulator, with a filling of one particle per site in a 3D lattice, no theoretical prediction to our knowledge was done yet in order to compare to our data.

7.3.2 Entropy

In a second experiment, we characterize the adiabaticity of the lattice loading and estimate the entropy per particle in the lattice. For this, we measure the entropy per particle before lattice loading and compare it to a round-trip experiment. The round trip consists of loading the atoms into the lattice and then back to the optical dipole trap. In the optical dipole trap, the entropy per particle of a non-interacting Fermi gas can be determined via the reduced temperature T/T_F as we saw in section 5.3.1, where T_F denotes the Fermi temperature of the gas. The round-trip experiment allows studying the entropy increase due to the lattice loading and yields an upper and a lower bound for the specific entropy in the lattice.

Fig. 7.12 shows the average entropy per particle of the SU(6) and SU(3) gas before lattice loading and after the round-trip experiment for various interaction strengths. The entropy in the lattice is below the measured value after the round trip but above or equal to the entropy measured before lattice loading. For low lattice depths, we observe a constant entropy increase when loading the atoms into the lattice. At $U \approx t^*$, we measure an additional increase in entropy coinciding with the appearance of the incompressible Mott phase. This effect exists also for slower ramp speeds and is more pronounced for the SU(6) gas. It is presumably caused by a reduced mass flow upon entering the Mott regime. In addition to the observed entropy increase,
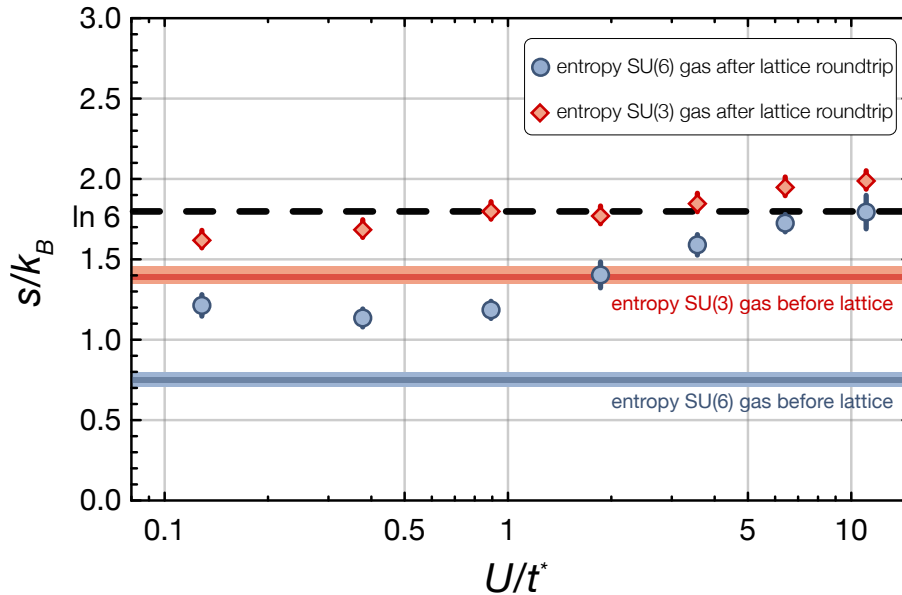
Figure 7.12: Entropy per particle *s* of the SU(6) and SU(3)-symmetric gas before and after the lattice round-trip sequence for various interaction strengths. The blue and red line show the entropy of the SU(6) and SU(3) gas respectively, measured in the bulk before loading the Fermi gas into the lattice. Blue points (SU(6) gas) and red diamonds (SU(3) gas) denote the entropy measurements after the round trip, when loading the atoms into the lattice and back to the bulk. The entropy of the gas in the lattice is constrained to the region between the entropy after the round trip and the bulk measurement before lattice loading. The entropy of the SU(6) gas in the lattice with our system parameters and fully random spin orientations possesses an entropy per particle close to $s/k_B = \ln 6$ (black line). Error bars and colored shaded regions are the s.e.m. of the temperature measurements.

we measure a specific entropy of the SU(6) gas that is at or below the maximum spin entropy per particle, $s_{spin} = k_B \ln(6)$, even after a full round trip, which includes the second reversed ramp. For the atom number used in our experiment we expect an entropy per particle of $s = k_B \ln(6)$ in the lattice for an SU(6) gas with random spin orientation between sites. Therefore, as a maximum spin entropy implies random spin orientations between sites, this indicates that partial, short-range spin correlations between neighboring lattice sites must be present in the SU(6) case.

The entropy per particle measured in the round-trip experiment can be compared to the corresponding entropy that is obtained from the fitted temperature of the HTSE model. In the limit of its validity, the HTSE model yields a higher entropy for the SU(6) gas in the lattice ($s_H/k_B \simeq 2.4$) compared to the round-trip experiment although the model fits the density profile for the gas quite well. An explanation for the observed behavior could be that the suppression of mass flow close to the

Mott regime prevents the formation of sharp Mott shell edges, yielding a higher fitted temperature and therefore a higher entropy when the density distribution freezes out. Similar effects, e.g. a reduced mass transport after expansion from a lattice potential of a fermionic band-insulating state, have been reported already at modest interactions for a two-component Fermi gas [248]. Nevertheless, the measured entropy after the round trip indicates that this non-adiabatic process would have to be mostly reversible in order to explain the fact that the entropy after the round trip is below the one obtained from the HTSE model fit in the lattice.

The discrepancy between the entropy obtained from the round-trip experiment and the HTSE model exists only for the SU(6) gas. As explained when discussing the equations of state in the section above, the temperature of the SU(3) gas in the lattice is higher due to the weaker Pomeranchuk cooling effect. Because of this effect, the corresponding entropy per particle of the SU(3) gas is above the spin entropy $k_B \ln(3)$. Due to the higher temperature in the lattice, we observe therefore a wider metallic region and the entropy estimate with the HTSE model for this temperature yields $s_H/k_B \simeq 1.9$, which in this case is compatible with the measured entropy per particle in the round-trip experiment. In addition, the observed entropy increase in the round-trip experiment is smaller for the SU(3) gas and approximately $0.35k_B$ compared to $0.6k_B$ in the SU(6) case. A possible explanation for the different behavior of the two gases is a reduced mass transport accompanied by a freezing of the density distribution, which becomes only relevant at low temperatures such as in the SU(6) case. However, the origin of this effect remains to be understood.

7.3.3 Three-body losses

During the course of the measurements, we observed an atom loss occurring at very high densities in the lattice. We attribute this loss to three-body recombinations. To our knowledge, the three-body recombination rate has not been determined for ^{173}Yb ground-state atoms. A knowledge of this rate is actually useful for estimating the experimental feasibility of implementing e.g. Heisenberg spin Hamiltonians or SU(N) Hubbard models with fillings higher than two [63, 151, 162].

At fillings above $nd^3 = 2$ we observe a fast, lattice-depth-dependent decay of atoms in the central region of the lattice, in addition to a slow decay of atoms due to the vacuum lifetime and lattice heating. The observed atom loss is illustrated in Fig. 7.13 for a $15\,E_r$ deep lattice. The atom loss is modeled with the following rate equation

$$
\begin{aligned}
n_0(t) &= \gamma_v n_1(t) + \gamma_3 n_3(t) \\
n_1(t) &= -\gamma_v n_1(t) + 2\gamma_v n_2(t) \\
n_2(t) &= -2\gamma_v n_2(t) + 3\gamma_v n_3(t) \\
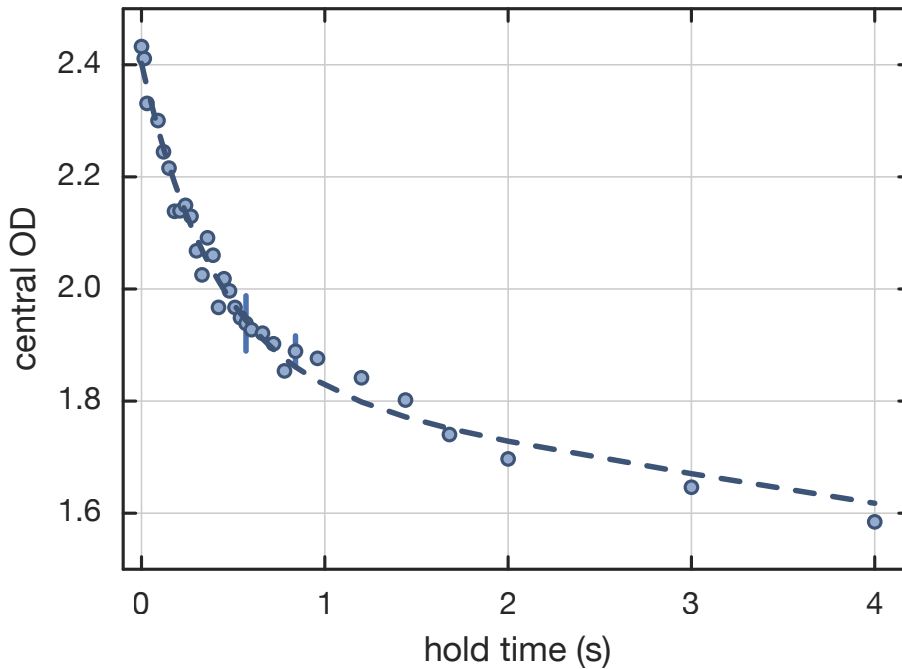n_3(t) &= -3\gamma_v n_3(t) - 3\gamma_3 n_3(t),
\end{aligned} \tag{7.6}
$$

Figure 7.13: Atom loss in a $15E_r$ deep optical lattice at high densities. The plot shows the mean optical density in the center of the cloud in a region of $5 \times 5\,\mu$m. The dashed curve is a double exponential fit given by Eq. 7.7 with $\tau_3 = 340\,\text{ms}$, $\tau_v = 31\,\text{s}$ and $n_d/n_3 = 3.84$.

where $n_{0,1,2,3}$ are the densities for empty, single, doubly and triply occupied lattice sites and $\gamma_{v,3}$ denotes the loss rate due to the finite vacuum lifetime and three-particle recombination respectively. Under the assumption that the three-body loss rate is much higher than the vacuum loss rate, $\gamma_v \ll \gamma_3$, the solution to the rate equation can be modeled by a double exponential decay to good approximation.

We therefore determine the loss rate by fitting a double exponential decay to the central density of the cloud

$$n(t) = n_d * e^{-t/\tau_v} + n_3 * e^{-t(3/\tau_v + 1/\tau_3)}. \tag{7.7}$$

In this equation, $n_d = n_1 + n_2$ denotes the density of singly and doubly occupied lattice sites, n_3 denotes the density of triply occupied sites, $\tau_v = 1/\gamma_v$ is the decay due to the finite vacuum lifetime and technical heating and $\tau_3 = 1/\gamma_3$ denotes the three-body loss timescale. For the lattice depth $V = 15E_r$ we extract a loss rate $\gamma_3 = 2.4(3)\,\text{Hz}$ and a slow vacuum decay $\gamma_v \approx 32\,\text{mHz}$. The three-body loss rate is expected to scale with the lattice depth as

$$\gamma_3 = \beta_3 \int d^3\mathbf{x}\, w(\mathbf{x})^6, \tag{7.8}$$

where $w(\mathbf{x})$ is the lattice-depth-dependent Wannier function and β_3 the three-body
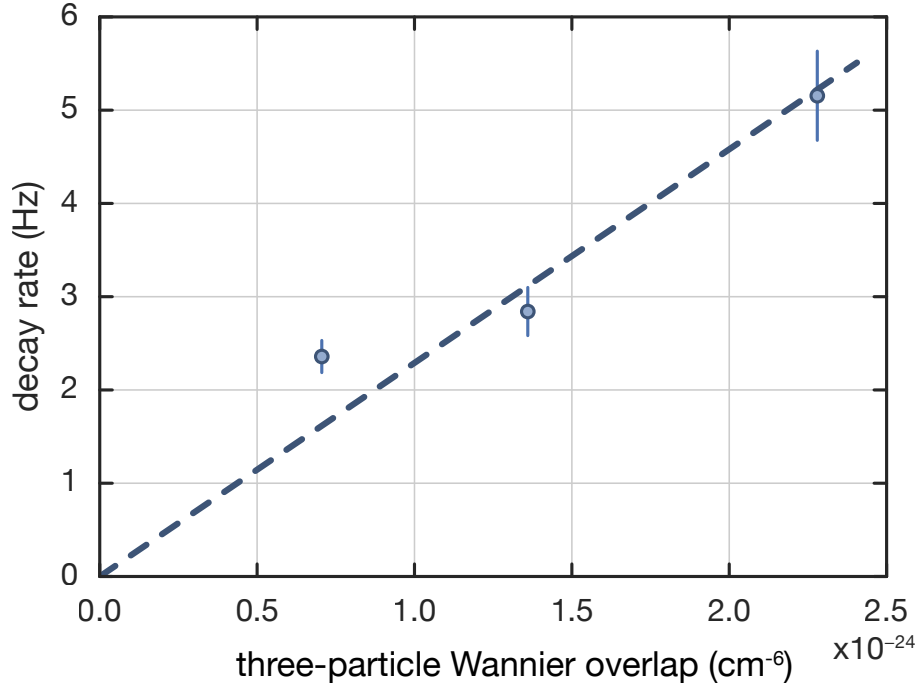
Figure 7.14: Particle decay rate $\gamma_3 = 1/\tau_3$ measured for different lattice depths as a function of the three-particle Wannier overlap. The dashed line shows the linear regression through the data points yielding a three-body loss coefficient $\beta_3 = 2.1 \pm 0.2 \times 10^{-29}\,\mathrm{cm}^6/\mathrm{s}$.

loss coefficient. Fig. 7.14 illustrates the measured loss rate for three different lattice depths as a function of the lattice depth dependent Wannier overlap $\int d^3\mathbf{x}\,w(\mathbf{x})^6$. A linear regression yields a three-body loss coefficient $\beta_3 = 2.1 \pm 0.2 \times 10^{-29}\,\mathrm{cm}^6/\mathrm{s}$. This value is similar to the loss coefficient that was measured for alkali atoms [249], e.g. for ^{87}Rb a value of $\beta_3 \approx 1.8 \pm 0.5 \times 10^{-29}\,\mathrm{cm}^6/\mathrm{s}$ was found [250].

In the limit of a weakly bound molecular state in the interatomic potential, which is characterized by a large positive scattering length for two-particle collisions, a scaling relation of the three-body loss coefficient with the scattering length can be given [251]

$$\beta_3^{theo} = \frac{3.9\hbar a^4}{m}. \tag{7.9}$$

Here m denotes the atom mass and a the scattering length of the atom pair. This theoretical scaling with a^4 has also been confirmed experimentally in a measurement with ^{133}Cs where a Feshbach resonance was used to tune the scattering length [252].

Equation 7.9 holds in the case of a weakly bound diatomic molecular state with binding energy ϵ_0 where the size of the formed molecule l is larger than the characteristic interaction radius R_e of the colliding atom pair, $l \gg R_e$. The scattering length in this limit can then be expressed by $a = \hbar/\sqrt{m\epsilon_0} \sim l$. For large scattering lengths

the effective potential for three-body collisions turns out to be independent from the exact shape of the interaction potential at low energies $E \ll \epsilon_0$. The interaction radius can be estimated by the Van der Waals radius $R_e = (mC_6/\hbar^2)^{1/4}/2$. For ^{173}Yb this coefficient is $C_6 = 1929(29) \, a_0$ [253] and we obtain $R_e \simeq 79 \, a_0$, which is smaller than the scattering length $a = 200 \, a_0$ and justifies the use of Eq. 7.9. By using this equation, we obtain $\beta_3^{theo} = 1.8 \times 10^{-29} \, \text{cm}^6/\text{s}$, which is in quite good agreement with the experiment value.

Chapter 8

Conclusion and outlook

In this thesis, we reported on the experimental study of the equation of state (EoS) of the 3D SU(N) Fermi-Hubbard model for different interaction regimes. The SU(N)-symmetric interactions of the ground state and the lowest meta-stable state in ytterbium allow probing many-body physics with enlarged spin symmetry. These models extend the conventional spin-1/2 case, which is usually studied in condensed matter physics and are expected to show novel types of exotic phases in the low temperature regime.

We demonstrated that fermionic ytterbium atoms in an optical lattice offer a highly tunable and versatile system for the realization of the SU(N) Fermi-Hubbard model. Owing to the optical resolution of the imaging system, we were able to measure local observables of the Fermi gas. In this way, the presence of Mott shells in a high spin system could be directly revealed for sufficiently strong interactions. Using the inverse Abel transformation, we obtained the density of the atomic sample in a 3D lattice, which allowed us to acquire model-free access to the equation of state of the gas. The equation of state and the local compressibility of the system were presented for different interaction regimes by tuning the interaction strength in the optical lattice. This constitutes the first measurement of the EoS of an SU(N) Fermi gas and the obtained results reach beyond currently available models. The behavior in the weakly interacting regime could be understood qualitatively by comparing the system with Fermi liquid theory. In the strongly interacting regime, we compared the measured EoS to a low tunneling model and found direct evidence of an enhanced Pomeranchuk cooling effect that depends on the number of spin components. Moreover, by using the local compressibility of the gas, we investigated the emergence of Mott shells for an SU(3) and SU(6) gas as a function of interaction and obtained good agreement with a theoretical prediction of the Mott crossover in the case of SU(3). In addition, the lattice loading process of the SU(N) Fermi gas was studied. We found a measurable increase in entropy upon entering the Mott insulating regime for the SU(6) gas, which we attribute to a suppression of mass

flow when reaching the strongly interacting regime. The origin of this effect remains to be understood. Nevertheless, we achieved a very low specific entropy below the maximum spin entropy of the SU(6) Fermi gas, which might enable the observation of spin-correlated phases of the SU(N) Fermi-Hubbard model in the low temperature regime.

Outlook

Ytterbium atoms in optical lattices provide a versatile tool to investigate single and two-orbital models with enlarged symmetry. The reported results and the low entropy that was achieved in the SU(6) gas may pave the way towards studying SU(N) spin Hamiltonians for different fillings and with varying number of spin components. This would allow to map out the phase diagram of the SU(N) Heisenberg model and would facilitate to probe spin chains in one dimension or spin Hamiltonians on square and cubic lattices [154, 162, 164, 254]. By extending the setup to prepare an ytterbium quantum gas in a single 2D layer, it would be possible to probe the equation of state without Abel inversion and investigate 2D Fermi-Hubbard physics. The large degeneracy of the ground state of such highly spin-symmetric systems is expected to lead to novel phases that range from states with complex magnetic long-range order – beyond Néel order – to chiral spin liquids [255]. These phases could potentially be probed with nuclear spin-dependent Bragg scattering or by noise correlations in time-of-flight [27, 28, 256]. In addition, lattice modulation spectroscopy might reveal nearest neighbor correlations already at intermediate temperatures above magnetic long-range order [257, 258]. Such short-range correlations are already expected for the low entropies, obtained for the SU(6) gas in the optical lattice.

In addition, the second orbital in ytterbium can be employed to extend these studies to two-orbital systems. For this, a state-selective lattice is ideal to implement the Kondo lattice Hamiltonian [58]. A large exchange coupling that was measured for ^{173}Yb [72] in addition to a favorable ratio of the elastic to inelastic scattering lengths can be used to access the regime of strong coupling in order to probe the Kondo insulator. The large coupling that was measured is favorable in this respect, as the overlap between the two orbitals can be reduced in a bichromatic lattice configuration to lower the coupling strength [230]. Moreover, a confinement-induced resonance in one dimension could be employed to change the magnitude as well as the sign of the coupling [180]. The ability to realize the Kondo lattice model (KLM) would allow investigating heavy Fermion properties as well as magnetic order with ultracold atoms that possess SU(N) symmetry. For weak couplings, the type of magnetic order, which is mediated by RKKY interaction, is expected to range from ferromagnetic to antiferromagnetic order and will depend on various system parameters such as the dimension, as explained in section 3.3. In this way, a better understanding of the phases and the phase transitions contained within this model

could be gained by exploiting state-dependent lattices and realizing a KLM quantum simulator. For this, the ability to probe the thermodynamic properties of the atomic sample as presented in this thesis will constitute a very useful tool to identify the different phases that are predicted by theory.

Furthermore, a recently measured orbital Feshbach resonance in ^{173}Yb allows studying two-orbital Fermi liquids for various interactions [76, 127]. This extends the range of systems that can be investigated as it overcomes the limitation of a fixed interaction strength between the two orbitals in alkaline earth-like atoms. This resonance features a two-gap Fermi superfluid for attractive interactions and is expected to possess a higher transition temperature for the superfluid compared to conventional wide magnetic Feshbach resonances that are used for alkali elements [126, 129]. Therefore, the equation of state of this superfluid is expected to differ from alkali systems and could possibly be measured with the same technique that permitted to address the EoS of the FHM that was presented in this thesis.

Appendix A

Retrieving the inverse Abel transformation from the pressure

In the case of a harmonic confinement potential, we can assume radial symmetry of the column density

$$\tilde{n}(x,y) = \int_{-\infty}^{\infty} n(x,y,z)dz. \tag{A.1}$$

Therefore, it is possible to parametrize the column density with r

$$r^2 = x^2 + \frac{\omega_y^2}{\omega_x^2}y^2 \tag{A.2}$$

$$\frac{\partial r}{x} = \frac{x}{r} \tag{A.3}$$

$$y = \frac{\omega_x}{\omega_y}\sqrt{r^2 - x^2} \tag{A.4}$$

$$dy = \frac{\omega_x r dr}{\omega_y \sqrt{r^2 - x^2}} \tag{A.5}$$

The result of Eq. 7.4 derived from the pressure of the system can be rewritten

$$n(x) = -\frac{\omega_y \omega_z}{\omega_x^2 2\pi x} \int_{-\infty}^{\infty} \frac{\partial \tilde{n}(x,y)}{\partial x} dy \tag{A.6}$$

$$= -\frac{\omega_y \omega_z}{\omega_x^2 \pi x} \int_{0}^{\infty} \frac{\partial \tilde{n}(x,y)}{\partial x} dy \tag{A.7}$$

$$= -\frac{\omega_y \omega_z}{\omega_x^2 \pi x} \int_{0}^{\infty} \frac{\partial \tilde{n}(r)}{\partial r} \frac{\partial r}{\partial x} dy. \tag{A.8}$$

By substituting Eq. A.4 and Eq. A.5 into Eq. A.8, we obtain

$$n(x) = -\frac{\omega_y \omega_z}{\omega_x^2 \pi x} \int_0^\infty \frac{\partial \tilde{n}(r)}{\partial r} \frac{\partial r}{\partial x} dy \tag{A.9}$$

$$= -\frac{\omega_z}{\pi \omega_x} \int_x^\infty \frac{\partial \tilde{n}(r)}{\partial r} \frac{dr}{\sqrt{r^2 - x^2}}. \tag{A.10}$$

Eq. A.10 is the inverse Abel formula as given in Eq. 7.1 for $\rho = x$ and $y = 0$ that accounts with the correct rescaling ω_z/ω_x for the trap aspect ratio.

Bibliography

[1] V. L. Ginzburg and L. D. Landau, "On the Theory of superconductivity", Zh. Eksp. Teor. Fiz. **20**, 1064–1082 (1950) (See page: 1).

[2] J. Bardeen, L. N. Cooper, and J. R. Schrieffer, "Theory of Superconductivity", Physical Review **108**, 1175–1204 (1957) (See page: 1).

[3] D. M. Lee, "The extraordinary phases of liquid ^{3}He", Reviews of Modern Physics **69**, 645–666 (1997) (See pages: 1, 39).

[4] J. Hubbard, "Electron Correlations in Narrow Energy Bands", Proceedings of the Royal Society of London A: Mathematical, Physical and Engineering Sciences **276**, 238–257 (1963) (See page: 1).

[5] P. W. Anderson, "The Resonating Valence Bond State in La2CuO4 and Superconductivity", **235**, 1196–1198 (1987) (See pages: 1, 30).

[6] I. Affleck and J. B. Marston, "Large-n limit of the Heisenberg-Hubbard model: Implications for high-T_c superconductors", Physical Review B **37**, 3774–3777 (1988) (See pages: 1, 30).

[7] V. Z. Kresin and S. A. Wolf, "*Colloquium*: Electron-lattice interaction and its impact on high T_c superconductivity", Reviews of Modern Physics **81**, 481–501 (2009) (See page: 1).

[8] A. W. Sleight, J. L. Gillson, and P. E. Bierstedt, "High-temperature superconductivity in the BaPb1-xBixO3 systems", Solid State Communications **17**, 27–28 (1975) (See page: 1).

[9] J. G. Bednorz and K. A. Müller, "Possible highT_c superconductivity in the Ba–La–Cu–O system", Zeitschrift für Physik B Condensed Matter **64**, 189–193 (1986) (See page: 1).

[10] P. A. Lee, N. Nagaosa, and X.-G. Wen, "Doping a Mott insulator: Physics of high-temperature superconductivity", Reviews of Modern Physics **78**, 17–85 (2006) (See page: 1).

[11] W. Wu, J. Cheng, K. Matsubayashi, P. Kong, F. Lin, C. Jin, N. Wang, Y. Uwatoko, and J. Luo, "Superconductivity in the vicinity of antiferromagnetic order in CrAs", Nature Communications **5**, 5508 (2014) (See page: 1).

[12] M. H. Anderson, J. R. Ensher, M. R. Matthews, C. E. Wieman, and E. A. Cornell, "Observation of Bose-Einstein Condensation in a Dilute Atomic Vapor", **269**, 198–201 (1995) (See page: 2).

[13] K. B. Davis, M.-O. Mewes, M. R. Andrews, N. J. van Druten, D. S. Durfee, D. M. Kurn, and W. Ketterle, "Bose-Einstein Condensation in a Gas of Sodium Atoms", Physical Review Letters **75**, 3969–3973 (1995) (See page: 2).

[14] C. C. Bradley, C. A. Sackett, J. J. Tollett, and R. G. Hulet, "Evidence of Bose-Einstein Condensation in an Atomic Gas with Attractive Interactions", Physical Review Letters **75**, 1687–1690 (1995) (See page: 2).

[15] B. DeMarco and D. S. Jin, "Onset of Fermi Degeneracy in a Trapped Atomic Gas", **285**, 1703–1706 (1999) (See page: 2).

[16] S. Inouye, M. R. Andrews, J. Stenger, H.-J. Miesner, D. M. Stamper-Kurn, and W. Ketterle, "Observation of Feshbach resonances in a Bose–Einstein condensate", **392**, 151–154 (1998) (See page: 2).

[17] T. Bourdel, J. Cubizolles, L. Khaykovich, K. M. F. Magalhães, S. J. J. M. F. Kokkelmans, G. V. Shlyapnikov, and C. Salomon, "Measurement of the Interaction Energy near a Feshbach Resonance in a ^{6}Li Fermi Gas", Physical Review Letters **91**, 020402 (2003) (See page: 2).

[18] K. M. O'Hara, S. L. Hemmer, M. E. Gehm, S. R. Granade, and J. E. Thomas, "Observation of a Strongly Interacting Degenerate Fermi Gas of Atoms", (2002) `10.1126/science.1079107` (See page: 2).

[19] C. A. Regal, C. Ticknor, J. L. Bohn, and D. S. Jin, "Creation of ultracold molecules from a Fermi gas of atoms", **424**, 47–50 (2003) (See page: 2).

[20] S. Jochim, M. Bartenstein, A. Altmeyer, G. Hendl, C. Chin, J. H. Denschlag, and R. Grimm, "Pure Gas of Optically Trapped Molecules Created from Fermionic Atoms", Physical Review Letters **91**, 240402 (2003) (See page: 2).

[21] D. Jaksch, C. Bruder, J. I. Cirac, C. W. Gardiner, and P. Zoller, "Cold Bosonic Atoms in Optical Lattices", Physical Review Letters **81**, 3108–3111 (1998) (See page: 2).

[22] U. Schneider, L. Hackermüller, S. Will, T. Best, I. Bloch, T. A. Costi, R. W. Helmes, D. Rasch, and A. Rosch, "Metallic and Insulating Phases of Repulsively Interacting Fermions in a 3D Optical Lattice", **322**, 1520–1525 (2008) (See pages: 2, 103).

[23] R. Jördens, N. Strohmaier, K. Günter, H. Moritz, and T. Esslinger, "A Mott insulator of fermionic atoms in an optical lattice", **455**, 204–207 (2008) (See pages: 2, 103).

[24] M. Imada, A. Fujimori, and Y. Tokura, "Metal-insulator transitions", Reviews of Modern Physics **70**, 1039–1263 (1998) (See pages: 2, 30).

[25] R. P. Feynman, "Simulating physics with computers", International Journal of Theoretical Physics **21**, 467–488 (1982) (See page: 2).

[26] M. Greiner, I. Bloch, O. Mandel, T. W. Hänsch, and T. Esslinger, "Exploring Phase Coherence in a 2D Lattice of Bose-Einstein Condensates", Physical Review Letters **87**, 160405 (2001) (See page: 2).

[27] S. Fölling, F. Gerbier, A. Widera, O. Mandel, T. Gericke, and I. Bloch, "Spatial quantum noise interferometry in expanding ultracold atom clouds", **434**, 481–484 (2005) (See pages: 2, 126).

[28] T. Rom, T. Best, D. van Oosten, U. Schneider, S. Fölling, B. Paredes, and I. Bloch, "Free fermion antibunching in a degenerate atomic Fermi gas released from an optical lattice", **444**, 733–736 (2006) (See pages: 2, 126).

[29] J. F. Sherson, C. Weitenberg, M. Endres, M. Cheneau, I. Bloch, and S. Kuhr, "Single-atom-resolved fluorescence imaging of an atomic Mott insulator", **467**, 68–72 (2010) (See pages: 2, 68, 107).

[30] W. S. Bakr, A. Peng, M. E. Tai, R. Ma, J. Simon, J. I. Gillen, S. Fölling, L. Pollet, and M. Greiner, "Probing the Superfluid–to–Mott Insulator Transition at the Single-Atom Level", **329**, 547–550 (2010) (See pages: 2, 68, 107).

[31] S. Fölling, S. Trotzky, P. Cheinet, M. Feld, R. Saers, A. Widera, T. Müller, and I. Bloch, "Direct observation of second-order atom tunnelling", **448**, 1029–1032 (2007) (See page: 2).

[32] J. Dalibard, F. Gerbier, G. Juzeliunas, and P. Öhberg, "*Colloquium* : Artificial gauge potentials for neutral atoms", Reviews of Modern Physics **83**, 1523–1543 (2011) (See page: 2).

[33] P. Soltan-Panahi, J. Struck, P. Hauke, A. Bick, W. Plenkers, G. Meineke, C. Becker, P. Windpassinger, M. Lewenstein, and K. Sengstock, "Multi-component quantum gases in spin-dependent hexagonal lattices", Nature Physics **7**, 434–440 (2011) (See page: 2).

[34] L. Tarruell, D. Greif, T. Uehlinger, G. Jotzu, and T. Esslinger, "Creating, moving and merging Dirac points with a Fermi gas in a tunable honeycomb lattice", **483**, 302–305 (2012) (See page: 2).

[35] J. Struck, C. Ölschläger, R. L. Targat, P. Soltan-Panahi, A. Eckardt, M. Lewenstein, P. Windpassinger, and K. Sengstock, "Quantum Simulation of Frustrated Classical Magnetism in Triangular Optical Lattices", **333**, 996–999 (2011) (See page: 2).

[36] K.-K. Ni, S. Ospelkaus, M. H. G. de Miranda, A. Pe'er, B. Neyenhuis, J. J. Zirbel, S. Kotochigova, P. S. Julienne, D. S. Jin, and J. Ye, "A High Phase-Space-Density Gas of Polar Molecules", **322**, 231–235 (2008) (See page: 3).

[37] J. G. Danzl, E. Haller, M. Gustavsson, M. J. Mark, R. Hart, N. Bouloufa, O. Dulieu, H. Ritsch, and H.-C. Nägerl, "Quantum Gas of Deeply Bound Ground State Molecules", **321**, 1062–1066 (2008) (See page: 3).

[38] F. Lang, K. Winkler, C. Strauss, R. Grimm, and J. H. Denschlag, "Ultracold Triplet Molecules in the Rovibrational Ground State", Physical Review Letters **101**, 133005 (2008) (See page: 3).

[39] T. Lahaye, C. Menotti, L. Santos, M. Lewenstein, and T. Pfau, "The physics of dipolar bosonic quantum gases", Reports on Progress in Physics **72**, 126401 (2009) (See page: 3).

[40] L. D. Carr, D. DeMille, R. V. Krems, and J. Ye, "Cold and ultracold molecules: science, technology and applications", New Journal of Physics **11**, 055049 (2009) (See page: 3).

[41] M. Lu, N. Q. Burdick, and B. L. Lev, "Quantum Degenerate Dipolar Fermi Gas", Physical Review Letters **108**, 215301 (2012) (See page: 3).

[42] K. Aikawa, A. Frisch, M. Mark, S. Baier, R. Grimm, and F. Ferlaino, "Reaching Fermi Degeneracy via Universal Dipolar Scattering", Physical Review Letters **112**, 010404 (2014) (See page: 3).

[43] M. Weidemüller, "Rydberg atoms: There can be only one", Nature Physics **5**, 91–92 (2009) (See page: 3).

[44] M. Saffman, T. G. Walker, and K. Mølmer, "Quantum information with Rydberg atoms", Reviews of Modern Physics **82**, 2313–2363 (2010) (See page: 3).

[45] Y. Takasu, K. Maki, K. Komori, T. Takano, K. Honda, M. Kumakura, T. Yabuzaki, and Y. Takahashi, "Spin-Singlet Bose-Einstein Condensation of Two-Electron Atoms", Physical Review Letters **91**, 040404 (2003) (See pages: 3, 18).

[46] S. Kraft, F. Vogt, O. Appel, F. Riehle, and U. Sterr, "Bose-Einstein Condensation of Alkaline Earth Atoms: ^{40}Ca", Physical Review Letters **103**, 130401 (2009) (See page: 3).

[47] S. Stellmer, M. K. Tey, B. Huang, R. Grimm, and F. Schreck, "Bose-Einstein Condensation of Strontium", Physical Review Letters **103**, 200401 (2009) (See page: 3).

[48] Y. N. M. de Escobar, P. G. Mickelson, M. Yan, B. J. DeSalvo, S. B. Nagel, and T. C. Killian, "Bose-Einstein Condensation of ^{84}Sr", Physical Review Letters **103**, 200402 (2009) (See page: 3).

[49] S. Taie, R. Yamazaki, S. Sugawa, and Y. Takahashi, "An SU(6) Mott insulator of an atomic Fermi gas realized by large-spin Pomeranchuk cooling", Nature Physics **8**, 825–830 (2012) (See pages: 3, 41).

[50] N. Hinkley, J. A. Sherman, N. B. Phillips, M. Schioppo, N. D. Lemke, K. Beloy, M. Pizzocaro, C. W. Oates, and A. D. Ludlow, "An Atomic Clock with 10–18 Instability", **341**, 1215–1218 (2013) (See pages: 3, 91).

[51] B. J. Bloom, T. L. Nicholson, J. R. Williams, S. L. Campbell, M. Bishof, X. Zhang, W. Zhang, S. L. Bromley, and J. Ye, "An optical lattice clock with accuracy and stability at the 10-18 level", **506**, 71–75 (2014) (See pages: 3, 91).

[52] S. Bize, P. Laurent, M. Abgrall, H. Marion, I. Maksimovic, L. Cacciapuoti, J. Grünert, C. Vian, F. Pereira dos Santos, P. Rosenbusch, P. Lemonde, G. Santarelli, P. Wolf, A. Clairon, A. Luiten, M. Tobar, and C. Salomon, "Advances in atomic fountains", Comptes Rendus Physique, Fundamental metrology **5**, 829–843 (2004) (See page: 3).

[53] M. Fischer, N. Kolachevsky, M. Zimmermann, R. Holzwarth, T. Udem, T. W. Hänsch, M. Abgrall, J. Grünert, I. Maksimovic, S. Bize, H. Marion, F. P. D. Santos, P. Lemonde, G. Santarelli, P. Laurent, A. Clairon, C. Salomon, M. Haas, U. D. Jentschura, and C. H. Keitel, "New Limits on the Drift of Fundamental Constants from Laboratory Measurements", Physical Review Letters **92**, 230802 (2004) (See page: 3).

[54] T. Rosenband, D. B. Hume, P. O. Schmidt, C. W. Chou, A. Brusch, L. Lorini, W. H. Oskay, R. E. Drullinger, T. M. Fortier, J. E. Stalnaker, S. A. Diddams, W. C. Swann, N. R. Newbury, W. M. Itano, D. J. Wineland, and J. C. Bergquist, "Frequency Ratio of Al+ and Hg+ Single-Ion Optical Clocks; Metrology at the 17th Decimal Place", **319**, 1808–1812 (2008) (See page: 3).

[55] P. W. Graham, J. M. Hogan, M. A. Kasevich, and S. Rajendran, "New Method for Gravitational Wave Detection with Atomic Sensors", Physical Review Letters **110**, 171102 (2013) (See page: 3).

[56] LIGO Scientific Collaboration and Virgo Collaboration et al., "Observation of Gravitational Waves from a Binary Black Hole Merger", Physical Review Letters **116**, 061102 (2016) (See page: 3).

[57] A. V. Gorshkov, A. M. Rey, A. J. Daley, M. M. Boyd, J. Ye, P. Zoller, and M. D. Lukin, "Alkaline-Earth-Metal Atoms as Few-Qubit Quantum Registers", Physical Review Letters **102**, 110503 (2009) (See page: 4).

[58] A. V. Gorshkov, M. Hermele, V. Gurarie, C. Xu, P. S. Julienne, J. Ye, P. Zoller, E. Demler, M. D. Lukin, and A. M. Rey, "Two-orbital SU(N) magnetism with ultracold alkaline-earth atoms", Nature Physics **6**, 289–295 (2010) (See pages: 4, 16, 44, 47, 126).

[59] A. J. Daley, M. M. Boyd, J. Ye, and P. Zoller, "Quantum Computing with Alkaline-Earth-Metal Atoms", Physical Review Letters **101**, 170504 (2008) (See page: 4).

[60] N. R. Cooper, "Optical Flux Lattices for Ultracold Atomic Gases", Physical Review Letters **106**, 175301 (2011) (See page: 4).

[61] M. Knap, A. Shashi, Y. Nishida, A. Imambekov, D. A. Abanin, and E. Demler, "Time-Dependent Impurity in Ultracold Fermions: Orthogonality Catastrophe and Beyond", Physical Review X **2**, 041020 (2012) (See page: 4).

[62] M. Hermele, V. Gurarie, and A. M. Rey, "Mott Insulators of Ultracold Fermionic Alkaline Earth Atoms: Underconstrained Magnetism and Chiral Spin Liquid", Physical Review Letters **103**, 135301 (2009) (See pages: 4, 30).

[63] M. Hermele and V. Gurarie, "Topological liquids and valence cluster states in two-dimensional SU(N) magnets", Physical Review B **84**, 174441 (2011) (See pages: 4, 43, 44, 121).

[64] C. Honerkamp and W. Hofstetter, "Ultracold Fermions and the SU(N) Hubbard Model", Physical Review Letters **92**, 170403 (2004) (See pages: 4, 30, 31, 42).

[65] Y. Tokura and N. Nagaosa, "Orbital Physics in Transition-Metal Oxides", **288**, 462–468 (2000) (See pages: 4, 30).

[66] Á. Rapp, G. Zaránd, C. Honerkamp, and W. Hofstetter, "Color Superfluidity and "Baryon" Formation in Ultracold Fermions", Physical Review Letters **98**, 160405 (2007) (See pages: 4, 31).

[67] D. Banerjee, M. Bögli, M. Dalmonte, E. Rico, P. Stebler, U.-J. Wiese, and P. Zoller, "Atomic Quantum Simulation of **U**(N) and SU(N) Non-Abelian Lattice Gauge Theories", Physical Review Letters **110**, 125303 (2013) (See page: 4).

[68] M. Foss-Feig, M. Hermele, and A. M. Rey, "Probing the Kondo lattice model with alkaline-earth-metal atoms", Physical Review A **81**, 051603 (2010) (See page: 4).

[69] P. Gegenwart, Q. Si, and F. Steglich, "Quantum criticality in heavy-fermion metals", Nature Physics **4**, 186–197 (2008) (See page: 4).

[70] S. Sykora and K. W. Becker, "Heavy fermion properties of the Kondo Lattice model", Scientific Reports **3** (2013) `10.1038/srep02691` (See pages: 4, 98).

[71] K. I. Kugel' and D. I. Khomskii, "The Jahn-Teller effect and magnetism: transition metal compounds", Soviet Physics Uspekhi **25**, 231 (1982) (See page: 4).

[72] F. Scazza, C. Hofrichter, M. Höfer, P. C. De Groot, I. Bloch, and S. Fölling, "Observation of two-orbital spin-exchange interactions with ultracold SU(N)-symmetric fermions", Nature Physics **10**, 779–784 (2014) (See pages: 5, 6, 15, 18, 49, 91, 94, 126).

[73] F. Scazza, "Probing SU(N)-symmetric orbital interactions with ytterbium Fermi gases in optical lattices", PhD thesis (Ludwig-Maximilians-Universität München, Feb. 23, 2015) (See pages: 5, 9, 51, 54, 59, 94).

[74] M. Spießl, "Aufbau und Charakterisierung eines Verdopplungsresonators für den Ytterbium-Uhrenübergang", Bachelor's thesis (Ludwig-Maximilians-Universität, München, 2011) (See page: 5).

[75] C. Hofrichter, L. Riegger, F. Scazza, M. Höfer, D. R. Fernandes, I. Bloch, and S. Fölling, "Direct Probing of the Mott Crossover in the SU(N) Fermi-Hubbard Model", Physical Review X **6**, 021030 (2016) (See pages: 6, 104, 112).

[76] M. Höfer, L. Riegger, F. Scazza, C. Hofrichter, D. R. Fernandes, M. M. Parish, J. Levinsen, I. Bloch, and S. Fölling, "Observation of an Orbital Interaction-Induced Feshbach Resonance in ^{173}Yb", Physical Review Letters **115**, 265302 (2015) (See pages: 6, 18, 20, 127).

[77] D. R. Lide, "The Elements", in *CRC Handbook of Chemistry and Physics, 81st Edition* (CRC Press, June 6, 2000) (See page: 8).

[78] J. R. de Laeter and N. Bukilic, "The isotopic composition and atomic weight of ytterbium", International Journal of Mass Spectrometry **252**, 222–227 (2006) (See page: 8).

[79] J. E. Sansonetti and W. C. Martin, "Handbook of Basic Atomic Spectroscopic Data", Journal of Physical and Chemical Reference Data **34**, 1559–2259 (2005) (See page: 8).

[80] Y. Takasu, K. Komori, K. Honda, M. Kumakura, T. Yabuzaki, and Y. Takahashi, "Photoassociation Spectroscopy of Laser-Cooled Ytterbium Atoms", Physical Review Letters **93**, 123202 (2004) (See page: 9).

[81] S. G. Porsev and A. Derevianko, "Hyperfine quenching of the metastable $^{3}P_{0,2}$ states in divalent atoms", Physical Review A **69**, 042506 (2004) (See pages: 9, 14).

[82] K. Beloy, J. A. Sherman, N. D. Lemke, N. Hinkley, C. W. Oates, and A. D. Ludlow, "Determination of the $5d6s\ ^3D_1$ state lifetime and blackbody-radiation clock shift in Yb", Physical Review A **86**, 051404 (2012) (See pages: 9, 10, 24).

[83] S. G. Porsev, Y. G. Rakhlina, and M. G. Kozlov, "Electric-dipole amplitudes, lifetimes, and polarizabilities of the low-lying levels of atomic ytterbium", Physical Review A **60**, 2781–2785 (1999) (See page: 9).

[84] M. Baumann, M. Geisler, H. Liening, and H. Lindel, "Lifetime- and quantum-beat measurements in the excited 4f14 6s6d D-states in the Yb I-spectrum using stepwise laser excitation", Optics Communications **38**, 259–261 (1981) (See page: 9).

[85] J. W. Cho, H.-g. Lee, S. Lee, J. Ahn, W.-K. Lee, D.-H. Yu, S. K. Lee, and C. Y. Park, "Optical repumping of triplet-P states enhances magneto-optical trapping of ytterbium atoms", Physical Review A **85**, 035401 (2012) (See pages: 9, 11).

[86] D. Das, S. Barthwal, A. Banerjee, and V. Natarajan, "Absolute frequency measurements in Yb with 0.08 ppb uncertainty: Isotope shifts and hyperfine structure in the 399-nm $^1S_0 \to^1 P_1$ line", Physical Review A **72**, 032506 (2005) (See page: 11).

[87] K. Pandey, A. K. Singh, P. V. K. Kumar, M. V. Suryanarayana, and V. Natarajan, "Isotope shifts and hyperfine structure in the 555.8-nm $^1S_0 \to ^3P_1$ line of Yb", Physical Review A **80**, 022518 (2009) (See page: 11).

[88] N. Poli, Z. W. Barber, N. D. Lemke, C. W. Oates, L. S. Ma, J. E. Stalnaker, T. M. Fortier, S. A. Diddams, L. Hollberg, J. C. Bergquist, A. Brusch, S. Jefferts, T. Heavner, and T. Parker, "Frequency evaluation of the doubly forbidden $^1S_0 \to^3 P_0$ transition in bosonic ^{174}Yb", Physical Review A **77**, 050501 (2008) (See pages: 11, 13).

[89] C. W. Hoyt, Z. W. Barber, C. W. Oates, T. M. Fortier, S. A. Diddams, and L. Hollberg, "Observation and Absolute Frequency Measurements of the $^1S_0$-$^3P_0$ Optical Clock Transition in Neutral Ytterbium", Physical Review Letters **95**, 083003 (2005) (See page: 11).

[90] C. J. Bowers, D. Budker, E. D. Commins, D. DeMille, S. J. Freedman, A.-T. Nguyen, S.-Q. Shang, and M. Zolotorev, "Experimental investigation of excited-state lifetimes in atomic ytterbium", Physical Review A **53**, 3103–3109 (1996) (See page: 10).

[91] N. Poli, R. E. Drullinger, G. Ferrari, J. Léonard, F. Sorrentino, and G. M. Tino, "Cooling and trapping of ultracold strontium isotopic mixtures", Physical Review A **71**, 061403 (2005) (See page: 11).

[92] K. Honda, Y. Takahashi, T. Kuwamoto, M. Fujimoto, K. Toyoda, K. Ishikawa, and T. Yabuzaki, "Magneto-optical trapping of Yb atoms and a limit on the branching ratio of the $^1P_1$ state", Physical Review A **59**, R934–R937 (1999) (See page: 11).

[93] P. G. Mickelson, Y. N. M. d. Escobar, P. Anzel, B. J. DeSalvo, S. B. Nagel, A. J. Traverso, M. Yan, and T. C. Killian, "Repumping and spectroscopy of laser-cooled Sr atoms using the (5s5p) 3 P 2 –(5s4d) 3 D 2 transition", Journal of Physics B: Atomic, Molecular and Optical Physics **42**, 235001 (2009) (See page: 11).

[94] E. Luc-Koenig, "Relativistic effects on transition probabilities $^3P_1 \rightarrow {}^1S_0$ for group II elements", Journal of Physics B: Atomic and Molecular Physics **7**, 1052 (1974) (See page: 11).

[95] T. Kuwamoto, K. Honda, Y. Takahashi, and T. Yabuzaki, "Magneto-optical trapping of Yb atoms using an intercombination transition", Physical Review A **60**, R745–R748 (1999) (See page: 11).

[96] J. Migdalek and W. E. Baylis, "Relativistic transition probabilities and lifetimes of low-lying levels in ytterbium", Journal of Physics B: Atomic, Molecular and Optical Physics **24**, L99 (1991) (See page: 11).

[97] H. Stoehr, F. Mensing, J. Helmcke, and U. Sterr, "Diode laser with 1 Hz linewidth", Optics Letters **31**, 736 (2006) (See page: 13).

[98] A. D. Ludlow, X. Huang, M. Notcutt, T. Zanon-Willette, S. M. Foreman, M. M. Boyd, S. Blatt, and J. Ye, "Compact, thermal-noise-limited optical cavity for diode laser stabilization at 1×10^{-15}", Optics Letters **32**, 641 (2007) (See page: 13).

[99] J. Alnis, A. Matveev, N. Kolachevsky, T. Udem, and T. W. Hänsch, "Sub-hertz linewidth diode lasers by stabilization to vibrationally and thermally compensated ultralow-expansion glass Fabry-Pérot cavities", Physical Review A **77**, 053809 (2008) (See page: 13).

[100] S. G. Porsev, A. Derevianko, and E. N. Fortson, "Possibility of an optical clock using the $6^1S_0 \rightarrow 6^3P_0^o$ transition in ^{171,173}Yb atoms held in an optical lattice", Physical Review A **69**, 021403 (2004) (See page: 13).

[101] A. V. Taichenachev, V. I. Yudin, C. W. Oates, C. W. Hoyt, Z. W. Barber, and L. Hollberg, "Magnetic Field-Induced Spectroscopy of Forbidden Optical Transitions with Application to Lattice-Based Optical Atomic Clocks", Physical Review Letters **96**, 083001 (2006) (See pages: 14, 100).

[102] Z. W. Barber, C. W. Hoyt, C. W. Oates, L. Hollberg, A. V. Taichenachev, and V. I. Yudin, "Direct Excitation of the Forbidden Clock Transition in Neutral ^{174}Yb Atoms Confined to an Optical Lattice", Physical Review Letters **96**, 083002 (2006) (See page: 14).

[103] S. Kato, S. Sugawa, K. Shibata, R. Yamamoto, and Y. Takahashi, "Control of Resonant Interaction between Electronic Ground and Excited States", Physical Review Letters **110**, 173201 (2013) (See page: 14).

[104] K. Shibata, R. Yamamoto, Y. Seki, and Y. Takahashi, "Optical spectral imaging of a single layer of a quantum gas with an ultranarrow optical transition", Physical Review A **89**, 031601 (2014) (See page: 14).

[105] R. Yamamoto, J. Kobayashi, T. Kuno, K. Kato, and Y. Takahashi, "An ytterbium quantum gas microscope with narrow-line laser cooling", New Journal of Physics **18**, 023016 (2016) (See page: 14).

[106] T. D. Lee, K. Huang, and C. N. Yang, "Eigenvalues and Eigenfunctions of a Bose System of Hard Spheres and Its Low-Temperature Properties", Physical Review **106**, 1135–1145 (1957) (See page: 15).

[107] S.-K. Yip and T.-L. Ho, "Zero sound modes of dilute Fermi gases with arbitrary spin", Physical Review A **59**, 4653–4656 (1999) (See page: 15).

[108] N. Bornemann, P. Hyllus, and L. Santos, "Resonant Spin-Changing Collisions in Spinor Fermi Gases", Physical Review Letters **100**, 205302 (2008) (See page: 16).

[109] J. S. Krauser, J. Heinze, N. Fläschner, S. Götze, O. Jürgensen, D.-S. Lühmann, C. Becker, and K. Sengstock, "Coherent multi-flavour spin dynamics in a fermionic quantum gas", Nature Physics **8**, 813–818 (2012) (See page: 16).

[110] C. Wu, J.-p. Hu, and S.-c. Zhang, "Exact SO(5) Symmetry in the Spin-3/2 Fermionic System", Physical Review Letters **91**, 186402 (2003) (See page: 16).

[111] S.-K. Yip, B.-L. Huang, and J.-S. Kao, "Theory of SU(N) Fermi liquids", Physical Review A **89**, 043610 (2014) (See pages: 17, 86).

[112] G. Pagano, M. Mancini, G. Cappellini, P. Lombardi, F. Schäfer, H. Hu, X.-J. Liu, J. Catani, C. Sias, M. Inguscio, and L. Fallani, "A one-dimensional liquid of fermions with tunable spin", Nature Physics **10**, 198–201 (2014) (See page: 17).

[113] M. Kitagawa, K. Enomoto, K. Kasa, Y. Takahashi, R. Ciuryło, P. Naidon, and P. S. Julienne, "Two-color photoassociation spectroscopy of ytterbium atoms and the precise determinations of *s*-wave scattering lengths", Physical Review A **77**, 012719 (2008) (See pages: 17, 18).

[114] T. Fukuhara, S. Sugawa, and Y. Takahashi, "Bose-Einstein condensation of an ytterbium isotope", Physical Review A **76**, 051604 (2007) (See page: 18).

[115] S. Sugawa, R. Yamazaki, S. Taie, and Y. Takahashi, "Bose-Einstein condensate in gases of rare atomic species", Physical Review A **84**, 011610 (2011) (See page: 18).

[116] N. D. Lemke, J. von Stecher, J. A. Sherman, A. M. Rey, C. W. Oates, and A. D. Ludlow, "*p*-Wave Cold Collisions in an Optical Lattice Clock", Physical Review Letters **107**, 103902 (2011) (See page: 18).

[117] G. Cappellini, M. Mancini, G. Pagano, P. Lombardi, L. Livi, M. Siciliani de Cumis, P. Cancio, M. Pizzocaro, D. Calonico, F. Levi, C. Sias, J. Catani, M. Inguscio, and L. Fallani, "Direct Observation of Coherent Interorbital Spin-Exchange Dynamics", Physical Review Letters **113**, 120402 (2014) (See page: 18).

[118] C. Chin, R. Grimm, P. Julienne, and E. Tiesinga, "Feshbach resonances in ultracold gases", Reviews of Modern Physics **82**, 1225–1286 (2010) (See pages: 19, 22).

[119] E. Tiesinga, B. J. Verhaar, and H. T. C. Stoof, "Threshold and resonance phenomena in ultracold ground-state collisions", Physical Review A **47**, 4114–4122 (1993) (See page: 20).

[120] A. J. Moerdijk and B. J. Verhaar, "Prospects for Bose-Einstein Condensation in Atomic ^{7}Li and ^{23}Na", Physical Review Letters **73**, 518–521 (1994) (See page: 20).

[121] P. O. Fedichev, Y. Kagan, G. V. Shlyapnikov, and J. T. M. Walraven, "Influence of Nearly Resonant Light on the Scattering Length in Low-Temperature Atomic Gases", Physical Review Letters **77**, 2913–2916 (1996) (See page: 20).

[122] M. Theis, G. Thalhammer, K. Winkler, M. Hellwig, G. Ruff, R. Grimm, and J. H. Denschlag, "Tuning the Scattering Length with an Optically Induced Feshbach Resonance", Physical Review Letters **93**, 123001 (2004) (See page: 20).

[123] K. Enomoto, K. Kasa, M. Kitagawa, and Y. Takahashi, "Optical Feshbach Resonance Using the Intercombination Transition", Physical Review Letters **101**, 203201 (2008) (See page: 20).

[124] S. Blatt, T. L. Nicholson, B. J. Bloom, J. R. Williams, J. W. Thomsen, P. S. Julienne, and J. Ye, "Measurement of Optical Feshbach Resonances in an Ideal Gas", Physical Review Letters **107**, 073202 (2011) (See page: 20).

[125] M. Yan, B. J. DeSalvo, B. Ramachandhran, H. Pu, and T. C. Killian, "Controlling Condensate Collapse and Expansion with an Optical Feshbach Resonance", Physical Review Letters **110**, 123201 (2013) (See page: 20).

[126] R. Zhang, Y. Cheng, H. Zhai, and P. Zhang, "Orbital Feshbach Resonance in Alkali-Earth Atoms", Physical Review Letters **115**, 135301 (2015) (See pages: 20, 21, 127).

[127] G. Pagano, M. Mancini, G. Cappellini, L. Livi, C. Sias, J. Catani, M. Inguscio, and L. Fallani, "Strongly Interacting Gas of Two-Electron Fermions at an Orbital Feshbach Resonance", Physical Review Letters **115**, 265301 (2015) (See pages: 20, 127).

[128] C. A. Regal, M. Greiner, and D. S. Jin, "Lifetime of Molecule-Atom Mixtures near a Feshbach Resonance in ^{40}K", Physical Review Letters **92**, 083201 (2004) (See page: 22).

[129] J. Xu, R. Zhang, Y. Cheng, P. Zhang, R. Qi, and H. Zhai, "Orbital Feshbach Resonance: A "wide"narrow resonance for Higher Transition Temperature Fermi Superfluid", (2016) (See pages: 22, 127).

[130] R. Grimm, M. Weidemüller, and Y. B. Ovchinnikov, "Optical Dipole Traps for Neutral Atoms", in *Advances In Atomic, Molecular, and Optical Physics*, Vol. 42, edited by B. B. H. Walther (Academic Press, 2000), pp. 95–170 (See pages: 23, 62, 76).

[131] V. A. Dzuba and A. Derevianko, "Dynamic polarizabilities and related properties of clock states of the ytterbium atom", Journal of Physics B: Atomic, Molecular and Optical Physics **43**, 074011 (2010) (See pages: 23, 97).

[132] N. D. Lemke, A. D. Ludlow, Z. W. Barber, T. M. Fortier, S. A. Diddams, Y. Jiang, S. R. Jefferts, T. P. Heavner, T. E. Parker, and C. W. Oates, "Spin-1/2 Optical Lattice Clock", Physical Review Letters **103**, 063001 (2009) (See pages: 24, 91).

[133] W. Kohn, "Analytic Properties of Bloch Waves and Wannier Functions", Physical Review **115**, 809–821 (1959) (See page: 28).

[134] H. Yokoyama and H. Shiba, "Variational Monte-Carlo Studies of Hubbard Model. I", Journal of the Physical Society of Japan **56**, 1490–1506 (1987) (See page: 30).

[135] C. J. Halboth and W. Metzner, "Renormalization-group analysis of the two-dimensional Hubbard model", Physical Review B **61**, 7364–7377 (2000) (See page: 30).

[136] M. Hinczewski and A. N. Berker, "Two superconducting phases in the d=3 Hubbard model", The European Physical Journal B - Condensed Matter and Complex Systems **48**, 1–17 (2005) (See page: 30).

[137] P. W. Anderson, "Theory of magnetic exchange interactions: exchange in insulators and semiconductors", Solid state physics **14**, 99–214 (1963) (See page: 30).

[138] Y. Nagaoka, "Ferromagnetism in a Narrow, Almost Half-Filled *s* Band", Physical Review **147**, 392–405 (1966) (See page: 30).

[139] T. Obermeier, T. Pruschke, and J. Keller, "Ferromagnetism in the large-U Hubbard model", Physical Review B **56**, R8479–R8482 (1997) (See page: 30).

[140] G. Senatore and N. H. March, "Recent progress in the field of electron correlation", Reviews of Modern Physics **66**, 445–479 (1994) (See page: 30).

[141] T. Esslinger, "Fermi-Hubbard Physics with Atoms in an Optical Lattice", Annual Review of Condensed Matter Physics **1**, 129–152 (2010) (See page: 30).

[142] E. H. Lieb and F. Y. Wu, "Absence of Mott Transition in an Exact Solution of the Short-Range, One-Band Model in One Dimension", Physical Review Letters **20**, 1445–1448 (1968) (See page: 30).

[143] F. H. L. Essler, V. E. Korepin, and K. Schoutens, "Complete solution of the one-dimensional Hubbard model", Physical Review Letters **67**, 3848–3851 (1991) (See page: 30).

[144] R. W. Cherng, G. Refael, and E. Demler, "Superfluidity and Magnetism in Multicomponent Ultracold Fermions", Physical Review Letters **99**, 130406 (2007) (See page: 30).

[145] N. Read and S. Sachdev, "Some features of the phase diagram of the square lattice SU(N) antiferromagnet", Nuclear Physics B **316**, 609–640 (1989) (See page: 30).

[146] R. Micnas, J. Ranninger, and S. Robaszkiewicz, "Superconductivity in narrow-band systems with local nonretarded attractive interactions", Reviews of Modern Physics **62**, 113–171 (1990) (See page: 31).

[147] M. Iskin and C. A. R. S. de Melo, "Superfluid and Insulating Phases of Fermion Mixtures in Optical Lattices", Physical Review Letters **99**, 080403 (2007) (See page: 31).

[148] A. Moreo and D. J. Scalapino, "Cold Attractive Spin Polarized Fermi Lattice Gases and the Doped Positive U Hubbard Model", Physical Review Letters **98**, 216402 (2007) (See page: 31).

[149] A. F. Ho, M. A. Cazalilla, and T. Giamarchi, "Quantum simulation of the Hubbard model: The attractive route", Physical Review A **79**, 033620 (2009) (See page: 31).

[150] R. Staudt, M. Dzierzawa, and A. Muramatsu, "Phase diagram of the three-dimensional Hubbard model at half filling", The European Physical Journal B - Condensed Matter and Complex Systems **17**, 411–415 (2000) (See page: 33).

[151] N. Blümer and E. V. Gorelik, "Mott transitions in the half-filled SU($2M$) symmetric Hubbard model", Physical Review B **87**, 085115 (2013) (See pages: 33, 121).

[152] H. Yanatori and A. Koga, "Finite Temperature Phase Transitions in the SU(N) Hubbard model", (2016) (See page: 33).

[153] H. Song and M. Hermele, "Mott insulators of ultracold fermionic alkaline earth atoms in three dimensions", Physical Review B **87**, 144423 (2013) (See page: 34).

[154] S. R. Manmana, K. R. A. Hazzard, G. Chen, A. E. Feiguin, and A. M. Rey, "SU(*N*) magnetism in chains of ultracold alkaline-earth-metal atoms: mott transitions and quantum correlations", Physical Review A **84**, 043601 (2011) (See pages: 34, 42, 126).

[155] K. Huang, *Statistical mechanics* (Wiley, 1987), 516 pp. (See pages: 34, 82).

[156] D. F. B. ten Haaf and J. M. J. van Leeuwen, "High-temperature series expansions for the Hubbard model", Physical Review B **46**, 6313–6327 (1992) (See page: 36).

[157] J. A. Henderson, J. Oitmaa, and M. C. B. Ashley, "High-temperature expansion for the single-band Hubbard model", Physical Review B **46**, 6328–6337 (1992) (See page: 36).

[158] J. Oitmaa, C. Hamer, and W. Zheng, *Series expansion methods for strongly interacting lattice models* (Cambridge University Press, 2006) (See page: 36).

[159] S. Fuchs, E. Gull, L. Pollet, E. Burovski, E. Kozik, T. Pruschke, and M. Troyer, "Thermodynamics of the 3D Hubbard Model on Approaching the Néel Transition", Physical Review Letters **106**, 030401 (2011) (See page: 36).

[160] K. R. A. Hazzard, V. Gurarie, M. Hermele, and A. M. Rey, "High-temperature properties of fermionic alkaline-earth-metal atoms in optical lattices", Physical Review A **85**, 041604 (2012) (See page: 36).

[161] Z. Cai, H.-H. Hung, L. Wang, and C. Wu, "Quantum magnetic properties of the *SU*(2*N*) Hubbard model in the square lattice: A quantum Monte Carlo study", Physical Review B **88**, 125108 (2013) (See page: 42).

[162] F. F. Assaad, "Phase diagram of the half-filled two-dimensional SU(*N*) Hubbard-Heisenberg model: A quantum Monte Carlo study", Physical Review B **71**, 075103 (2005) (See pages: 43, 44, 121, 126).

[163] T. A. Tóth, A. M. Läuchli, F. Mila, and K. Penc, "Three-Sublattice Ordering of the SU(3) Heisenberg Model of Three-Flavor Fermions on the Square and Cubic Lattices", Physical Review Letters **105**, 265301 (2010) (See pages: 43, 44).

[164] P. Corboz, A. M. Läuchli, K. Penc, M. Troyer, and F. Mila, "Simultaneous Dimerization and SU(4) Symmetry Breaking of 4-Color Fermions on the Square Lattice", Physical Review Letters **107**, 215301 (2011) (See pages: 43, 44, 126).

[165] S. Capponi, P. Lecheminant, and K. Totsuka, "Phases of one-dimensional SU(N) cold atomic Fermi gases –from molecular Luttinger liquids to topological phases", (2015) (See page: 42).

[166] L. Messio and F. Mila, "Entropy Dependence of Correlations in One-Dimensional SU(N) Antiferromagnets", Physical Review Letters **109**, 205306 (2012) (See page: 42).

[167] G. Szirmai, E. Szirmai, A. Zamora, and M. Lewenstein, "Gauge fields emerging from time-reversal symmetry breaking for spin-5/2 fermions in a honeycomb lattice", Physical Review A **84**, 011611 (2011) (See page: 44).

[168] M. P. Sarachik, E. Corenzwit, and L. D. Longinotti, "Resistivity of Mo-Nb and Mo-Re Alloys Containing 1% Fe", Physical Review **135**, A1041–A1045 (1964) (See page: 45).

[169] S. Doniach, "The Kondo lattice and weak antiferromagnetism", Physica B+C **91**, 231–234 (1977) (See pages: 45, 98).

[170] K. Andres, J. E. Graebner, and H. R. Ott, "4f-Virtual-Bound-State Formation in CeAl$_3$ at Low Temperatures", Physical Review Letters **35**, 1779–1782 (1975) (See page: 45).

[171] J. D. Thompson, J. M. Lawrence, and Z. Fisk, "Scaling in heavy-fermion systems", Journal of Low Temperature Physics **95**, 59–74 (1994) (See page: 45).

[172] F. Steglich, J. Aarts, C. D. Bredl, W. Lieke, D. Meschede, W. Franz, and H. Schäfer, "Superconductivity in the Presence of Strong Pauli Paramagnetism: CeCu$_2$Si$_2$", Physical Review Letters **43**, 1892–1896 (1979) (See page: 46).

[173] C. Petrovic, P. G. Pagliuso, M. F. Hundley, R. Movshovich, J. L. Sarrao, J. D. Thompson, Z. Fisk, and P. Monthoux, "Heavy-fermion superconductivity in CeCoIn 5 at 2.3 K", Journal of Physics: Condensed Matter **13**, L337 (2001) (See page: 46).

[174] B. D. White, J. D. Thompson, and M. B. Maple, "Unconventional superconductivity in heavy-fermion compounds", Physica C: Superconductivity and its Applications, Superconducting Materials: Conventional, Unconventional and Undetermined **514**, 246–278 (2015) (See page: 46).

[175] C. Lacroix and M. Cyrot, "Phase diagram of the Kondo lattice", Physical Review B **20**, 1969–1976 (1979) (See pages: 47, 98).

[176] H. Tsunetsugu, M. Sigrist, and K. Ueda, "The ground-state phase diagram of the one-dimensional Kondo lattice model", Reviews of Modern Physics **69**, 809–864 (1997) (See page: 48).

[177] M. A. Ruderman and C. Kittel, "Indirect Exchange Coupling of Nuclear Magnetic Moments by Conduction Electrons", Physical Review **96**, 99–102 (1954) (See page: 48).

[178] T. Kasuya, "A Theory of Metallic Ferro- and Antiferromagnetism on Zener's Model", Progress of Theoretical Physics **16**, 45–57 (1956) (See page: 48).

[179] K. Yosida, "Magnetic Properties of Cu-Mn Alloys", Physical Review **106**, 893–898 (1957) (See page: 48).

[180] R. Zhang, D. Zhang, Y. Cheng, W. Chen, P. Zhang, and H. Zhai, "Kondo effect in alkaline-earth-metal atomic gases with confinement-induced resonances", Physical Review A **93**, 043601 (2016) (See pages: 49, 126).

[181] H. J. Metcalf and P. van Straten, *Laser cooling and trapping* (Springer, Berlin, 2002) (See page: 51).

[182] H. J. Metcalf and P. van Straten, "Deceleration of an Atomic Beam", in *Laser Cooling and Trapping* (Springer, Berlin, 2002) (See page: 54).

[183] B. E. A. Saleh and M. C. Teich, "Nonlinear optics", in *Fundamentals of Photonics* (John Wiley & Sons, 2007) (See page: 58).

[184] M. Tabachnyk, "Aufbau eines Referenzlasers für den 399nm $^1S_0 \rightarrow {}^1P_1$ Übergang von Ytterbium.", Bachelor's thesis (Ludwig-Maximilians-Universität, München, 2012) (See page: 58).

[185] E. D. Black, "An introduction to Pound–Drever–Hall laser frequency stabilization", American Journal of Physics **69**, 79–87 (2001) (See page: 59).

[186] P. Ketterer, "A stable laser setup for the 578 nm clock transition of Ytterbium", Master's thesis (Ludwig-Maximilians-Universität, München, 2012) (See page: 59).

[187] E. L. Raab, M. Prentiss, A. Cable, S. Chu, and D. E. Pritchard, "Trapping of Neutral Sodium Atoms with Radiation Pressure", Physical Review Letters **59**, 2631–2634 (1987) (See page: 59).

[188] H. J. Metcalf and P. van Straten, "Optical Traps for Neutral Atoms", in *Laser Cooling and Trapping* (Springer, Berlin, 2002) (See page: 59).

[189] R. Maruyama, R. H. Wynar, M. V. Romalis, A. Andalkar, M. D. Swallows, C. E. Pearson, and E. N. Fortson, "Investigation of sub-Doppler cooling in an ytterbium magneto-optical trap", Physical Review A **68**, 011403 (2003) (See page: 59).

[190] X. Xu, T. H. Loftus, M. J. Smith, J. L. Hall, A. Gallagher, and J. Ye, "Dynamics in a two-level atom magneto-optical trap", Physical Review A **66**, 011401 (2002) (See page: 59).

[191] P. J. Ungar, D. S. Weiss, E. Riis, and S. Chu, "Optical molasses and multilevel atoms: theory", Journal of the Optical Society of America B **6**, 2058 (1989) (See page: 60).

[192] J. Dalibard and C. Cohen-Tannoudji, "Laser cooling below the Doppler limit by polarization gradients: simple theoretical models", Journal of the Optical Society of America B **6**, 2023 (1989) (See page: 60).

[193] C. N. Cohen-Tannoudji and W. D. Phillips, "New mechanisms for laser cooling", Physics Today **43**, 33–40 (1990) (See page: 60).

[194] S. Stellmer, B. Pasquiou, R. Grimm, and F. Schreck, "Laser Cooling to Quantum Degeneracy", Physical Review Letters **110**, 263003 (2013) (See page: 60).

[195] S. Stellmer, R. Grimm, and F. Schreck, "Production of quantum-degenerate strontium gases", Physical Review A **87**, 013611 (2013) (See page: 60).

[196] H. J. Metcalf and P. van Straten, "Evaporative cooling", in *Laser Cooling and Trapping* (Springer, Berlin, 2002) (See page: 64).

[197] K. D. Nelson, X. Li, and D. S. Weiss, "Imaging single atoms in a three-dimensional array", Nature Physics **3**, 556–560 (2007) (See page: 68).

[198] E. Haller, J. Hudson, A. Kelly, D. A. Cotta, B. Peaudecerf, G. D. Bruce, and S. Kuhr, "Single-atom imaging of fermions in a quantum-gas microscope", Nature Physics **11**, 738–742 (2015) (See page: 68).

[199] D. Greif, M. F. Parsons, A. Mazurenko, C. S. Chiu, S. Blatt, F. Huber, G. Ji, and M. Greiner, "Site-resolved imaging of a fermionic Mott insulator", (2015) (See page: 68).

[200] L. W. Cheuk, M. A. Nichols, M. Okan, T. Gersdorf, V. V. Ramasesh, W. S. Bakr, T. Lompe, and M. W. Zwierlein, "Quantum-Gas Microscope for Fermionic Atoms", Physical Review Letters **114**, 193001 (2015) (See page: 68).

[201] O. Morice, Y. Castin, and J. Dalibard, "Refractive index of a dilute Bose gas", Physical Review A **51**, 3896–3901 (1995) (See page: 68).

[202] C. C. Bradley, C. A. Sackett, and R. G. Hulet, "Bose-Einstein Condensation of Lithium: Observation of Limited Condensate Number", Physical Review Letters **78**, 985–989 (1997) (See page: 69).

[203] M. R. Andrews, D. M. Kurn, H.-J. Miesner, D. S. Durfee, C. G. Townsend, S. Inouye, and W. Ketterle, "Propagation of Sound in a Bose-Einstein Condensate", Physical Review Letters **79**, 553–556 (1997) (See page: 69).

[204] F. Zernike, "Phase contrast, a new method for the microscopic observation of transparent objects part II", **9**, 974–986 (1942) (See page: 69).

[205] F. Zernike, "Phase contrast, a new method for the microscopic observation of transparent objects", **9**, 686–698 (1942) (See page: 69).

[206] F. Zernike, "How I Discovered Phase Contrast", **121**, 345–349 (1955) (See page: 69).

[207] G. Reinaudi, T. Lahaye, Z. Wang, and D. Guéry-Odelin, "Strong saturation absorption imaging of dense clouds of ultracold atoms", Optics Letters **32**, 3143 (2007) (See page: 70).

[208] C. Jeff, *Depth of Field in Depth*, (2004) http://www.largeformatphotography.info/articles/DoFinDepth.pdf (visited on 03/30/2016) (See page: 71).

[209] C.-L. Hung, X. Zhang, L.-C. Ha, S.-K. Tung, N. Gemelke, and C. Chin, "Extracting density–density correlations from in situ images of atomic quantum gases", New Journal of Physics **13**, 075019 (2011) (See page: 72).

[210] L. P. Pitaevskii and S. Stringari, *Bose-Einstein Condensation* (Clarendon Press, Apr. 3, 2003), 392 pp. (See page: 72).

[211] M. Inguscio, W. Ketterle, and C. Salomon, *Ultra-cold Fermi Gases* (IOS Press, Apr. 18, 2008), 933 pp. (See page: 72).

[212] M. Greiner, O. Mandel, T. Esslinger, T. W. Hänsch, and I. Bloch, "Quantum phase transition from a superfluid to a Mott insulator in a gas of ultracold atoms", **415**, 39–44 (2002) (See page: 75).

[213] T. Stöferle, H. Moritz, C. Schori, M. Köhl, and T. Esslinger, "Transition from a Strongly Interacting 1D Superfluid to a Mott Insulator", Physical Review Letters **92**, 130403 (2004) (See page: 75).

[214] F. Gerbier, A. Widera, S. Fölling, O. Mandel, T. Gericke, and I. Bloch, "Interference pattern and visibility of a Mott insulator", Physical Review A **72**, 053606 (2005) (See page: 75).

[215] S. Stellmer, R. Grimm, and F. Schreck, "Detection and manipulation of nuclear spin states in fermionic strontium", Physical Review A **84**, 043611 (2011) (See page: 76).

[216] S. Taie, Y. Takasu, S. Sugawa, R. Yamazaki, T. Tsujimoto, R. Murakami, and Y. Takahashi, "Realization of a $SU(2) \times SU(6)$ System of Fermions in a Cold Atomic Gas", Physical Review Letters **105**, 190401 (2010) (See page: 76).

[217] L. D. Carr, G. V. Shlyapnikov, and Y. Castin, "Achieving a BCS Transition in an Atomic Fermi Gas", Physical Review Letters **92**, 150404 (2004) (See page: 83).

[218] S. Giorgini, L. P. Pitaevskii, and S. Stringari, "Theory of ultracold atomic Fermi gases", Reviews of Modern Physics **80**, 1215–1274 (2008) (See page: 84).

[219] G. M. Bruun and C. W. Clark, "Ideal gases in time-dependent traps", Physical Review A **61**, 061601 (2000) (See page: 84).

[220] L. D. Landau, "The Theory of a Fermi Liquid", Journal of Experimental and Theoretical Physics **3**, 920 (1956) (See page: 86).

[221] L. D. Landau, "Oscillations in a Fermi Liquid", Journal of Experimental and Theoretical Physics **5**, 101 (1957) (See page: 86).

[222] R. Jáuregui, N. Poli, G. Roati, and G. Modugno, "Anharmonic parametric excitation in optical lattices", Physical Review A **64**, 033403 (2001) (See page: 89).

[223] K. M. Jones, E. Tiesinga, P. D. Lett, and P. S. Julienne, "Ultracold photoassociation spectroscopy: Long-range molecules and atomic scattering", Reviews of Modern Physics **78**, 483–535 (2006) (See page: 90).

[224] J. Weiner, V. S. Bagnato, S. Zilio, and P. S. Julienne, "Experiments and theory in cold and ultracold collisions", Reviews of Modern Physics **71**, 1–85 (1999) (See page: 90).

[225] A. D. Ludlow, M. M. Boyd, J. Ye, E. Peik, and P. O. Schmidt, "Optical atomic clocks", Reviews of Modern Physics **87**, 637–701 (2015) (See page: 91).

[226] X. Zhang, M. Bishof, S. L. Bromley, C. V. Kraus, M. S. Safronova, P. Zoller, A. M. Rey, and J. Ye, "Spectroscopic observation of SU(N)-symmetric interactions in Sr orbital magnetism", **345**, 1467–1473 (2014) (See page: 91).

[227] J. Ye, H. J. Kimble, and H. Katori, "Quantum State Engineering and Precision Metrology Using State-Insensitive Light Traps", **320**, 1734–1738 (2008) (See page: 93).

[228] H. Katori, M. Takamoto, V. G. Pal'chikov, and V. D. Ovsiannikov, "Ultrastable Optical Clock with Neutral Atoms in an Engineered Light Shift Trap", Physical Review Letters **91**, 173005 (2003) (See page: 93).

[229] Z. W. Barber, J. E. Stalnaker, N. D. Lemke, N. Poli, C. W. Oates, T. M. Fortier, S. A. Diddams, L. Hollberg, C. W. Hoyt, A. V. Taichenachev, and V. I. Yudin, "Optical Lattice Induced Light Shifts in an Yb Atomic Clock", Physical Review Letters **100**, 103002 (2008) (See page: 93).

[230] C. Schweizer, "A bi-chromatic optical lattice setup for Kondo-lattice physics with ultracold ytterbium atoms", Master's thesis (Ludwig-Maximilians-Universität, München, 2013) (See pages: 93, 126).

[231] G. K. Campbell, M. M. Boyd, J. W. Thomsen, M. J. Martin, S. Blatt, M. D. Swallows, T. L. Nicholson, T. Fortier, C. W. Oates, S. A. Diddams, N. D. Lemke, P. Naidon, P. Julienne, J. Ye, and A. D. Ludlow, "Probing Interactions Between Ultracold Fermions", **324**, 360–363 (2009) (See page: 94).

[232] A. D. Ludlow, N. D. Lemke, J. A. Sherman, C. W. Oates, G. Quéméner, J. von Stecher, and A. M. Rey, "Cold-collision-shift cancellation and inelastic scattering in a Yb optical lattice clock", Physical Review A **84**, 052724 (2011) (See pages: 94, 98).

[233] A. M. Rey, A. V. Gorshkov, and C. Rubbo, "Many-Body Treatment of the Collisional Frequency Shift in Fermionic Atoms", Physical Review Letters **103**, 260402 (2009) (See page: 94).

[234] O. Mandel, M. Greiner, A. Widera, T. Rom, T. W. Hänsch, and I. Bloch, "Controlled collisions for multi-particle entanglement of optically trapped atoms", **425**, 937–940 (2003) (See page: 95).

[235] O. Mandel, M. Greiner, A. Widera, T. Rom, T. W. Hänsch, and I. Bloch, "Coherent Transport of Neutral Atoms in Spin-Dependent Optical Lattice Potentials", Physical Review Letters **91**, 010407 (2003) (See page: 95).

[236] D. Jaksch, H.-J. Briegel, J. I. Cirac, C. W. Gardiner, and P. Zoller, "Entanglement of Atoms via Cold Controlled Collisions", Physical Review Letters **82**, 1975–1978 (1999) (See page: 95).

[237] D. L. Haycock, P. M. Alsing, I. H. Deutsch, J. Grondalski, and P. S. Jessen, "Mesoscopic Quantum Coherence in an Optical Lattice", Physical Review Letters **85**, 3365–3368 (2000) (See page: 95).

[238] G. Jotzu, M. Messer, F. Görg, D. Greif, R. Desbuquois, and T. Esslinger, "Creating State-Dependent Lattices for Ultracold Fermions by Magnetic Gradient Modulation", Physical Review Letters **115**, 073002 (2015) (See page: 95).

[239] P. M. Duarte, R. A. Hart, T.-L. Yang, X. Liu, T. Paiva, E. Khatami, R. T. Scalettar, N. Trivedi, and R. G. Hulet, "Compressibility of a Fermionic Mott Insulator of Ultracold Atoms", Physical Review Letters **114**, 070403 (2015) (See pages: 103, 107).

[240] S. Nascimbène, N. Navon, K. J. Jiang, F. Chevy, and C. Salomon, "Exploring the thermodynamics of a universal Fermi gas", **463**, 1057–1060 (2010) (See pages: 107, 110).

[241] N. Gemelke, X. Zhang, C.-L. Hung, and C. Chin, "In situ observation of incompressible Mott-insulating domains in ultracold atomic gases", **460**, 995–998 (2009) (See page: 107).

[242] V. Dribinski, A. Ossadtchi, V. A. Mandelshtam, and H. Reisler, "Reconstruction of Abel-transformable images: The Gaussian basis-set expansion Abel transform method", Review of Scientific Instruments **73**, 2634–2642 (2002) (See pages: 108, 113).

[243] T.-L. Ho and Q. Zhou, "Obtaining the phase diagram and thermodynamic quantities of bulk systems from the densities of trapped gases", Nature Physics **6**, 131–134 (2010) (See page: 110).

[244] A. J. R. Heck, R. N. Zare, and D. W. Chandler, "Photofragment imaging of methane", The Journal of Chemical Physics **104**, 4019–4030 (1996) (See page: 112).

[245] S. J. Cavanagh, S. T. Gibson, M. N. Gale, C. J. Dedman, E. H. Roberts, and B. R. Lewis, "High-resolution velocity-map-imaging photoelectron spectroscopy of the O^- photodetachment fine-structure transitions", Physical Review A **76**, 052708 (2007) (See page: 112).

[246] L. Montgomery Smith, D. R. Keefer, and S. I. Sudharsanan, "Abel inversion using transform techniques", Journal of Quantitative Spectroscopy and Radiative Transfer **39**, 367–373 (1988) (See page: 113).

[247] E. V. Gorelik and N. Blümer, "Mott transitions in ternary flavor mixtures of ultracold fermions on optical lattices", Physical Review A **80**, 051602 (2009) (See page: 119).

[248] U. Schneider, L. Hackermüller, J. P. Ronzheimer, S. Will, S. Braun, T. Best, I. Bloch, E. Demler, S. Mandt, D. Rasch, and A. Rosch, "Fermionic transport and out-of-equilibrium dynamics in a homogeneous Hubbard model with ultracold atoms", Nature Physics **8**, 213–218 (2012) (See page: 121).

[249] B. D. Esry, C. H. Greene, and J. P. Burke, "Recombination of Three Atoms in the Ultracold Limit", Physical Review Letters **83**, 1751–1754 (1999) (See page: 123).

[250] J. Söding, D. Guéry-Odelin, P. Desbiolles, F. Chevy, H. Inamori, and J. Dalibard, "Three-body decay of a rubidium Bose–Einstein condensate", Applied Physics B **69**, 257–261 (2014) (See page: 123).

[251] P. O. Fedichev, M. W. Reynolds, and G. V. Shlyapnikov, "Three-Body Recombination of Ultracold Atoms to a Weakly Bound *s* Level", Physical Review Letters **77**, 2921–2924 (1996) (See page: 123).

[252] T. Weber, J. Herbig, M. Mark, H.-C. Nägerl, and R. Grimm, "Three-Body Recombination at Large Scattering Lengths in an Ultracold Atomic Gas", Physical Review Letters **91**, 123201 (2003) (See page: 123).

[253] M. S. Safronova, S. G. Porsev, and C. W. Clark, "Ytterbium in Quantum Gases and Atomic Clocks: van der Waals Interactions and Blackbody Shifts", Physical Review Letters **109**, 230802 (2012) (See page: 124).

[254] B. Bauer, P. Corboz, A. M. Läuchli, L. Messio, K. Penc, M. Troyer, and F. Mila, "Three-sublattice order in the SU(3) Heisenberg model on the square and triangular lattice", Physical Review B **85**, 125116 (2012) (See page: 126).

[255] M. A. Cazalilla and A. M. Rey, "Ultracold Fermi gases with emergent SU(N) symmetry", Reports on Progress in Physics **77**, 124401 (2014) (See page: 126).

[256] R. A. Hart, P. M. Duarte, T.-L. Yang, X. Liu, T. Paiva, E. Khatami, R. T. Scalettar, N. Trivedi, D. A. Huse, and R. G. Hulet, "Observation of antiferromagnetic correlations in the Hubbard model with ultracold atoms", **519**, 211–214 (2015) (See page: 126).

[257] R. Sensarma, D. Pekker, M. D. Lukin, and E. Demler, "Modulation Spectroscopy and Dynamics of Double Occupancies in a Fermionic Mott Insulator", Physical Review Letters **103**, 035303 (2009) (See page: 126).

[258] A. Tokuno and T. Giamarchi, "Finite-temperature dynamical properties of SU(N) fermionic Hubbard models in the spin-incoherent regime", Physical Review A **86**, 053614 (2012) (See page: 126).

Danksagung

Ganz herzlich möchte ich mich auch bei ldiko Kecskesi, Marianne Kargl und Kristina Schuldt bedanken, die mit ihrer stets freundlichen und hilfsbereiten Art bei organisatorischen Abläufen, mir hilfreich zur Seite standen.

Zu guter Letzt möchte ich mich bei meinen Eltern für die großartige Unterstützung in all den Jahren bedanken.